Eloïse Bovet

Mechanics of Snow Avalanches and Interaction with Structures

Tesi per il conseguimento del titolo di Dottore di Ricerca
XXIV Ciclo (2009 - 2010 - 2011 - 2012)

Dottorato di Ricerca in Ingegneria delle Strutture
Politecnico di Torino

Dicembre 2012

To Antonio, Cédric
and my parents

Acknowledgments

Summary

The interaction between snow avalanches and structures represents a topic of interest both from a scientific point of view, since different study domains and knowledge are involved (structural mechanics, fluid dynamics. . .), and due to its applicability in practice for a correct design of structures located in avalanche risk areas. In this thesis the interaction between the snow avalanches and structures is investigated together with the avalanche dynamics.

   Chapter 1 deals with the state of the art of the avalanche dynamics and interaction between snow in movement and structures. The snow avalanches are classified, giving the basics concepts. Secondly the different approaches to study the interaction between avalanches and structures are analysed. The observations of the damages caused on structures by real events are not sufficient to understand all the complex processes inner the dynamics itself and the impact strictly. Furthermore experiments are carried in order to analyse deeper velocity profiles, to which pressure ones are linked, entrainment of snow, from which the volumes involved depended as well as the pressure behaviour. In fact pressure values evolve in time and in space and change with the obstacle shape. Experimental studies are made at real scale avalanches, in the test sites, or at reduced scale, in laboratory chutes. To translate the results from the small scale to the real one similitude criteria have to be satisfied. Hence the dimensional analysis is proposed. Another approach to study the problem in object is to use analytical and numerical models. For this reason a summary of the state of art of dynamics models is proposed, focusing the attention on those taking into account the erosion and the interaction with obstacles. From both experimental and theoretical analysis recommendations are born in order to help the expert to correctly design the structures in avalanche areas.

   In **Chapter 2** a new model is described, able to provide the pressure and the velocity in all the points of the avalanche, without impose a proportional relationship between them. The model describe the evolution of the avalanche shape thanks to the level set method, suitable for free-boundary problems, and the Navier-Stokes equations, since the avalanche is considered a fluid. A first validation on experimental data of a laboratory chute is given. Afterwards the attention is set at the avalanche

bottom. In particular the boundary condition of the slip velocity is analysed, giving an analytical justification. The slip condition, coupled with a non-newtonian fluid, is able to correctly describe the velocity profile. Finally a new model for the erosion is proposed, starting from general continuum mechanics hypothesis. In particular both the avalanche and the snow at rest are considered as the same fluid having a viscosity depending from the shear rate. It is shown as the model is in agreement with other theories in the literature and takes into account the influence of snow and avalanche properties, the avalanche depth, the slope angle, and the position in the avalanche (front or tail).

Chapter 3 focuses the attention on the definition of a model to describe the impact of an avalanche with obstacles. Different approaches can be pursued: a stationary and a transient ones, as well as a two-dimensional analysis in the avalanche depth plane, in the slope plane and a three-dimensional one. Some preliminary simulations are shown and qualitatively compared with the state of the art concerning the impact pressure. For instance the pressure profile along the avalanche depth, the influence on the obstacle shape and dimension, and the dependence on the relative position obstacle-avalanche (directly or not directly exposed) are investigated.

In **Chapter 4** the new Italian P.ta Seehore test site is described. Its peculiarity is to study the small-medium avalanches that occurred with high frequency, since artificially triggered for safe reasons. The attention is focused on the design of an obstacle, located in the avalanche track, to study the interaction between snow in movement and structure. The static and dynamic test carried to characterise it are shown as well as its instrumentation. Finally an overview of the surveys is proposed focusing the attention on the measurements carried in some events.

Chapter 5 deals with the analysis of the measurement data concerning experiments in the P.ta Seehore test site from different point of view. Firstly, the erosion and deposition processes are analysed, using laser scan data, analytical and numerical methods and presenting a new cheap test to detect the net erosion and deposition. Secondly, a commercial dynamics model is applied to obtain the flow density and velocity at the obstacle, data not experimentally recorded. Thirdly, our dynamics model is used for instance to simulate the creation of a dihedral shape upward the obstacle, experimentally measured and to give information on the pressure. Finally analytical approaches are used to describe the pressure, applying for instance the Mohr-Coulomb criterion, to simulate the pressure in the avalanche tail. Concepts reported in the available recommendations, as for instance the compressibility of the snow during the impact are used too.

In **Chapter 6** applications concerning the impact against houses destroyed in 15th of December 2008 are reported. In particular both the transient and stationary models (in their two and three-dimensional versions) are applied and compared with a back-analysis of damages. General laws for the influence of the impact angle on the pressure are respected as well as the areas of positive and negative pressure.

In addition, the protection role played by a house on the structures downstream, especially in term of reduced pressures, is analysed.

The **Conclusions and outlooks** finalize the work.

Contents

Chapter 1

State of the art on snow avalanche-structure interaction

1.1 Slow and fast kinematics of snow

1.1.1 Avalanche definition and classification

Snow avalanche is defined as a rapid gravity-driven mass of snow that, once released by the snow pack rupture, moves down mountain slopes [15]. In fact the movement of the avalanche is principally due to the gravity, and not to the wind as in the snowdrift process, and it is rapid, with a velocity measured in m/s to contrast the creep and glide movements (see Sec. 1.1.2) that are measured in order of mm/day or cm/day.

An avalanche path can be divided into [205]:

the release zone: the area where the snow becomes unstable and, after the snow pack rupture, starts to move. Depending on the characteristic of this zone the avalanche can be classified into a **loose snow** avalanche (Fig. 1.12.a) or a **slab** one (Fig. 1.12.b). The former starts from a point and, collecting mass, develops into a fan-like shape, usually of small dimensions. It requires wet or dry cohesionless snow. The second has a well defined fracture line which confines the release zone. If its crown (upper limit) and its flanks (lateral limit) are well visible, the lower limit (the "stauchwall") is not always recognizable. Slab originates when a strong layer of cohesive snow is deposited on a weak layer, or when weak bonds between layers exist. Usually slab avalanches have more catastrophic effects than the loose snow avalanches, since they involve larger masses.

the flowing zone or the track: the slope between the starting zone and the de-

position one. It can be canalized (**channeled** avalanche) or an open slope (**open-slope** avalanche). Here, the avalanche is fully developed and attains its maximum velocity. The avalanche can erode significant quantity of mass, while generally the deposit is insignificant and arrives only in gullies and behind rocks.

the run-out zone: where the avalanche decelerates rapidly and deposits (Fig. 1.2.a).
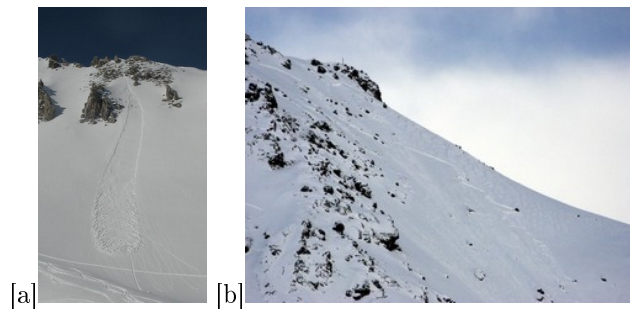
Figure 1.1: [a] Loose snow avalanche near Davos (CH). [b] A slab release at Seehore (see Ch. 4). Photos E. Bovet.

Several types of classifications exist for avalanches, based on different criteria. For instance, depending on the position of the the sliding surface, the **surface-layer** avalanches sliding within the snowcover are distinguished from the **full depth** ones moving on the ground (Fig. 3.16.b).

Based on the form of movement, three types of avalanches are defined: (i) flowing or dense-snow avalanches, which move close to the ground, (ii) powder or aerosol avalanches, which are less affected by the topography and (iii) mixed avalanches.

After the release, avalanche moves towards the valley. Impacting the ground irregularities, the slab creates rounded snow particles. The interstitial space is filled by air. Frequently a powder part surrounds the dense core. In this case a **mixed** avalanche is formed [204]. It is composed by three components: (i) the avalanche core or dense layer, (ii) the saltation layer and the (iii) powder cloud or aerosol.

The avalanche core is the densest part (200-500 kg/m^3) of the avalanche. It is composed by rounded particles with a diameter of few centimeters or rounded lumps of several meters: greater the cohesion in the snow and larger the particles. The motion of this layer is governed by the friction and collisional processes of the moving snow particles. The dense core is easily perturbed by irregularities in the terrain. Measurements from [74] show that the density is higher in the front of the avalanche than in the body. Usually density measurements are done with snow at rest, in the undisturbed snow cover or in the deposit. A **dense** avalanche is composed only by

this core. The velocity ranges between 1 and 30 m/s, its flow height between 0.3 and 3 m, and the pressure between 10 and 1000 kPa. The wet snow avalanches, compared to the dry ones, are slower (few meters per second up to 30 m/s) and therefore the runout distance is usually shorter. However, the impact on obstacles is considerable due to the higher density of wet snow.

The **saltation** layer is formed by particles ejected from the dense layer. It is located ahead and above the dense layer. The saltation layer contains particles ranging in size from fine-grained snow to snowballs up to about 50 centimeters in diameter. By video and pressure measurement [103, 185] the saltation layer can been identified. In fact this layer is characterised on having numerous individual peaks probably produced whenever a clods of snow strikes the load cell. The density is assumed to vary between 10 and 100 kg/m^3, the velocity between 20 and 60 m/s, the height between 1 and 5 m and the pressure between 20 and 200 kPa.

The powder cloud is formed by the particles that, from the saltation layer or directly from the snow cover, are brought into suspension by the airborne shear stress. Typical particle sizes are in a range from 0.1 mm to 1.2 mm. Powder clouds and saltation layer may move independently from the dense layer and are less influenced by terrain irregularities. The cloud part frequently covers longer distances. The dynamics of the powder snow avalanches is dominated by the turbulent air flow. Powder avalanches are normally generated from a dry, non-cohesive and low density new snow cover. The density is estimated between 1 and 10 kg/m^3, the velocity between 20 and 100 m/s, the height can reach hundred of meters and the pressure about between 1 and 20 kPa. **A powder or airborne** avalanche is an avalanche dominated by this component (Fig. 1.2.a).
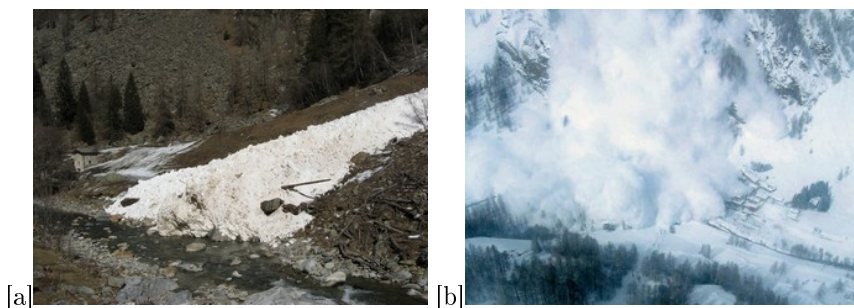
Figure 1.2: [a] A granular deposit in Gressoney's valley (AO). Photo E. Bovet. [b] A powder avalanche in Rhêmes' valley (AO). Photos RAVDA.

As concerns the avalanche size [78], the following classification by runout length and volume is made: **sluff** (path < 50 m, volume < 100 m^3), **small** (path < 100 m,

volume < 1.000 m^3), **medium** (path < 1.000 m, volume < 10.000 m^3), **large** (path 1-2 km, volume < 100.000 m^3) and **very large** (path $\sim$ 3 km, volume > 100.000 m^3) avalanches.

1.1.2   Creep and snow glide

In this section, to be complete, a general overview of the slow movements of the snow is given.

The snow cannot be considered a solid, since deformation stops after a limited time under a limited load, but a compressible fluid. A Newtonian fluid can be used with an axial viscosity, i.e. the ratio between stresses and deformation rates, remaining constant. This is an acceptable approximation, even if snow is better described as a non-Newtonian fluid, having the viscosity changing with load and deformation [181]. Because of its high viscosity, slow internal movements downwards take place [181]. Due to its internal weight the snowpack moves slowly and continuously down slope following two types of movement [112, 142]: snow creep and snow glide. **Snow creep** is caused by the weight of the snow cover that generates perpendicular and parallel to the slope forces. Hence snow creep v is the resultant of the vertical settlement w (associated to the fact that snow is a compressible fluid) of the snow cover and the internal shear deformation u parallel to the slope (Fig. 1.3). Typical creep rates are mm to cm per day. At the ground the snow creep is zero [140].
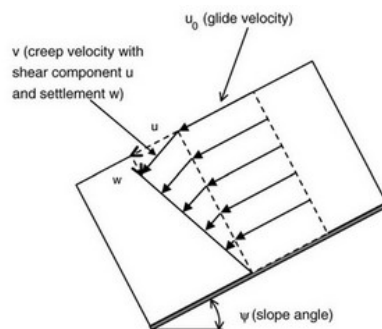
Figure 1.3: Creep and snow glide definition, from [140].

A movement in the snow-ground interface may occur too, called **snow glide** u_0. It represents the slip of the entire snow cover over the ground without essential deformation within the snow cover. Typical glide rates are mm to more than m per day. Remember that, on the other hand, the avalanches (the main object of this thesis) is of order of m per second.

The glide is facilitated by many factors [112, 121, 140], like a wet ground or with a low roughness, as long-bladed grass or bare rock. The bottom of the snow cover must have a temperature above 0 °C in order that a thin free water layer can be formed. In fact with a dry boundary layer (a temperature below 0°) snow cover does not glide even on a grass surface. A wet snow layer can be formed by a rainfall prior the first snow fall, melting by solar radiation or intrusion of liquid water flowing along the ground. Snow glide starts at a slope of 15° and increases with increasing inclinations ψ. Finally, since the weight increases the shear stress, a large snow depth (h) increases snow glide velocity. Sometimes this influence is obscured by changes in characteristic of the snow. Since the snow viscosity depends on temperature, each temperature change must cause a modification in glide viscosity [112].

Free water at the interface has two principal effects on glide mechanics. Firstly it promotes separation of the snowpack from the ground at the interface. In this way the irregularities on the ground surface are drowned, the friction diminishes and hence the snow can move [146]. Secondly, the increasing of water content decreases the snow viscosity. This influence on the stiffness of the snow slab makes movement of the snowpack over ground roughness features easier [146].

Pressure

Dynamic avalanche loads can be exceeded by higher static loads (<100 kN/m) on narrow masts or longer structures due to the creep and gliding, especially in areas with large snow depths and low ground roughness. Different snow pressure laws are presented in [140]. The snow pressure depends on the snow density, snow depth, slope angle, gliding factor and efficiency factor (i.e. the ratio of the real snow pressure to that acts on an infinitely long plane). If the design for supporting structures built in long lines is well know, the pressure on narrow structures like mast is not well established.

Based on the "back-pressure zone" concept, that is the range behind the barrier where additional compressive stresses are created, the Swiss guidelines affirm that the snow pressure S'_N [kN/m] per unit length across the slope on a rigid wall is:

$$S'_N = \rho g \frac{H^2}{2} KN \qquad (1.1)$$

where H is the vertical snow depth. N is a gliding factor and depends on the ground roughness and slope exposition. The creep-factor K depends on snow density ρ and on slope angle ψ. This formula is valid for infinitely long plane. On small obstacles, since additional end-effects are to be considered, additional terms, depending on the snow thickness and on the width of the structure, appear [140].

Another conservative model to calculate snow forces acting on a mast consists on considering an isolated snow block gliding free on the ground [140]. This model provides an upper limit for the snow pressure.

Finally [132, 133] found that snow creep pressure q on a mast is given by:

$$q = K_2 \rho g h^2 C \sin \psi \qquad (1.2)$$

where h is the depth measured perpendicular to the ground, K_2 is a factor depending on the snow depth and C depends on the mast diameter and on the slope angle ψ. This model gives a lower boundary for the snow pressure force [140].

The stresses in different sections of the masts can be computed from the strains. Measurements showed that the load increased with depth below the surface of the snow. The load distribution with depth for the mast is almost linear in the earlier winter but tends to be more uniform in the later winter, when the pressure was at its maximum [132]. The distribution for the wall element is different, with the highest pressure in the middle height of the element for the whole winter [143].

Plan de la Tour test site

In order to measure the snow-gliding and the pressure on defence structures, within the Operational programme Italy - France (Alps - ALCOTRA) Project "RiskNat − Gestione in sicurezza dei territori di montagna transfrontalieri" the "Plan de la Tour" test site has been realized. It is located in Aosta Valley in the release area of the avalanche that the 15th of December 2008 destroyed houses of Les Thoules village (see Ch. 6). The site is at 2550 m asl and it is characterised by a slope angle between 28° and 45°. Installed in October 2010, the instrumentation is located in the upper part of the release zone. In order to measure the snow-gliding two couples of snow-shoes connected to related specific snow-gliding sensors were placed: a couple within the area covered by snow umbrellas and another outside it. Data-loggers measuring the temperature at the snow/soil interface were placed close to each couple. The data are recorded continuously every 30 minutes. In addition the measurements of the pressure, caused by the slow movements on the defence structures, are performed by monitoring the deformation of one of the cross beams, composing the snow umbrella, and the overall force on the foundation. Eight strain transducers were installed on a beam of the retaining structure in order to evaluate the curvature under the snow load. Besides, strain gauges were directly stuck on both the plates constituting the link between the mast and the foundation rod. Power supply is given by a nearby solar panel and the acquisition system is composed by a programmable device which records the strain every 30 minutes. The combination of snow-gliding data with snow pressure measurements might help to understand the behaviour of snow umbrellas in avalanche release areas [19].

Model description

In this section a model, to describe both the slow movements of the snow cover and the related pressure, is proposed. It will be tested on the "Plan de la Tour" experimental

Table 1.1: Different values for the coefficients in Eq. 1.5.

Author	a_0	a_1
Kojima [126]	$8.64\ 10^6$	0.022
Mellor [150]	$5.00\ 10^7$	0.021
Fromm et al.[99]	$6.20\ 10^6$ (x-dir)	0.020 (x-dir)
	$6.4\ 10^6$ (z-dir)	0.026 (z-dir)

data when they will be available. A preliminary study on the creep is done considering the snow cover as a Stokes flow, since the low velocities involved [99]:

$$\nabla \cdot (\eta \nabla \mathbf{u}) = \nabla p + \mathbf{f} \qquad (1.3)$$

$$\nabla \cdot \mathbf{u} = 0 \qquad (1.4)$$

with η the viscosity, $\mathbf{u}$ the velocity vector, p the pressure and $\mathbf{f}$ the external force, that in our analysis is the gravitational one.

In literature different laws for the viscosity are present. For instance it can be estimated as:

$$\eta = a_0 e^{a_1 \rho} \qquad (1.5)$$

where the coefficients a_0 and a_1 are reported in Tab. 1.1.

Let's note that [99] used two different parameterizations to investigate the creep parallel (x-direction) and perpendicular to the slope (z-direction).

Two-dimensional analysis

A sample 2D of 0.2 m length for 1 m depth is considered. Eq. 1.3 is solved using the Finite Element Method Comsol Multiphisics tool [3]. As boundary condition the normal stress equal to zero on all the boundaries and a no-slip condition at the base are imposed. The density is considered equal to ρ=300 kg/m^3. Different slopes (Fig. 1.4.a,b) as well as various coefficients (Fig. 1.4.c) of the viscosities can be considered obtaining different results of pressure and displacement. Let note that the velocity is of order of 10^{-6}-10^{-8} m/s, comparable with the measures in mm-cm/day. An example of the snow deformed is shown in (Fig. 1.5.a). Finally the results are compared with a hydrostatic pressure showing that this last one is more cautionary in respect of the pressure calculated introducing a viscosity law (Fig. 1.5.b).

1.2   Different study approaches

Snow avalanches involve several aspects of human life, i.e civil constructions, transportation, tourism and energy supply (Fig. 1.6). To mitigate avalanche risk authorities
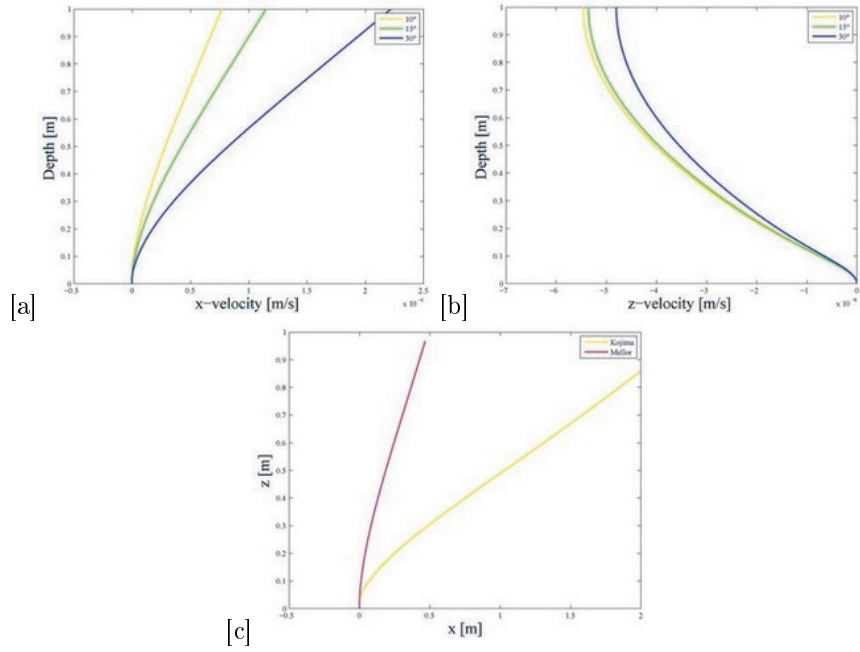
Figure 1.4: [a] Velocity parallel and [b] perpendicular to the ground for a slope of 10°, 15°, 30° for the Kojima case. [c] Displacement for a slope of 10°for the Kojima and Mellor case.
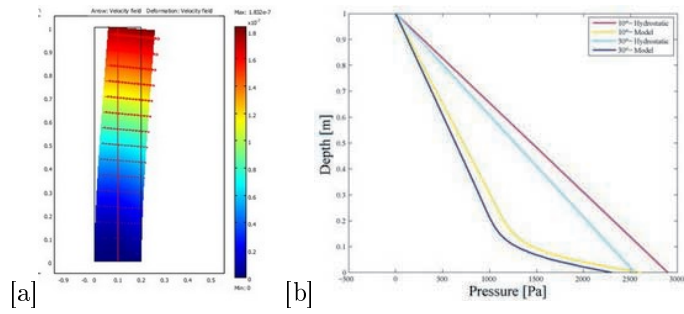
Figure 1.5: [a] Deformed shape at 10°for the Mellor cases and [b] comparison between the pressure obtained by the model and the hydrostatic pressure.

Table 1.2: Impact pressure and potential damage, from [145].

Impact pressure P_{dyn} [kPa]	Potential Damage
1	Break windows
5	Push in doors
30	Destroy wood-framed structures
100	Uproot mature spruce
1000	Move reinforced-concrete structures

can exploit two kinds of defense strategies: urban planning based on hazard maps and structural defenses. However, both these instruments are based on an estimation of the destructive forces induced by the avalanche impact.

The evaluation of the pressure caused by an impacting avalanche is fundamental in order to design correctly the structures located in avalanche area and, consequently, to guarantee the safety of persons, animals and objects. To reach this goal different basic concepts will be introduced, as the non-dimensional numbers useful to characterise the different regimes assumed by an avalanche, as well as the role of the dimension of the obstacle, of the avalanche kind (dense or powder) and of the dense flow-regime (gravitional or dilute). However, before to introduce this concepts and the different laws describing the pressure on obstacles, it must be briefly remembered the methods used by researchers in order to study this very complex problem: (i) back-analysis of real events, (ii) experimental approach at full-scale in test sites or at small-scale in laboratory, (iii) analytical methods and (iv) numerical techniques.

1.2.1 Back-analysis of real events

On the basis of the damages effects of real events [145], thanks to a structural analysis, the impinging pressure can be estimated (see Ch. 6) [37, 41, 97]. This analysis has to be pursued taking into account that the same magnitude pressure of a dense or of a powder avalanche can have a different effect on the damages [172]. The approximate average impact pressure and potential damage is given in Tab. 1.2, from [145], or in Fig. 1.7, in which differences occur depending on the avalanche kind, and in Figg. 1.8 and 1.9, in which the effects are divided into damages on people, building, natural spaces, infrastructures and works.

1.2.2 Experimental approach

The observation of the damages caused on structures by real events are not sufficient to understand all the complex processes inner the dynamics itself and the strictly impact.

Figure 1.6: [a] Damages of a building occurred in 1972 in Rhêmes' aalley (AO). [b] Damages during winter 2008-09 occurred in Champorcher's valley (AO). [c] Avalanche on the road in Gressoney's valley (AO) in 2008. [d] Damages on a ski-lift in 1971 in Aosta Valley. [e] Damages to wood, [f] to a car crashed, [g] to a pole, [h] to a house caused by the powder part of an avalanche occurred in Morgex (AO) in 1999. Photos RAVDA.

Impact pressure (kPa)	Avalanche type	Potential damages
1-3	Powder snow/ Aerosol	Destroys a lonely tree (without forest protection)
1-4		Breaks the windows
>5-10		Destroys the forest
3-6	Dense snow	Pushes the gates, brooks/ crushes walls, roofs
3		Turnaround of a freight car (18 t)
8.5		Turnaround of a locomotive (120 t)
10		Serious damage of timber structures
20-30		Destroys timber structures, breaks the trees
50-100		Destroys a well developed forest
100		Pulling out large fir trees
>300		Movement of large blocks
1000		Movement of the reinforced concrete structures

Figure 1.7: Swiss classification according to impact pressures and potential damages, from [172].

Degree	Physical parameters (order of magnitude)	Foreseeable effects on the stakes (part 1)	
		People *	Buildings
1 Very low	Affected surface: ~ 0,2 ha Average slab thickness: ~ 20 cm Deposited volume: ~ 100 m³ Impact pressure: ~ 2 kPa	Observer staying cool (except if somebody is carried along). Person carried along: - possible state of shock: momentary psychological disorder, - Light injury (requiring only basic medical cares without hospitalisation), - extremely rare death (except if the head is buried and if intervention time is over 15 minutes).	Generally no damages. Light structural damage: - furniture: damaged, - opening: pushed door, broken pane of window. Partial and very localised burying.
2 Low	Affected surface : ~ 1,0 ha Average slab thickness : ~ 40 cm Deposited volume : ~ 1 000 m³ Impact pressure : ~ 10 kPa	Calm observer but "being on the alert" (except if somebody is carried along). Person carried along: - frequent state of shock: temporary psychological distress which can be prolonged, nervous breakdown possible, - frequent slight injury, but usually without after-effects nor disability, - serious injury (requiring thorough/ intensive care with a hospitalisation: traumatism, hypothermia.), - possible death as the flow stops.	Low structural damage: - opening (doors, windows, shutters): often unusable, - balcony: damaged, - masonry wall: fissuring and possible partial collapse, - roof: partial crushing, torn off edge, ploughed up chimney. Buildings touched: partial burying and/ or destruction of a few.
3 Medium	Affected surface : ~ 5 ha Average slab thickness : ~ 80 cm Deposited volume : ~ 10 000 m³ Impact pressure : ~ 50 kPa	Agitated observer starting to fear for himself. Person carried along: - systematic state of shock: strong psychological disorder, nervous breakdown possible, - frequent serious injury, with possibility of after-effects or disablement, - frequent death.	Moderate structural damage: - opening: destroyed, - walls: fissuring, deformation, possible collapse, - roof: general crushing, or partial transport. Buildings touched: destruction of the majority. Destruction of old dwellings.
4 High	Affected surface : ~ 20 ha Average slab thickness : ~ 150 cm Deposited Volume : ~ 80 000 m³ Impact pressure : ~ 200 kPa	Nearby observer which can panic. Person carried along: - almost systematic serious injury, - rapid and very frequent death.	Significant structural damage: - walls: levelling (possible by level of construction), multiple collapses, - roof: destruction. Buildings touched: Almost total destruction. Often total burying.
5 Very high	Affected surface : ~ 50 ha Average slab thickness: ~ 250 cm Deposited Volume: ≥~ 400 000 m³ Impact pressure: ~ 500 kPa	Observer panicking. Person carried along: - almost systematic fatal injury, - instantaneous death.	Total structural damage, generalized ruin: - walls: levelling, systematic collapses, - particularly reinforced concrete structures: fissuring /at least partial destruction.

* : non relevant criterion in its number

Figure 1.8: Intensity scale for the avalanche risk (part I), from [172].

| Degree | Foreseeable effects on the stakes (part 2) | | Other criteria |
	Infrastructures and works	Natural and agricultural spaces	
1 Very low	No damages. Road locally and temporarily slippery and blocked, but which can still be used by a well-equipped 4x4 vehicle.	Broken branches of tree.	-
2 Low	Low damage: - wood/ lattice post, line: partial destruction, - cars, bus: turned around (and buried). Road can turn out to be locally and temporarily impracticable (even for a equipped 4x4 vehicle): loss of the layout under the deposit, necessity of clearing.	Broken trees, insulated or in groups.	Perception of the sound from the flow: possible.
3 Medium	Moderate damage: - crash barrier, concrete/ steel post: generalized destruction, - loaded truck, freight car: turnaround (and burying). Impracticable road: loss of the layout, necessity of extensive clearing work.	Locally broken mature forest: transport of trees. Pulling out and transport of stones/ blocks. Possible obstruction of waterways by the snow deposit.	Perception of the sound from the flow: frequent. Effect of blast: possible. Avalanche inside many others: possible.
4 High	Significant damage: - superstructure not especially adapted and forming obstacle: generalized destruction, - locomotive: possible turnaround. Total cover and/or damage over a significant length of roadway. Engineering avalanche works: - possible partial overflow, - possible partial destruction.	Destruction of about ten hectares of forest. Pulling out and transport of rocks bigger than 1 m^3. Generation of a wave in a lake. Notorious temporary modification of local topography (deposit of snow). Possible formation of a dam and a lake.	Eccentric/ rare trajectory: possible. Avalanche inside many others: frequent. Temporary control measures (evacuation or restrictions): possible.
5 Very high	Very significant and generalized damage. Engineering avalanche works: - possible repeated and/or extended overflow, - possible frequent and/or extended destruction.	Very wide destruction of any shrubby vegetation. Landscape radically transformed by this destruction. Strong accumulation of transported things.	Eccentric/ rare trajectory: extended/ frequent. Temporary control measures (evacuation or restrictions): generalized.

Figure 1.9: Intensity scale for the avalanche risk (part II), from [172].

Furthermore experiments are carried in order to analyse deeper velocity profiles, to which pressure ones are linked, entrainment of snow, from which the volumes involved depend as well as the pressure behaviour. In fact pressure values evolve in time, in space and change with the obstacle shape. Experimental studies are made in real avalanches scale in the test sites, or in reduced scale in laboratory chutes.

Real scale test sites

In Europe several test sites at real scale are present to study the avalanche dynamics and interaction with structures. They allow to study into detail physical dynamics processes (as erosion and deposition, powder formation...) and, consequently, to validate and calibrate dynamics models. They are (for a comprehensive review see [115, 119]): Col du Lautaret (Fig. 1.11.a) and Taconnaz in France (Fig. 1.11.b), Núria in Spain, Ryggfonn in Norway, Vallée de la Sionne (Fig. 1.11.c,d), Val Medel and Mettlenruns in Switzerland, Monte Pizzac [188] in Italy, Großer Gröben and Schnannerbach in Austria, Flateyri in Iceland.

At present, only few of them are still operative. In Fig. 1.10 some of the peculiarities of some of these test sites are reported [12, 37, 103, 157, 173, 197, 200]. The steps to follow in order to instrument a test site (the individuation of the site, the choice of the instrumented obstacle and the procedures to follow during the experiments) for the study of the dynamics and of the interaction between an avalanche and a structure are presented in [12].

The avalanche impact pressure is measured by means of load transducers or indirect methods. The obstacles simulating real building and structures exposed to avalanche are of different types: beam-supported plates with adjustable height, wedge-shaped mounds, variable-angle wedge-shaped objects, girder masts, oval-shaped or circular towers, impact walls, roofs of avalanche shed, power line cables, dams, and tunnel-bridges with pressure transducers.

Among them the new Italian Seehore test site (see Ch. 4) was equipped, distinguishing from the other existing test sites for different aspects:

- the avalanches are of small size, contrarily to the majority of the others sites;

- the obstacle is vertically placed and not perpendicular to the flow;

- the frequency of the events is higher, under favorable meteorological conditions;

- the release processes are studied into detail.

The experiments at real scale, although allow the investigation of the real dynamics processes, have the disadvantage to be expensive, to have a complex logistics, and to be meteorological condition dependent. Besides due to the variability and the complexity of the snow, and to the destructive effects of the avalanche, it is difficult

	Col du Lautaret	Taconnaz	Rygfonn	Vallée de la Sionne
Ownership/Country	IRSTEA	IRSTEA	NGI	SLF
Country	France	France	Norway	Switzerland
Site in operation	Since 1973 with interruption		Since early 1980s.	Preliminary studies since winter 1994/95. Normal operation since winter 1997/98.
Drop height [m]	450	2900	975	1300
Path length [m]	800	7500	2100	2700
Average inclination	34°	46%	31°	29
Starting zone	Bowl-shaped, 45°, SE	On Glacier, at altitude between 3000-4000 m	Bowl-shaped, 35- 45°, NNE	Open slopes, 30-40°, ESE, SE
Track	Gully, 30m wide, 36°	mean width of 300-400 m.	100m wide, 30°	Open slope, gully, 30-35°
Run-out	Open slope		Small river fan, 8°	Open slope, 15-20°
Spontan. Aval./year	3-4	Almost once a year	2-3	2-5
Initial volume[m3]	500-10000	1800000 (for retourn period of 100 years)	10000-100000	3000-300000
Artificial release	GasEx, Catez, Avalhex	no	explosives	Explosives by helicopter, mortar shelling
Front velocity	High speed photogrammetric system		Stereo photography, Doppler radar of ILWF	Video, FMCW radar
Flow depth	At sensor support (from video)		Not measured	FMCW radar
Seismic and acoustic signals	Geophones		Geophones	Geophones, acoustic goniometry
Velocity profile	hydraulic propeller	2 sensors on 2 breaking mounds	Doppler radar , geophones	Doppler and FMCW radar
Flow density	Acoustic (experimental)		Not measured	capacitance probes
Pressure	a one square meter plate integrates the pressure all over the flow height (strain gage signals for pressure reconstruction by inverse analysis) and a mast records pressure each 20 cm	Normal and tangential forces on 2 pressure sensors	Strain gauges or pressure plates at 2 or 3 levels on 3 structures in lower track and runout zone	5 piezo-electric load cells (15kHz) on narrow wedge, 4 cells o tower in run-out zone
Intraction with obstacles	A 3 m-high mast records pressure and velocity each 20 cm, and a one square meter plate integrates the pressure all over the flow height	5 Deflecting/catching dams, 14 braking mounds, 11 "flowspreading" cones.	A 16-17 m high and 100 m long catching dam with at top a 6.5 m high steel mast, 6 m high tubular steel tower, a 4.5 m high concrete structure, grider masts to side the path, power line cables	Grider mast, oval-shaped tower, impact wall, roof of avalanche shed, narrow wedge
Entrainment	Field observations		Field observations	FMCW radars, field observations, photogram m
Typical velocities [m/s]	10-30	Maximum estimated at the measurent point: 60	30-60	
Typical pressures [kPa]		Maximum estimated at the measurent point:100	300-600	
Typical deposit area	5000-15000 m2 at depth 0.2-1.5 m		150x100 m2, depth 3-8 m	

Figure 1.10: Peculiarities of some existant test sites, data from [12, 119]

Figure 1.11: [a] Col du Lautaret: one of the two obstacle devices. [b] Taconnaz test site: the dam, the braking mounds and a damaged deflecting wall. [c] Vallée de la Sionne: avalanche path and bunker for observations. [d] Vallée de la Sionne: some obstacles. Photos E. Bovet.

to achieve systematic measurements. To avoid such problems experiments at small scale are done. An additional positive point in laboratory the initial conditions are controllable and tests are reproducible.

Small scale laboratory experiments

Small scale laboratory experiments (for details see [119]) can be done with granular flows (as at Bristol (UK), Grenoble-IRSTEA (F), Pavia(I), Reykjavík (IS), Rutschbahn (CH)), suspension flows (Grenoble-IRSTEA (F), Zurich-VAW-ETHZ (CH) or with snow flows (Col du Lac Blanc- IRSTEA (F) and Weisslfuhjoch (CH)).

For instance in the Weisslfuhjoch chute (Fig. 1.12.a), 34 m long and 2.5 m wide, up to 25 m^3 snow are released. The chute is equipped with velocity (Fig. 1.12.b) and force measurement devices. Many studies (for instance [116, 123, 124, 168, 201]) are done concerning impact force on retarding walls, snow retention capacity of rigid avalanche defence structures and snow nets, test on sensors for the measurement of velocity and density, basal friction, velocity profiles and the rheology of snow. In particular a detailed study concerning the velocity profile will be done in Sec. 2.1.3.

[a] [b]
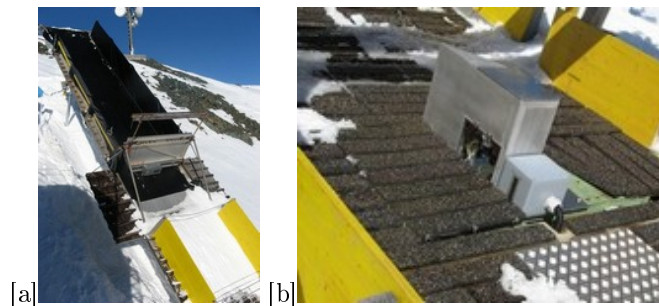
Figure 1.12: [a] The chute at Weissfluchjoch (CH) of the SLF and [b] its velocity sensors. Photos E. Bovet.

However, in order to extrapolate the results obtained in small scale to the real one, a dimensionless analysis (see Sec. 1.3.1) has to been carried. Unfortunately it is difficult to find a material able to respect all the similarity criteria with the consequence that is questionable to extrapolate results to different scales [200]. Full-scale experiments are therefore always necessary to validate small-scale experiments as well as numerical models of avalanche dynamics.

1.2.3   Analytical and numerical approaches

Analytical laws are proposed basing on the analogies with fluids [118], granular materials [58, 88, 89] or projectiles [108]. The interaction between avalanches and structures is modeled thanks to numerical techniques [166], as the FEM (Finite Element Method) [39, 45] or the VOF (Volume Of Fluid) method [62]. The DEM (Discrete Element Method) can be used to investigate basic physical processes at small-scale [88, 94, 95]. The results can be combined with full-scale terrain observations [46, 153] or with laboratory experiments [89, 105, 153, 156, 198, 199]. A summary of the existing models is proposed, based on the European report [109] (see the bibliography within for major details on each model developed until 1998 describing the avalanche dynamics).

State of the art: empirical models

The empirical models are based on statistical elaboration of data, without taking into account the physics of the problem (see [25, 109] and the bibliography within for an exhaustive state of the art). The advantages of the empirical models are the simplicity in use to estimate the runout distance and that the existence of uncertainly in measurements and modeling of physical processed is known and can be quantified. The disadvantages are to regardless of the physics problem and to not determine velocity, flow depth and pressure.

Such methods allow the determination of the runout distance through a regressive analysis (topographical-statistical models) or through the nearest neighbors method (comparative models).

The **topographical-statistical** models contain both the regressive and the inferential models. The first ones are based on statistical regressions, in which the maximum runout distance is related to topographical peculiarities of the avalanche path, as the total height difference between the starting point and the lowest point or the curvature of the avalanche path. In particular the $\alpha\beta$-model relates the inclination of the total avalanche path α to the slope β, between starting zone and the point of $10°$ inclination along terrain profile, with a linear law [18, 135]:

$$\alpha = m\beta + c. \tag{1.6}$$

Applications on Italian cases studies are done too [29, 40, 56].

The second ones are based on the adaptation of distribution probability laws to sample runout distances [147]. In particular the additional term δ, defined as the angle of the runout zone (between β and α points), is added. On the basis of the acceptable risk, it is used for land-use planning purposes by defining the probability of non-exceed (having an Extreme Value Type I or Gumbel distribution) a specified value of the runout ratio:

$$RR = \frac{\tan\beta - \tan\alpha}{\tan\alpha - \tan\delta}. \tag{1.7}$$

In the **comparative** laws a multi-variate statistic is used. The nearest neighbors method consists on finding the similarities between two or more paths considering the meteorological situations too. A multi-dimensional space, containing the relevant parameters for the prediction of the dependent variable (i.e. runout distance), is coupled to a table of known values for the dependent variable. Hence, knowing the independent variable, the prediction of the dependent one can be made searching the nearest neighbor in this space [109].

Finally some models evaluate the **risk** to people inhabiting structures in avalanche-prone terrain, based on historical information too [109]. Risk is defined as the product of the encounter probability (the temporal and spatial excess probability of avalanching as a function of the location), the exposure (time that people or object are under threat) and vulnerability (damage that is caused to the exposed people or objects).

State of the art: dynamical models

The dynamical models, on the contrary, are based on the physics of the processes and allow to determinate, for instance, the velocity and the flow depth. The first dynamics models were developed in the former Soviet United at the end of years '30, but translated and thus known to the rest of Europe only at the end of the '90 [182]. Hence, Voellmy [208] is often considered the first to study avalanche dynamics.

Models can have different dimensions. Let underline that a "quasi two-dimensional model" means one-dimensional equation with depth or width averaged, while a "quasi three-dimensional model" means a one-dimensional model with weight and height averaged, or a two-dimensional model with averaged height.

At the time of [109] any models are able to calculate the punctual distribution of the pressure, and only the Voellmy-Salm-Gubler model [183] is able to give the pressure on the obstacle.

In the following models for dense, powder avalanches will be presented, as well as the combination of these. Finally slush models exist too [109].

Before to explain the different avalanche dynamics models, a model describing the **trigger** is analysed. A new stress-energetic model for snow avalanche triggering based on a shear lag model is proposed by [59, 61]. The model is extended through two different approaches to identify the failure condition: a tensional approach and a fracture mechanics one. They suppose the presence of a defect, called the super weak zone, above the weak layer. In general, shear failure initiates in the weak layer beneath the slab and then it propagates as a shear fracture within the weak layer. Hence the avalanche can release only if the energy release rate is larger than the critical value and the stress at the defect border is larger than the shear strength.

Dense avalanche models.   The dense avalanches can be considered as a sliding block or a deformable body (see [109] and the bibliography within for an exhaustive state of the art).

In the **sliding block** approach, the motion is described for a rigid body on a linear slope (or a flexible body following the terrain) or for its center of mass using the conservation of the moment. To contrast the gravitational force, the resistant force can be expressed as [55, 180]:

$$R = \mu N + Bu + Cu^2 \tag{1.8}$$

that is the sum of a Coulomb term (proportional to the normal force N through the dry friction term μ), the viscous force Bu and a velocity squared term similar to the Chezy resistance for turbulent water flow in open channels (in many models C is a function of ξ, well described later). The viscous force is often neglected [167, 208], even if [159] show its importance expecially in the boundary shear-layer near the bottom, on the basis of the velocity profiles. μ can be constant [54] or velocity dependent too [147, 159]. For practical use the sliding blocks models were used following for instance the procedures in [183], even if more complex models, as AVAL-1D [34, 63, 190] supplanted it. The combination of the two terms $\mu N + Cu^2$ is now known as a Voellmy fluid.

The motion can be also described through the energy conservation among the kinetic, potential and losses of energy which occur [127].

A centre-of-mass model for avalanche motion on deflecting dam is proposed by [113]. Using a simplified geometry for the dam the influence of impact velocity, run-up height, terrain slope angle, dam configuration and orientation is studied. The effects of energy loss due to impact may be investigated too.

The avalanche can be considered a **deformable body**. The flowing snow is a continuum medium that can be considered [109] a fluid subjected to hydraulics laws, a granular material or a block series [111].

The **hydraulic laws** are based on the shallow water equations (also called Saint Venant equations). It is assumed, in fact, that the avalanche flow depth is small in comparison to the sliding extent of the avalanche with the consequence that the model is depth averaged. Hence no information on the velocity or pressure profiles along the avalanche depth can be investigated.

Firstly the attention is focused on the *RAMMS* model, since applied in Sec. 5.1.4 and Sec. 5.2. RAMMS is developed by the WSL-SLF of Davos (CH), as an evolution of the AVAL-1D [34, 63, 190], no more described here. Avalanche is considered a unsteady and non-uniform motion with varying mean velocity $\mathbf{U}(x, y, t)$ and height h. The depth averaged mass and momentum balance equations are [30, 31, 32, 66, 65]:

$$
\begin{aligned}
&\partial_t(h) + \partial_x(hU_x) + \partial_y(hU_y) = \dot{Q}(x, y, t) \\
&\partial_t(hU_x) + \partial_x(hU_x^2 + g_z \tfrac{h^2}{2}) + \partial_y(hU_xU_y) = G_x - S_x \\
&\partial_t(hU_yx) + \partial_x(hU_xU_y) + \partial_y(yhU_y^2 + k_{a/p}\tfrac{h^2}{2}) = G_y - S_y
\end{aligned}
\tag{1.9}
$$

to which an additional equation accounting for the random kinetic energy $R(x, y, t) = \frac{1}{h} \int_0^h \frac{1}{2}[u_x^2 + u_y^2 + u_z^2]$ associated with particle velocity fluctuations (u_x, u_y and u_z) is added:

$$\partial_t(hR) + \partial_x(hRU_x) + \partial_y(hRU_y) = \alpha(\mathbf{S}\dot{U}) - \beta(Rh) \qquad (1.10)$$

$G_x = g_x h$ and $G_y = g_y h$ are the driving, gravitational acceleration, $\mathbf{S} = (S_x, S_y)'$ is the friction:

$$
\begin{aligned}
S_x &= \frac{U_x}{||U||}[\mu(R)g_z h + \frac{g||U||^2}{\xi(R)}] \\
S_y &= \frac{U_y}{||U||}[\mu(R)g_z h + \frac{g||U||^2}{\xi(R)}]
\end{aligned}
\qquad (1.11)
$$

The Voellmy frictions μ and ξ coefficients are reduced with R as the following:

$$
\begin{aligned}
\mu(R) &= \mu_0 \exp(-\frac{R}{R_0}) \\
\xi(R) &= \xi_0 \exp(-\frac{R}{R_0})
\end{aligned}
\qquad (1.12)
$$

with $\mu(R = 0) = \mu_0$ and $\xi(R = 0) = \xi_0$. $\alpha(S\dot{U})$ represents the production of fluctuation energy and $-\beta(Rh)$ its decay. Snow is entrained at a rate of $\dot{Q}(x, y, t) = \frac{\rho_i}{\rho}\kappa_i U$ until no more snow can be entrained. Hence $\dot{Q}(x, y, t)$ depends on the mean velocity $U = \sqrt{U_x^2 + U_y^2}$, the density of the avalanche ρ and the density of the layer i eroded through a dimensionless entrainment coefficient κ_i. $\kappa_i = 0.8 - 1$ allows to describe the ploughing or the frontal erosion [102], producing large flow height at the avalanche head, while smaller values (less than 0.5) represent the basal erosion [30, 66, 65]. Conversely, snow deposition, that occurs when the mean velocity is zero, is modeled starting from the consideration that avalanches have different flow regimes at the front and at the tail suggesting a position-dependent frictional component. As the random kinetic energy decreases towards the tail, friction increases, causing avalanches to deposit mass and stop even on steep slopes. Some application of the model are present in [57, 64, 139].

The *NIS* model [161, 162], proposed by Norem, Irgens and Schieldrop, considers the avalanche a material with constitutive relations including the viscosity and visco-elasticity of a Criminale–Ericksen–Filbey fluid [70], combined with plasticity for a cohesive material:

$$
\begin{aligned}
\tau_{xz} &= a + bp_e^k + \rho m\dot{\gamma}^n & (1.13) \\
\sigma_x &= -(p_e + p_u) - \rho(\nu_1 - \nu_2)\dot{\gamma}^n & (1.14) \\
\sigma_y &= -(p_e + p_u) - \rho\nu_2\dot{\gamma}^n & (1.15) \\
\sigma_z &= -(p_e + p_u) & (1.16) \\
\tau_{yz} &= \tau_{yx} = 0 & (1.17)
\end{aligned}
$$

with p_e the effective pressure, p_u the pore pressure, ρ the density, ν_1 and ν_2 the normal stress viscosities, m the shear stress viscosity, $\dot{\gamma}$ the shear velocity, a the cohesion, b

the dry friction coefficient and $n=2$ for inertial regime avalanches. Since the shear stress is not zero, the vertical velocity profile is not constant. In particular the ratio between the velocity at the base u_0 and at the top surface u_h of the flow of height h depends on the ground roughness through the coefficient of viscous sliding s:

$$\frac{u_h}{u_0} = \left[1 + \frac{2h}{3}\sqrt{\frac{s}{\rho(m - b\nu_2)}}\right] > 1 \qquad (1.18)$$

Other examples of depth-averaged models are the Italian $VARA$ [25] and the model of the *Moscow State University* [109].

Some models consider avalanche a **granular material**, cohesionless, incompressible and subjected to the Coulomb internal friction, as in the *Savage-Hutter* model [79, 184, 209]. Their depth-averaged equations, here reported in the 1-dimensional form for simplicity, are:

$$\begin{aligned}
&\frac{\partial h}{\partial t} + \frac{\partial}{\partial x}(hu) = 0 \\
&\frac{\partial u}{\partial t} + u\frac{\partial u}{\partial x} = \sin\zeta - \tan\delta\, sgn(u)(\cos\zeta + \lambda\kappa u^2) - \epsilon K_{ap}\cos\zeta\frac{\partial h}{\partial x}
\end{aligned} \qquad (1.19)$$

with h and u the height and velocity of the flow, ζ the slope angle, δ the non-constant bed friction angle, λ the ratio between the longitudinal length scale and the scale for the radius of curvature of the bed profile, κ the curvature, K_{ap} the earth pressure coefficient and ϵ the ratio between the depth scale and the longitudinal length scale.

As a consequence of internal friction, longitudinal active and passive stresses in the avalanche body are present [180]. Body is rigid and cannot deform until stresses are lower than a critical value, since a Mohr–Coulomb yield condition is supposed. When velocity gradients reach the critical value, deformation takes place: an elongation (active state) with increasing speed, and a compression (passive state) with decreasing speed.

Barpi and *Borri Brunetto* applied the Cellular Automata to describe the avalanche motion in three dimensions [28]. The avalanche is divided into small regular elements (cells or elementary automata) interacting by simple laws, obtaining a reduction from a computational point of view. The erosion occurs if the impact pressure of the avalanche leading edge is larger than the strength of the layer. The deposition is possible only when its kinetic energy falls below a threshold value. Each cells is characterised by different heights: non-erodible height (i.e. altitude of the ground), erodible heights (i.e. snow cover layers), flow height, kinetic head (i.e. height corresponding to the kinetic energy per unit of weight of the snow material associated to the cell). From each cell the flow can go to the neighboring cells, leading to variation of their height. The motion is then modeled assuming that the whole system tends to a configuration of maximum stability. The capabilities of the model are

shown simulating documented avalanches that occurred in Susa valley (Western Italian Alps). Using a digital terrain model, the model is able to reproduce the correct three-dimensional avalanche path and the deposit volume.

The *Smoothed Particles Hydrodynamics* (SPH) is applied to the avalanche dynamics too [96]. This technique, similarly to the MPS (moving-particle semi-implicit) method [165], is based on the transformation of the mesh in particles (Fig. 1.13). The input parameters are the terrain topography and the release volume. Snow is considered a granular material, modeled as a incompressible continuum medium, characterised by density, viscosity and shear modulus. A coulomb friction is introduced. The model is compared with experimental data collected at the Seehore test site (see Ch. 4), in particular considering the front velocity, the impact pressure and the runout distance. Finally considerations on the velocity profile are done.
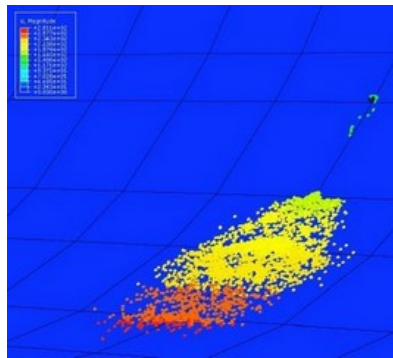
Figure 1.13: The deposition zone after the impact against the obstacle at the Seehore test site modeled with the SPH method, from [96].

Powder avalanche models. The powder snow avalanche can be modeled as a block, a density current or a biphase current (see [109] and the bibliography within for an exhaustive state of the art).

Density current models are based on local balances of total mass and linear momentum. They are often integrated over the current height, or on each layer. In a binary description, mass and momentum balances are formulated for each of the phases and their interaction is accounted for by the mutual interaction force. The interaction must be prescribed by a constitutive relation. An intermediate approach is to consider separate mass balances for snow and air, but only one momentum balance for the mixture. Extra diffusive and advection terms can be incorporated in the snow mass and mixture momentum balances to approximately describe the effects

of relative motion. Since powder-snow avalanches are highly turbulent, the equations have to be time averaged and closed by a turbulence closure model, e.g. a $k-\epsilon$ model. A steady flow condition is often supposed and a set of ordinary differential equations involving variations in the direction of the flow is derived.

In the **block models** the powder avalanche is treated as a mass point described by ordinary differential equations at which additional equations for the size change are specified. In such zero-dimensional models, the centre-of-mass (or front) of coordinate $x(t)$ is the basic dynamical variable from which the velocity is derived. On the contrary in models describing the avalanche as a flow, the basic dynamical variable is the velocity and the coordinate x plays the role of a parameter like the time. Nevertheless, for practical applications the recent numerical models for powder snow avalanches seem now to be able to reasonably simulate runout zones and stagnation pressure distributions.

The *AVAER* model can be applied only if the powder part is independent from the dense core. It derives from laboratory experiments done using water and water with salt [36, 202] or with powder in order to simulate the powder of an avalanche. The avalanche maintains its semi-ellipsoidal shape, while length, height and width growing due to air entrainment. The mass balance takes into account air entrainment, while the snow entrainment is specified by the user. *Rastello* [174] proposed a simplified model that gives analytical solutions for the velocity, volume and density. The eroded snow is a percentage of the snow cover. This model is implemented using the fuzzy logic too [27]. Giving a predetermined degree of variation, or fuzziness, in model parameters (as volume, difference between snow density and air density, height of the snow cover, added mass coefficient) it is possible to quantify the influence of the incertitude on the results of the model (velocity and pressure). In particular the pressure is the more influenced parameter by the imprecision in the input parameters.

Besides, *Kulikovskiy and Sveshnikova* [109] consider the powder avalanche as a cloud of prescribed geometrical form, that changes during the motion. *Fukushima and Parker* [109] model the cloud as an elliptic half cylinder in which the ratio between length and the height are dependent on the slope angle. Other models are based on the similarity with submarine turbidity currents, as in [100]. There the body of the avalanche rather its head is described through four equations (the conservation equations of fluid mass, snow-particle mass, momentum of the cloud and kinetic energy of the turbulence). *SL-1D* describes the avalanche through the saltation and suspension layers [114]. The suspension layer is described thanks to balance equations for air mass, snow mass, total momentum, turbulent kinetic energy and dissipation. In the saltation layer the air mass and momentum are neglected while the snow mass and momentum are solved. The height of the saltation layer is proportional to the velocity squared.

Coupled models. Coupled models are used to describe the dense and the powder part of the avalanche [203, 204] (see [109] and the bibliography within for an exhaustive state of the art). The *SL-1D* model can be coupled to a model for the dense layer giving a complete coupled model [114]. The *Russian* quasi two-dimensional coupled model [109] considers the avalanche as two layers: a dense layer underneath a powder one, interacting with each other. The velocity and the density are averaged over the thickness of the layer, as in the hydraulic approach.

The *Naaim's* quasi three-dimensional coupled avalanche model [155] simulates the dense part as a granular dense flow using the shallow water equations. The friction term τ allows to describe different rheological behaviour, as the Bingham fluids, the granular ones and the Voellmy fluids. The balance of mass and momentum read:

$$
\frac{\partial}{\partial t}\begin{pmatrix} h \\ hu \\ hv \end{pmatrix} + \frac{\partial}{\partial x}\begin{pmatrix} hu \\ hu^2 \\ huv \end{pmatrix} + \frac{\partial}{\partial y}\begin{pmatrix} hv \\ huv \\ hv^2 \end{pmatrix} + \begin{pmatrix} 0 \\ \partial_x \\ \partial_y \end{pmatrix}\left(\frac{1}{2}kg\cos\theta h^2\right) =
$$
$$
= -gh\begin{pmatrix} 0 \\ \cos\theta_x \\ \cos\theta_y \end{pmatrix} - \frac{1}{\|\vec{u}_d\|}\begin{pmatrix} 0 \\ u \\ v \end{pmatrix}\frac{\tau}{\rho_d} \tag{1.20}
$$

where h is the flow depth, $\mathbf{u} = (u, v)'$ is the velocity, θ_x and θ_y are the terrain slope angle in the x and y directions, k is the active or passive earth pressure coefficient.

The powder part [155] is supposed to be a two-phases flow formed by air and snow particles in suspension, subjected to the gravity. Mass and momentum conservations are considered separately for each phase (air and particle). The model is based on the classical $k - \epsilon$ model. The erosion occurs only when a threshold value is overcame. Under this value deposition occurs.

Models for entrainment

Different approaches are used for the entrainment. In this section only some of them are reported: see [23, 83, 102] for an exhaustive state of the art. For instance *Maeno and Nishimura* [159, 109] consider the entrainment rate α dependent on the velocity

$$
\alpha = \alpha_\infty(1 - \exp(-u/u_m)) \tag{1.21}
$$

where α_∞ is the rate at large velocity and u_m is a constant.

Brugnot and Pochat [52] insert the entrainment of snow supposing that a given snow depth h_0, provided by the user in each section, is completely recovered at the avalanche front level, and not in the avalanche body as it is supposed to be in the reality. In their model the density ρ varies with the velocity following:

$$
\rho = \frac{\rho_0}{1 + \alpha(u - u_o)} \tag{1.22}
$$

where ρ_0 is the density at rest, u_0 the threshold velocity at which the density varies and α the coefficient of variation.

The *Hungr*'s [111] continuum model, ideated for rapid flow slides, debris flows and avalanches, considers the flowing mass a series of blocks contacting each other, free to deform and with a constant volume. Entrainment and deposition are simulated changing the volume of each boundary and mass block in each time step, in assigned entrainment or deposition zones along the path, by an amount proportional to the distance traveled. The rates of deposition and erosion are constant percentages of the cross-sectional area per unit displacement. However the implementation and results of the changing mass model are not presented in Hungr's work.

In the model of *Briukhanov et al.* [51] entrainment at the flow front is modeled as an hydraulic jump. The boundary between the moving avalanche snow and the static snow is supposed to be a shock wave perpendicular to the flow. Proper boundary conditions therefore describe the snow entrainment.

Grigorian and Ostroumov [23, 106] proposed a gradual entrainment from the bed, assuming that the boundary of the moving avalanche and the undisturbed snow cover is a compressive shock wave (inclined to the bed), in which the snowpack is destructed and involved into the motion. The quantity of eroded snow is proportional to the load p (sum of hydrostatic and dynamic pressure) generated by the moving snow on the static snow. In the model the compression of the eroded snow is taken into account. This theory is applied by [190] who include entrainment in a depth-averaged numerical avalanche dynamics model and back-calculate some well documented avalanche events of the Monte Pizzac and Vallée de la Sionne test sites. The erodible snow is constituted by several layers with different densities and heights. The entrainment friction is considered to be negligible in comparison to the other friction sources.

Eglit [81] models the avalanche as two layers: a lower dense layer (with density ρ_1 and velocity u_1) and an upper powder one (with density ρ_2 and velocity u_2). Mass is exchanged between these two components and between the dense/powder parts and the underlying snowcover (with density ρ_0). The volume exchange rate between the dense layer and the snowpack is proportional to $|u_1|\frac{\rho_1\rho_0}{\rho_1+\rho_0}$ while the volume exchange rate between the powder part and the static snow is proportional to $|u_2|\frac{\rho_2\rho_0}{\rho_2+\rho_0}$.

Naaim et al. [153] consider avalanches a cold, dry and cohesion-less gravitational granular flow. Hence they apply the shallow water theory to granular flow by Savage and Hutter. Their formulation of deposition and erosion processes is based on properties of the granular flows [155, 169].

The *SAMOS* model [179] considers both the dense part and the powder part. Separate models for the layers are employed. For the dense core a two-dimensional shallow-water model with a Mohr-Coulomb-like fluid is used. The powder part is considered a fluid of variable density, according to the volume fraction of snow particles. The turbulent friction is taken into account through a standard $k - \epsilon$ model. The models are coupled by an additional transition-method that describes the exchange

of mass and momentum between the layers. Erosion occurs in the frontal part of the avalanche and the snow eroded goes partially in the dense layer and in part in the powder component depending on (i) the ratio between the flow height and the erodible snow height, (ii) the ratio between the density of the dense flow and of the erodible snow cover and (iii) the Froude number.

1.3 General notions

In this section the following notation is used: $u = |\mathbf{u}|$ is the velocity (depth-averaged velocity); p the pressure; ρ the density (depth-averaged density); g the gravity acceleration; h and H the flow depth and the obstacle height, respectively; l and D the avalanche and the obstacle width, respectively; φ and ψ the deflecting and slope angle, respectively.

1.3.1 Dimensional analysis

The procedure to follow to translate the results obtained in a small scale to a real scale is presented here. In fact, while the geometry may be simply scaled, other parameters, such as pressure, velocity and type of fluid need to be altered.

Results on small scales are applicable to real scale when the **similitude** is achieved. To this aim the following criteria are required: (i) geometric similarity: the model is scaled; (ii) kinematic similarity: fluid flows have similar streamlines; (iii) dynamic similarity: ratios of all forces acting on corresponding fluid particles and boundary surfaces in the two systems are constant.

To obtain a dynamic similitude it is sufficient that all the dimensionless groups are equal in the small scale situation and in the real one. In the following the dimensionless analysis is therefore presented.

The physical variables have dimensions, i.e. are measured through basic instruments. The basic instruments necessary to measure all the physical variables identify the set of fundamental units. For instance, in the International System of Units (SI) the length, the mass and the time measured respectively in m, kg and s are fundamental quantities.

The **Buckingham theorem** [149] affirms that from m physical variables expressed as a function of n fundamental independent quantities, $m - n$ independent dimensionless groups can be formed.

A dimensionless group is not unique, since it can be replaced, for instance, by its inverse or potence.

Hence, when the set of group is identified, it is not necessary to use the dimension analysis. The link between the different groups is experimentally established or defined using physical laws. If only a group is present, it is a constant.

An example of application of this theory is to consider, like in [149], a submarine under water. Its velocity is due to the motors force and to the resistance (Dr) of the water. Dr is a function of the velocity u of the submarine, as well as of the physics properties of water (such as the density ρ and the friction, measured through the viscosity μ), and of the submarine length l. We suppose that all the submarines have the same shape, in order that all the linear dimensions (diameter,...) are proportional to l. Hence the $n = 5$ physical variables (Dr, u, ρ, μ and l) are a function of $m = 3$ fundamental independent quantities (length, mass and time). Consequently the dimensionless groups are $5 - 3 = 2$.

A first group can be defined as $\rho l^a v^b \mu^c$ corresponding to the SI units:

$$[\text{kg/m}^3] \cdot [\text{m}^a] \cdot [(\text{m/s})^b] \cdot [(\text{kg/ms})^c] \tag{1.23}$$

To have a dimensionless value $c = -1$, $b = 1$ and $a = 1$. Therefore the first group is $\rho l v / \mu$. The second group has to be independent from the first one: it is sufficient that at least one parameter belonging to the first group is not present in the second one. In our case Dr replaces μ. The second group is hence $Dr \rho^d l^e u^f$, with the exponents $d = -1, e = -2$ and $f = -2$. Therefore it is $Dr / \rho l^2 u^2$.

The physical meaning of the groups is the following. $\rho l u / \mu = Re$ is the Reynolds number and can be considered a dimensionless velocity. It appears in mechanics of fluids in which the inertia and the viscosity of the fluid play an important role. Re gives a measure of the ratio of inertial forces to viscous forces. In practice this number characterizes different flow regimes, such as laminar or turbulent flow. $Dr / \rho l^2 u^2$ can be rewritten in function of the area A as $Dr / 0.5 \rho u^2 A = C_d$. C_d represents the drag coefficient and can be considered a dimensionless resistance. Finally giving the Re the best shape of submarine is the one that minimizes the C_d value.

Avalanche application of the dimensionless analysis

Those concepts can be easily translated into the avalanche interaction with obstacles, with the only difference that the structure is at rest and the fluid (the avalanche) is in movement.

In this case the variables are: the velocity u, the density ρ, the height h and the width l of the avalanche, the height and width of the obstacle H and D, the impact pressure p (that corresponds to the previous drag resistance Dr). Both H and D are necessary to study obstacles having different shapes. In addition to the flow height h the avalanche width l of the avalanche is introduced to distinguish the case of an impact against a large obstacle (where the avalanche width l is of the same order of the obstacle width D) from an impact against a small one.

Hence we have $m = 7$ physical variables expressed in the $n = 3$ fundamental quantities. Therefore 4 groups are necessary. The first one is $u^a h^b$ with $a = 1, b = 1/2$.

Introducing the gravity acceleration g it becomes the **Froude number**:

$$Fr = u/\sqrt{gh} \qquad (1.24)$$

that is the ratio between the kinetic energy and the potential one. In the second group there are p, ρ and u obtaining the **drag coefficient**:

$$C_d = \frac{2p}{\rho u^2} \qquad (1.25)$$

The third group is the ratio D/l, that indicates if the obstacle is **small or large** in comparison to the flow.
Finally the fourth group is the **aspect number**:

$$A_{obs} = H/h \qquad (1.26)$$

defined as the ratio between the obstacle height H and the flow depth h.

Finally let note that the definition of these 4 groups is valid for the inertial regime (in which $Fr \gg 1$), hence in the gravitational regime ($Fr \ll 1$) the pressure is not $p = \frac{1}{2} C_d \rho v^2$ but $p = \zeta \rho g h$, see Sec. 1.4). In this case the group C_d should be replaced by $\zeta = \frac{p}{\rho g h}$.

For instance, on the basis of the Fr and A_{obs} number, [91] distinguish the formation of an upstream granular jump, from a downstream jet and from an upstream dead zone.

Let note that in the case in which the viscosity μ of the avalanche is considered, since an additional variable is introduced, the new group **Reynolds number**:

$$Re = \rho D u / \mu \qquad (1.27)$$

has to be introduced. A simple relationship links Re to the Fr number:

$$Fr = \frac{u}{(gh)^{1/2}} = \frac{uh}{\mu} \frac{\mu}{g^{1/2} h^{3/2}} = Re \frac{\mu}{g^{1/2} h^{3/2}} \qquad (1.28)$$

If usually in the common avalanche models present in the literature the viscosity of avalanche is neglected, in the new model presented in Ch. 2 it is present. Hence the Re number should be taken into account too.

In the interaction between avalanches and obstacles other dimensionless numbers can be used like the Froude number of the obstacle $Fr_{obs} = u/\sqrt{gH}$, that is linked, for large obstacles, to the previous dimensionless numbers:

$$Fr_{obs}^2 = Fr^2 \frac{1}{H/h} \qquad (1.29)$$

In the following the **slope corrected Froude number**:

$$Fr^* = u/\sqrt{gh\cos\psi} \tag{1.30}$$

that takes into account of the slope ψ will be used too, as well as the ratio D/h in the case of small obstacles.

For small-scale powder avalanche, in addition to the Re number other possible groups as (i) the densimetric Froude number $Fr_d = \dfrac{u}{\sqrt{\frac{\rho-\rho_{ref}}{\rho_{ref}}gh}}$, (ii) the density ratio $\dfrac{\rho-\rho_{ref}}{\rho_{ref}}$ are used, where ρ is the aerosol density and ρ_{ref} is the ambient fluid density, and (iii) the velocity ratio $\dfrac{u}{u_{cp}}$ between the avalanche velocity u and the particles chute speed u_{cp} [87].

To conclude, to translate the concepts obtained by laboratory experiments to the real scale avalanches all the dimensionless groups has to be conserved, in order to obtain a perfect similitude. Unfortunately, it is often impossible to achieve strict similitude [131]. In these cases some aspects of similitude may be neglected, focusing on only the most important parameters. For instance, in granular experiments a geometrical similitude criterion used is that based on the ratio between the flow height h and the diameters of the grains in the flow d_g. However this criterion is not always satisfied, since usually the real avalanches, especially those of dry snow, have the ratio h/d_d more bigger than that of the granular experiment.

1.4   Influence of avalanche kind

Considering the avalanche an homogenous fluid, the equation of the conservation of the momentum in its integral form ($\mathcal{V}$ is the control volume) is given by [16]:

$$\int_{\mathcal{V}} \frac{\partial \rho\mathbf{u}}{\partial t}dV + \int_{\partial\mathcal{V}} (\rho\mathbf{uu} - p\mathbf{1} + \sigma)\cdot\mathbf{n}dA = \int_{\mathcal{V}} \rho\mathbf{g}dV \tag{1.31}$$

That is the velocity variation is given by the difference between the gravitational term and the flux of $\rho\mathbf{uu} - p\mathbf{1} + \sigma$ through $\partial\mathcal{V}$. If the surface $\partial\mathcal{V}$ contains the obstacle surface $\partial\mathcal{O}$, the force exerted on the obstacle is given by:

$$\mathbf{F} = \int_{\partial\mathcal{O}} (\rho\mathbf{uu} - p\mathbf{1} + \sigma)\cdot\mathbf{n}dA \tag{1.32}$$

Consequently three contributions are present [16]:

- kinetic term: even if it is possible to find the magnitude order of $|\mathbf{u}|$ and of ρ it is difficult to calculate the kinetic tensor;

- pressure: it is possible to calculate it for a permanent and uniform regime and for a fixed geometry;

- the stresses generated inside the fluid ($\tau = \sigma \cdot \mathbf{n}$): the behaviour law of the sliding snow are not well known.

Since these terms have not the same magnitude order, it is possible to distinguish, thanks to the Froude number definition, three different regimes [16]:

inertial regime: $Fr \gg 1$: $\rho u^2 \gg -p + \tau$, (where $u = |\mathbf{u}|$ and $\tau = \sigma \cdot \mathbf{n}$) that means the kinetic terms is preponderant, for instance, to the friction with the soil. For this kind of regime, the avalanche is assimilated to a perfect fluid. The aerosol avalanches and the very fast dense dry avalanches can be considered in this class. The obstacle can be easily surrounded by the top or by the side. The pressure depends essentially on the velocity and on the density ($p = \frac{1}{2}C_d\rho u^2$). More details will be done in Sec. 1.6, 1.7 and 1.8. The pressures generated are not always catastrophic [16]. Since the velocity depends on the flow depth and on the slope, the Froude number is independent on the velocity and on the flow depth, but only depending on the slope, on the fluid rheology and on the limit conditions [87]. A shear velocity profile is found in this supercritical regime [195].

gravitational regime: $Fr \ll 1$: $\rho u^2 \ll -p + \tau$, that means the snow rheology and the boundary conditions (for instance if there is a slip or a no-slip condition along the obstacle) play the most important role [16]. In this regime the flow is very slow and quasi static, and can be considered a granular flow. Since in this situation the avalanche is similar to a very viscous fluid, the wet-snow avalanches in the deposit area can be considered in this class, but also, under certain circumstances (low velocity), the tail of dry snow avalanches [195]. The obstacle can stop the snow, as well as it can create a dead zone after it, as well as it can be submerged by a succession of snow waves. The destructive effect is linked to the moving mass (even several meters of deposits (h) can occur): $p = \zeta\rho gh$. For details see Sec. 1.4.1 and 1.4.2. Hence the main role is played by the height and the inclination, and not by the velocity. The pressure magnitude order is lower than this of the inertial regime. The friction force is proportional to the avalanche weight, and consequently to the flow depth. A plug flow velocity profile is found in this subcritical regime [195].

intermediate regime [87]: $Fr \simeq 1$: the basal friction depends on the square of the velocity, typical of the inertial regime, and a constraint linked to the flow depth, typical of the gravitational one. The Froude number is relied to the flow depth.

1.4.1   Design of protection dams impacted by a slow regime (gravity) avalanche

A particular case of the gravity regime is due by wet-snow avalanches. In fact they are characterised by a slower velocity and a higher flow depth giving a low Froude number. Their particular behaviors, even if they are not quantitatively described, should be considered during the dam design (see [117] and the bibliography therein).

Their slow velocities have as consequence that the avalanche follows more the terrain morphology and even a little obstruction can deviate the flow, making the direction unpredictable with possible negative consequences particularly at the lower end of the dams. Besides, the storage volume (since the snow is piled up), as well as the deposit depth, are more important factors than the velocity for the design purpose. If multiple events occur, the storage space has to be calculated as twice the volume of the maximum avalanche. In addition wet avalanches can carry rocks and large quantities of loose materials. The ploughing and the compression of snow are preponderant on the entrainment process. Sometimes their boundaries are distinct, in other cases they can widen laterally. Finally, due to the large friction angle, the accumulation can occur at the terrain above 25°.

1.4.2   Wet avalanches: the Mohr-Coulomb criterion application

The approach proposed by [26] can be used in order to estimate the pressure of a wet avalanche acting on an obstacle. The model proposed in [26] is based on a theory concerning the formation and destruction of chains of stress around structures in wet snow avalanches [192, 196]. For Froude numbers less than 1 the pressure is not significantly velocity dependent, even if practitioners use the same formula (Eq. 1.41) used for the inertial regime as there is no established alternative. Recently [103] show that the Bernoulli formula underestimates the impact pressure in the case of the gravitational regime [196]. In wet avalanches the pressure linearly increase with the depth ($p = \zeta \rho g h$, with ζ a fitting parameter) and it is about eight times larger than the hydrostatic snow pressure. In addition the amplitude of pressure fluctuations increases with flow depth in wet dense avalanches, while the dry ones have the opposite behavior. The drag force is originated from a distribution of force chains that depart from the object and disperse into the bulk. The fluctuations arise from the formation and rupture of these chains. [192] expect that ζ is lower for larger obstacle diameter. For densities above a minimum threshold value, force chains evolve and pressure increases with density.

At a macroscopic scale, such mechanism is explained by a shear failure occurring between freely flowing snow and a packed snow dead-zone volume against the structure, according to a Mohr–Coulomb failure criterion.

According to [192] the pressure can be calculated as:

$$p = \zeta \rho g h \tag{1.33}$$

where ζ is an empirical parameter, g is the gravity acceleration, ρ and h are the avalanche density and flow height. In order to estimate ζ the following theory is presented.

Thanks to the linearity of Eq. 1.33 the Mohr–Coulomb shear failure criterion, where the yield shear stress depends on the normal pressure, can be used. The avalanche forms shear failure surfaces between freely flowing snow and a confined snow volume against the obstacle.
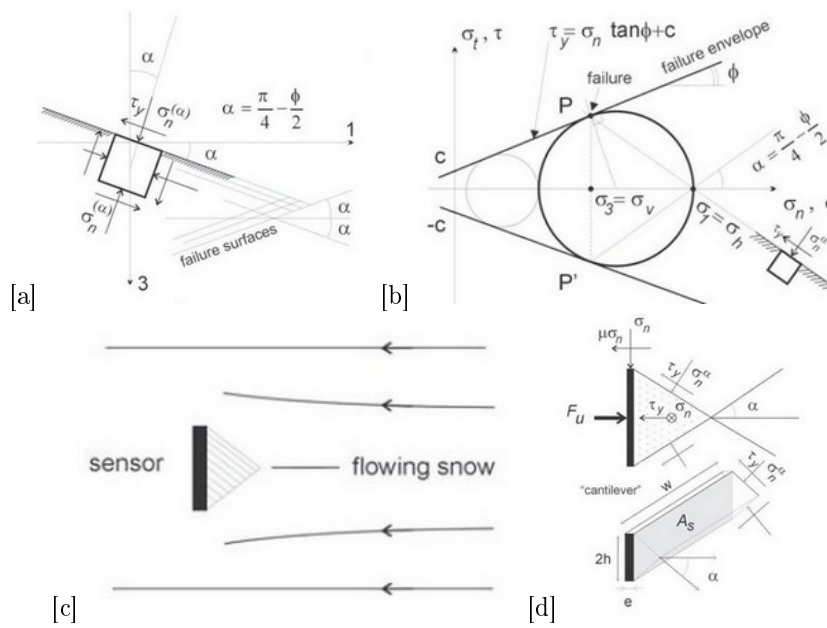
Figure 1.14: [a] Failure surface orientation. [b] Passive pressure at failure given by the Mohr–Coulomb criterion. [c] Snow deposited on the sensor surface: [d] cantilever sensor, from [26].

The failure surfaces and their directions (defined through the angle α) are related to the internal friction angle of the material ϕ (Fig. 1.14) through: $\alpha = \pi/4 - \phi/2$. This surface depends on the properties of the snow and on the structure geometry.

The yield stress of snow is reached on such failure surfaces and represents the macroscopic threshold force necessary to break the microscopic chain forces between snow particles [192].

The Mohr-Coulomb approach, known as "yield-line theory", is commonly used to estimate the limit-load of structures or soils. Soil mechanics approaches have already been applied to avalanche sciences [79].

We consider a general case in which a wall is pushed slowly against the snow in the horizontal direction until snow failure. The horizontal pressure σ_h (named the passive lateral earth pressure) is proportional to the vertical pressure σ_v at the same point through the HPEP coefficient K_p:

$$Kp = \sigma_h/\sigma_v \tag{1.34}$$

The passive pressure σ_h corresponds to an upper equilibrium on Mohr's circle.

The shear stress τ on an arbitrary surface in the snow is assumed to be limited by the Mohr– Coulomb failure criterion (the soil mechanics formalism is used in coherence with [192]):

$$\tau < c + \sigma_n \tan\phi \tag{1.35}$$

where c denotes the cohesion. The passive earth pressure coefficient K_p is given [192]:

$$K_p = \frac{\cos^2\phi}{\cos\delta[1 - \sqrt{\sin(\delta+\phi)\sin\phi/cos\delta}]} \tag{1.36}$$

and σ_h is equal to [192]:

$$\sigma_h = K_p\sigma_v + 2c\sqrt{K_p(1 + c_w/c)} = K_p\sigma_v + K_{pc}c \tag{1.37}$$

where c_w represents the friction forces.

[26] assume that a dead zone forms locally against the obstacle and that its inclination follows the failure surfaces (related to α). The impact pressure is then found by Eq. 1.38:

$$p = \sigma_h = K_p'\rho gz + K_{pc}'c \tag{1.38}$$

since $\sigma_v = \rho gz$. The local HPEP coefficients K_p' and K_{pc}' are introduced taking into account the obstacle geometry and the corresponding snow deposit having a dihedral shape [26]:

$$K_p' = K_p\left[\mu\frac{2e}{w} + \frac{\tan\phi}{\tan\alpha}\frac{h}{w} + \sin^2\alpha\left(1 + \frac{\tan\phi}{\tan\alpha}\right)\right] + \mu\frac{e}{h} + \cos^2\alpha\left(1 + \frac{\tan\phi}{\tan\alpha}\right) \tag{1.39}$$

$$K_{pc}' = cK_{pc}\left[\mu\frac{2e}{w} + \frac{\tan\phi}{\tan\alpha}\frac{h}{w} + \sin^2\alpha\left(1 + \frac{\tan\phi}{\tan\alpha}\right)\right] + c\left(1 + \frac{h}{w}\right)\cot\alpha \tag{1.40}$$

where h is the structure height, w its width, e its thickness and μ is the Coulomb sliding friction coefficient.

From Eq. 1.33, the empirical coefficient ζ is equal to K_p'.

1.5 Influence of size

Size obstacle influence

In addition, also the dimension of the obstacle can influence the impact pressure. For instance, a small obstacle size (as a pylon, masts of electrical power lines, ski lift, cable cars, a little breaking mound) does not modify significantly the flow velocity, direction and depth. The impact pressure, if the flow is inertial, can be calculated by $p \propto \rho u^2/2$. On the contrary, a large obstacle (as a wall, a house, a dam, a big breaking mound) can modify and stop the flow, and consequently the velocity field (for instance the flow direction) and the pressure [16]. For instance, for a deflecting dam, for high values of the Froude number ($Fr \geq \sqrt{2/\cos\varphi}$) [16], the avalanche can overlap the dam. On the contrary, for lower values of the Froude number, the avalanche is deflected. Consequently the impinging pressure has to be calculated on the two phases: the impact (i) with the undisturbed avalanche front and (ii) with the deviated flow, in which the centrifugal force created by the curvature of the streamlines, as well as the influence of the deviation angle, have to be taken into account. The different approaches used for large and small obstacles impacted by an avalanche in the inertial regime are described in Sec. 1.7 and Sec. 1.8.

In addition, the dimensionless coefficients C_d and ζ depend on the obstacle size too. For instance, in the inertial regime C_d, deepened in Sec. 1.6.1, decreases when l/D decreases and it is relied to H/h. In the gravitational regime, ζ is linked to width, surface properties, morphology and packing of grains, or to width and thickness of the channel. Besides, ζ depends on h/D, on the internal friction and cohesion of the flowing material and on the wall friction.

Finally the ratio between the tangential stress and the normal one increases with smaller obstacles, explained by [196] considering the larger the obstacle the larger the deposit. The deposit changes the angle of incidence between avalanche and obstacle increasing the tangential component of the stress.

Size sensors influence

Depending on the size of the sensors different avalanche features can be investigated [200].

Large scale sensors [103, 128, 196] allow to collect measurements that can be used to validate models based on fluids mechanics equations for a homogenous and continuous media, because at such scale the avalanche has those properties. Since the values of the pressure are integrated on the whole surface of the obstacle, information concerning the spatial variability of pressure and, consequently, the internal structure of the flow is loosen [200].

Large plate gives peak pressures having an order of magnitude lower than this measured with small cells. The size effect is more pronounced for wet avalanches,

maybe due to larger particles on average [148].

To this goal small load cells have to be used [122, 130, 148, 160, 163, 185]. Even in this way, however, there are some disadvantages. Firstly avalanche can't be considered a continuous flowing medium, since the snow heterogeneities are too big compared to the scale of measurement, becoming hence questionable a fluid mechanics approach. Due to this heterogeneity, and in particular to the fact that a sensor can be hit by a snow block or particles, short and high peak of pressure [148] are measured. If these values are extrapolated to a large area, the mean pressure is overestimated [148, 196] if the sensor size is smaller than the particle one. To reach consistency with larger scale results, the high temporal variations are smoothed with a low pass filter [196]. In particular, the frequency of particles impacts, and consequently, the flow density decrease rapidly from bottom to the top of the flow [148]. However, for instance in the Vallée de la Sionne test site, this feature doesn't influence the results, since the most frequent particle dimensions are comparable with the sensor ones. In fact, because of the inverse segregation the larger particles are more frequent in the deposition area. Besides, even when a large particle impact, it fractures transmitting only a part of the particle impulse.

Secondly, the sensors are located on structures that, to resist to the avalanche impact have to be of a large size. Consequently they are subjected to the obstacle effect, like the creation of a stagnation zone and vertical or lateral deviation, present, for instance, in the granular medium and in the plastic flows too. This mechanism of snow deposition behind the obstacle can be related to the local avalanche deceleration [196]. Besides larger the obstacle is more snow is deposited.

A third approach is proposed by [200] who, thanks to a suitable experimental structure, quantified both the snow-obstacle interaction and the impact pressure (determined from an inverse analysis of the obstacle deformation) at the scale of the structure. In this way the characteristic of the flow can be derived even considering the overall response of the structure and consequently with the fluid mechanics approach.

1.6   Impact pressure calculation

The pressure from avalanche is by nature strongly time-dependent [26, 38, 195, 196, 187] with (i) more or less large fluctuations at high frequency around the mean value, (ii) the presence of a maximum mean pressure p_{max}, (iii) the probable occurrence –in some circumstances– of several peaks in pressure (p_p before the maximum p_{max}) that may correspond to various surges, (iv) the possible existence of a residual pressure p_{res} (generally for large obstacles relatively to the flow size). For an example of the residual pressure see Sec. 5.4.2. Large fluctuations in the inertial regimes are associated to single-particles or clusters impacts. In the gravity regime, instead, oscillations are explained by the formation and rupture of force chains present in the granular media

and the stick-slip processes among the grains or between grain and obstacles [26, 192]. Finally, spatially fluctuations are recorded on large obstacles [128]. In the following, we do not consider the spatio-temporal force fluctuations. We will only refer to the time-averaged pressure.

Generally, for practical design of protection against avalanches, the analogy with the fluid mechanics is used to calculate the impact pressure as the product between the dynamic pressure and the drag coefficient C_d [183]:

$$p = \frac{1}{2} C_d \rho u^2 \tag{1.41}$$

However, this is only a possible way to calculate the pressure [16]. In fact, the impact pressure, and consequently its expression, depends on the avalanche kind and flow regime, on the obstacle dimension and shape and on the relative position of the obstacle in the confront of the avalanche flow. However, nowadays, the classical methods do not take into account all these aspects.

Usually, the following simplifications are done [16]. Firstly, the impact dynamic pressure is related to the static one, in coherence with the Eurocode [7] considering the static equivalent. Secondly, only pressure mean values are considered. In fact, as seen before, the signal is very variable (there are peak of pressure of 2-3 times major than the mean values). Thirdly, fluctuations in flow density are assumed to be small and have little influence on the motion of the avalanche.

1.6.1 Drag coefficient C_d

The drag coefficient definition derives from the fact that the total drag force on a body F_D is the sum of the pressure drag F_p and the friction drag F_f:

$$F_D = C_d A \frac{\rho u_\infty^2}{2} = F_p + F_f = C_p A \frac{\rho u_\infty^2}{2} + C_f B L \frac{\rho u_\infty^2}{2} \tag{1.42}$$

where A is the projected area of the body normal to the flow, u_∞ is the flow velocity upstream the body, L is the length of the surface parallel to the flow and B the width of the surface. The coefficients C_p and C_f, and consequently C_d too, depend on the geometry of the body and on factors defining the flow state, as the Froude and Reynolds numbers. If the flow is around two sides of the body, F_f has to be multiplied by a factor 2, since Eq. 1.42 gives the drag on only one side of the body.

In addition to the dynamic drag, a static load F_{static} has to be added in the case of only partly immersed obstacles [117]:

$$F_{static} = (\rho - \rho_{air}) g \cos \psi D \frac{(h_1 - h_2)^2}{2} \tag{1.43}$$

where ρ_{air} is the air density, h_1 and h_2 are the flow depths upstream and downwind the obstacle and D is the obstacle width across the flow. In these cases, in fact, a

fluid-free zone, named "vacuum" area, is developed behind the obstacle. Its depth and extent depends on properties and velocities of the flow. F_{static} becomes negligible for $Fr^* \gg 1$, while for $Fr^* < 1$ (as in the snow creep or gliding) dominates the drag. Remember that Fr^* is the slope corrected Froude number (see Sec. 1.3.1). A static load from avalanche deposits continues to be present after the stop of the avalanche since the cohesive strengths of the avalanche prevent the "vacuum" behind from closing. Finally, small obstacles partially submerged have a reduced overall drag compared with a confined setting due to the increased possibility of the material to flow around the obstacle [117].

C_d depends on obstacle dimension and shape as well as on the kind of snow. For instance masts hit by a powder part or fluidised layer (saltation) have C_d varying among 1, 1.5 and 2 according to the geometry shape (circular, triangular and squared respectively). For a dry dense avalanche the difference is for a circular shape in which $C_d = 1.5$. The values grow for a wet dense avalanche: $3 - 5$ for a circular shape, $3 - 6$ for a triangular one and $4 - 6$ for a squared one, as recommended by [117]. Those values probably overestimate the actual impact pressure for high velocities, since generally the mean density decreases with increasing of the velocity, and thus C_d should decrease. However, in combination with ρ=300 kg/m^3 they are a compromise in order to take into account the effects of the snow clods impacts. Different studies are made experimentally, i.e. [148, 163, 185, 186], finding quite similar values. For example, from the Ryggfonn (N) data a value of C_d equal to 2.5 for dry-snow avalanches and to 6.3 for wet-snow avalanches is proposed. A different approach is pursued differentiating the C_d value only on the shape of the masts (1 if circular, 1.5 if triangular and 2 if squared). Finally [183] recommended C_d equal to 2 for big obstacles and for small rectangular ones, and C_d equal to 1 for small cylindrical ones with a ρ=300 kg/m^3. This value can be increased until 6 for very small structures.

The difference in the C_d values should be practically translated the preference of circular shapes to the squared ones: hence a chimney with a circular base should be preferred.

[195] show a dependence on the flow regime (i.e. slow wet avalanches or fully fluidized powder flow) too. In particular, like in [200], they suggest that C_d decreases with increasing Fr. Additional consideration on the drag coefficient are present in [103].

Furthermore the drag factor can be expressed [200] as the product of two factors:

$$C_d = C_r C_0(\alpha) = C_r 2(1 - \cos \alpha) \tag{1.44}$$

where C_r is the contribution of the flow regime and C_0 of the geometry obstacle through α, that is the half of the angle of the dihedral stagnation zone upward the obstacle. Thereby, by increasing the angle (due to the formation of the deposit), the pressure decreases. The same result is noticed by [196]: in the first second there are

peaks of pressure that are suddenly reduced, because of the snow deposition in front of the obstacle that partially protects the structure. For a Froude number of 5, the product $C_r C_0$ is close or lower than 2, in good agreement with the Swiss procedure [200]. Finally

$$C_r = AFr^{-n} \tag{1.45}$$

with $A = 10.8$, $n = 1.3$ (fitted values by [200]). Other values for n are found in Bingham case ($n = 2$) and in viscoplastic yield-stress fluids ($n = 1.7$). Finally, remember that, Eq. 1.41 should be limited to flow regimes with F_r greater than 1.

Granular experiments   Granular experiments are made to find the C_d coefficient too, as in [95, 110].

For instance, [94, 95] use glass beads in a channel 2 m long. Even if the C_d is generally defined in the steady state, they extent the results to the transient regime since the time evolution of the different flow characteristics involved is known. To study the only interaction with the obstacle, a previous simulation (based on the discrete element method) is carried by [95] to determine the characteristics of the flow (depth, velocity and density) outside the zone of the obstacle influence. This latter is estimated as 3.75 times the width of the obstacle from the obstacle. Their studies concern the influence of the open angle and curvature too. [94, 95] find that C_d varies with the ratio between the obstacle height and the flow thickness. The C_d for a frontal obstacle is on average 30% higher than with a 45° one. In the 45° obstacle, since the grains are deviated, their energy, and by consequence their force, is less transmitted.

The tallest obstacles have a C_d about 30% more than that had by obstacles with the height comparable to the flow thickness [94, 110]. For a height of the obstacle between 0.5 and 3.5 times the flow thickness the variation of the C_d do not depend on the obstacle shape [94]. The drag coefficient do not vary for obstacles tall more two times the flow thicknesses. In fact the grains can not jump the obstacle, since they are sidewards deviated by the obstacle.

The interaction between supercritical granular flow against mast (like those of electrical power lines, cable cars, ski lifts) is investigated too. Some experiments were carried out in a chute 7.5 m long and 0.35 m wide of the Hydraulics and environmental Engineering Department of the University of Pavia. [110] analyse the dependence between the total force against high rectangular and cylindrical obstacles and the width, height and shape. Besides they study the height of the run up and the characteristic of the flow.

The results are similar in the case in which the obstacle is exceeding about 3 times the flow depth [110]: the granular material, thrown upwards and to the sides, produces an airborne, fan shape stream of material. They show as the run-up and the throw-height are independent relatively on the width and on the shape of the structure. Besides the rise in the flow depth and in the load are similar in shape,

while they disagree in the tail. Finally, for the cylindrical obstacles, the total force is about 30 % lower than that for the rectangular ones, obtaining a C_d of about 0.7-0.85.

1.6.2   Involved height and height of run up

For the dense component, the height involved H_{tot} in the impact is calculated as the sum of the snow cover depth (H_s), the avalanche depth (h) and the height of run up (h_r):

$$H_{tot} = H_s + h + h_r \tag{1.46}$$

To estimate the run-up several attempts can be applied [92].

Kinetic energy approach

In the first approach, practically used by engineering, the height of run-up derives from the conversion of the kinetic energy into potential energy:

$$\frac{h + h_r}{h} = 1 + \frac{1}{2}(Fr^* \sin\varphi)^2 \tag{1.47}$$

where φ is the angle between the deflector and the flow, $Fr^* = \dfrac{u}{\sqrt{gh\cos\psi}}$, ψ is the slope angle [92]. In this formulation no energy is lost during the impact. Consequently

$$h_r = \frac{1}{2}\frac{(u\sin\varphi)^2}{g\cos\psi} \tag{1.48}$$

By $\sin\varphi$ is considered only the component of the velocity perpendicular to the flow. For the details in the Swiss recommended expressions see Sec. 1.7.1 and 1.8.1.

The same concept of the run-up was used by [144] to evaluate how much an avalanche can climb in the opposite slope depending on the kinetic energy and the energy dissipated in the impact.

Shock theory approach

The second one is based on the shock theory in the shallow flows and it is relevant for small-scale laboratory flows of water or granular materials ([92] and the bibliography within). Thanks to the conservation of mass and momentum the ratio between the depth h upstream and $h + h_r$ downstream the shock is given by:

$$\frac{h + h_r}{h} = \frac{1}{2}(\sqrt{1 + 8(Fr^* \sin\beta)^2} - 1) \tag{1.49}$$

where β is the shock angle.

Figure 1.15: Example of a catching dam in Airolo (CH). Photo E. Bovet.

Laboratory chute scale: application. For instance, [92] experimentally study the maximal flow height using a channel 10 m long and 0.2 m wide putting at the end a deflector dam. They have two cameras to film the experience, showing two transient phases (when the front of the snow interacted with the obstacle and when the flow came to rest) intermediated by a stationary phase, in which the flow depth is calculated.

In the stationary phase the maximum run-up is higher with higher Froude number, or for a fixed Froude number, it increases for higher deflecting angle with the obstacle [92].

Their experimental results are in agreement with the kinetic energy approach, while are overestimated by the shock theory one [92].

Recent dam approach

Recent studies (see [117] and the bibliography therein) found that the dam height H (Fig. 1.15), normal to the terrain, is given by:

$$H = h_r + h_s, \tag{1.50}$$

where h_r is the run-up of the avalanche and h_s is the snow depth upstream of the dam. In particular the shock dynamics and the necessity to prevent supercritical overflow are used to derive run-up heights:

$$h_r = \max(H_{cr} + h_{cr}, h_2 + \Delta H_{\psi_\perp} + \Delta H_k), \tag{1.51}$$

where:

$$H_{cr} + h_{cr} = \frac{h_1}{k} + \frac{(u_1 \sin\varphi)^2}{2g\cos\psi}k^2(1 - k^{-2}(Fr_\perp)^{-4/3}) \tag{1.52a}$$

$$Fr = \frac{u_1}{\sqrt{g\cos\psi h_1}} \tag{1.52b}$$

$$Fr_\perp = Fr\sin\varphi \tag{1.52c}$$

$$\begin{cases} k = 0.75 \text{ for } \alpha > 60°, \\ k = 0.75 + 0.1(60° - \alpha)/30° \text{ for } 30° \leq \alpha \leq 60° \end{cases} \tag{1.52d}$$

$$h_2 = h_1(2\sqrt{(6Fr_\perp^2 + 4)}\cos\delta + 1))/3 \tag{1.52e}$$

$$\delta = \frac{1}{3}\left[\frac{\pi}{2} - \tan^{-1}\left(\frac{9Fr_\perp^2 - 8}{Fr_\perp\sqrt{27(16 + 13Fr_\perp^2 + 8Fr_\perp^4)}}\right)\right] \tag{1.52f}$$

$$\Delta H_{\psi_\perp} = \frac{\sqrt{2}\tan\psi_\perp}{2Fr\cos\varphi}\xi \tag{1.52g}$$

$$\Delta H_k = \frac{\sqrt{2}(u_1\cos\varphi)^2}{2Fr\cos\varphi g\cos\psi R_k}\xi \tag{1.52h}$$

$$H_D = \frac{\cos\psi - \sin\varphi\sin\psi\cot\alpha}{1 - \cos^2\varphi\sin^2\psi}H \tag{1.52i}$$

u_1 and h_1 are the velocity and the flow depth at the dam, φ is the deflecting angle ($\varphi = 90°$ for a catching dam), k is the momentum loss coefficient (only for dams higher several times h_1), α is the angle of the upper dam side with respect to the terrain, H_{cr} is the critical dam height (that is the height at which the avalanche changes from a supercritical flow state to a subcritical one), h_{cr} is the corresponding critical flow depth, h_2 is the flow depth downstream the shock, $\Delta H_{\psi_\perp}$ is the extra deflecting dam height due to terrain slope towards the dam, ξ is the distance along the dam from its upstream end, ΔH_k is the extra height due to the centripetal force and occurs for deflecting dams with a radius of curvature R_k, and H_D is the vertical dam height measured in a vertical cross section normal to the dam axis in an horizontal plane.

Besides $\varphi \leq \varphi_{max} - 10°$, with $\varphi_{max} = \frac{\pi}{2} - \frac{2^{3/4}}{Fr^{1/2}} - \frac{2^{1/4}}{6Fr^{3/2}}$ otherwise h_2 in Eq.(1.52e) has to be calculated whit $\varphi = 90°$. Finally, the possibility of an increased run-out distance and the lateral spreading for a deflecting dam, as well as the storage volume for a catching dam have to be considered during the design.

Some practical examples are reported in [12].

1.7 Loads on large obstacles: walls

1.7.1 Swiss recommendations

Dense flow

As concern large obstacles of height H [183] the perpendicular pressure p_n is calculated with $C_d = 2$:

$$p_{dn} = \frac{1}{2} C_d \rho u^2 \sin^2 \varphi. \tag{1.53}$$

The deflection angle φ is equal to $90°$ in the case of perpendicular impact. A minimum of $\varphi = 20°$ has to be considered for the edges parallel to the flow. For safety reasons, $\rho = 300$ kg/m^3. The Swiss normative considers that a wall can create a dead zone downwind, assuming an angle of 20°, while some French technicians rises the angle to 45° [104]. Besides, note that velocity u is constant along the avalanche depth.

The tangential pressure (p_t) is obtained by

$$p_{dt} = \mu p_{dn} \tag{1.54}$$

with $\mu = 0.3 - 0.4$ [183].

The impact against a wall can create a vertical pressure, acting for instance against the advanced roof or a balcony, equal to 0.4 times the reference pressure [80, 104].

The snow deposited on a structures creates a vertical pressure equal to $(h - H)\rho g$. Finally, the deviation in the vertical plane has to be taken into account too [9, 80].

Eq. 1.48 becomes

$$h_r = \frac{u^2}{2g\lambda}. \tag{1.55}$$

The empirical dissipation coefficient λ depends on the kind of the snow: $\lambda = 1.5$ for dry, mostly fluidised flows, and $2 \leq \lambda \leq 3$ for dense flows.

At the heights H_s, h and h_r a different load is associated: in the snow cover any forces are transmitted, in the h the pressure distribution is uniform, while in the h_r it decreases linearly to 0.

Some authors disagree with these rules. For instance [195] recognize that the load can be transmitted through the snowcover, since a part of the snow-cover can be entrained by the avalanche. However, to consider a higher snow cover depth is precautionary since the moments calculated become larger. Besides [196] show as even if the magnitude of the total force experimentally measured is consistent with the Swiss procedure, unless a case explained with the flow regime, the load distribution is quite different. In particular, the lower part is underestimated. In addition avalanche run-up is not visible, on the contrary of the Swiss procedure [196].

Besides on the whole height of application $h_a = h + u^2/3g$, where h is the avalanche depth and the second term represent the run-up, [16] associate a uniform pressure.

Table 1.3: Actions on a snow shed [9].

Action	Normal to the ground surface	Parallel to the ground surface
Natural snow cover [kN/m^2]	$q_{nS} = \gamma d_S \cos\beta$	$q_{pS} = q_{nS} \tan\beta$
Avalanche deposit [kN/m^2]	$q_{nA} = \gamma d_A \cos\beta$	$q_{pA} = q_{nA} \tan\beta$
Sliding avalanche [kN/m^2]	$q_{nL} = \gamma d_L \cos\beta$	$q_{pL} = \mu q_{nL}$
Deviation force [kN/m^2]	$q_{nU} = \frac{\gamma d_L u_L^2 \sin\alpha}{6 d_L g}$	$q_{pU} = \mu q_{nU}$

Finally, let note that in France [104] the height at which the impact pressure has to be applied is defined as a fixed value (3m, 4m, 5m) depending on the different French regions.

Snow sheds.   Particular guidelines are defined to determine avalanche actions on snow sheds [9, 141]. The loads (Tab. 1.3) are calculated in relation to the inclination β of the snow shed roof and the deviation angle α, that is the difference between the slope angle and β. In particular the actions due to (i) the natural snow cover, (ii) the avalanche deposit and (iii) the sliding avalanche have to be calculated, in both the normal and parallel to the ground surfaces, in function of β. A deviation force, related to α is added and it becomes bigger close to the deviation point. The specific weights γ and the friction coefficient μ are defined for different types of snow and sliding surfaces. d_S, d_A, d_L are the heights of the natural snow cover, avalanche deposit and sliding flow respectively, u_L is the velocity and g=9.81 m/s^2.

Several studies are made with granular materials concerning snow sheda. For instance, [71] analyse the vulnerability of an avalanche protection gallery giving incertitudes on some input parameters too. They conclude that a dynamic analysis is necessary to complement the static analysis, not only for its greater values, but also to adapt reinforcement rod geometry to dynamic action. The concrete can be damaged before reaching the static reference load [71]. The vertical pressure P_n and the tangential one P_t can be calculated by the following :

$$P_n = \frac{E h_0 \sin\beta}{L} \tag{1.56}$$

$$P_t = c P_n \tag{1.57}$$

where E is the dynamic pressure, h_0 the avalanche thickness before the break in slope, L the distance between the avalanche edge and the break in slope, β the deviation angle between the gallery and the ground slope and c a coefficient varying from 0.3 and 0.4.

Besides [136] study the snow avalanche loading against a snow shed both in a real scale and in laboratory with a granular flow. They find that the ratio between the tangential and normal pressure varies between 0.2 and 0.6. From the laboratory test they find that the pressure is very high just after the change of the slope and decreases with the distance, in particular it reaches the hydrostatic pressure when the ratio between the distance from the change of the slope and the thickness of the flow is higher than 5. The impact pressure plays a very important role since it can be 7-10 times greater than the hydrostatic pressure. To have the same damage effect the static load must be 1.5-1.7 times larger than the maximum value of the dynamic loading. Consequently, considering the safety coefficients around 2, the dynamic effect is not critical [136].

Fluidised/saltation layer and powder part

Issler considers the impact pressure:

$$p_{pn} = f\rho u^2 \sin^2 \varphi \tag{1.58}$$

where f is between 0.5 and 1. It is closer to 1 the higher the velocity u, the deflecting angle φ, the density ρ of the powder part and the particle size within the flow. In addition, $f = 1$ is recommended for perpendicular impact. Vertical profiles of pressure and density are not specified. The density is 10-50 kg/m^3 within the saltation layer and 1-10 kg/m^3 in the powder part. The depth of the saltation layer is 1-5 m and the depth of the powder part several tens of meters.

1.7.2 European recommendations

Since large obstacles make the flow direction, not only a normal force but also a horizontal and a vertical shear forces are present [117]. The vertical force [208], one of the major cause for the destruction of buildings, is in the range of 0.3 to 0.5 times the normal force.

Peak of pressure

To be more precise, Eq. 1.31 and consequently Eq. 1.41 is not true during the first milliseconds of a vigorous impact. For instance, [130, 185] observed a short peak pressure p_{peak} of order of milliseconds, which is several times the base pressure. In the experiments this peak of pressure is not usually recorded at the initial impact instant, due to its short duration. However thanks to an inverse analysis, this effect can be taken into account [38].

As explained in [117], using the impulse force, the difference in pressure Δp is given by:

$$\Delta p = \rho C_{ps} u \tag{1.59}$$

where the celerity of the pressure (sonic) wave is $C_{ps} \sim 30$ m/s.

Experiments found $p_{peak}/\rho u^2 \approx 2.4 - 3.3$ [185] in agreement with other reported values. For instance $p_{peak}/\rho u^2 \approx 6$ for the dry and moist avalanches and $p_{peak}/\rho u^2 \approx 2.6$ for the wet ones [148], equal to 2.46 for [163]. In addition dry avalanches show higher values of peak of pressure and higher ratio between peak and averaged pressure, by about a factor 2, then the wet avalanches [148]. In general [82, 129] the ratio increases when the velocity u_1 and the density ρ_1 upstream decrease and when the flow height h_1 upstream increases. Wet avalanches have hence a lower peak of pressure and higher average pressures then dry avalanches for a given speed [148].

Finally, let note that some peaks of pressure, during the motion of the avalanche, can be also associated with velocity surges, impact of solid debris chunks, peaks in density, or a combination of these effects [148].

Loading after the initial peak and compressibility of snow

On longer time-scales than the duration of the pressure peak the avalanche, when meets the obstacle, begins to spread outside ways and splash up and it is prevented from moving ahead. At the same time, the mixture of air and snow close to the wall is compressed and stopped. Consequently, the snow is piled up in front of the wall and a wave propagates upstream through the incoming avalanche with a velocity $\mathbf{w}$. The wave front is a non material discontinuity. From the jump conditions across the singularity $\mathbf{w}$ can be found:

$$\mathbf{w} \approx \frac{(\mathbf{u}_1 \cdot \mathbf{n})\mathbf{n}}{(\rho_2 h_2 / \rho_1 h_1) - 1} \tag{1.60}$$

where the subscript 1 indicates quantities upstream of the shock and 2 denotes quantities on the downstream side. Let note that the ratio $\rho_2 h_2 / \rho_1 h_1$ is larger than 1. Hence the dynamic impact force becomes:

$$F_{Ix} = \rho_1 u_1^2 \left[\left(1 + \frac{1}{(\rho_2 h_2 / \rho_1 h_1) - 1} \right) + \frac{1}{2Fr_1^2} \right] h_1 b \tag{1.61}$$

and thus greater than the equation without the snow compression. In particular, for $Fr_1 > 2.5$, the difference is lower than 25%. For $Fr_1 > 2$ the pressure can be reduced proportional to h_1/h_2, due to the increase in flow depth, while for $Fr_1 < 2$ the impact force should be increased by a factor 1.2, and even more if $Fr_1 < 1$. The densities and the depths before and after the shock are related each others through the Froude number. The jump $\rho_2 h_2 - \rho_1 h_1$ depends on the impact pressure, on the ability of the avalanche to change direction and to increase its height h_2 (for laterally extended obstacles) and on the compressibility of snow-air mixture:

$$\frac{\rho_2}{\rho_1} \left(\frac{h_2}{h_1} \right)^2 - \frac{h_2}{h_1} - 1 + \left(\frac{\rho_2}{\rho_1} \frac{h_2}{h_1} \right)^{-1} - 2Fr_1^2 = 0 \tag{1.62}$$

Snow compressibility

The field measurements around the obstacle of test sites as well around the structures impacted by avalanches show as the the snow is compressed. Voellmy [208] proposed the following relationship linking the density ρ to the dynamic overpressure p:

$$\frac{\rho}{\rho_0} = \frac{1 + \frac{p}{p_0}}{1 + \frac{\rho_0}{\rho_F}\frac{p}{p_0}} \tag{1.63}$$

where ρ_0 is the initial density, $p_0 \approx 10^5$ Pa is the atmospheric pressure, and ρ_F is the upper limit density, depending on the kind of snow ($\rho_F = 600$ kg·m^{-3} for dry large-grained snow, $\rho_F = 800$ kg·m^{-3} for dry fine-grained snow, $\rho_F = 1000$ kg·m^{-3} for water-saturated snow). Generally the density is $1.5-3$ times ρ_0. However, the density measured can be higher since this compression of snow happens instantaneously with the consequence that the encapsulated air has not the time to escape during this compression, but only during the consolidation. [128] found a similar relationship (with a factor of 2) linking the density before and after the impact of the flowing avalanche. [129] found that the maximal density increase depends on the velocity and may be up $2-3$. Furthermore, the final density ρ_f, with a maximum of $\rho_f = 600$ kg/m^3 can be linked to the maximum pressure p_{max} through the following relationship [151]:

$$\rho_f = \rho_0 \left(\frac{p_{max}}{p_{max} - u^2\rho_0} \right) \tag{1.64}$$

Design loads

To design buildings or wall-like structures it is important to estimate the maximum force **F** and moment **M** due to the avalanche. Here the wall is considered wide enough so that the majority of the avalanche does not flow horizontally around it and it is at least laterally confined by the neighboring flow. To be applied in the design these calculated loads have to be multiplied by safety factors [117].

The avalanche expert should decide case-by-case which flow component consider (Fig. 1.16). For instance, a wet avalanche may not have the powder part.

Pressure transmitted through the snowpack

The pressure is:

$$p_s(z) = \begin{cases} p_d \frac{z - z_0}{h_s - z_0} & \text{for} \quad z > z_0 \\ 0 & \text{for} \quad z \leq z_0 \end{cases} \tag{1.65}$$

where h_s and h_d are the heights of the snowpack and of the dense flow, respectively, $z_0 = max(h_s - 2h_d, 0)$, and p_d is the dynamic pressure of the dense flow at the lower boundary (Eq. 1.67). The total lift force is negligible. In this section static loads
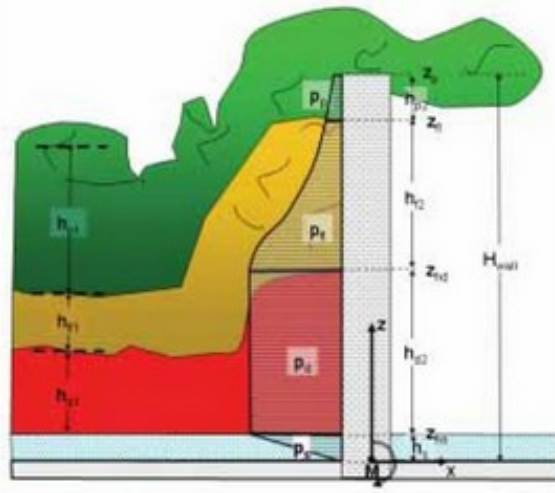
Figure 1.16: Impact pressure distribution due to an avalanche on a wall in the different components, from [117].

related to the snow cover on the ground or previous deposit are not taken into account [117].

Dense flow

A peak value reasonably estimated of $p_{peak} = 3\rho_1 u_1^2$ affecting an area of height h_1 has to be considered, depending on the risk accepted. In addition its pulse in moment associated, in which the point of attack should be at a minimum distance $h_s + h_1$ from the ground, has to be taken into account [117].

After this time of peak pressure, estimated on the order of 0.1 s, the pressure decreases to the recommended mean values [117]:

$$F_{dx} = \rho_1 u_1^2 \left[\left(1 + \frac{1}{(\rho_2 h_2/\rho_1 h_1)-1}\right) + \frac{1}{2Fr_1^2} \right] \frac{h_1}{h_2}(z_{hd} - z_{hs})b$$
$$F_{dz} = c_1 F_{dx} \tag{1.66}$$

where z_{hd} and z_{hs} are the z-coordinates of the fluid flow and of the snowpack, respectively (see Fig. 1.16), c_1 is between 0.1 and 0.6 depending on avalanche type [141, 208] and ρ_1=300 kg/m^3 usually. Consequently:

$$p_d \approx \rho_1 u_1^2 \left[\left(1 + \frac{1}{(\rho_2 h_2/\rho_1 h_1) - 1}\right) + \frac{1}{2Fr_1^2} \right] \frac{h_1}{h_2} = \rho_1 u_1^2 \left[f(Fr_1) + \frac{1}{2Fr_1^2} \right] \frac{h_1}{h_2} \tag{1.67}$$

with $f(Fr_1) \approx 1.2$ and $h_2/h_1 = 3 - 8$. The moment about the y-axis is:

$$M_{dy} = \frac{z_{hs} + z_{hd}}{2} F_{dx} \tag{1.68}$$

For the balcony or ledges the vertical forces have to be considered in the moment too.

Fluidised flow or saltation layer

The dynamic pressure is assumed to decrease with increasing height [117]:

$$p_{fl} = p_{zhfl} + (p_d - p_z hfl) \left(\frac{z_{hfl} - z}{z_{hfl} - z_{hd}} \right)^{n_f} \tag{1.69}$$

where $h_{hfl} = z_h d + c_e(0.1)u_1$, $1 < c_e < 3$, $p_{zhfl} = \rho_e \frac{u_1^2}{2}$, ρ_e=15kg/m^3, $n_f = 1$ is recommended even id $n_f = 4$ was proposed. For the corresponding $F_{flx}, F_{flz}, M_{fly}$ see [117]. If the avalanche is preceded by a fast moving fluidised head the equations have to be used with an appropriate ρ_1.

Suspension part or powder part

The dynamic pressure rapidly decreases with height from the value of lower boundary (p_d or p_{fl}) to the one of the upper boundary p_a [117]:

$$p_p(z) = max \left(p_{zhfl} \left(\frac{z_{hp} - z}{z_{hp} - z_{hfl}} \right)^3, p_a \right) \tag{1.70}$$

where $p_a = \rho_a \frac{u_1^2}{2}$, ρ_a=1.25 kg/m^3 is the air density, the height of the snow cloud $h_p = (10^{-5}s^{-2})l_{track}u_1^2$ depends on the travel distance along the track l_{track}. For the corresponding F_{px}, F_{pz} and M_{py} see [117].

Deflecting angle

If a wall is hit by an avalanche with an angle φ, the velocity to be used in the determination of the pressures is equal to $u_1 \cos \varphi$, while it remains the same in the thickness of the fluidised and powder part [117]. Tangential components are $F_{dy} = \min(c_1 F_{dx}, \tau_y \mathfrak{A})$ and $F_{fly} = \min(c_1 F_{flx}, \tau_y \mathfrak{A})$ with τ_y=10kPa is the critical stress [196], and $\mathfrak{A}$ is the contact area of the structure hit by an avalanche [117].

1.7.3 A frictional model of large flat obstacles

In the case of large obstacles peculiar effects linked with the modification of the flow geometry (strong deflection of the free-surface and of the internal streamlines) in

the vicinity of the obstacle should be considered. For instance, a general equation giving the force impressed on a wall impacted by a free-surface gravity-driven flow is recently derived for granular flows [58, 88, 89]. This equation takes into account the formation of a quasi-static, dead zone upstream of the wall that coexists with the inertial zone above that allows the flow to over the wall. The force (per unit width) is then expressed as the sum of different contributions:

$$F = F_u^N + F_h + F_w^N - \bar{\mu}_{zm} \left[F_w^T + F_u^T \right] \tag{1.71a}$$

$$F_u^N/L = \rho u^2 h[1 - (1 - \kappa\varphi)\cos\varphi] \tag{1.71b}$$

$$F_h/L = \frac{1}{2}\rho g h^2 \cos\psi \tag{1.71c}$$

$$F_w^N/L = \rho_0 \frac{V_0}{L} g \sin\psi \tag{1.71d}$$

$$F_w^T/L = \rho_0 \frac{V_0}{L} g \cos\psi \tag{1.71e}$$

$$F_u^T/L = -\rho u^2 h(1 - \kappa\varphi)\sin\varphi \tag{1.71f}$$

where F_u^N is the normal kinetic force associated with the deflection of the flow, F_h is the hydrostatic force related to the incoming flow and $F_w^N - \bar{\mu}_{zm} \left[F_w^T + F_u^T \right]$ is the apparent weight of the volume disturbed by the wall (component of the weight parallel to the slope, F_w^N, minus the basal friction force between the dead zone and the flow bottom, which takes into account the tangential kinetic force associated with the flow deflection). The effects concerning the dead zone process can also occur in presence of small obstacles [26]. We defined the following variables: $\kappa = (1 - e)/(\pi/2)$ is the velocity reduction coefficient where e is the restitution coefficient of snow granules, L is the width of the wall close to the transverse width of the incoming avalanche, V_0 is the volume disturbed upstream of the obstacle, and φ (rad.) is the mean deflection angle at the top of the wall. As a first approximation, φ can be estimated with the following equation from the minimum (ψ_{min}) and maximum (ψ_{max}) friction angles:

$$\varphi = \frac{1}{2} \left(\frac{\psi_{max}}{\psi_{max} - \psi_{min}} \right) (\psi - \psi_{min}). \tag{1.72}$$

An exact solution is provided for V_0/ℓ in [58, 89]. However, as a first approximation, V_0/ℓ can be expressed as:

$$\frac{V_0}{\ell} = \frac{hH}{2\tan\varphi} \left(2 + \frac{H}{h} \right), \tag{1.73}$$

where H is the wall height. ρ is the fluid density of the incoming undisturbed flow ($= \phi\rho_P$ for a granular fluid where ϕ is the volume fraction and ρ_P the particle density) and ρ_0 denotes a mean density to take into account the compaction of the

material inside the dead zone (ρ_{max} being the density of the material inside the dead zone):

$$\rho_0 V_0 = \rho \left(V_0 - \frac{H^2 \ell}{2 \tan \varphi} \right) + \rho_{max} \frac{H^2 \ell}{2 \tan \varphi}.$$ (1.74)

The previous equation is not valid if $L/\ell << 1$: lateral fluxes should be considered here, as discussed in [90].

1.7.4 Powder component: wind effects approach

Besides, the interaction between an aerosol and a structure can be compared with the wind effects. The technical regulations concerning the wind actions on structures, in fact, introduce an additional parameter, named the pressure coefficient C_p (to be more precise the external pressure coefficient C_{pe} and the internal one C_{pi}), to relate the values on the different parts of the structure. For instance, [7] proposes for a square of edge B and an area larger than 10 m² a factor C_{pe} equal to +0.8 for the upwind side, to -0.5 for the downwind one, and to a factor varying from -1.2 in the first $B/5$ reached by the flow, to -0.8 in the remaining lateral side. Let us note that these values are quite different in other regulations as in [5, 8, 10]. Finally, in Switzerland there are three possibilities to find a reference pressure for the powder component: (i) using the result of a numerical model, (ii) doing a damages back-analysis or (iii) taking a values in the range of 3-5 kPa.

1.8 Load on small obstacles: masts

1.8.1 Swiss recommendations

The impact force on narrow obstacles is:

$$F_m = C_d A p(z)$$ (1.75)

where C_d=1, 1.5, 2 depending on the shape (circular, triangular and squared, respectively), $A = h_{tot} D$ is the projected area, W the obstacle width, $h_{tot} = h_d + h_{stau}$, h_d the flow height, $h_{stau} = \frac{u^2}{2g\lambda} f(\frac{D}{h_d})$, with λ as in Sec. 1.7.1, $f(\frac{D}{h_d})$ depends on the ratio D/h_d ($0.1 \leq f(\frac{D}{h_d}) \leq 1$) [183]: smaller the obstacle higher the possibility to escape laterally is. Besides smaller flow depth avalanches have a larger force than the bigger ones, due to the function $f(b/H_f)$. Unfortunately, for small obstacles, the last term shows some deficiencies. Within the flow height the pressure is constant, while it decreases linearly in the run-up height.

Figure 1.17: C_{pe} from CNR [5].

1.8.2   European recommendations

Pressure transmitted through the snowpack

The same pressure (Eq. 1.65) of the wall case is used.

Dense flow

The force exerted is:

$$F_{dx} = C_{d*}D(z_{hd} - z_{hs})p_d \tag{1.76}$$

where $p_d = \rho_d u_f^2/2$, ρ_d=300 kg/m^3, $z_{hd} = min(h_d + z_{hs}, H_{mast})$, $C_{d*} = C_d + f_s(h_d)/Fr^2$, $f_s(h_d) \approx \sqrt{h_d/D}$ in the wet-snow avalanche, C_d as in Sec. 1.6.1. As for large obstacle, a pressure peak has to be considered for a time of 0.1 s, without using a C_d coefficient. In particular for the squared masts (no analysis are made for circular and triangular shapes) it is $p_{peak} = 2\rho_d u_f^2$. A factor 2, and not a factor 3 has to be considered, due to the flexibility of the flow to diffuse the peak towards the sides, and to upward propagation towards the free surface.

Fluidised flow or saltation layer

The same pressure expression (Eq. 1.69) of the wall is used, while the forces and moment of the wall case are multiplied by the coefficient C_d.

Suspension part or powder part

The same pressure expression (Eq. 1.70) of the wall is used, while the forces and moment of the wall case are multiplied by the coefficient C_d.

1.8.3   A non-newtonian viscous model for small obstacles

Recent measurements on full-scale snow avalanches evidenced the fact that the pressure can remain high in spite of a low incoming velocity [192, 195, 200]. The theoretical framework to take into account this behaviour assumed that it is attributed to the prevailing effect of the fluid rheology in the low-velocity flow regime [154]. This theory is based on the analogy with viscous fluids. A collection of experimental data on drag coefficients –concerning both newtonian and non-newtonian fluids at intermediate and low values of the Reynolds number Re are taken. Under the hypothesis of shallow flows, the macroscopic viscosity η and a Reynolds number based on depth-averaged velocity and obstacle width, $Re = uD/\eta$ are derived. With the assumption of the Reynolds similitude, the obtained formulae for simple fluids are extended in order to find a general formulation, relating the drag coefficient C_d to the Froude number Fr,

the slope angle ψ and the ratio between the flow depth and the obstacle width h/D [93, 154]:

$$C_d(Re, n) = 271(3 + \log Re)^{-3.37} f(n) Re^{\frac{n-1}{5}}, \tag{1.77}$$

where:

$$f(n) = \frac{n^3}{3} - \frac{5n^2}{4} + \frac{7n}{6} + \frac{3}{4}, \tag{1.78a}$$

$$Re(n) = \left[\left(\frac{2n+1}{n} \right) \frac{D}{h} \right]^n \frac{Fr^2}{\tan\psi(\cos\psi)^n}, \tag{1.78b}$$

$$Fr = \frac{u}{\sqrt{gh\cos\psi}}. \tag{1.78c}$$

n is the power index of the constitutive law that characterises the fluid rheology. $n = 1$ for newtonian fluids, $n < 1$ for shear thinning fluids and $n > 1$ for shear thickening fluids (for their definition see Ch. 2). Usually a shear thinning behaviour is assumed.

Therefore the drag coefficient is relied to the equivalent Reynolds number that depends on the regime type (laminar or turbulent, gravitative or inertial). Even if the quantification of n remains a challenge, the pressure from snow avalanches on small obstacles can be derived:

$$p = C_d(Re, n) \frac{1}{2} \rho u^2. \tag{1.79}$$

1.9   Specific recommendations

1.9.1   Impacts of solid bodies

Within avalanches debris of different kind (boulders, tree trunks, snow clods ...) can be present and can cause, in an impact with a structure, a local force during 1-100 ms with the consequent damages. Different theories are proposed [117]:

- the Hertz's formula [120] gives the impact force depending on the geometry and material characteristics:

$$F_I = \frac{4}{3} R^{1/2} E^* \delta^{3/2} \tag{1.80}$$

with $1/R = 1/R_b + 1/R_w$, $1/E^* = (1 - \nu_b^2)/E_b + (1 - \nu_w^2)/E_w$, R_b, R_w are the radii of boulder and wall, E_b, E_w the elastic modula, ν_b, ν_w the Poisson ratio and δ the compression during the impact. In particular, if the wall is plane: $R_w = \infty$. The maximum contact pressure, for circular point contact, is:

$$p = \frac{3}{2\pi} \left(\frac{4E^*}{3R^{3/4}} \right)^{4/5} \left(\frac{5}{4} mu^2 \right)^{1/5} \tag{1.81}$$

where $1/m = 1/m_b + 1/m_w$ is the effective mass and u is the velocity at impact. Plastic failure occurs when p_0 reaches a critical value of about $1.6Y$, where Y is the yield stress of the softer body.

For a sphere impacting a wall, the impinging speed necessary for the onset of failure can be deduced by the simplification of Eq. 1.81 (valid if $\rho_b u^2 / Y < 10^{-1}$):

$$\frac{\rho_b u^2}{Y} = 26(Y/E^*)^4 \qquad (1.82)$$

where $\rho_b = m/((4/3)\pi R_b^3)$ is the density of the impacting body. Since the intensity of the contact pressure pulse is then reduced, due to the occurrence of plastic deformation, Hertz's formula gives an upper value of the maximum contact pressure. The mean contact pressure, instead, increases until the full plastic failure from about $1.1Y$ to $3Y$.

- in Switzwerland [80], in the zones where the velocities are lower than 10 m/s, it is assumed that a boulder or a tree can hit an obstacle simultaneously to the dense avalanche giving a impact force of:

$$F_I = 3.3\rho u^2 \qquad (1.83)$$

The local impact pressure acting on a disc with a diameter 0.25 m is:

$$p_I = 66.6\rho u^2 \qquad (1.84)$$

This load is typically considered an accidental one with the consequence that a safety factor equal to 1 is generally used. Let is note that no formal recommendations exists concerning the correct values coefficient when the speeds are higher than 10 m/s.

- in [80] the concentrated load due to the hit of debris is similar to the rocks fall. The static force is:

$$Q'_e = (Q_e 2.5 I_h)/(0.3 I_s) \qquad (1.85)$$

where Q_e is a tabulated value [80] depending on the boulder mass, avalanche velocity, impact surface and breaking mode (ductile or fragile), I_h and I_s are the wall thickness and width. This force acts only on the impact area and hits the wall simultaneously to the avalanche.

1.9.2 Local dissipation of kinetic energy caused by dams

In order to evaluate the retarding effect of catching dams and breaking mounds, experiments with granular flow, as well as at full-scale, in particular at the Ryggfonn test site (see Sec. 1.2.2), are carried.

For instance [125] reproduce a mixed dense/powder avalanche with granular material. They estimate that the $2/3$ of the avalanche energy is dissipated to the impact on a snowcatcher. A transition from a super critical flow to a sub critical one can be observed [125].

To investigate the energy dissipation (see [117] and the bibliography therein), since the velocity is technically hard to measure, a posteriori analysis is made on the base of the reduction in the run out (its maximum distance or this associated to the center of mass). In laboratory experiments the ratio λ_e between the dissipation of the kinetic energy caused by the dam and the potential energy corresponding to the dam height is given by:

$$\lambda_e = \frac{1}{2} Fr^2 \frac{1 - l_{ovr}/l_{cont}}{H/h_b} \tag{1.86}$$

where l_{ovr} is the overrun distance, l_{cont} is the horizontal run-out distance of the tip (or the center of mass) of the avalanche beyond the location of the dam, H is the dam height and h_b the upstream flow depth. In particular, Eq.1.86 shows as λ_e is linearly dependent with the Froude squared and it depends on the slope of the line representing the relationship between the run-out distance and the dam height. However, the dissipation of kinetic energy in natural avalanche impacts with obstacles, seems to be lower than that found by granular experiments but greater than that measured at the Ryggfonn test site. Given this incertitude, to reduce the hazard areas below a catching dam is not obvious and should be used only in existing settlements, rather than to justify expansion of new urban areas. Often a value of $\lambda_e = 1.5$ is taken for catching dams built from loose materials and $\lambda_e = 2$ for steeper catching dams with a reinforced upstream side. Finally $\lambda_e = 1$ for deflecting dams. A greater reduction in run-out than that evaluated in Ryggfonn but less than that indicated in laboratory is observed. Hence, a lack of knowledge of some dynamics processes has to be filled in order to evaluate more correctly the loss of momentum and thus λ_e.

1.9.3   Jet theory

Experiments, made with both snow at Weissfluhjoch (CH) and with glass particles, show that the avalanche, when impacts a dam or a mound, detaches from the obstacle and forms an airborne jet [108]. This can be modeled as a two dimensional ballistic projectile motion with negligible air resistance. From the conservation momentum follows:

$$\ddot{\mathbf{x}} = \mathbf{g} - (f/h_j)\dot{\mathbf{x}}|\dot{\mathbf{x}}| \tag{1.87}$$

with $\mathbf{x} = (x, z)$ the location of the projectile in horizontal and vertical directions, where the origin is at the top of the obstacle, the dot represents a time derivative, $\mathbf{g}$ denotes the gravitational acceleration, f is a dimensionless constant representing the turbulent drag caused by air resistance and h_j is the core thickness of the jet. The parameters that define the trajectory of the jet are the speed u_1, at which the jet is

launched from the top of the obstacle, and the deflection β of the jet by the obstacle. The horizontal length of the jump L is found by solving numerically Eq. 1.87 with appropriate u_1, β and f/h_j. In particular $u_1 = k\sqrt{u_0^2 - 2gH\cos\psi}$ derives from simple energy conservation, with u_0 the incoming speed, H the obstacle height and k the energy dissipation (generally 0.5-0.9). β depends on the ratio h/H and f/h_j=0.004 m^{-1} for the computation of the throw length.

Such experiments, although done at different scales with open questions regarding the applicability of the results to large scale, provide useful indications for designers of retarding structures for snow avalanches in the absence of data from measurements at real scale. In this case the Froude number has the same order of magnitude to maintain the dynamic similarity.

From a practical point of view the airborne jet formed has consequences for the use of multiple rows of mounds or combinations of rows of mounds and catching dam. In fact the space between the rows has to be sufficiently large so that the snow launched from the top of the mounds does not jump over structures farther down the slope. Finally higher the dam more energy in the impact is lost and the trajectory taken by the jet becomes steeper.

Chapter 2

A new model for avalanche dynamics

In Sec. 1.2.3 several models for the avalanche dynamics are reported. They use different approaches varying from a centre-of-mass consideration to a density current one. Further models describe the avalanche as a deformable body, in particular as a continuum, with an hydraulics approach based on depth-averaged equations or as a granular material.

Different approaches are also used to describe the constitutive behaviour of flowing snow: Newtonian fluids, Criminale-Ericksen-Filby fluid [162], Bingham fluid [76, 159] or Cross fluid [124]. The choice of using for snow a non-Newtonian fluid, in which the shear stress is a non linear function of the shear strain rate, is based for instance on the analysis of the velocity profile along the depth of an avalanche measured experimentally [75, 124, 152, 159] that shows the presence of two layers having different shear strain rate, that can be translated into a shear dependent viscosity (see Sec. 2.2). In addition the snow has the property to rest with a finite depth [69], contrarily to newtonian fluids which can deform themselves until reaching a negligible depth (see Sec. 5.1). That means that for the snow, a yield value occurs when the deformations become small, and consequently the snow can rest with a non zero shear stress. Hereby in order to start deformations a threshold stress value must be overcome [76]. This is the reason why in this thesis we treat the snow as a shear thinning fluid and as a Bingham fluid. If the viscosity at low shear rates is very hight also a shear thinning fluid can describe the behaviour of the snow at rest, or more precisely flowing down very slowly. In fact they would behave like a very viscous material, almost like a solid, for low stress values. In a very small interval, that can be modeled as a single yield stress, its viscosity falls down suddenly. Above the yield stress the material behaves like a low viscosity liquid, allowing to describe the flowing snow. Since the stress is

not constant in the whole body, some portions can flow while others still behave like solids. This property, in particular, will be used in our avalanche model.

The constitutive behavior of the pseudoplastic or **shear thinning** fluids, as Fig. 2.1 shows, is characterized by a progressively decreasing slope $\mu_a = \tau/\dot{\gamma}$ (called apparent viscosity) of the shear stress as a function of the strain rate. For high values of $\dot{\gamma}$ it reaches a constant value μ_∞. The viscoplastics materials or **Bingham** fluids have
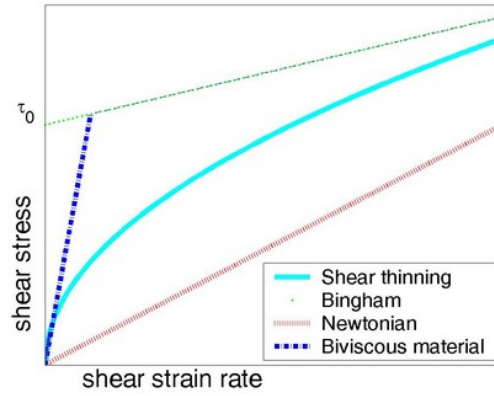

Figure 2.1: Newtonian and non-Newtonian links.

a little or no deformation, till a determined yield stress value. Above this threshold value, they behave like fluids. Some examples are paint, for the first time studied in 1916 by E.C. Bingham, (thus the name Bingham fluids), oil [84, 85, 86], as well as materials of common use as toothpaste or ketchup [137].

Bingham, in his original paper, didn't consider the response below a threshold value (Fig. 2.1), that is, the material was assumed completely rigid for values $\tau < \tau_0$:

$$\begin{cases} \dot{\gamma} = 0 & \text{for} \quad \tau < \tau_0 \\ \tau = \eta\dot{\gamma} + \tau_0 & \text{for} \quad \tau \geq \tau_0 \end{cases} \tag{2.1}$$

To emphasize the difference among the different fluids and in particular the fact that a Bingham fluid can be considered a limit situation of the shear thinning link, the velocity profiles of different flows in a channel are reported in Fig. 2.2. The profile, from a parabolic shape of the Newtonian case (Fig. 2.2.a), changes its shape in the shear thinning behaviour (Fig. 2.2.b,c,d) similar to the Bingham case, characterized by a plug flow in the centre of the channel and a high strain rate on the boundaries.

Some properties of such fluids are used in this chapter to describe the entrainment
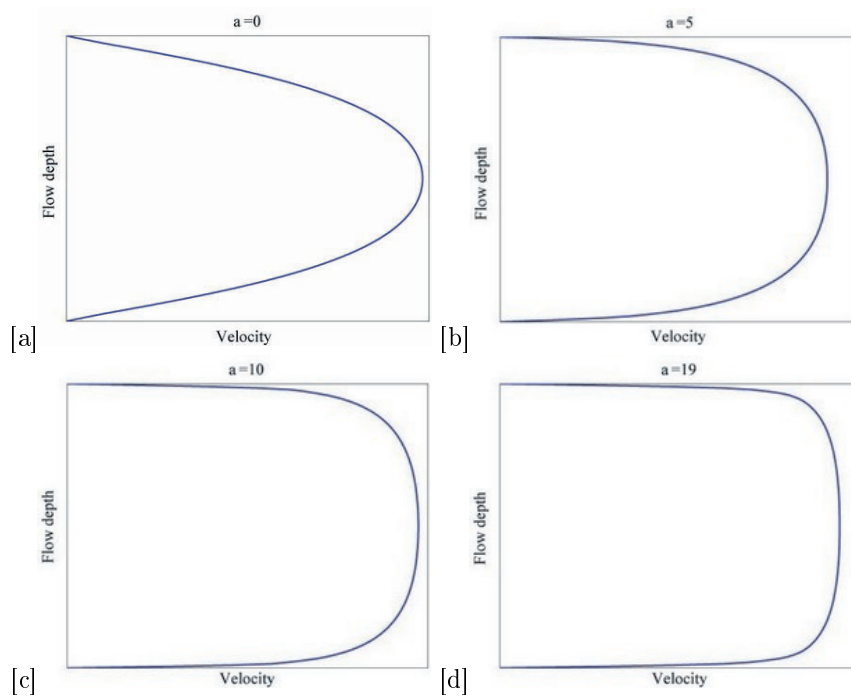
Figure 2.2: Velocity profile comparison of fluids in a channel having $\eta = 1/\left[1 + a \cdot \text{abs}\left(\partial u/\partial y + \partial v/\partial x\right)\right]$: [a] Newtonian ($a = 0$), [b]-[d] shear thinning cases with [b] $a = 5$, [c] $a = 10$ and [d] $a = 19$.

of the snow too. In the model presented a new approach is proposed to describe entrainment as a natural consequence of the chosen constitutive law.

2.1 Model definition

Let us consider a slope as an inclined plane[1] with an inclination θ described by the x coordinate (Fig. 2.3). Let us $H_s(x)$ be the snow cover thickness measured orthogonally to the ground along the y_{tot} direction. At the initial time $t = 0$ s a snow mass having the front in $x = 0$ begins to slip. The air-snow interface is described by the material interface $s_2(\mathbf{x}, t) = 0$. We defined by the function $s_1(\mathbf{x}, t) = 0$ or $y_{tot} = l(x, t)$ the bottom limit of the avalanche, that divides the snow cover ($y_{tot} < l(x, t)$) from the moving mass ($y_{tot} > l(x, t)$). It represents the transition layer where entrainment occurs. To characterise $y_{tot} = l(x, t)$ it is necessary to describe (i) the erosion and deposition processes in order to understand the whole dynamics as well as well as the (ii) velocity of the avalanche there. The coordinate system y perpendicular to the profile is introduced to focus the attention inside the avalanche flow. Hence $y = y_{tot} - l(x, t)$. The velocity parallel to the slope $u(x, t)$ varies along the avalanche depth too. To take into account this property, the variable strain rate $\frac{\partial u}{\partial y} = \frac{\partial u}{\partial y_{tot}} = \dot{\gamma}$ plays an important role.
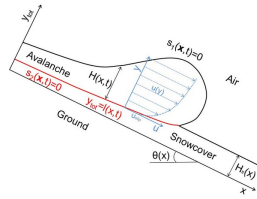

Figure 2.3: Coordinates system of the avalanche and of the snowcover. The avalanche is characterised by a velocity profile with a slip velocity in its bottom part. The interface between the flowing snow and the snow at rest is defined by $y_{tot} = l(x, t)$. The time variation of this quantity defines if erosion or deposition occur, from [49].

Let us consider, besides, that the avalanche and the snow cover have the same density ρ and are incompressible. The first hypothesis is in agreement, for instance, with Sovilla [189] who considers that the flowing snow, the entrained one and the snow cover have the same density. The hypothesis of incompressibility is common

---

[1]This hypothesis is easily removable and generalizable for slopes of arbitrary shape through a change in curvilinear coordinates, where one describes the ground topography (local tangent), while the second one is perpendicular to the soil (local normal).

in almost all the existent models, even if some experimental measures show that the avalanche flowing slightly changes its density [68] (see Sec. 1.7.2 and 5.4.1).

In the model developed, fluids having a Bingham and shear thinning behaviour are used.

The original Bingham model Eq. 2.1 is extended to the case in which the (solid) material has an elastic behavior for $\tau < \tau_0$. In this case, the Eq. 2.1 can be rewritten by the following relations (Fig. 2.1):

$$\begin{cases} \tau = G\gamma & \text{for} \quad \tau < \tau_0 \\ \tau = \eta\dot{\gamma} + \tau_0 & \text{for} \quad \tau \geq \tau_0 \end{cases} \tag{2.2}$$

where G is the shear modulus and γ is the shear strain.

The three-dimensional formulation of the system (Eq. 2.2) is deduced by introducing the second [2] invariant $I\!I$ of the tensor:

$$\begin{cases} \underline{\underline{\tau}} = G\underline{\underline{B}} & \text{for} \quad |I\!I| < \tau_0^2 \\ \underline{\underline{\tau}} = \left[\eta + \dfrac{\tau_0}{|I\!I|^{1/2}}\right] 2\underline{\underline{D}} & \text{for} \quad |I\!I| \geq \tau_0^2 \end{cases} \tag{2.3}$$

where $\underline{\underline{B}} = \underline{\underline{F}}\,\underline{\underline{F}}^T$ is the Cauchy-Green strain tensor, $\underline{\underline{F}}$ is the deformation gradient tensor and $2\underline{\underline{D}} = (\nabla\mathbf{u} + (\nabla\mathbf{u})')$. Other models were proposed by Herschel-Bulkley [137], to take in account high shear rate intervals:

$$\underline{\underline{\tau}} = \begin{cases} 2\eta\underline{\underline{D}} & \text{for} \quad |I\!I|^{1/2} \leq \dot{\gamma}_c \\ 2\left[\dfrac{\tau_0}{|I\!I|^{1/2} + m|I\!I|^{(n-1)/2}}\right]\underline{\underline{D}} & \text{for} \quad |I\!I|^{1/2} > \dot{\gamma}_c \end{cases} \tag{2.4}$$

and by Papanastasiou [137] who, using an exponential function, allows the use of only one equation for the whole flux:

$$\tau = \left\{\eta + \dfrac{\tau_0[1 - \exp(-a\dot{\gamma})]}{\dot{\gamma}}\right\}\dot{\gamma} \tag{2.5}$$

The latest two models have a viscoplastic constitutive equation that results advantageous in numerical simulations. Using the modifications put forward by Papanastasiou, the 3D formulation of the Herschel-Bulkley equation can be rewritten as

$$\underline{\underline{\tau}} = \left\{m|I\!I|^{(n-1)/2} + \dfrac{\tau_0(1 - \exp(-a|I\!I|^{1/2}))}{|I\!I|^{1/2}}\right\}2\underline{\underline{D}} \tag{2.6}$$

where m, n, a are calibration parameters.

---

[2] $|I\!I|_A = \dfrac{1}{2}[(\operatorname{tr} A)^2 - \operatorname{tr} A^2]$ where $\operatorname{tr} A$ is the trace of A.

The system composed by the snow cover and the flowing mass is considered as a shear thinning (SH) fluid or a Bingham one (B). In the second case, the avalanche is supposed to be in a fluid phase (in which $\tau > \tau_0$), while the layer of non eroded snow results to be in the solid phase ($\tau < \tau_0$). This represents a substantial difference from the Dent and Lang's "biviscous modified Bingham" model [75, 76] in which the avalanche itself is considered as a combination between two linear viscous fluids, where the lower one has a viscosity higher than the upper one, as justified by the velocity profiles observed in laboratory experiences [159].

Note that the model, at the actual stage of development, can only perform simulations with constant width. The results obtained have to be compared, consequently, only with experimental data from adequate geometry, like, for instance, the snow chute at the Weissfluhjoch near Davos, Switzerland [123, 124] (see Sec. 2.1.3).

Under the incompressibility hypothesis, the Navier–Stokes equations become:

$$\nabla \cdot \mathbf{u} = 0 \tag{2.7}$$

$$\rho \left(\frac{\partial \mathbf{u}}{\partial t} + \mathbf{u} \cdot \nabla \mathbf{u} \right) = \nabla \cdot \underline{\underline{T}} + \rho \mathbf{g} \tag{2.8}$$

where $\mathbf{u}$ is the velocity, $\mathbf{g}$ is the gravitational acceleration and $\underline{\underline{T}}$ is the stress tensor given by the following expression:

$$\underline{\underline{T}} = -p\underline{\underline{I}} + Z(\nabla \mathbf{u} + (\nabla \mathbf{u})') \tag{2.9}$$

where p is the pressure and Z is

$$Z = \begin{cases} Z_B = \left(\eta_0 + \dfrac{\tau_0}{|\mathit{I\!I}|^{1/2}} \right) & \text{(B) case} \\[4mm] Z_{SH} = \left\{ m|\mathit{I\!I}|^{(n-1)/2} + \dfrac{\tau_0(1 - \exp(-a|\mathit{I\!I}|^{1/2}))}{|\mathit{I\!I}|^{1/2}} \right\} & \text{(SH) case} \end{cases} \tag{2.10}$$

where η_0, τ_0, m, n, and a are constants defining the Bingham and shear thinning constitutive laws. Adapting the three-dimensional formulation to the two-dimensional situation, the second invariant $\mathit{I\!I}$ of the tensor $2\underline{\underline{D}}$ is:

$$|\mathit{I\!I}| = \left| 4\frac{\partial u}{\partial x}\frac{\partial v}{\partial y} - \left(\frac{\partial u}{\partial y} + \frac{\partial v}{\partial x} \right)^2 \right|, \tag{2.11}$$

and in the one-dimensional case it is :

$$|\mathit{I\!I}|^{1/2} = \frac{\partial u}{\partial y} = \dot{\gamma}. \tag{2.12}$$

Let note that $\frac{\partial u}{\partial y} = \frac{\partial u}{\partial y_{tot}} = \dot{\gamma}$ Consequently, the momentum conservation equation becomes:

$$\rho \left(\frac{\partial \mathbf{u}}{\partial t} + \mathbf{u} \cdot \nabla \mathbf{u} \right) = \nabla \cdot [Z(\nabla \mathbf{u} + (\nabla \mathbf{u})')] - \nabla p + \rho \mathbf{g} \tag{2.13}$$

where $Z = Z_{SH}$ in the (SH) case and $Z = Z_B$ in the (B) one.

Let's note that if in the (SH) situation Eq. 2.13 is available for the whole domain, that is $\forall I\!I$, in the (B) case Eq. 2.13 is valid only inside the avalanche, that is where $|I\!I| \geq \tau_0^2$. Outside, the snow cover is described by

$$\underline{\underline{\tau}} = G\underline{\underline{B}} \quad \text{for} \quad |I\!I| < \tau_0^2 \tag{2.14}$$

2.1.1 Considerations about the interfaces

Since for the moving avalanche the differential problem is a parabolic one, two conditions are requested on the interface: a kinematic one and a dynamic one.

Avalanche/air interface $s_2(\mathbf{x}, t) = 0$

Let's $s_2(\mathbf{x}, t) = g(x, t) - y_{tot} = 0$ be the equation describing the interface between the two different materials, snow avalanche and air. By deriving with respect to time this expression, the advection equation is deduced:

$$\frac{\partial g}{\partial t} - v + u\frac{\partial g}{\partial x} = 0. \tag{2.15}$$

In this way it is possible to deduce the interface evolution by knowing the initial shape $s_2(\mathbf{x}, t = 0) = 0$. This represents a different approach, for instance, with respect to the depth averaged models (see Sec. 1.2.3), in which the depth itself appears directly in the momentum equation. In fact, it is supposed that avalanche modifies its shape with time.

As a matter of fact, the distribution of the mass in the avalanche body can influence significantly the dynamics, with the consequence that the runout distances, heights and velocities are different. Besides, the description of the flow depth allows to make calculations for the design, e.g. of a dam or an house [80] along the avalanche path.

To define the boundary conditions, let's note that the velocity continuity is necessary, that is the avalanche velocity must be equal to that of the air. By the scalar product of the above equality by the normal $\mathbf{n} = \dfrac{1}{c_2}(\dfrac{\partial g}{\partial x}, -1)'$, where $c_2 = 1/\sqrt{(\partial g/\partial x)^2 + 1}$ is the normalisation coefficient, the following equation is obtained:

$$\mathbf{u}_{air} \cdot \mathbf{n} = \mathbf{u}_{ava} \cdot \mathbf{n}. \tag{2.16}$$

This expression implicates the non-penetrability between air and avalanche.

Moreover, the continuity of the normal stress is valid, that is:

$$\underline{\underline{T}}_{air}\mathbf{n} = \underline{\underline{T}}_{ava}\mathbf{n}. \tag{2.17}$$

However, since $\underline{\underline{T}}_{air}$ is negligible, Eq. 2.17 can be reduced to:

$$\underline{\underline{T}}_{ava}\mathbf{n} = 0. \tag{2.18}$$

Eq. 2.18 is expressed by the following system, on the interface $s_2(\mathbf{x}, t) = 0$:

$$\begin{cases} \left[2Z\dfrac{\partial u}{\partial x} - p\right]\dfrac{\partial g}{\partial x} - Z\left(\dfrac{\partial u}{\partial y_{tot}} + \dfrac{\partial v}{\partial x}\right) = 0 \\[4mm] \left[Z\left(\dfrac{\partial u}{\partial y_{tot}} + \dfrac{\partial v}{\partial x}\right)\right]\dfrac{\partial g}{\partial x} - 2Z\dfrac{\partial v}{\partial y_{tot}} + p = 0 \end{cases} \tag{2.19}$$

where $Z = Z_{SH}$ in the (SH) case and $Z = Z_B$ in the (B) one, noting that the expression for the avalanche, and not that for snowcover, is taken into account.

The snow/avalanche interface $s_1(\mathbf{x}, t) = 0$

The interface $\sigma = s_1(\mathbf{x}, t) = l(x, t) - y_{tot} = 0$ identifies the bottom limit of the avalanche, that divides the snow cover ($y_{tot} < l(x, t)$) from the mass in movement ($y_{tot} > l(x, t)$), by considering the erosion/entrainment and deposit phenomena. The first constraint is linked to the definition of erodible snow:

$$l(x, t) \leq H_s(x). \tag{2.20}$$

Besides, the shear stress is defined by the fact that the surface s_1 is equal to the threshold value τ_0,

$$\mathbf{t}'_{s_1} \cdot \underline{\underline{T}}\mathbf{n}_{s_1} = \tau_0 \tag{2.21}$$

where $\mathbf{t}_{s_1} = \dfrac{1}{c_1}(1, \partial l/\partial x)'$ and $\mathbf{n}_{s_1} = \dfrac{1}{c_1}(\partial l/\partial x, -1)'$ (where $c_1 = \sqrt{(\partial l/\partial x)^2 + 1}$), are respectively the tangential and normal vector at the interface. Hence:

$$\frac{1}{\left[\left(\dfrac{\partial l}{\partial x}\right)^2 + 1\right]}\left\{2\dfrac{\partial l}{\partial x}\left(\dfrac{\partial u}{\partial x} - \dfrac{\partial v}{\partial y_{tot}}\right) + \left[\left(\dfrac{\partial l}{\partial x}\right)^2 - 1\right]\left(\dfrac{\partial u}{\partial y_{tot}} + \dfrac{\partial v}{\partial x}\right)\right\} = \frac{\tau_0}{Z} \tag{2.22}$$

where $Z = Z_{SH}$ or $Z = Z_B$ in the (SH) case or in the (B) one, respectively.

It is finally necessary to assign the condition for describing the interface evolution $y_{tot} = l(\mathbf{x}, t)$. Let's note that the advection equation (Eq. 2.15) is not applicable, because the interface is a non-material one. In thermodynamics the evolution of the boundary is proportional to the jump of the heat flux due to the latent heat. Similarly we demonstrate the evolution of the interface is related to the jump of the stress (see Sec. 2.3 for more details):

$$\frac{dl}{dt} \propto (\tau_0 - \tau_{ava}). \tag{2.23}$$

2.1.2 Numerical simulations

Front-tracking strategy

A first technique investigated to implement the model is the front-tracking strategy, based on transforming the complex domain of the avalanche always in the same simple one. This approach is possible because the shape of the avalanche can change in time, but not drastically. For this reason, using a lagrangian coordinate system moving with the avalanche, instead of an eulerian one could be advantageous. Therefore, to simulate the evolution of the mass in movement without regenerating the mesh in each temporal step, the avalanche volume is transformed in a simple domain.

Let's consider the situation in which the domain of the avalanche alone (coordinates x, y) is transformed in a rectangular domain of unit height (coordinates ξ, ψ) through the following:

$$\begin{cases} \psi = \dfrac{y_{tot} - l(x,t)}{g(x,t) - l(x,t)} \\ \xi = x \end{cases} \Leftrightarrow \begin{cases} y_{tot} = \psi[g(\xi,t) - l(\xi,t)] + l(\xi,t) \\ x = \xi \end{cases} \tag{2.24}$$

In this way, the interface $s_2(\mathbf{x}, t) = 0$ is the upper side of the rectangle, that is $\psi = 1$, while $s_1(\mathbf{x}, t) = 0$ is the lower side, that is $\psi = 0$.

To determine the differential operators in the coordinates (ξ, ψ) it is necessary to calculate the Christoffel's symbols, defined, using the Einstein's notation according to which the summation over up and down repeated indices is understood, by the following formula:

$$\Gamma^l_{ik} = \frac{1}{2} g^{lj} \left(g_{ij,k} + g_{jk,i} - g_{ik,j} \right) \tag{2.25}$$

where $g_{ij} = \mathbf{e}_i \cdot \mathbf{e}'_j$ is the metric tensor, obtained by the product between the vectors of the basis in the reference frame (ξ, ψ), g^{ij} is its inverse matrix and $g = \det(g_{ij}) = h^2$. The notation $g_{ij,k}$ means that the derivative of g_{ij} by the kth component (where $k = 1$ is the derivative by ξ and $k = 2$ by ψ) is carried out. Using a simplified notation for the avalanche thickness $h = g - l$ and l, even if they depend on ξ e t, we obtain:

$$\begin{aligned} &\Gamma^1_{11} = \Gamma_{12,1} = \Gamma^1_{21} = \Gamma^1_{22} = \Gamma^2_{22} = 0 \\ &\Gamma^2_{11} = \frac{1}{h} \left(\psi \frac{\partial^2 h}{\partial \xi^2} + \frac{\partial^2 l}{\partial \xi^2} \right) \\ &\Gamma^2_{12} = \Gamma^2_{21} = \frac{1}{h} \frac{\partial h}{\partial \xi}. \end{aligned} \tag{2.26}$$

It is possible now to calculate the differentials terms included in the Navier-Stokes equation using the definitions given in [178]. In particular from:

$$\nabla \cdot \mathbf{u} = v^h_{,h} + \Gamma^h_{lh} v^l \tag{2.27}$$

we obtain:

$$\nabla \cdot \mathbf{u} = \frac{\partial v_\xi}{\partial \xi} + \frac{\partial v_\psi}{\partial \psi} + \frac{1}{h}\frac{\partial h}{\partial \xi} v_\xi. \tag{2.28}$$

Hence by:

$$\nabla p = g^{ij} p_{,j} \mathbf{e}_i \tag{2.29}$$

is derived:

$$\nabla p = \left(\frac{\partial p}{\partial \xi} - \frac{1}{h}\frac{\partial p}{\partial \psi} \left(\eta \frac{\partial h}{\partial \xi} + \frac{\partial l}{\partial \xi} \right), \frac{1}{h}\frac{\partial p}{\partial \psi} \right)' \tag{2.30}$$

Finally the velocity laplacian, not calculated here, can be evaluated by the substitution in

$$\nabla \cdot \underline{\underline{Q}} = \left(\frac{1}{\sqrt{g}}(\sqrt{g}A^{kl}), k + \Gamma^l_{pk}A^{kp} \right) \mathbf{e}_l \tag{2.31}$$

of the tensor

$$\underline{\underline{Q}} = \nabla \mathbf{u} = (v^k_{,h} + \Gamma^k_{lh}v^l)g^{hi}\mathbf{e}_k \otimes \mathbf{e}_i. \tag{2.32}$$

In order to transform the system made by the avalanche and snow domain (coordinates x, y) in a rectangular domain having the unitary height (coordinates $\hat{x}, \hat{y}$), it is sufficient to replace in the previous case $l(x,t) = 0$ and $h(x,t) = g(x,t)$:

$$\begin{cases} \hat{y} = \dfrac{y_{tot}}{g(x,t)} \\ \hat{x} = x \end{cases} \Leftrightarrow \begin{cases} y = \hat{y}g(x,t) \\ x = \hat{x} \end{cases} \tag{2.33}$$

Formulation under self-similarity hypothesis

To focus the attention on how the volume changes with the variation of the lowest interface $l(\mathbf{x}, t)$, we simplify our model supposing that the avalanche evolves maintaining the same shape, increasing the volume because of the snow entrainment. A similar hypothesis was used by different authors, like [36], as reported in [174], i.e. the avalanche keeps a self-similar shape during its evolution (see Sec. 1.2.3).

Hence let's consider that an initial configuration (Fig. 2.4), in which the abscissa varies in $0 \leq \hat{x} \leq L_0$, can be expanded until the abscissa varies in $0 \leq x \leq L(t)$. A similar reasoning is available also for the vertical coordinate, that is:

$$\begin{cases} x = \alpha\hat{x} \\ y_{tot} = \alpha\hat{y} \end{cases} \tag{2.34}$$

and for the two-dimensional volume A:

$$A = \alpha^2 A_0 \tag{2.35}$$

where $\alpha = \dfrac{L(t)}{L_0}$ and A_0 is the initial area.
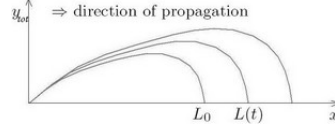
Figure 2.4: Self-similar growth of the avalanche: the Lagrangian coordinate system has the origin fixed on the avalanche tail.

The variation of this two-dimensional volume in time can be calculated by deriving Eq. 2.35:

$$\frac{dA}{dt} = \frac{2A_0}{L_0^2} L(t) \frac{dL}{dt} \tag{2.36}$$

or by using the density definition $\rho_0 = \dfrac{M}{A}$, related to the fact that mass variation is due to entrainment of the snow in the area $L\dfrac{dl}{dt}dt$, where $l(x,t)$ is the interface between the motionless snow and the avalanche.

It is therefore possible to deduce that (the boundary terms being negligible):

$$\frac{dA}{dt} = \frac{1}{\rho_0}\frac{dM}{dt} = \int_0^{L(t)} \frac{\partial l(x,t)}{\partial t}dx \tag{2.37}$$

Equating Eq. 2.36 to Eq. 2.37, we obtain:

$$\frac{dL}{dt} = \frac{L_0^2}{2A_0 L(t)} \int_0^{L(t)} \frac{\partial l(x,t)}{\partial t}dx \tag{2.38}$$

Therefore, Eq. 2.38 indicates that the avalanche length L varies proportionally to the mean value of the entrainment rate:

$$\overline{l'} = \frac{1}{L(t)} \int_0^{L(t)} \frac{\partial l(x,t)}{\partial t}dx \tag{2.39}$$

Observe that, in the simplifying assumption of constant entrainment (in space):

$$\frac{dL}{dt} = \frac{L_0^2}{2A_0}\frac{dl}{dt} \tag{2.40}$$

We also note that if the entrainment is only active in the frontal region $[\beta L(t), L(t)]$, with $0 < \beta < 1$, then the evolution law of the avalanche length is Eq. 2.40 multiplied by the constant $1 - \beta$.

The level set method

An alternative approach to simulate avalanche dynamics consists in using the level set method, suitable for free boundary problems [50, 67, 134, 164].

To test this method, for the sake of simplicity, only the avalanche, is considered, neglecting the snow cover and its entrainment.

To this aim, let's consider the system constituted by air and avalanche as a domain composed by two fluids, modelled by the Navier-Stokes equations and having different densities and viscosities:

$$
\begin{cases}
\rho \left(\dfrac{\partial \mathbf{u}}{\partial t} + \mathbf{u} \cdot \nabla \mathbf{u} \right) = \nabla \cdot [-p\underline{\underline{I}} + \eta(\nabla \mathbf{u} + (\nabla \mathbf{u})^T)] + \mathbf{F} \\[3mm]
\nabla \cdot \mathbf{u} = 0
\end{cases}
\tag{2.41}
$$

where ρ is the density, $\mathbf{u} = (u, v)'$ is the velocity, p is the pressure, $\underline{\underline{I}}$ is the identity, η is the viscosity and $\mathbf{F}$ takes into account the gravitational and friction forces (both a Coulomb force and a viscous one).

The method describes the evolution of the interface between the two fluids, tracing an isopotential curve of the level set function Φ. The interface is described by $\Phi = 0$, the more dense and more viscous fluid is placed in the domain where $\Phi > 0$ and the less dense and less viscous one is situated in the zone characterized by $\Phi < 0$. The function Φ is transported by the advection equation:

$$
\frac{\partial \Phi}{\partial t} + \mathbf{u} \cdot \nabla \Phi = 0.
\tag{2.42}
$$

It is important to underline that the density and the viscosity have to be described through the level set function, since they move jointly to the function Φ. Thanks to the Heaviside function, they can be defined in the whole domain according to:

$$
\rho = \rho_1 + H(\Phi)(\rho_2 - \rho_1)
\tag{2.43}
$$

$$
\eta = \eta_1 + H(\Phi)(\eta_2 - \eta_1)
\tag{2.44}
$$

where ρ_1 (η_1) and ρ_2 (η_2) are, respectively, the density (viscosity) of the air and of the avalanche, and $H(\Phi)$ is the Heaviside function:

$$
H(\Phi) = \begin{cases} 0 & \text{if} \quad \Phi < 0 \\ 1 & \text{if} \quad \Phi > 0 \end{cases}
\tag{2.45}
$$

In the simulations reported in this section, carried out using the Comsol Multiphysics tool, a shear thinning fluid is used. This is possible giving an appropriate viscosity law (η_2 depending on $\dot{\gamma}$) as in [76], or calculated experimentally by [124]. It

is important to underline that the results obtained are still qualitative, because the model need further calibration with experimental data.

The first case considered, describes an avalanche through a non-Newtonian fluid using typical values for the density (300 kg/m^3) and for the viscosity (varying from 0.6 to 30 kg s^{-1}m^{-1} [76]). By the analysis of the flow depth evolution along the path, shown in Fig. 2.5, we can conclude that the flow depth distribution calculated is reasonable. Besides thanks to the introduction of friction forces the avalanche stops by itself. Moreover the velocity representation (Fig. 2.6) shows that the front of the avalanche is faster than the tail, as confirmed by several experimental observations.

2.1.3 Validation of the level set method: case study of the Weissfluchjoch chute

In this section a first validation of the model is carried. The results of the simulations obtained with the level set method are compared with the experimental data collected by the researchers of the Institute for Snow and Avalanche Research (SLF) at the Weissfluchjoch near Davos, Switzerland [123] (see Sec. 1.2.2 and Fig. 1.12.a).

They fill the half upper part of their 34 m long and 2.5 m wide chute with snow, that can be released by opening a gate. On the sidewall and in the middle of the 32° section of the chute some optoelectronic sensors (Fig. 1.12.b) are placed to measure the velocity profile. Since the chute is cleaned from the snow, only the model without entrainment can be simulated, namely the system composed only by air and avalanche.

The input parameters are measured experimentally: a mass of snow having a density of 400 kg m^{-3}, length 10 m and thickness 0.4 m. To be able to compare the data with the experimental ones the same law of the viscosity in [124] is used for the avalanche:

$$\eta_2 = \frac{\rho_2(\mu_0 + \mu_1 k_c |I\!\!I|^{1/2})}{(1 + k_c |I\!\!I|^{1/2})} \tag{2.46}$$

with μ_0=2.1 m^{2}s^{-1}, μ_1=0.0027 m^{2}s^{-1} and $k_c = 1.1$. This is a shear thinning law, called Cross model, similar to Eq. 2.67, for which [124] have calculated the calibration parameters. For air ρ_1=1.295 kg m^{-3} and η_1=1.81 10^{-5}kg m^{-1}s^{-1}.

From a numerical point of view, since it is important to know the avalanche behaviour and not the air one, the mesh is required to be refined only in the snow sliding area and not in the whole domain. Besides, an algorithm is implemented to move the mesh with the avalanche. Let's note that in comparison with a whole domain refinement, the degrees of freedom that have to be calculated is reduced as well as the computational time, without loss of details, as Fig. 2.7 shows. The major friction introduced in the 32° (reaching a dry Coulomb friction coefficient of 0.72), due to the presence of rubber bars, decelerates the flowing snow, as Fig. 2.7.b shows.

One of the most important features of the model is that it allows to describe the velocity profile along the depth of the avalanche (see Sec. 2.2 for more detailed
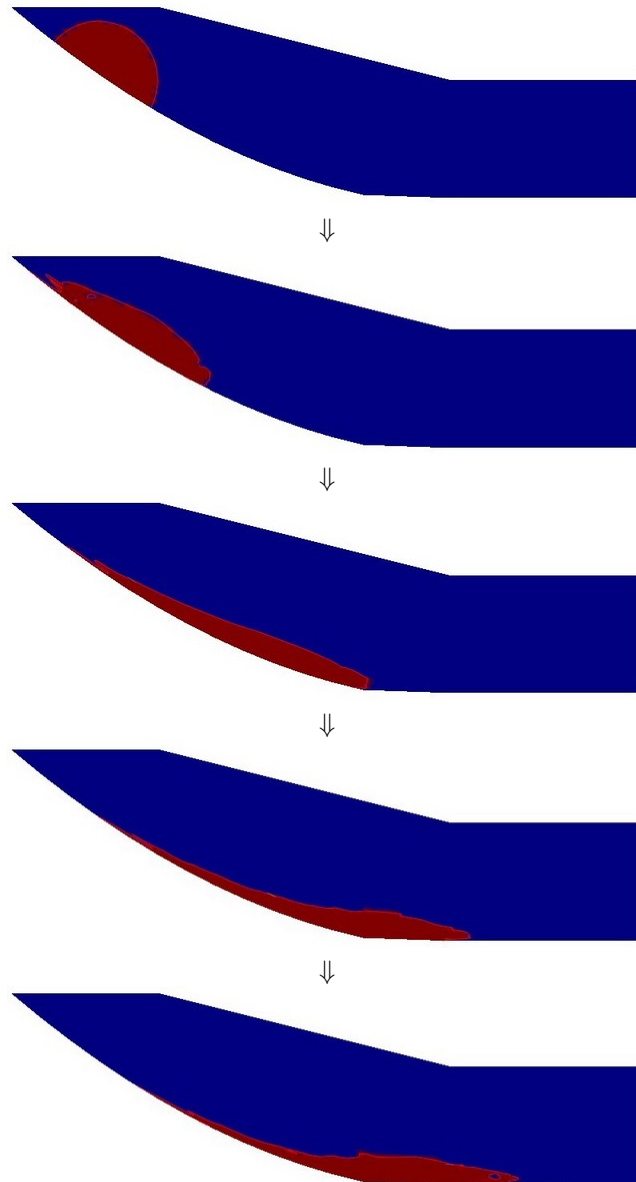
Figure 2.5: Snapshots showing the evolution of the flow depth at time t=0, 1, 3, 5 and 7 s. The avalanche is the red zone, while the air is the blue one.
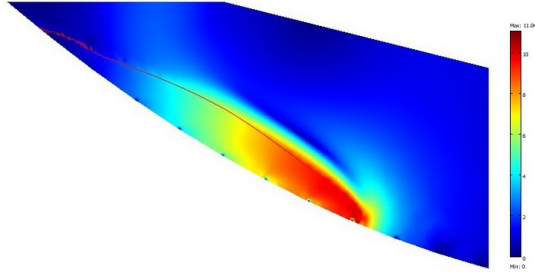
Figure 2.6: Snapshot showing the velocity field (surface) and the interface between the two phases (solid red line) at time 1.2 s.

analysis). This feature is not taken in account by the majority of the models in the literature, which consider a depth-averaged velocity or give a constant law for the velocity dependence on the depth (see Sec. 1.2.3).

The data collected, show that the 0.4 m deep flow has in its lowest 5 cm of snow a shear layer (with actually a slip velocity of $u(0)$=5.46 m/s) and a strain rate at the base $\dot{\gamma}(0)$=69 s^{-1}, while the upper part is like a plug flow, i.e. $\dot{\gamma}(0.4) = 0$ with a velocity of 7.05 m/s. A similar behaviour is observed by [206].

In Fig. 2.8.a a comparison with the velocity profile calculated and experimentally measured shows the capability of the model. Since the experimental data are obtained mediating in time, the results of our simulation are averaged in time too. Our simulations show that the stationary situation is not attainted yet. In fact the maximal value reached between the time 2.5 s (when the avalanche arrives to the sensors) and 3.4 s varies between 7.3 ms^{-1} and 8.1 ms^{-1}. The estimation of the upper part of the flow is correct. On the contrary we were not able to fit the velocity in the shear boundary layer. This is probably due to a mesh too large for this layer, that is only 5 cm. Hence, to describe more precisely the boundary velocity a more sophisticated mesh should be realised. Besides, regarding the boundary conditions along the chute, a slip condition as in [124] is imposed. However the slip velocity value itself on the boundary in our simulation, on the contrary of [124], is not specified.

Fig. 2.8.b shows a comparison between the experimental data of the front velocity with those simulated. The velocity is obtained dividing the distance gained by the avalanche by the time, similarly to [124].The agreement is more than satisfactory.

2.2 Velocity profile

To investigate deeper the interface avalanche and snow it is important to analyse the boundary conditions, and examine in details the slip velocity at the avalanche base,
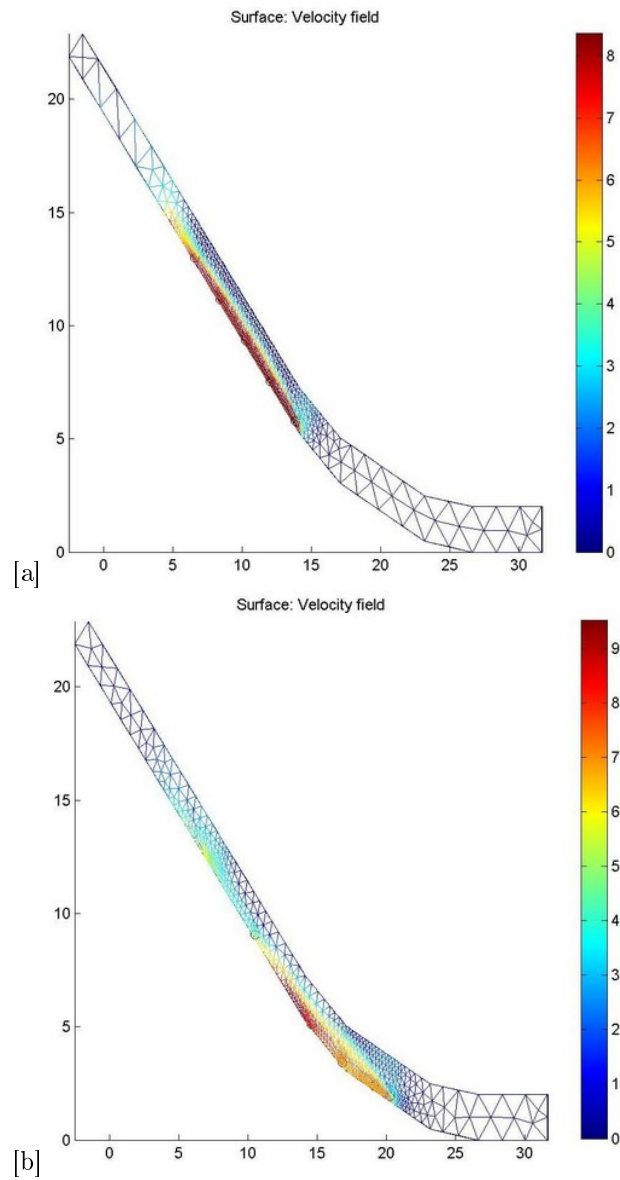
Figure 2.7: Snapshot showing the velocity field (surface) and the moving mesh at time [a] 2.4 s and [b] 3.4 s.

[a]   [b]
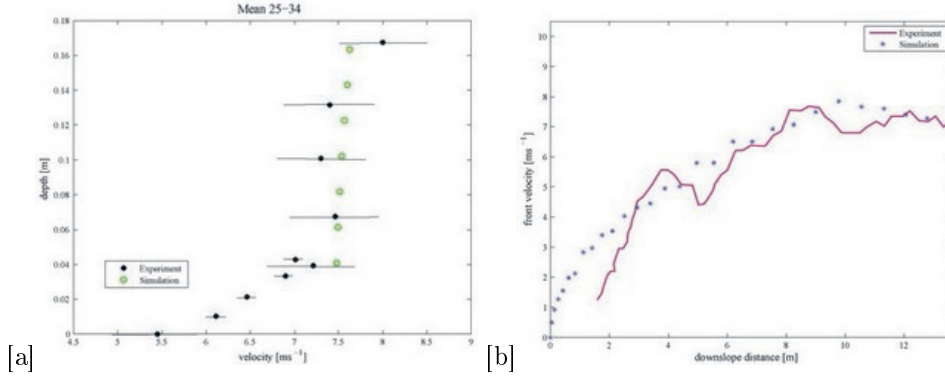
Figure 2.8: [a] Comparison between experimental data and simulated ones averaged in 1 s. [b] Comparison with the front velocity of the avalanche along the chute measured experimentally [124] and simulated. The downslope is measured from the release gate.

as well as the entrainment process (see Sec. 2.3). Experimentally the slip velocity allows to fit better the data. Hence an analytical model is proposed to justify the presence of the slip velocity and to link it to the basal tangential stress. In order to confirm the importance of the role played by the boundary conditions, a comparison between the velocity profile experimentally recorded and the one simulated by varying the boundary condition is proposed.

2.2.1   Slip velocity laws

In fluid mechanics a series of slip laws have been proposed. For example, for flows over porous media [35] boundary condition sets the slip velocity proportional to the wall shear rate through a coefficient c_1 depending on properties of the fluid and on the permeability of the porous wall over which the fluid slides:

$$u_{slip} = c_1 \dot{\gamma}(0). \tag{2.47}$$

The situation of $c_1 = 0$ corresponds to the no-slip condition. Hence, by extending this equation to avalanches, c_1 depends on the characteristics of the flowing snow and of the snow cover.

On the other hand a similar slip condition was proposed by [158] for rough surfaces, relating the tangential velocity to the local tangential stress:

$$u_{slip} = \alpha \tau(0), \tag{2.48}$$

where $\alpha \geq 0$ indicates the amount of slip. In particular, $\alpha = 0$ indicates a no-slip condition, $\alpha \neq 0$ a partial slip and $\alpha \to \infty$ a full slip with a stress-free boundary

condition. The Navier theory (Eq. 2.48) is not in contrast with the previous one (Eq. 2.47) because of the classical constitutive modelling relating stress and strain rate.

For instance, for the data by [124], since $\tau(0)$=794 Pa, $u_{slip} = 5.46m/s$ the constant α can be found equal to: $\alpha = \frac{u_{slip}}{\tau(0)} = 0.0069$ m^{2}s/kg.

In the case of avalanches, the coefficient of proportionality α depends on the characteristics of the flowing snow as well as on the snow cover underneath.

Finally [152] have experimentally found, for an avalanche in a snow chute at Col du Lac Blanc, that

$$u_{slip} = u_o \cdot (\tan\theta - \tan\theta_0), \qquad (2.49)$$

where u_0 and θ_0 are constants.

Analysing u_{slip} and $\dot{\gamma}(0)$ in different parts of the avalanche (front, bulk and tail), we will support Eq. 2.47 by the experimental data reported in [33, 168, 206, 103]. In their chute experiments with granular material, snow, wet snow and in a full-size test site respectively, they have shown that the velocity in the bottom layer is highest at the front of the avalanche, it decreases at the bulk and finally it is minimum at the tail.

The same behaviour is recorded for $\dot{\gamma}(0)$ in [53]: $\dot{\gamma}(0)$ is highest at the front, it decreases at the bulk and it assumes the minimum value at the tail. By consequence, assuming that these general trends are found in all avalanches, we suppose that an increasing relationship between the slip velocity and the gradient of velocity exists. From the data collected in [206] it seems that the relation cannot be strictly linear since, for instance, the authors measured an average slip velocity of about 8 m/s (7 m/s) and a shear rate of 62.5 s^{-1} (6 s^{-1}) in the bottom layer with thickness of 0.064 m respectively in the bulk and in the tail of the avalanche (Tab. 2.1). Hence, for the avalanches, Eq. 2.48 should be rewritten as

$$u_{slip} = c_2(\dot{\gamma}(0)). \qquad (2.50)$$

On the contrary, the results obtained for α (Tab. 2.1) in the bulk and tail of 0.007 and 0.0064 m^{2}s/kg are very close to each other. Hence Eq. 2.48 can explain the data available in [206]. For the evaluation of $\tau(0)$ the rheological law of Papanastasiou, described into detail in the following, and the corresponding values reported in Fig. 2.13.b, with a mean density of 475 kg/m^3 as reported in [206], are used.

2.2.2   Analytical justification of the slip velocity

In order to demonstrate the nature of the slip velocity and its dependence on the stress, i.e. Eq. 2.48, an analysis at the microscopic scale, considering the bonds created or broken at the interface between snowcover and avalanche, is carried out. The theory derives from [170]. Here it is assumed that the bonds between the particles

Table 2.1: Slip velocity laws: comparison. The data of u_{slip} and $\dot{\gamma}(0)$ are taken from [206].

Avalanche position	Bulk	Tail
u_{slip}	8 m7s	7 m/s
$\dot{\gamma}(0)$	62.5 s^{-1}	6s^{-1}
c_1 using Eq. 2.47	0.13 m	1.17 m
$\tau(0)$ using Eq. 2.65	1142 kg/(ms^2)	1086 kg/(ms^2)
α using Eq. 2.48	0.0070 m^{2}s/kg	0.0064 m^{2}s/kg

start breaking only after the microscopic force between particles $\tau(0)$ overcomes a threshold value τ_f. In the snow field, this can be interpreted by the evidence that avalanche triggering, and consequently the breaking of the bonds linking the snow at rest to the moving part, is possible when a stress value τ_f is overcome [60]. In fact the avalanche starts and moves when the gravitational forces are not equilibrated by the resistant ones. This situation continues during the sliding process (when erosion occurs) until the deposition begins. To explain that during the motion the shear stress is certainly larger than a threshold value, the field observation concerning the fact that the avalanche deposits have a finite depth is used. This behavior is in contrast to that of Newtonian fluids. These simpler fluids in fact deform till some stress is acting on them. Hence, if snow was modeled simply as a Newtonian fluid, it would move until it is completely spread on the terrain with a flow depth tending to zero. That can be explained with the fact that the snow rests, although with a non-zero stress: a yield value occurs when the deformations become small. In our model this is translated with the fact that during the motion the stress is certainly larger than a threshold value.

We focus now the attention on the interface between avalanche and snow cover at rest. Before avalanche triggering the grains into the snow cover have some bonds holding the particles together (Fig. 2.9, on the left). When the avalanche arrives, the bonds between the snow cover grains and those eroded by the avalanche are broken, to allow the movement into the flowing mass (Fig. 2.9, on the right). Let ς be the function that indicates the breaking of bonds. At the interface between snow and avalanche the bonds of the grains are broken when the microscopic stress at the avalanche base $\tau_{mic}(0)$ becomes larger than the threshold value τ_f:

$$\varsigma(\tau_{mic}(0)) = \varsigma_0 H(\tau_{mic}(0) - \tau_f), \tag{2.51}$$

where ς_0 is a constant depending on the snow properties and H is the Heaviside function.

The characteristics and the behavior of the bonds are linked to snow properties,
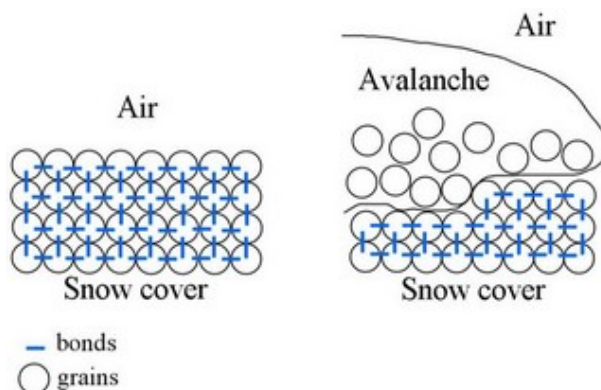
Figure 2.9: In the snowcover before the avalanche triggerring the bonds are intact. When the avalanche arrives some bonds are broken to allow the movement of the flowing mass.

and could be described by the shear strength of the interlocking snow crystals. The shear strength depends on density (higher density allows to create more bonds), type and dimension of grains (small and rounded grains with varying diameter provide more points of contacts that faceted ones or bigger ones) and on temperature (the lower the temperature, the stronger the snow cover) [145]. At the grain scale, the strength of interlocking depends on the density of bonds N_{max} (i.e. the maximal value of bonds that can be created in the unit volume), on the rate of formation of new bonds κ (i.e. how many bonds can be created in a unit volume in a second) and on the elastic constant of the microscopic bond k_{mic} (i.e. how strong a bond is, from which the microscopic stress directly depends). However, the complex evaluation of these experimental values is not pursued in this thesis.

Let us call f the probability of forming an adhesion bond between the snow cover and the avalanche and a_g the age of the bond. [170] proposed the following quasi-stationary problem:

$$\begin{cases} \frac{\partial f}{\partial a_g} = -\varsigma(\tau_{mic}(0))f \\ f(a_g = 0, t) = \beta(N_{max} - \int_0^{+\infty} f da_g). \end{cases} \tag{2.52}$$

The first equation describes the detachment process indicating that the variation of the probability of forming a bond depends on the magnitude stress exerted on it and on its age. The second one supposes that the formation of new bonds is proportional through the value β to the bonds that can still be formed.

The interaction stress is related to the microscopic stress by the following rule:

$$\tau(0) = \int_0^{+\infty} \tau_{mic}(0) f \, da_g. \tag{2.53}$$

Solving the previous differential equation it can be demonstrated (see the mathematical passages reported in [170]), that the interaction shear stress $\tau(0)$, is given by:

$$\tau(0) = N_{max} \frac{\hat{\tau}_f^2 + \hat{\tau}_f \tau_f + \frac{1}{2}\tau_f^2}{W + \hat{\tau}_f + \tau_f}, \tag{2.54}$$

where $\hat{\tau}_f = k_{mic}|\mathbf{u}_{snow} - \mathbf{u}_{ava}|/\varsigma_0$ and $W = k_{mic}|\mathbf{u}_{snow} - \mathbf{u}_{ava}|/\kappa$. For our purpose it is convenient to rewrite Eq. 2.54 as a function of the slip velocity u_{slip}. In fact the difference $|\mathbf{u}_{snow} - \mathbf{u}_{ava}| = u_{slip}$ because the vertical component of the velocity are considered negligible, as well as the creep ($u_{snow} = 0$ m/s). Hence:

$$\tau(0) = N_{max} \frac{\frac{k_{mic}^2}{\varsigma_0^2} u_{slip}^2 + \frac{k_{mic}}{\varsigma_0} u_{slip} \tau_f + \frac{1}{2}\tau_f^2}{k_{mic}(\frac{1}{\kappa} + \frac{1}{\varsigma_0}) u_{slip} + \tau_f}. \tag{2.55}$$

Using the Mac Laurin series at the first order, for $u_{slip} \to 0$, Eq. 2.55 reads:

$$\begin{aligned} \tau(0) \quad &\approx N_{max} \frac{\frac{1}{2}\tau_f^2 + \frac{k_{mic}}{\varsigma_0}\tau_f u_{slip}}{\tau_f \left[1 + \frac{k_{mic}}{\tau_f}(\frac{1}{\kappa} + \frac{1}{\varsigma_0}) u_{slip}\right]} \approx \\ &\approx N_{max} \left[\frac{1}{2}\tau_f + \frac{k_{mic}}{\varsigma_0} u_{slip}\right] \left[1 - \frac{k_{mic}}{\tau_f}(\frac{1}{\kappa} + \frac{1}{\varsigma_0}) u_{slip}\right] \approx \\ &\approx N_{max} \left[\frac{1}{2}\tau_f + \frac{1}{2}k_{mic}\left(\frac{1}{\varsigma_0} - \frac{1}{\kappa}\right) u_{slip}\right] \end{aligned} \tag{2.56}$$

In the situation where the ratio of bond rupturing is higher than the ratio of formation of new bonds ($\varsigma_0 > \kappa$), that corresponds to the case in which the avalanche flows and erodes, Eq. 2.56 means that the interaction stress $\tau(0)$ decreases for small velocities. On the contrary, when $\varsigma_0 < \kappa$ the interaction force is always growing.

In the limit when $u_{slip} \to \infty$, Eq. 2.54 becomes:

$$\begin{aligned} \tau(0) \quad &\approx N_{max} \frac{\frac{k_{mic}}{\varsigma_0^2}}{k_{mic}(\frac{1}{\kappa} + \frac{1}{\varsigma_0})} u_{slip} = \\ &= \frac{k_{mic}}{\varsigma_0^2(\frac{1}{\kappa} + \frac{1}{\varsigma_0})} u_{slip} \end{aligned} \tag{2.57}$$

Therefore Eq. 2.48 is obtained:

$$u_{slip} = \frac{\varsigma_0^2(\frac{1}{\kappa} + \frac{1}{\varsigma_0})}{k_{mic} N_{max}} \tau(0) = \alpha \tau(0). \tag{2.58}$$
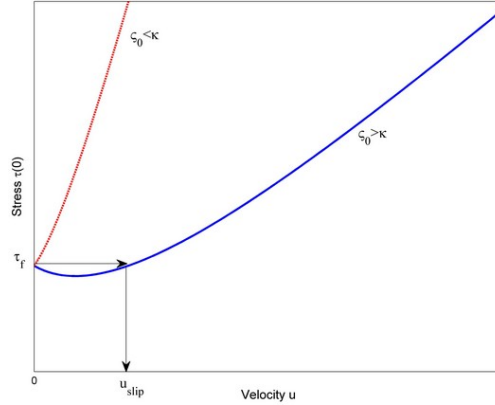
Figure 2.10: The graphical representation of the analytical model of the slip velocity. The $\varsigma_0 > \kappa$ condition, corresponding to a flowing avalanche, combined to a stress larger than τ_0 implies a slip velocity. On the contrary if $\varsigma_0 < \kappa$ the stress always increases with the velocity.

Hence the slip velocity attains larger values for higher breaking rates (ς_0 is higher), if the strength of links k_{mic} or the maximum density N_{max} of bonds is lower or if only few bonds are created even if the possibility to be created was high (κ lower). Hence α is a coefficient that depends on the characteristics of the snow like its strength, density, temperature, type and dimensions of the crystals. In the avalanche field Eq. 2.58 shows that the slip velocity is higher if the snow grains have few and weak links and the number of the breaking bonds is high. In Nature this is the case of avalanches occurring in dry snow (where the bonds between the grains are weak), that reach higher velocity with respect of the wet ones. Finally, Eq. 2.58 shows that the coefficient α cannot be equal to zero, and thereby a no-slip condition is not possible, since $\varsigma_0 \neq 0$ to get trigger.

Namely Fig. 2.10 shows that, if $\varsigma_0 > \kappa$, for small relative velocity the interaction force decreases until reaching a minimum, while after that it grows to infinity. In our case, consequently, starting from rest, when the interaction stress overcomes the threshold value τ_f, grains necessarily detach with a slip velocity. In the case when the interaction force decreases below the minimum, as in the deposition process, the grains attach again.

Conversely, if $\varsigma_0 < \kappa$ when the interaction stress is lower than τ_f, no flow occurs. On the contrary, for values higher than τ_f the flow has a regular velocity increase, without jump, depending on the interaction stress.

Hence, even if in this thesis the method of bonds breaking is not the main focus, the existence of a slip velocity can be justified.

No detailed experimental studies have been conducted to measure adhesion between snowcover and avalanche, giving no more information on the velocity during sliding.

On the contrary, avalanche triggering has been studied extensively, since it is related to the snow stability. In any case, it would be better to speak about cohesion in the snow cover, instead of adhesion, since the attraction occurs between molecules of the same kind. The broken bonds can be those within a homogeneous snowpack loosing its cohesion, for loose snow avalanches, or at the so-called weak layer, for snow slab avalanches [60].

2.2.3 Model fit to velocity profile data

After found the law describing the u_{slip} value, it is possible to show the model used to study the velocity profile.

The flow is modeled like a fluid, hence the Navier-Stokes equations, in their two-dimensional form, are used:

$$\nabla \cdot \mathbf{u} = 0, \tag{2.59}$$

$$\rho \left(\frac{\partial \mathbf{u}}{\partial t} + \mathbf{u} \cdot \nabla \mathbf{u} \right) = \nabla \cdot \underline{\underline{T}} + \rho \mathbf{g} - \mathbf{F_a}, \tag{2.60}$$

where $\mathbf{u} = (u, v)$ is the velocity, $\mathbf{g}$ is the gravitational acceleration, $\mathbf{F}_a$ is the frictional force and

$$\underline{\underline{T}} = -p\underline{\underline{I}} + Z(\nabla \mathbf{u} + (\nabla \mathbf{u})'), \tag{2.61}$$

is the stress tensor, p is the pressure, Z is the viscosity.

Considering the flow as stationary when it reaches the velocity sensors, to find a good fit of the model with the experimental data, a stationary situation is imposed.

Neglecting the component of the velocity v normal to the ground (i.e. along the y axis), the two-dimensions Navier-Stokes equations are simplified to:

$$\frac{\partial}{\partial y} \left[Z_{av} \frac{\partial u}{\partial y} \right] = -\rho g \sin \theta + F_a, \tag{2.62}$$

where u is the velocity along the ground slope, $\frac{\partial u}{\partial y} = \dot{\gamma}$ is the strain rate, $Z_{av} = Z_{av} \left(\frac{\partial u}{\partial y} \right)$ is the viscosity of the avalanche depending on the strain rate and θ is the slope angle.

For the Newtonian case, where Z_{av} is constant, a parabolic profile is trivially obtained. Consequently it is not possible to describe both the shear layer and the

Table 2.2: Different boundary conditions plotted in Fig. 2.11.

Name	$u(0)$	$u(0.4)$	$\dot{\gamma}(0)$	$\dot{\gamma}(0.4)$
A	5.46 m/s	-	-	0 s^{-1}
B	5.46 m/s	7.05 m/s	-	-
C	-	7.05 m/s	69 s^{-1}	-
D	5.46 m/s	-	69 s^{-1}	-
E	-	7.05 m/s	-	0 s^{-1}
F	0 m/s	7.05 m/s	-	-
G	0 m/s	-	-	0 s^{-1}
H	0 m/s	-	69 s^{-1}	-

surrounding plug flow. Hence it is necessary to utilize a non-Newtonian fluid, e.g., the Cross model [124]:

$$Z_{av} = \frac{\nu_0 + \nu_1 k_c \dot{\gamma}}{1 + k_c \dot{\gamma}}, \tag{2.63}$$

where ν_0, ν_1 and k_c are constants.

For low values of the shear strain, $\dot{\gamma} \to 0$, (corresponding to the upper part of the profile where a plug flow occurs), the kinematic viscosity tends to ν_0. On the contrary, for higher values of $\dot{\gamma}$ ($\dot{\gamma} \to \infty$) the kinematic viscosity tends to the lower value ν_1 thus allowing to describe the shear layer.

Eq. 2.62 can be analysed through the following system in which $y_1 = u$, $y_2 = \dot{\gamma}$ and the derivative is done with respect to y:

$$\begin{cases} y_1' = y_2, \\ y_2' = \dfrac{-\rho g \sin\theta + F_a}{\mu_1 + \dfrac{\mu_0 - \mu_1}{(1 + k_c y_2)^2}}, \end{cases} \tag{2.64}$$

Two boundary conditions are needed to define the problem. As stated before, different quantities are investigated: velocity at the base or at the top as well as shear rate at the base or at the top.

The different combinations of boundary conditions are summarised in Tab. 2.2.

As far as it is concerned, Fig. 2.11 shows the influence of the different boundary conditions on the velocity profile in the Cross-model situation. It is clear that the imposition of a velocity at the basis allows to fit easily the experimental profile. On the contrary, with this particular set of parameters values, if a no-slip condition is imposed, the fit is not good.
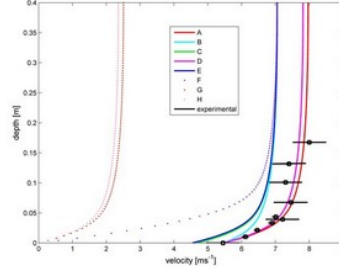
Figure 2.11: Experimental data collected in a snow chute of SLF Davos (CH) [124] with their error variance and dependence of the Cross law on the different boundary conditions. Values are $\nu_0 = 2.1$ m^{2}s^{-1}, $\nu_1 = 0.0027$ m^{2}s^{-1}, $\rho = 400$ kg m^{-3}, $k_c = 1.1$ s as proposed by [124]. The meaning of the legend is explained in Tab. 2.2. The dotted lines correspond to no-slip condition.

As shown in Fig. 2.12, even using the more complex Papanastasiou model [137]:

$$Z_{av} = m + \frac{\tau_0[1 - \exp(-a\dot{\gamma})]}{\dot{\gamma}}, \qquad (2.65)$$

with m, τ_0 and a constants, it is not possible to get a satisfactory model fit using the no slip boundary conditions.

Consequently, similarly to the procedure applied for the Cross model, the system to integrate is the following:

$$\begin{cases} y_1' = y_2, \\ y_2' = \dfrac{-\rho g \sin\theta + F_a}{m + a\tau_0 \exp(-ay_2)}, \end{cases} \qquad (2.66)$$

To be able to find a good fit of parameters an analysis of their influence on the velocity profile is carried out.

In this model a indicates how fast the transition from the lowest viscosity to the highest one occurs: $a = 0$ corresponds to the Newtonian case of a classical parabolic profile. Higher values of a represent the velocity profile closer to the Bingham's one (Fig. 2.12a). The lower m is the highest the strain rate (Fig. 2.12b), since it represents the viscosity near the slope. Finally the higher τ_0 is, the smaller the sheared layer depth is (Fig. 2.12c). Hence, the velocity at the top depends on both m and τ_0.

On the basis of these considerations, a first fit of the data, shown in Fig. 2.13a, is found. The parameter values are m=0.0003 kg/ms, τ_0=1.93 kg/m and a=1 s. Comparing those results with those in literature and in particular with the Cross
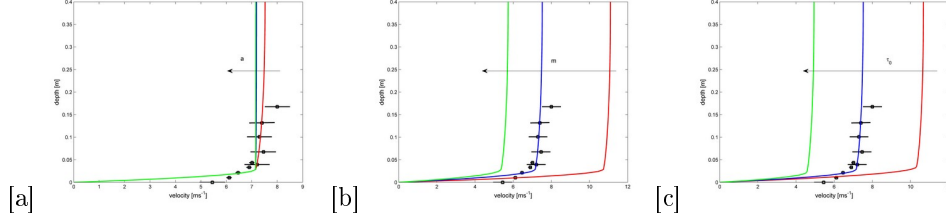
Figure 2.12: Dependence of the velocity profile [a] on a, varying in the interval 1, 10, 100 s, with m=0.0003 kg/ms and τ_0=1.93 kg/m , [b] on m varying in the interval 0.0003, 0.0005, 0.0007 kg/ms with a=1 s, τ_0=1.93 kg/m and [c] on τ_0 varying in the interval 1.90, 1.93, 1.96 kg/m with a=1 s, m=1.93 kg/ms.

model, the viscosity in the shear layer is lowered with the consequence that the fluid appears less viscous, due to the no-slip condition that imposes a higher gap of velocity in the fixed depth of the shear layer. $\dot{\gamma}(0) \sim 500$ s^{-1} assumes a high value comparing to that experimentally found. However, the above model is coherent with [152] who supposed, alternately to a slip velocity, the existence of a thin layer where $\dot{\gamma}$ has a huge value (larger than 500 s^{-1}) coupled with a no-slip condition. This last hypothesis is based on a similitude with a fluid in contact with a wall at rest. In that case it was supposed that the boundary layer can not be measured experimentally, since it is very thin and the sensors cannot be efficient.
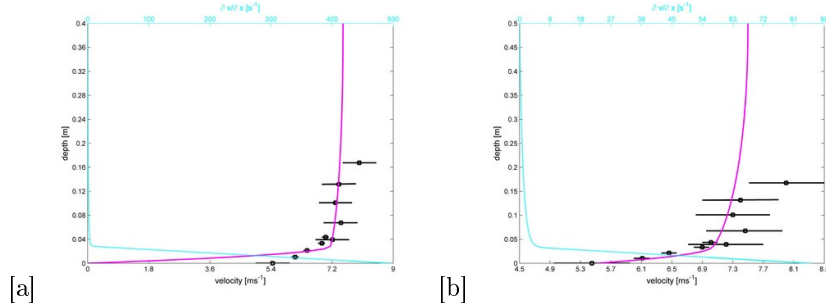

Figure 2.13: [a] Velocity profile with the best fit found for m=0.0003 kg/ms, τ_0=1.93 kg/ms^2 and a=1 s and the corresponding $\dot{\gamma}$. [b] Velocity profile for the Papanastasiou law with ρ=300 kg/m^3, $\theta = 30°$, $m = 0.002 \cdot \rho$ m^2/s, $n = 1$, $\tau_0 = 2.28 \cdot \rho$ m^2/s^2, $a = 1$ s, $\alpha = 0.0075$ m^{2}s/kg, H=0.5 m and the corresponding $\dot{\gamma}$.

Imposing a slip boundary condition proportional to the shear stress at the base,

a first fit of parameters for the Papanastasiou law can be given in Fig. 2.13.b. The velocities at the base and at the top are correctly estimated. Also $\dot{\gamma}(0)$, although slightly overestimated, is closer to the experimental data collected than in the case of a no-slip hypothesis.

Let us note that this first set of parameters has not the ambition to represent the best fit parameters, since an optimisation study is not carried out. In addition, for this simple analysis, the friction influence is taken into account only by decreasing the slope angle θ from 32° to 30° and using 300 kg/m^3, corresponding to a Coulomb friction coefficient of 0.18, that is underestimated, e.g., comparing to the values found by [168].

The previous examples show that a slip condition might be the most appropriate.

2.3 A new erosion model

2.3.1 The erosion process

In this section the attention is focused on the entrainment and deposition processes. Those aspects arouse interest since, even if they affect the whole avalanche dynamics and play a fundamental role for the snow-structure interaction analysis, they have not been adequately investigated up to now.

Recent observations recognized that the entrainment of snow strongly influences the dynamics of avalanches (Fig. 2.14). It was estimated that the majority of medium or large avalanches can increase their mass by a factor 2 or 3 (as in the Ryngfonn test site, [102]) or in Vallée de la Sionne even by a factor 12 [191], while the small avalanches (as those at Mount Pizzac test site [189]) even reach a factor 9. For this reason, it is understandable how the entrainment may significantly affect the avalanche behaviour and in particular its velocity, flow height, runout distance and impact pressure on obstacles.

The term entrainment includes two aspects [102]. The first one concerns the breaking up of the snowcover into particles. It is strictly linked to the erosion rate, that is the velocity, measured perpendicularly to the ground, at which the surface of the untouched snowcover is lowered because of the erosion. The second one consists on the incorporation of the eroded snow in the flow. To this concept is connected the entrainment rate (kg m^{-2} s^{-1}), e.g. the snow mass per unit time and unit area incorporated in the avalanche.

Three entrainment or erosion mechanisms are observed from experimental data [189]. The frontal entrainment or ploughing is characterized by a dry, low-density and cohesionless snow entrained by the avalanche that slides over a more resistant and older layer of snow. Since it lasts a very short time, compared with the time of the flowing of an avalanche in a point, mathematically it can be treated as a jump. The step entrainment takes places when low-strength snow layers are sandwiched between

Figure 2.14: Part of the snow cover has been eroded and at the same time local or continuous deposits are distributed along the path. Avalanche in Gressoney's Valley, March 2011. Photo E. Bovet.

ice/snow crusts. In fact, when a crust is broken, quickly a lot of snow enters the avalanche, even not in the front. Finally, the basal erosion occurs when the snow pack is constituted by high shear strength layers. The avalanche scrapes mass from the sliding surface along its body, proportionally to the shearing force exerted on the basal surface.

Recently, some dense-flow models describing the entrainment have been developed (for instance [190, 102, 153], for an exhaustive report on the state of the art see [23] and Sec. 1.2.3), but they are not used practically, except for instance the RAMMS model [66]. In the literature [83] entrainment rate is considered proportional to (i) the flow velocity, as in [66], with a coefficient depending on the snow properties and on the difference between the density of the snow cover and that of the avalanche, (ii) the square of the velocity or (iii) the flow height, and consequently to the overall avalanche load. Hence, since near the avalanche front the maximum values of velocity and flow depth are encountered, the entrainment rate is higher in the frontal part, as the measurements confirm. In fact, in the basal erosion the entrainment rate is lower (up to 10 kg/m^{2}s) than in the case of ploughing and step entrainment (up to 350 kg/m^{2}s) [191]. However the basal erosion lasts more time, with the consequence that the eroded masses are comparable.

In the model presented in the following a new approach is proposed to describe entrainment as a natural consequence of the chosen constitutive law. In particular, starting from general continuum mechanics hypothesis, a law for the entrainment process is found. This model takes into account the influence of snow and avalanche properties, the avalanche depth, the slope angle, and the position in the avalanche (front or tail).

2.3.2 The rheological model: the Papanastasiou's law

In this section a new model [49] used to describe the avalanche and the underneath snow cover is deepened.

The avalanche and the snow cover are now considered made of the same non-Newtonian fluid, having a very viscous behaviour in the snow cover, and a less viscous behaviour in the flowing mass [47]. In fact, since the stress is not constant in the whole body, some portions can flow while others still behave like solids.

Hence, since all the snow is modeled like a fluid, as in [47] the Navier-Stokes Eqq. 2.59 and 2.60 can be used.

For the viscosity $Z = Z_{SH}$ the *Papanastasiou*'s law is used [137]. The whole flow can be described through a single equation thanks to an exponential function, allowing to avoid numerical difficulties that occur when the shear rate approaches zero and the apparent viscosity becomes very large.

Introducing an additional parameter n, as in the *Herschel-Bulkley* model, the

following extension of the model can be obtained [210]:

$$
\begin{aligned}
\underline{\underline{\tau}} &= \left\{ m|\mathbb{II}|^{(n-1)/2} + \frac{\tau_0(1 - \exp(-a|\mathbb{II}|^{1/2})]}{|\mathbb{II}|^{1/2}} \right\} 2\underline{\underline{D}}, \\
&= Z_{SH} 2\underline{\underline{D}},
\end{aligned}
\tag{2.67}
$$

where $\mathbb{II}$ is the second invariant of the tensor $2\underline{\underline{D}}$ [3]. In the two-dimensional case it is:

$$
|\mathbb{II}| = \left| 4\frac{\partial u}{\partial x}\frac{\partial v}{\partial y} - \left(\frac{\partial u}{\partial y} + \frac{\partial v}{\partial x}\right)^2 \right|,
\tag{2.68}
$$

and in the one-dimensional case, as used before , it is :

$$
|\mathbb{II}|^{1/2} = \frac{\partial u}{\partial y} = \frac{\partial u}{\partial y_{tot}} = \dot{\gamma}.
\tag{2.69}
$$

Referring specifically to avalanches, in the Papanastasiou original form (i.e. with $n = 1$) m represents the viscosity of the avalanche, even if rigourously it should be only for $|\mathbb{II}|^{1/2} \to \infty$. The avalanche viscosity itself, to be more precise, as in the section before, is a function of the strain rate. However, for simplicity of notation we denote $m(|\mathbb{II}|^{1/2}) = m$. The expression $m + a\tau_0$ represents the viscosity for $|\mathbb{II}|^{1/2} = 0$ that is the viscosity in the snow cover. The value a represents, through the expression $-\tau_0 a^2/2$, the slope value when the viscosity decreases.

Let us notice that, depending of the value of n, the fluid displays two different behaviours (Fig. 2.15). In the case of $n < 1$ it is a *shear thinning* or a *pseudoplastic* fluid, characterized by a progressively decreasing slope (the apparent viscosity) of the shear stress as a function of the strain rate. For high values of $\dot{\gamma}$ it reaches a constant value m.

On the contrary, for values $n > 1$, the apparent viscosity increases for large shear rates denoting a *dilatant* behaviour.

In its general form, Eq. 2.67 includes others rheological models. When $a \to \infty$ it coincides with the Herschel-Bulkley law describing the fluid part of the material, and for $a \to \infty$ and $n = 1$ with the *Bingham* one [137]. Finally, if $n = 1$ and $a = 0$ the *Newtonian* case is recovered.

2.3.3   Entrainment at the snow/avalanche interface

In the previous sections all the basic theoretical concepts have been introduced. Now it is possible to focus on the study of the entrainment process. Let the reference system have $y_{tot} = 0$ at the level of the terrain. As seen before, we denote by σ the

---

[3] $\mathbb{II} = \dfrac{1}{2}[(\text{tr } D)^2 - \text{tr } D^2]$ where tr D is the trace of D
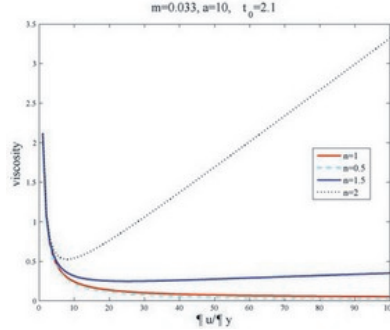
Figure 2.15: Dependence of the viscosity on n.

bottom limit of the avalanche, that divides the snow cover ($y_{tot} < l(x,t)$) from the moving mass ($y_{tot} > l(x,t)$). It represents the transition layer where entrainment occurs.

It is necessary to assign the condition for describing the interface evolution $y_{tot} = l(\mathbf{x}, t)$.

The Navier-Stokes equations (Eqs. 2.59, 2.60), using the notation $\Psi = \{\rho; \rho\mathbf{u}\}^T$, $\Phi = \{0; \underline{\underline{T}}\}$, $\mathbf{R} = \mathbf{0}; \rho\mathbf{g} - \mathbf{F_a}$ can be rewritten as:

$$\frac{\partial \Psi}{\partial t} + \nabla \cdot (\Psi\mathbf{u} - \Phi) = \mathbf{R}. \tag{2.70}$$

From continuum mechanics, for a general balance equation such Eq. 2.70, the boundary conditions are:

$$[\![\Psi(\mathbf{u} - \mathbf{u}_\sigma) \cdot \mathbf{n}]\!] - [\![\Phi \cdot \mathbf{n}]\!] = 0, \tag{2.71}$$

where $\mathbf{u}_\sigma$ is the velocity at the interface, $\mathbf{n}$ is the normal vector and the parenthesis [.] represent the jump between the values in the snowcover (indicated in the following by the subscript $_{snow}$) and in the avalanche (subscript $_{ava}$). Hence the boundary conditions for the Navier-Stokes equations are:

$$[\![\rho(\mathbf{u} - \mathbf{u}_\sigma) \cdot \mathbf{n}]\!] = 0, \tag{2.72}$$

$$[\![\rho\mathbf{u} \otimes (\mathbf{u} - \mathbf{u}_\sigma)\mathbf{n}]\!] - [\![\underline{\underline{T}}\mathbf{n}]\!] = 0. \tag{2.73}$$

Consequently, multiplying by the tangential vector $\mathbf{t}$:

$$[\![\mathbf{t} \cdot \mathbf{u}\rho(\mathbf{u} - \mathbf{u}_\sigma) \cdot \mathbf{n}]\!] = [\![\mathbf{t} \cdot \underline{\underline{T}}\mathbf{n}]\!], \tag{2.74}$$

and considering Eq. 2.72:

$$u_{slip}\rho(\mathbf{u} - \mathbf{u}_\sigma) \cdot \mathbf{n} = [\tau], \tag{2.75}$$

where $u_{slip} = [\mathbf{u}] \cdot \mathbf{t}$ and $\tau = \mathbf{t} \cdot \underline{\underline{T}}\mathbf{n}$. By defining the velocity of entrainment $v_{entr} = dl/dt = \mathbf{u}_\sigma \cdot \mathbf{n}$ and $v_{ava} = \mathbf{u} \cdot \mathbf{n}$, eq. 2.75 becomes:

$$\frac{dl}{dt} = \frac{\tau_{snow} - \tau_{ava}}{\rho_{ava} u_{slip}} + v_{ava}. \tag{2.76}$$

From Eq. 2.72:

$$v_{ava} = \frac{(\rho_{ava} - \rho_{snow})}{\rho_{ava}} \frac{dl}{dt}. \tag{2.77}$$

Consequently:

$$\frac{dl}{dt} = \frac{\tau_{snow} - \tau_{ava}}{\rho_{snow} u_{slip}}. \tag{2.78}$$

Under the hypothesis Eq. 2.48, rewritten in the new form:

$$u_{slip} = \alpha \tau_{ava}, \tag{2.79}$$

we find:

$$\frac{dl}{dt} = \frac{\tau_{snow} - \tau_{ava}}{\rho_{snow} \alpha \tau_{ava}} = \frac{1}{\alpha \rho_{snow}} \left(\frac{\tau_{snow}}{\tau_{ava}} - 1 \right). \tag{2.80}$$

From Eq. 2.72 we can find:

$$\rho_{ava}(\mathbf{u}_{ava} - \mathbf{u}_\sigma) \cdot \mathbf{n} = \rho_{snow}(\mathbf{u}_{snow} - \mathbf{u}_\sigma) \cdot \mathbf{n}, \tag{2.81}$$

and consequently:

$$\rho_{ava}\mathbf{u}_{ava} \cdot \mathbf{n} = (\rho_{ava} - \rho_{snow})\mathbf{u}_\sigma \cdot \mathbf{n}. \tag{2.82}$$

Therefore, with the same v_{entr}, the difference between the density of the snowcover and of the avalanche implies an expansion of the snow, as the term $\mathbf{u}_{ava} \cdot \mathbf{n}$ shows. On the contrary, if $\rho_{ava} = \rho_{snow}$ the term $v_{ava} = \mathbf{u}_{ava} \cdot \mathbf{n} = 0$ as well as $[\mathbf{n} \cdot \underline{\underline{T}}\mathbf{n}] = 0$. Anyway, since this expansion occurs instantaneously, Eqs. 2.59,2.60 are still assumed to be valid.

Similarly to the Bingham model, in which:

$$\begin{aligned}\underline{\underline{\tau}} &= \left(m + \frac{\tau_0}{|\underline{\underline{II}}|^{1/2}} \right) 2\underline{\underline{D}} &&\text{for } \tau \geq \tau_0, \\ |\underline{\underline{II}}|^{1/2} &= 0 &&\text{for } \tau < \tau_0,\end{aligned} \tag{2.83}$$

where the exponential term of the Papanastasiou law is not present, it is supposed that $\tau_{snow} = \tau_0$ is the maximum stress in the snowcover. Thus, Eq. 2.78:

$$\frac{dl}{dt} \propto (\tau_0 - \tau_{ava}), \tag{2.84}$$
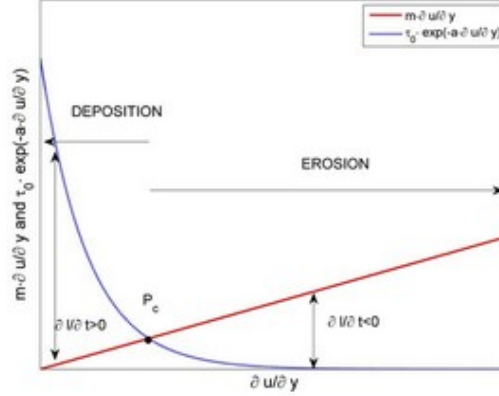
Figure 2.16: Graphical representation of the proposed model to explain the entrainment and deposition processes depending on $\dot{\gamma} = \frac{\partial u}{\partial y}$.

is equivalent to:

$$\frac{dl}{dt} \propto -m|\mathit{II}|^{n/2} + \tau_0 \exp(-a|\mathit{II}|^{1/2}). \tag{2.85}$$

Let underline that Eq. 2.84 is valid independently of the assumption for the slip velocity (Eq. 2.79). Firstly it is important to know the value of critical shear strain rate $\dot{\gamma}_c$ for which the interface does not move ($dl/dt = 0$), corresponding to the situation of no erosion and no deposit. This term can be graphically located, in Fig. 2.16, as the abscissa of the intersection point P_c between the two contributions of Eq. 2.85.

For values of $\dot{\gamma}$ greater than $\dot{\gamma}_c$ erosion occurs. In particular, the entrainment rate dl/dt is proportional to the difference between the two curves. Hence, it is obvious that for higher values of $\dot{\gamma}$, with $\dot{\gamma} > \dot{\gamma}_c$, the $|dl/dt|$ is greater, meaning that the snowcover is more quickly and easily eroded by the avalanche. On the contrary, for values $\dot{\gamma} < \dot{\gamma}_c$, $dl/dt > 0$, providing deposition phenomenon. Lower values of $\dot{\gamma}$ imply that the avalanche deposits in lower time.

As concerns the position of $\dot{\gamma}_c$, if $\dot{\gamma}_c$ is large, the range of $\dot{\gamma} > \dot{\gamma}_c$, for which the erosion is possible, is reduced. Consequently, it is more difficult to entrain snow, while it is simpler to deposit.

The presence of a yield value $\dot{\gamma}_c$ was also supposed by [176]: under a critical value of almost 5 s^{-1} in the upper part of the flow and a value of approximately 150 s^{-1} in the shear layer, the flow stops. The value $\dot{\gamma}_c$ corresponds the critical viscosity Z_{SH}^c.

Table 2.3: Parameters and variables governing the model.

Quantity	Explanation
ρ_{snow}	snow cover density
ρ_{ava}	avalanche density
l	interface between avalanche and snow cover
t	time
u	velocity parallel to the flow direction
u_{ava}	slip avalanche velocity
x	parallel to the flow direction
y, y_{tot}	perpendicular to the flow directions
$\dot{\gamma} = \dfrac{\partial u}{\partial y} = $ $= \dfrac{\partial u}{\partial y_{tot}} = |\mathbf{II}|^{1/2}$	shear strain rate
τ_{ava}	avalanche stress
$\dot{\gamma}_c$	critic shear strain rate
Z_{SH}^c	critical viscosity
m	avalanche viscosity
$m + a\tau_0$	snow cover viscosity
n	parameter from which depends the fluid nature (shear thinning, dilatant or Bingham)
τ_0	stress of the snow cover at the interface
α	function relating u_{slip} to τ_{ava}

2.3.4 Results and discussion

Snow cover and avalanche properties: influence on the entrainment

Focusing the attention on the role played by the different parameters, for high values of τ_0 it is more difficult to erode the snowcover, since $\dot\gamma_c$ increases. This aspect is physically confirmed: to erode a crust (higher τ_0) more time is necessary than to erode fresh snow (lower τ_0).

As the avalanche viscosity is concerned, for more viscous avalanches the erosion is higher, while for less viscous ones the erosion is lower. This feature can be confirmed by two different theories.

The first one considers the erosion rate proportional to the flow height, and consequently to the overall avalanche load [83]. The load is a function of the density too. The viscosity itself is exponentially related to the density, like in [77]. Consequently, more viscous avalanches are more dense, impress a higher load and show a higher erosion rate.

The second theory was proposed in [17], where the erosion rate was supposed to be proportional to the shear rate, with a coefficient depending on the difference between the thickness of the material at rest, and the equilibrium height. The redundancy in snow deposited can be translated, using Eq. 2.85, having an avalanche with a higher viscosity m. Consequently, the erosion rate is higher for both cases. In addition, comparing with Eq. 2.85, at the equilibrium height, $\dot\gamma_c$ coincides. Therefore for higher $\dot\gamma_c$, or higher equilibrium height, the erosion is lower.

Finally, the larger the parameter a, more easily the snow at rest is entrained by the avalanche, since $\dot\gamma_c$ is lower. On the contrary, with lower values of a, $\dot\gamma_c$ is higher. That means that even with not negligible values of $\dot\gamma$, the snowcover is not eroded.

Bulk and tail: influence on the entrainment

Eq. 2.85 can also explain the different entrainment rate along the avalanche body. In particular it shows that in the head and in the bulk of an avalanche the erosion is higher than in the tail, in which even deposition can occur. From the velocity profiles experimentally collected by [53] the value of $\dot\gamma$ close to the snow cover in the bulk and in the tail can be calculated. In the bulk $\dot\gamma$ is about 3-5 times the value of $\dot\gamma$ in the tail, essentially due to different velocities. That means that in the bulk, $\dot\gamma$ is higher, the entrainment rate is higher than in the tail, in which $\dot\gamma$ is lower. In addition, if in the tail $\dot\gamma < \dot\gamma_c$, deposition occurs. Consequently, by an analysis of the velocity profile when the avalanche erodes and when it deposits it could be possible to evaluate $\dot\gamma_c$.

Slope angle: influence on the entrainment

In order to analyse the influence of the slope angle on the entrainment phenomenon it is important to study the dependence of the slip velocity and of the basal shear rate

[a]   [b]
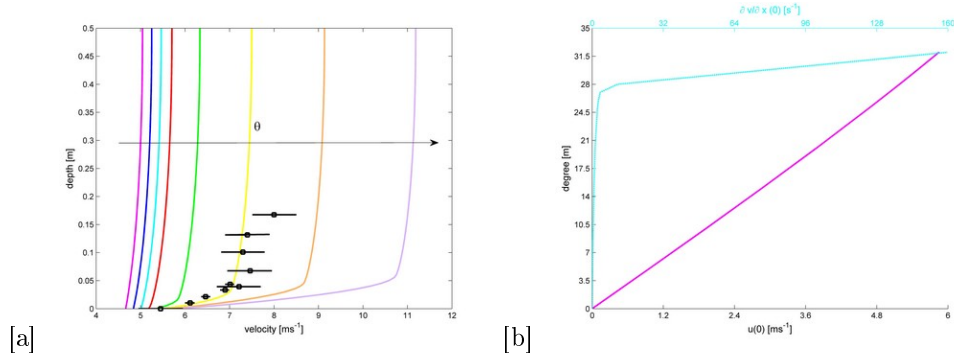
Figure 2.17: [a] Velocity profile for the Papanastasiou law with θ= 25°, 26°, 27°, 28°, 29°, 30°, 31°, 32°, [c] $u(0)$ and $\dot{\gamma}(0)$ vs. θ in the range θ= 0°-32°. $\dot{\gamma}(0)$ and $u(0)$ increases with the slope angle.

on the external force, that is traduced in our case in the dependence on the slope angle since a friction force law is not introduced. Some simulations are carried out using the parameters of Fig. 2.13.b, varying the slope angle from 0° to 32° (Fig. 2.17.a). For higher values a numerical error occurs, maybe due to a huge value of $\dot{\gamma}(0)$ or, using the theory proposed by [169], due to the fact that for a slope higher than a slope limit the steady flow is not possible. Qualitatively, a similar velocity profile is experimentally found in [177], showing that, as expected, flows are faster for higher slope angle. A similar trend was detected by [206], who observed that the effect of decreasing slopes on the reduction of velocity is lower for big avalanches, which possesses a higher release mass and higher velocities.

The results of our simulation (Fig. 2.17.b) show that the relationship between θ and $u(0)$ is linear. Besides, $\dot{\gamma}(0)$ is significantly different from zero only for values higher than 25-27° approximately. [194] observed that during the deposition process the avalanche moves as a plug, with the speed decreasing simultaneously in the whole depth. The authors suppose that, because of the cohesive and frictional forces, the flow in the whole depth freezes more or less instantaneously. That corresponds, using the data of our diagram, that for a slope lower than 25-27° the snow movement stops. The presence of a lower bound of the slope under which the avalanche stop is confirmed by the [169] theory too. Finally [176] found that below a yield of $\dot{\gamma}$ the flow stops too.

Applying these results to the erosion and the deposition processes, it is possible to conclude that for steeper slopes, $\dot{\gamma}(0)$ is higher and hence we move to the right of Fig. 2.16. This corresponds to a higher erosion in the steeper slope and a higher deposition in the flatter zone. This behaviour reminds the decreasing trend of the depth deposition with the slope angle experimentally observed by [194] and [44] or
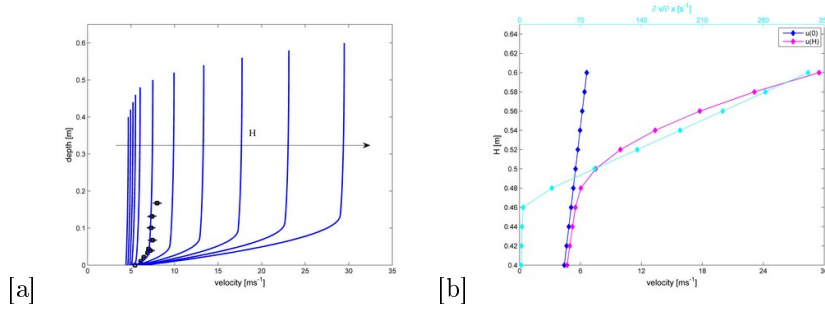
Figure 2.18: [a] Velocity profile for the Papanastasiou law with the avalanche depth H varying from 0.4 m to 0.6 m with a step of 0.02 m [b] The velocity at the base $u(0)$, at the top $u(H)$ and the basal shear strain rate $\dot{\gamma}(0)$ increase with the avalanche depth H.

empirically evaluated by [169].

Flow depth: influence on the entrainment

Finally $\dot{\gamma}(0)$ increases with the flow depth (Fig. 2.18.b), as results from the study of the variation of the velocity profile depending on the flow depth (Fig. 2.18.a). For thicker flows the slip velocity increases linearly, while the maximum velocity increases more quickly. For this reason thinner flows have a lower shear rate (similar to a plug) while thicker ones have even a shear layer at the base. This behaviour could even explain why in the front of an avalanche, having a higher depth, the shear rate is higher than in the slimmer tail.

This implies that thicker avalanches erode more than thinner ones, according to [83] in which the entrainment rate is proportional to the flow height. Experimentally, even [177] founnd that the mean velocity slightly increases with the flow depth and the shear strain rate decreases with the inverse of the flow depth.

Grain size: influence on the entrainment

From a granular approach a dry cohesionless avalanche can be assimilated to a granular material. Viscosity is proportional to the grain size [177]. Hence using the Papanastasiou law, the strain rate decreases with the grain size. Moreover, low values of the strain rate correspond to higher grain size, and consequently to the avalanche tail where the the random kinetic energy is lower [53] and the deposition occurs. On the contrary, with a higher strain rate the grain size is smaller and hence we are in the zone where the avalanche erodes.

Table 2.4: Parameters used for the 1-dimensional simulation.

Parameter	Value
m	$0.01 \cdot \rho$ kg/ms
τ_0	$3 \cdot 10^8$ kg/m
a	1 s
u_{ava}	20, 30, 45 m/s
ρ	200 kg/m^3
H_s	1.2 m
$\dot{\gamma}_c$	16.1 s^{-1}
Z_{SH}^C	$2.14 \cdot 10^7$ kg/ms

1-Dimensional analysis of the erosion

A further analysis is here carried to study evolution of the viscosity behind the snow cover with time. Let us suppose a 1-Dimensional sample representing a vertical segment of snow of depth H_s. The Navier-Stokes equations (Eqq. 2.59, 2.60) are consequently reduced to:

$$\rho \frac{\partial u}{\partial t} - \frac{\partial}{\partial y_{tot}} \left(Z_{SH} \dot{\gamma} \right) = 0. \tag{2.86}$$

with $Z_{SH} = Z_{SH}(\dot{\gamma})$.

The boundary condition of the differential equation is represented by a velocity equal to zero in $y = 0$ (where the snow is at rest close to the terrain) and a fixed velocity $u = u_{slip}$ indicating the velocity of the avalanche sliding over the snow cover (in $y = H_s$). Initially the snow cover is at rest ($u(y) = 0 \; \forall 0 \leq y < H_s$).

A Papanastasiou law (Eq. 2.67) is used. As concerns its parameters, experimental data are used. In particular, for m, representing the avalanche viscosity, the value indicated by [76] for the plug flow is used. τ_0 corresponds to the viscosity of a snowcover, since $a\tau_0 \gg m$ calculated with the formula proposed by [77] with T=-3°C, and $\rho = 200$ kg/m^3. Finally a is set equal to 1 s as well as $n = 1$ (see Tab. 2.4).

The results obtained solving this non linear parabolic equation are shown in Fig. 2.19. In the first time steps the upper part of the snowcover begins to move. Then the movement is propagated to the whole snowcover.

The layer of snow close to the moving mass is subjected to a higher $\dot{\gamma}$, corresponding to a lower viscosity. When $\dot{\gamma}$ becomes lower than its critical value, i.e. its viscosity is lower than the critical viscosity Z_{SH}^C, the snowcover is eroded by the avalanche (Fig. 2.20). The values of $\dot{\gamma}_c$ and of Z_{SH}^C derived, respectively, by Fig. 2.16 and by Eq. 2.67 are reported in Tab. 2.4.

Hereby the evolution of $l(t)$, or the depth of the snowcover which is not eroded, can be plotted in Fig. 2.21.

[a]   [b]
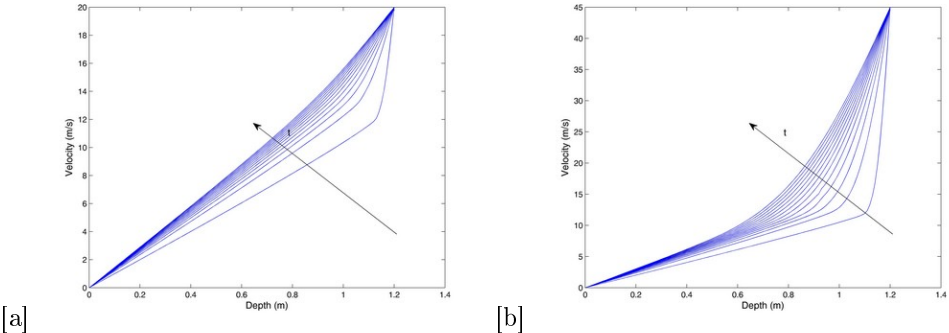
Figure 2.19: The velocity evolution in time from t=0.01 s to 5.01 s plotted every 0.04 s. The boundary condition at the interface is [a] 20 m/s and [b] 45 m/s.


[a]   [b]
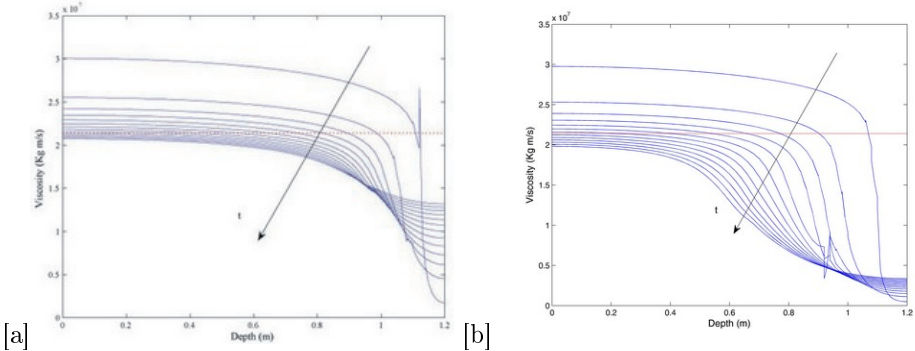
Figure 2.20: The viscosity evolution in time from t=0.01 s to 5.01 s plotted every 0.04 s. The boundary condition at the interface is [a] 20 m/s and [b] 45 m/s. The dotted line represents the critical viscosity.
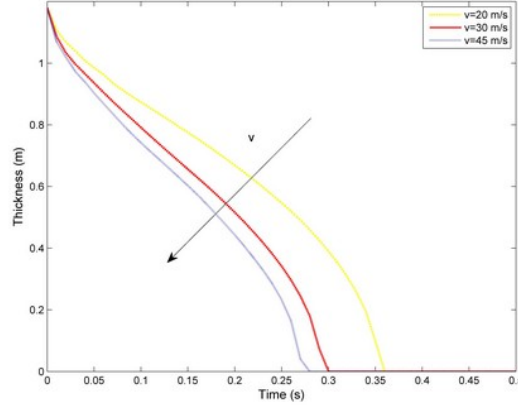
Figure 2.21: Time evolution of the snow cover thickness for three avalanche velocities: 20 m/s, 30 m/s, 45 m/s.

Imposing different slip velocities u_{slip}, it is possible to conclude that the erosion rate increases with u_{slip}. In fact, for our model this corresponds to a higher shear strain rate in the snowcover, and consequently to a higher $\partial l/\partial t$. This result is confirmed by the theory, reported in [83], considering the erosion rate proportional to the flow velocity. This is validated experimentally, for instance, by [22], in their study on the erosion process, using dry granular material.

In addition, a higher basal shear rate corresponds to a higher slip velocity and consequently to a higher erosion rate, as explained in Fig. 2.16.

From a first analysis, the results of Fig. 2.21 agree with the experimental measures that evaluated an avalanche able to erode the entire snow cover in a very short time (duration 0.1-2s) [193], as compared to the duration of whole avalanche flow passage for a point. Experimentally 350 kg/ms of snow eroded in the ploughing process are measured, corresponding to dl/dt equal to 2 m/s. The erosion rate measured accordingly, is of the same magnitude as the experimental one.

Conclusions

In this chapter the Papanastasiou shear thinning law is used to model the basic features of the snow avalanche behaviour. Firstly, it allows to describe the velocity profile along the avalanche depth. The analysis of the velocity profile allows to improve knowledge on the dependence of the velocity and of the strain rate, focusing on its value u_{slip} and $\dot{\gamma}(0)$ at the bottom of the avalanche. The numerical analysis showed the increase of u_{slip} and $\dot{\gamma}(0)$ with the slope angle and with the flow depth. Searching

an analytical justification of the slip condition, it seems that the slip velocity could depend on bonds between the grains and consequently on the snow characteristics (strength, density, temperature, type and dimensions of the crystals, cohesion ...). Additionally it is shown that u_{slip} should depend on the tangential stress at the base. To confirm this hypothesis, theoretically based, more experimental data should be collected and analysed focusing the attention to both the velocity characteristics (values at the base, gradient of the velocity ...) and the snow properties. In this way, the Papanastasiou law could be confirmed as well as the definition of the u_{slip}.

Secondly, the simple choice of the rheological Papanastasiou law, using continuum mechanics concepts, allows to describe the entrainment, taking into account the properties of the flowing mass as well as those of the snow cover. The model proposed is in agreement with other theories in the literature, that consider the erosion proportional, for instance, to the flow velocity and height. Besides it gives an explanation of the evidence that in the avalanche bulk erosion occurs, while in the tail deposition prevails considering the granular size too. In addition, its first validation with experimental data show that the method, opportunely refined, could well explain also the entrainment process. A further investigation should define the parameter values of the model as functions of the different kind of snow. Furthermore, more experimental data, from both small scale chute and real test site, are needed to validate the assumptions here assumed.

Introducing the proposed entrainment law into existing dynamics models, the new erosion model could be tested and validated. To this aim, a model without depth-average should be used, in order to obtain information concerning the basal gradient of velocity. However, models as RAMMS in which the velocity profiles and their evolution in time are described, through the production and decay of the kinetic energy of the random motion of the snow granules [53], could be used too. From a practical point of view, our erosion law, introduced into a dynamic model could contribute to better describe the avalanche motion and behaviour (velocity, masses, flow height, runout distance and impact pressure on obstacles) depending on the snow characteristics. Our model appears correct and consistent but only with the validation with more experimental data it can be practically used in a dynamic simulation.

Finally the concept of critical shear rate $\dot{\gamma}_c$, introduced for the entrainment, can be extended to the study of the avalanche release too. A higher $\dot{\gamma}_c$ corresponds to a huge creep movement, defined as the deformation of the snow, without the avalanche trigger. Consequently, $\dot{\gamma}_c$ may also indicate a degree of the snow cover stability. This aspect will be developed in a future work.

Chapter 3

Application of the model to avalanche-structure interaction

From regulations reported in Ch. 1 it is clear that to design aim it is necessary to know the velocity, pressure, density and depth of the flowing mass. These values are given by a model of avalanche dynamics.

Hence, in order to analyse the interaction between avalanche and structures a numerical technique is used. In particular, depending on the finality of each study, different methods can be used: two or three dimensional models as well as stationary or transient ones. Therefore in this chapter the different approaches are presented. They can be considered as a variation (for instance from the avalanche depth plane to the slope one) or a simplification (from transient analysis to stationary one) or an extension (from two dimensions to three dimensions) of the model presented in Ch. 2. However, to be more clear, the different models are presented.

They are all based on the assumption that the avalanche is an incompressible fluid. The Navier-Stokes (NS) equations are consequently used:

$$
\begin{cases}
\nabla \cdot \mathbf{u} = 0 \\
\rho \left(\dfrac{\partial \mathbf{u}}{\partial t} + \mathbf{u} \cdot \nabla \mathbf{u} \right) = \nabla \cdot [Z \left(\nabla \mathbf{u} + (\nabla \mathbf{u})' \right)] - \nabla p + \mathbf{F}
\end{cases}
\tag{3.1}
$$

where $\mathbf{u}$ is the velocity, p the pressure, Z the viscosity, ρ the density and $\mathbf{F}$ takes into account the gravitational and friction forces (both a Coulomb force and a viscous one). The peculiarities of those models are to give the values of the velocity and of the pressure in each point of the avalanche and to find the value of the pressure without any additional law, on the contrary of the majority of the models present in the literature.

All the models are numerically solved thanks to the FEM model called COMSOL Multiphysics [3].

In Ch. 2 appropriate laws, based on Non-Newtonian fluids, are proposed to describe correctly the avalanche rheology. In addition, since velocity and pressure are linked (Eq. 1.41), to study the impact with structures such rheology should be considered.

Nevertheless the majority of the models in the literature considers a depth-averaged velocity or give a predefined law for the velocity profile along the depth. The existent regulations (Ch. 1) use a constant value of the velocity on the depth too. Hence, to compare our simulations results with those obtained applying formulae available in literature a Newtonian fluid is used, as first approximation.

3.1   Transient case (T)

In the transient case the two-dimensional Navier-Stokes equations are coupled with the level set method (see Sec. 2.1.2), suitable for the free boundary conditions. In this way the evolution in time of the impact pressure against the obstacle can be described [48]. If the slope plane is chosen as reference system, the velocity and the pressure variations along the width can be detected. Otherwise, by an analysis along the vertical avalanche section, these quantities along the avalanche depth can be evaluated [45].

In detail, in this approach the domain of calculus takes into account the avalanche zone and the around air [45, 47, 50]. The two-phases (snow and air) are modeled introducing a fluid having density ρ and the viscosity Z:

$$\rho = \rho_a + H(\Phi)(\rho_{av} - \rho_a) \tag{3.2}$$

$$Z = \eta_a + H(\Phi)(\eta_{av} - \eta_a) \tag{3.3}$$

depending on the density/viscosity of air (a) and of avalanche (av) through the Heaviside function $H(\Phi)$. The level set function Φ (see Sec. 2.1.2) is characterized to be equal to zero on the free surface, to be positive in the zone of the more dense and more viscous fluid (avalanche) and to be negative where the less dense and less viscous one (air) is situated [50]. The interface is transported by the advection equation:

$$\frac{\partial \Phi}{\partial t} + \mathbf{u} \cdot \nabla \Phi = 0. \tag{3.4}$$

3.1.1   Two-dimensional model in the avalanche depth plane (T2Dxy)

This model, well described in Ch. 2, considers the avalanche depth plane. Hence the velocity $\mathbf{u} = (u, v)$ has two components, along the x and the y directions, with $\mathbf{x} = (x, y)$.

To deduce the value of the avalanche depth h, on the contrary of the depth averaged models (see Sec. 1.2.3) in which it appears directly in the momentum equation, a further equation has to be introduced.

Let the air-snow interface be described by the material interface $\Phi = s_2(\mathbf{x}, t) = y - g(x, t) = 0$, and the interface against the underlying motionless snow cover by the function $s_1(\mathbf{x}, t) = y - l(x, t) = 0$. The avalanche depth is:

$$h(x, t) = g(x, t) - l(x, t). \tag{3.5}$$

If the erosion/deposition is not taken into account (i.e. the interface $s_1(\mathbf{x}, t)$ is characterised by $l(x, t) = 0$) it results that $h(x, t) = g(x, t)$.

3.1.2 Two-dimensional model in the slope plane (T2Dxz)

A different approach is to study the avalanche in the slope plane, that is in the xz-plane (Fig. 3.1). In this situation the system composed by air and avalanche is considered as a fluid. For this reason the same equations of the Navier-Stokes (Eq. 3.1) and the advection one for the interface air-avalanche, with $\Phi = s_3(\mathbf{x}, t) = 0$ (Eq. 3.4), are used. The notation becomes $\mathbf{x} = (x, z)$ and $\mathbf{u} = (u, w)$ [45].

It allows to describe, although roughly, the pressure on an obstacle. This model is simpler than an averaged one in which even the depth of the avalanche is taken into account. However, to know the depth of the avalanche it is sufficient to calculate it with the two-dimensional model on the xy-plane.
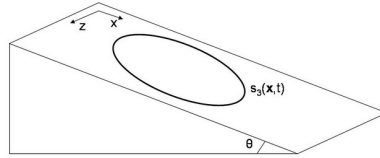
Figure 3.1: Coordinate system of the T2Dxz model.

3.2 Stationary case (S)

In its stationary version the Navier-Stokes equations (Eq. 3.1) are sufficient to describe the avalanche behavior. In particular all the domain of calculus is supposed being occupied by the avalanche. Hence the density and the viscosity are those of the avalanche: $\rho = \rho_{av}$ and $Z = \eta_{av}$.

3.2.1   Two-dimensional model (S2D)

The velocity has two components: $\mathbf{u} = (u, v)$ along the directions $\mathbf{x} = (x, y)$. In this thesis only the slope plane is considered, but it would be possible to analyse the avalanche depth plane too.

3.2.2   Three-dimensional model (S3D)

Thanks to the simplified nature of the stationary case it is possible to compute the simulation in the three dimensions. In particular the velocity has three components: $\mathbf{u} = (u, v, w)$, along the directions $\mathbf{x} = (x, y, z)$.

3.3   Obstacle

In the area of the obstacle the previous equations (Eq. 3.1 and eventually Eq. 3.4) are not solved (Fig. 3.2). As boundary conditions two choices are possible: no-slip condition or slip condition.
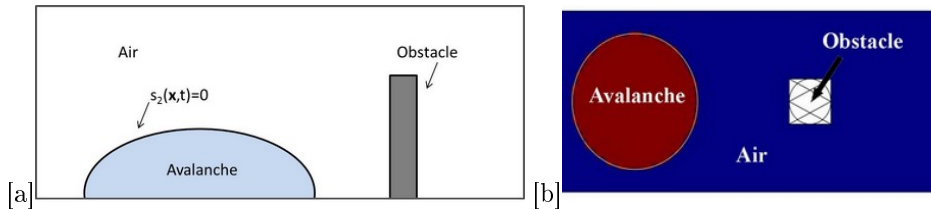
Figure 3.2: [a] Obstacle in the avalanche depth plane in the transient analysis. [b] Obstacle in the slope plane in the transient analysis. The obstacle can have different shapes. The red colour represents the avalanche density ρ_{av}, the blue one shows the air density ρ_a, the white one indicates the absence of fluid (since the obstacle is there).

3.4   T2Dxy: preliminary simulations

Once the models for the snow avalanche dynamics have been described, it is possible to simulate the interaction between a snow avalanche and various obstacles located along its path such as, for instance, a concrete dam, an energy transmission pole or a typical masonry house. In particular in this section preliminary simulations carried are compared to regulations reported in Sec. 1.6, 1.7 and 1.8. These first simulations results, although still qualitative, show the capabilities and deficiencies of the model.

Hence the model opportunely calibrated is be compared, quantitatively too, to real measurements (Sec. 5.3 and Ch. 6).

3.4.1 Pressure and height of run-up in a dam impact

A first set of simulations consists in the analysis of the interaction between avalanche and obstacle in the avalanche depth plane. In particular, the simulations reported here analyse the interaction between a dense avalanche and a dam.

Fig. 3.3 shows the effects that a dam has in containing the snow. Only part of the avalanche crosses the obstacle, whereas the main volume is stopped by the barrier.

In the following the pressure profile obtained by simulation is compared to the Swiss recommendations [80] (see Sec. 1.7.1). Fig. 3.4 shows the pressure along the dam at different time steps. At 1.1 s, when the avalanche reaches the dam (Fig. 3.5.a) there is a peak of pressure, than the upper part of the avalanche impacts the obstacle (Fig. 3.5.b,c). This behaviour is due to the particular shape (an ellipse) given as initial condition to the avalanche (the lower part arrives before the upper one). In this part of the dam, corresponding to the flowing height h the pressure attains the maximum values, in agreement with the Swiss recommendations [80]. Note that [196] found a bigger pressure in the lower part of the obstacle too.

In the run-up height H_r, instead, the pressure decreases linearly, according to the Swiss recommendations (see Fig. 3.4.b). On the obstacle the pressure does not go to 0, because a part of the snow is able to overcome the dam (Fig. 3.6) carrying with itself part of the kinetic energy and, consequently, of the pressure.

Hence such simulations, adequately calibrated, could allow in a design phase, to consider the right pressure and to estimate a more correct volume retained by the dam.

3.4.2 The jet length after obstacles

The dead zone created downward an obstacle can be studied too. The jet length created in the impact, for instance with a dam, as shown in Fig. 3.7 increases with the incoming flow velocity. This is in coherence with the jet theory proposed by [108] for the breaking mounds (see Sec. 1.9.3). In fact the trajectory of the jet launched directly over the obstacles can be approximated as a projectile motion in two dimensions and, consequently, is linked to the velocity.
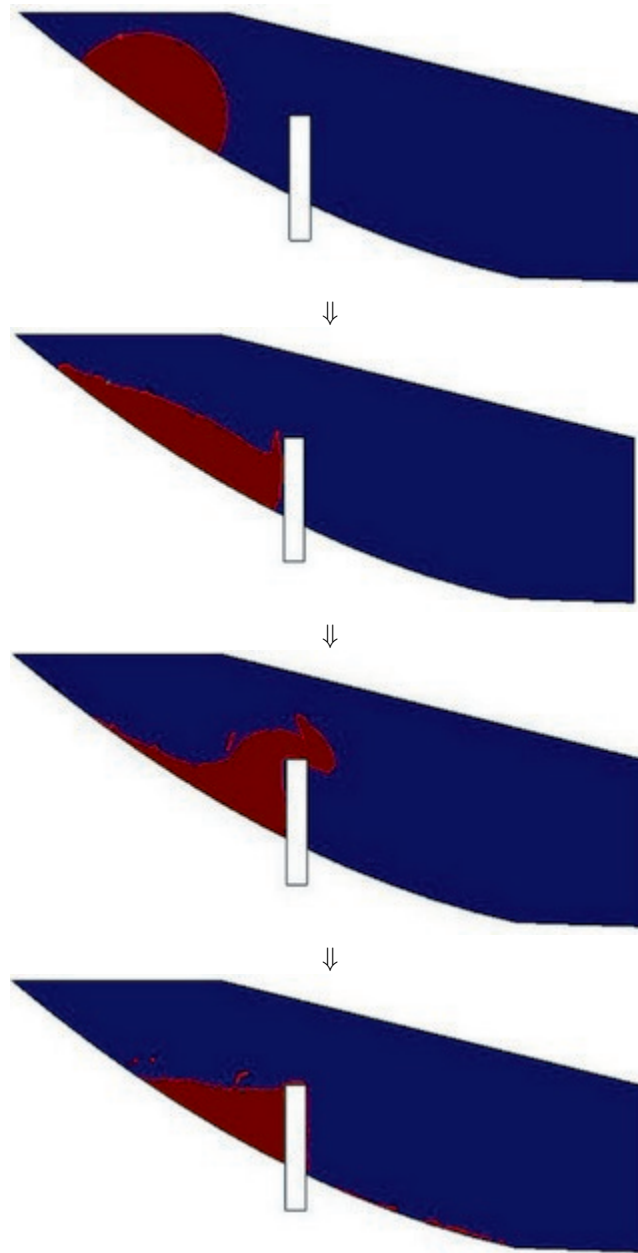
Figure 3.3: Snapshots showing the density at time t=0, 1, 2.5 and 5 s. The red area represents the avalanche, the blue one the air and the white one dam.
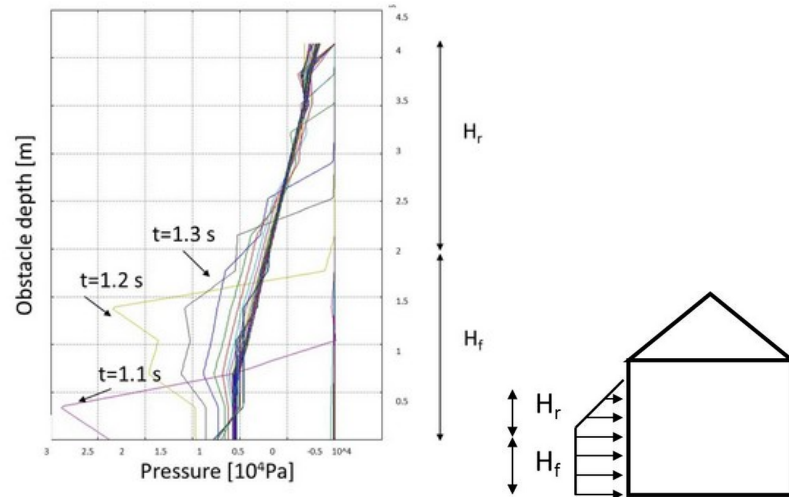
Figure 3.4: The pressure profile along the obstacle thickness in [a] simulation and in [b] Swiss recommendations.

3.5 T2Dxz: preliminary simulations

3.5.1 Influence of an open slope or a channeled one

A set of simulations in the slope plane shows the interaction between an avalanche and an obstacle having a squared or a circular shape with different dimensions. In this situation two scenarios are supposed: an open slope and a channeled one, thanks to appropriate boundary conditions (an open boundary with a normal stress condition, and a wall with a slip condition) [45].

The imposed boundary conditions play an important role when the obstacle has a size comparable with the channel. In fact, an avalanche can expand itself if an open slope is present (Fig. 3.8.a) or can remain confined if it slides in a channel (Fig. 3.8.b). Hereby, for practical design even the boundary conditions have to be taken into account. If the obstacle is small, on the contrary, the effects of the boundary conditions are less significant (Fig. 3.9) [45].

The influence of the boundary conditions is seen in literature too [16]. In fact the geometry of the channel influences the impact: in a gully the obstacle produces a local acceleration and a creation of a wake after the obstacle that can increase the interaction force. On the contrary if the obstacle is in an open slope the interaction is lower [16].
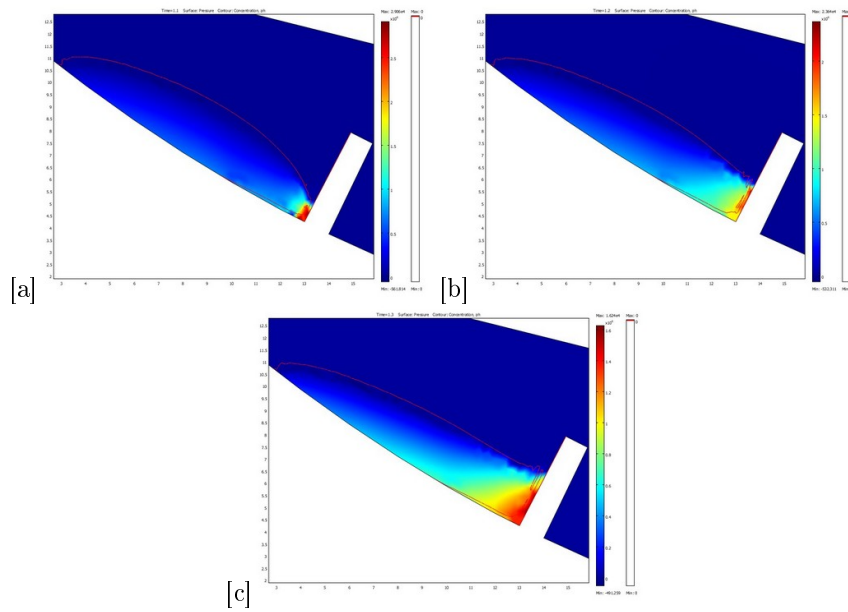
Figure 3.5: Avalanche pressure on a dam at time [a] t=1.1 s, [b] 1.2 s and [c] 1.3 s along the flowing height H_f. The avalanche at time t =0 s was at rest. The range of the scale pressure is adapted at each time step to evidence the area with the maximum pressure.

[a]   [b]

[c]
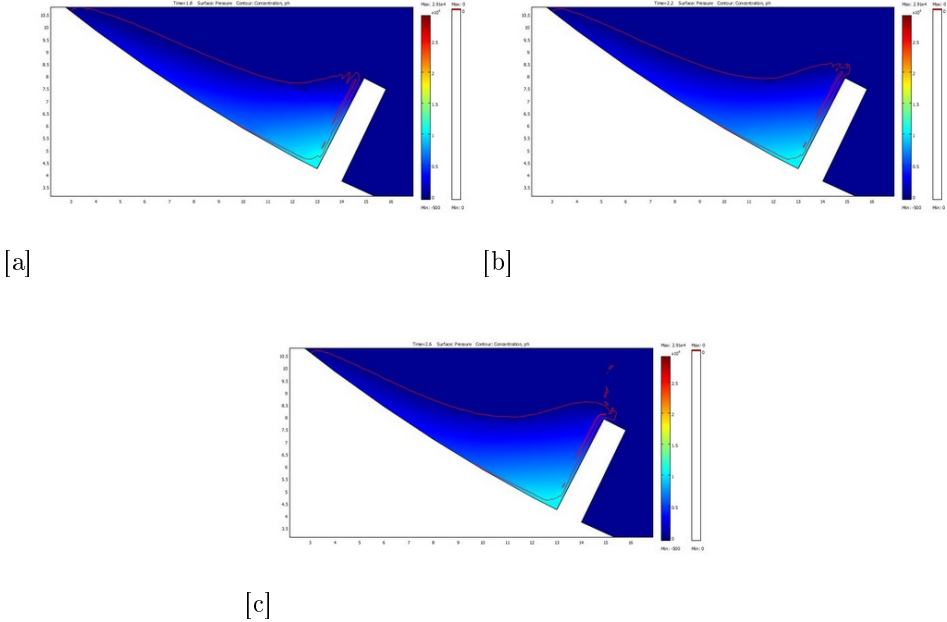
Figure 3.6: Avalanche pressure on a dam at time [a] t=1.8 s, [b] 2.2 s and [c] 2.8 s during the run-up height H_r phase. The range of the scale is that of Fig. 3.5.a.
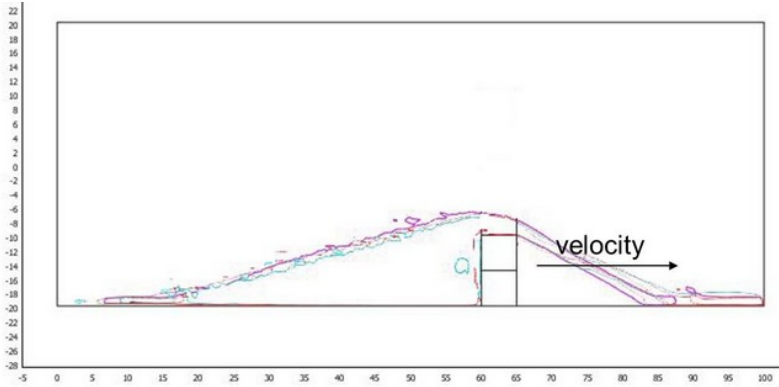
Figure 3.7: The length of the jump increases with the velocity.
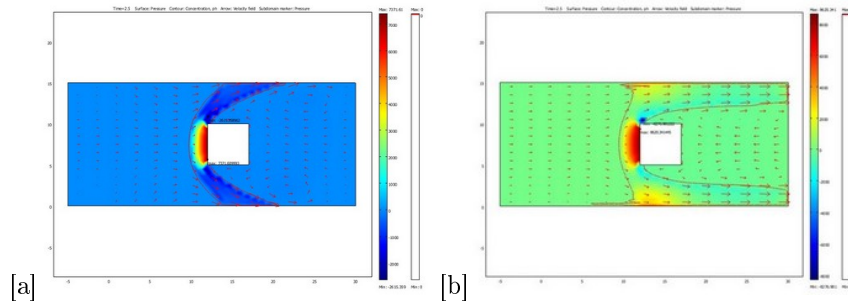
Figure 3.8: A dense avalanche with a density of 300 kg/m^3 [a] in a open slope and [b] in a channel at time 2.5 s impacting a large obstacle.
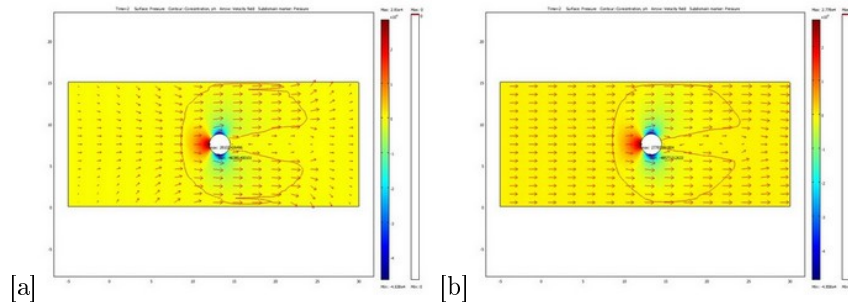
Figure 3.9: A dense avalanche with a density of 300 kg/m^3 [a] in a open slope and [b] in a channel at time 2.0 s impacting a small obstacle.

[a] [b]
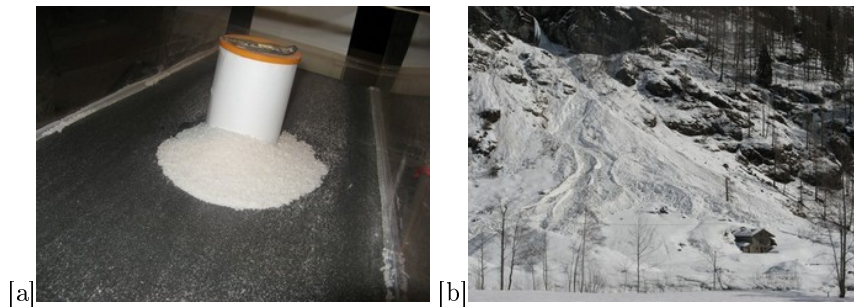
Figure 3.10: [a] The 1 m long and 0.4 m wide chute for granular experiments. [b] Avalanche close to a house in Gressoney's Valley (AO). Photos E. Bovet.

3.5.2 Dead zone

In this section some qualitative information concerning the dead zone down-wind an obstacle is analysed in addition to what seen in Sec. 3.4.2.

In the first simulations campaign two densities are supposed to take into account both a dense avalanche (density of 300 kg/m^3) and an aerosol one (density of 10 kg/m^3) [45]. In the case of the aerosol, a simplification of the problem is done, since the flow is not considered turbulent, but laminar.

In the second simulations campaign the dimensions of a laboratory chute, used practically for educational purposes (Fig. 3.10.a), 1 m long and 0.4 m wide, is used. The viscosity and the density (ρ_{av}=100 kg/m^3) of the avalanche is considered. As initial condition the flow is at rest. The slope of the chute is variable: hence for higher slope angles the driving force is higher and the avalanche moves quickly.

In the third simulations campaign the real scale is used with the same viscosity.

The results can be resumed as the follow:

- The obstacles having bigger dimensions, both in circular than in the square situation (Fig. 3.11.a), split the flow. Qualitatively the fan generated in the impact of the flow is similar to that observed experimentally by [110]. On the contrary, a circular shape of smaller dimension allows to the airborne flow to rejoin after the obstacle (Fig. 3.11.b) [45].

- The obstacle shape influences the formation of a dead zone downwind an obstacle, as Fig. 3.12 shows.

- In the chute simulations, since the Reynolds number is lower than the true one, the flow has a behaviour similar to a more viscous fluid. In fact the similitude criterion (see Sec. 1.3.1) is not respected. For this reason the flow wraps both a

[a]   [b]
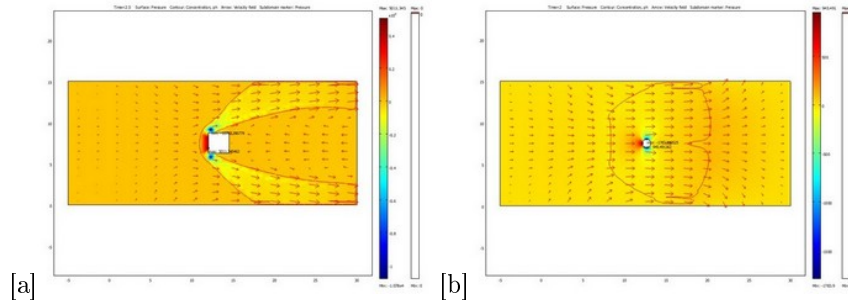
Figure 3.11: [a] Interaction between a dense avalanche (300 kg/m^3) and a square obstacle in an open slope condition at time 2.5 s. [b] Interaction between an airborne avalanche (10 kg/m^3) and a small circular obstacle in an open slope condition at time 2 s. The arrows indicate the velocity, the contour line in red is the interface avalanche-air, the surface plot indicates the pressure.


[a]   [b]
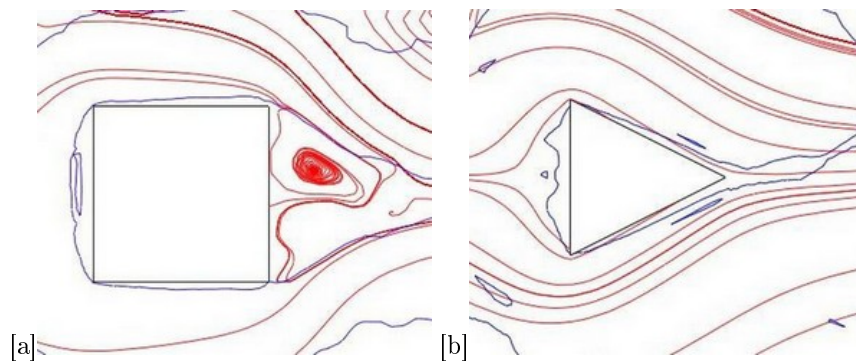
Figure 3.12: Simulations carried at chute scale (length 1 m), snow at t=0 s is at rest. The red lines are the streamlines, the blue ones the flow contour. [a] A squared obstacle allows the formation of a stagnation zone at a slope of 45 degrees, while [b] the flows wraps perfectly a triangular shape at a slope of 30 degrees.
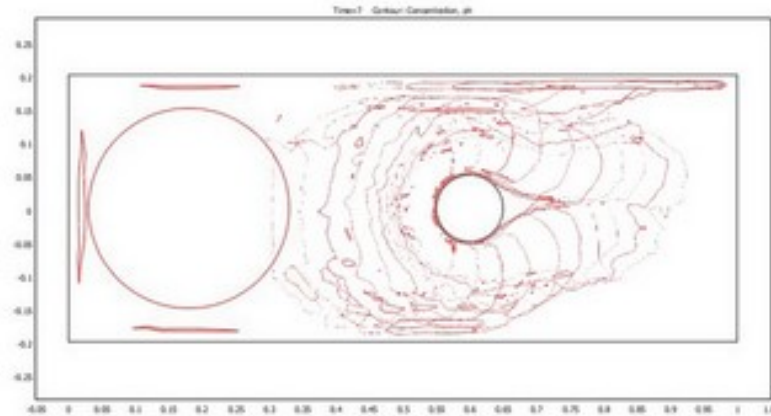
Figure 3.13: Avalanche contour in different time steps at a chute scale with a slope of 30 degrees impacting a circular obstacle having the diameter of 10 cm.

circular obstacle (Fig. 3.13) and a triangular one (Fig. 3.14). For higher slopes the dead zone length is longer Fig. 3.14.b. Therefore faster the avalanche is longer the dead zone is.

- At a real scale with a higher Froude number both the circular and triangular shapes separate the flow, as Fig. 3.15 shows.

Therefore, from the points above it is possible to suppose that for lower Reynolds (smaller obstacle, slower avalanche, higher viscosity) or lower Froude numbers (slower avalanches), the flow easier wraps the obstacles. Remember that low values of Re and Fr are peculiar of the deposit area (Fig. 3.10.b). Since in the T2Dxz model the flow height is not considered, the Froude number is only velocity dependent.

A closer study about the dead zone created by the obstacle, for instance, focusing on its size and shape, could be an instrument to conceive efficient passive protection measures, like deflection dams or wedged-shaped walls (Fig. 3.16.a). Besides, an analysis of the deviation of the flow due to obstacles could explain the formation of different branches sometimes created in the deposit area (Fig. 3.16.b) [45].

3.5.3 Variation in time of the pressure in a point

The model allows to calculate the variation in time of the the pressure in a point too. For instance, Fig. 3.17 shows the pressure in the central point upwind a square obstacle: in few seconds (because the avalanche simulated is very small) the avalanche
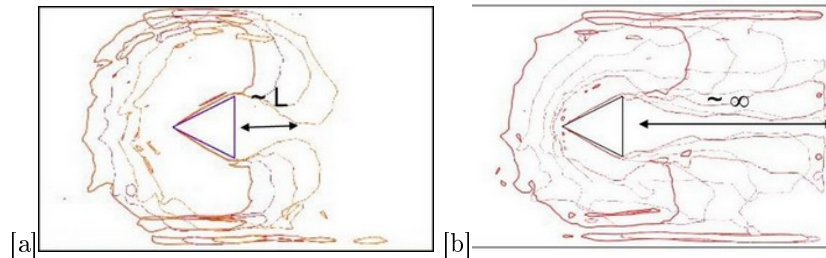
Figure 3.14: Zoom of the avalanche contour in different time steps at a chute scale with a slope of [a] 30 degrees and [b] 45 degrees.

simulated goes beyond the obstacle: the pressure increases quickly in the avalanche front and decreases slowly in its tail. This pressure is compared to the values obtained by the Eq. 1.41 in two different ways.

The first one is based on the velocity measured just before the obstacle (in fact, on the obstacle the velocity vanishes for a no-slip boundary conditions). For this situation we found the coefficient C_d using the maximum values of the velocity and of the pressure. It is important to underline that the avalanche, in our simulations, has not yet attained a stationary value when it crashes on the obstacle. This aspect can influence significantly the results obtained. In fact, pressure is derived from the velocity through Eq. 1.41 considering a stationary situation. In addition, for the nature of our simulation that lasts few seconds, the initial phase of the crash plays an important role. On the contrary in the experiences in the wind tunnel the initials steps of the interference are neglected, to consider only the stationary case [45].

A second approach consists on the evaluation of the pressure using the velocity measured in a condition without the obstacle. Fig. 3.17 shows as the air moved by the avalanche impacts the obstacle before the avalanche itself. Consequently a pressure is measured even before the avalanche. In fact the green curve is significantly different from zero later than the red and blue ones. In this situation, having a larger velocity leads to a lower C_d [45].

3.5.4   Peak of pressure

Considering the pressure in the central point upwind of an obstacle (Fig. 3.18.a) it is possible to note a peak of pressure in the first instant of the impact.

In the following analysis [46] the ratio between the maximum pressure p_{peak} and its mean is about 4, overestimating the value of 3 indicated in Sec. 1.7.2. Let note that our peak is very short, in agreement with [185] who observed a very short peak pressure.

[a]

[b]
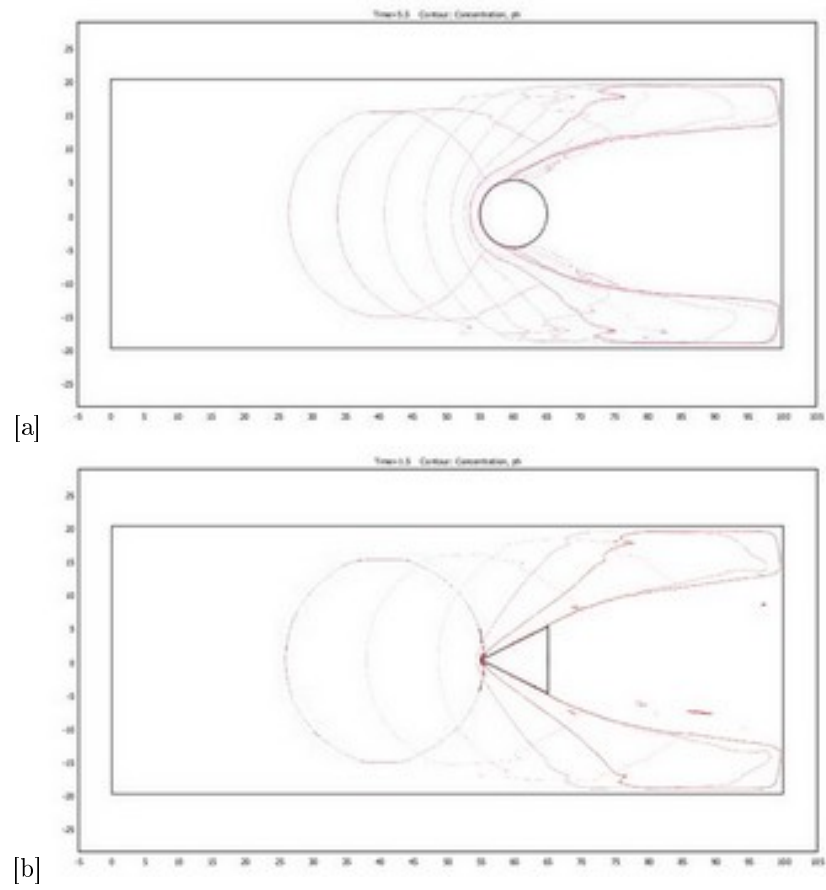
Figure 3.15: Real scale with Froude number equal to [a] 3 and [b] 7.
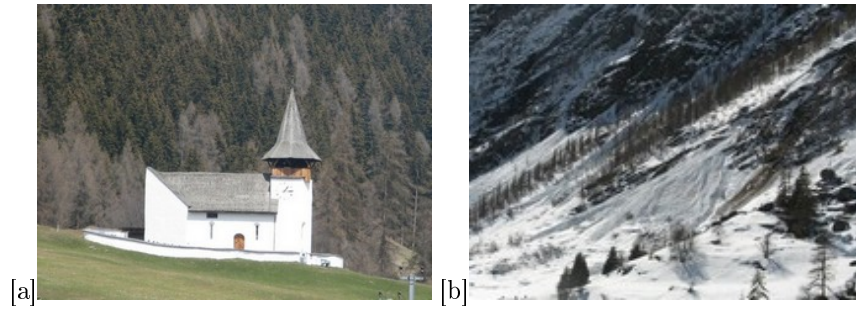
Figure 3.16: [a] A church in Switzerland with a wedge-shaped wall. [b] Branches in the deposition zone of an avalanche. On the right a full depth avalanche with debris in Gressoney's Valley occurred in March 2011. Photos E. Bovet.
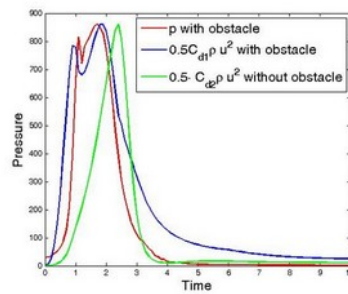

Figure 3.17: Variation in time of the pressure measured and calculated, with Eq. 1.41, in the central point upwind a square hit by an airborne avalanche. $C_{d1} = 0.78$ in the simulation with the obstacle and $C_{d2} = 7.55$ in the simulation without the structure.
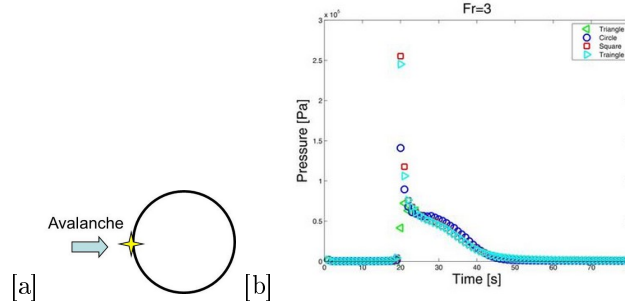
Figure 3.18: [a] Pressure calculated in the central point upwind. [b] The peak depends on the shape.

Hence a detailed analysis is done to study the peak properties (Fig. 3.18.b) of a flow having density ρ_{ava}=300 kg/m^3 and $\eta_{ava} = 2.1 \cdot \rho_{ava}$ kg/ms. The maximum of pressure depends on the obstacle shape: for instance, it is higher for a squared one than a circular one. The triangle with a vertical face upwind gives a value of pressure similar to the square one [48].

Additional simulations are carried, considering a circular shape, varying the Froude number. Remember that, since in the T2Dxz model the flow height is not considered, the Froude number is only velocity dependent. Fig. 3.19 shows that the peak magnitude is higher for higher Froude numbers and its duration decreases with the increase of the Froude number. Finally the peak is more accentuated for higher Froude numbers [48].

3.5.5 C_d coefficient

In this section a first attempt to analyse the C_d coefficient is made. From the analysis on the obstacle shape it is possible to conclude that the triangle can have the behaviour similar to a square, depending on its relative position with respect to the flow. In Fig. 3.20.a the vertical edge is upwind, while in Fig. 3.20.b is downwind.

Moreover, as concerns the dependence on obstacle size, Fig. 3.21 shows that larger obstacles have a lower C_d (see Sec. 3.6 for more details).

Finally, the ratio L/v^2 between the load and the velocity squared is shown in Fig. 3.22. C_d increases when Fr decreases, in analogy to [195, 200]:

$$C_d \propto c_1 + \frac{c_2}{Re} \propto c_1 + \frac{c_3}{Fr} \tag{3.6}$$

since the Reynold number Re is proportional to the velocity as well as the Froude number Fr.
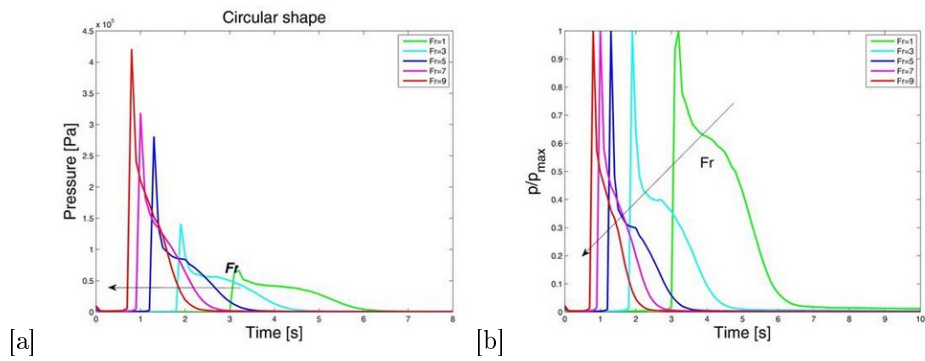
Figure 3.19: The duration and the magnitude of the peak of pressure depend on the Froude number.
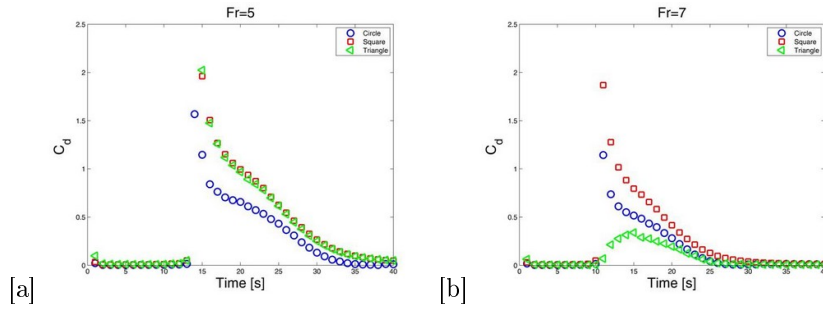

Figure 3.20: C_d calculated for different shapes for Froude values of [a] 5 and [b] 7. The triangle has the vertical edge [a] upwind and [b] downwind.
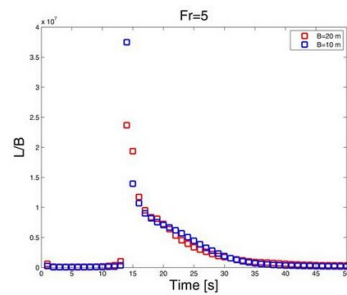

Figure 3.21: Larger obstacles have a lower C_d.
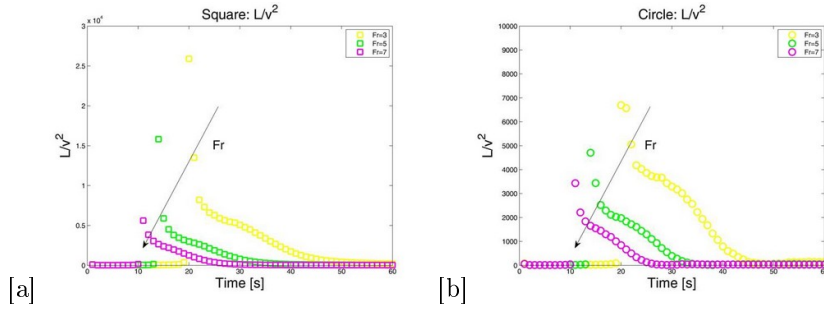
Figure 3.22: The ratio L/v^2 for different Froude number for [a] a square and [b] a circle.

3.5.6 Comparison with wind effects

In this section the impact pressure of an aerosol avalanche against a building is analysed. Remember that a simplification of the problem is done, since the flow is not considered turbulent, but laminar. Fig. 3.23 shows that on the windward side the pressure is positive, while in the other sides it is negative, similarly to the wind effects (see Sec. 1.7.4).

In this case the C_p is calculated using the extreme values derived by the simulation: the maximum value is 861 Pa in Fig. 3.24.a, the minimum values are -595 Pa in Fig. 3.24.b and -47 Pa in Fig. 3.24.c at the center of the edge. Consequently the pressure of impact becomes 1076.7 Pa, considering a pressure coefficient for the frontal edge of 0.8, as in [7].

As concerns the lateral edge, Fig. 3.24.b shows as there is a region of length $L/5$ in which the pressure is higher than in the remaining section, in agreement with [7]. Our C_p obtained is -0.6. This lower value could be due the fact that there is only a little part of the avalanche impacting on the side, on the contrary of the wind experiences in which the wind recovers the whole tunnel.

To interpret the results obtained in the downwind side, it is important to underline that in such simulation the avalanche does not impact on this side. Hence the pressure is given by the blast: using the air density, the C_p obtained is -0.3 on the obstacle rear [45].

An additional example, in which the $Fr = 5$ is reported in Fig. 3.25 with the results summarised in Tab. 3.1. When blast is indicated, C_p is calculated rescaling the pressure with the air density, as done before. From a practical point of view, the upwind edge of the structure should be more resistant on the corners, since there two higher pressure are recorded there.
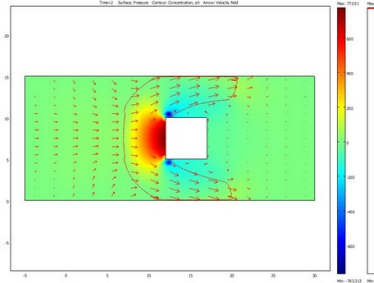
Figure 3.23: Interaction between an airborne avalanche (10 kg/m^3) and a square obstacle of big dimension in an open slope condition at time 2 s. The red colour indicates the positive values of pressure, the blue one the negative pressure.
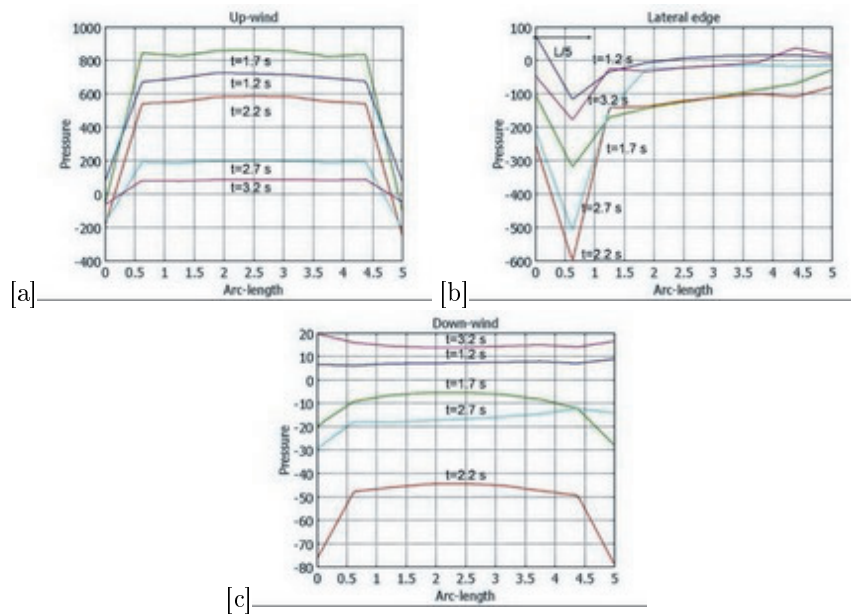

Figure 3.24: Avalanche pressure in time [a] up-wind, [b] in the lateral edge and [c] down-wind.
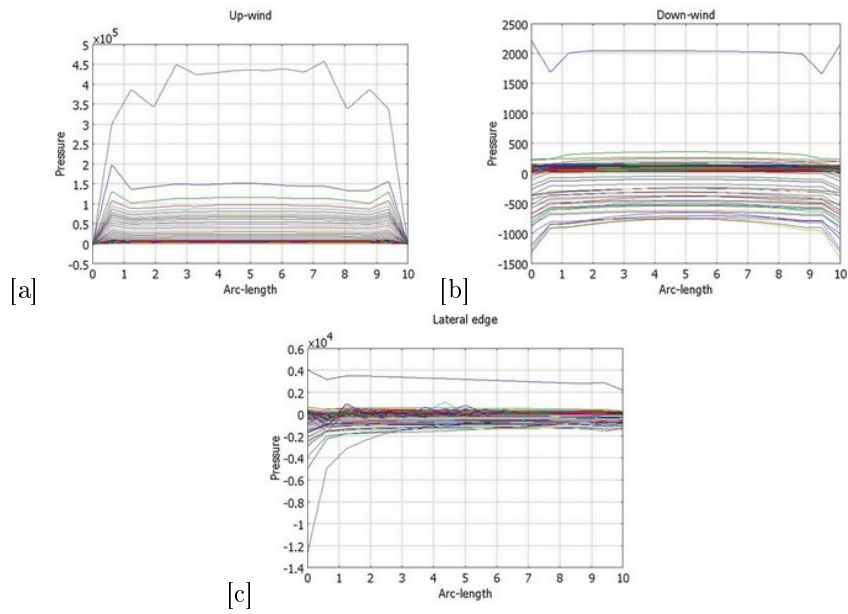
Figure 3.25: [a] Upwind [b] downwind and [c] lateral edges for the Froude number equal to 5.

Table 3.1: Results obtained by simulations and recommendation using the wind effect.

Edge	Simulated			Recommendation [7]
	Max pressure	**Density**	C_p	C_p
Up-wind	$4.45{\cdot}10^5$ Pa	avalanche	0.8	0.8
Down-wind	760 Pa	blast	-0.33	-0.3
Lateral	1500 Pa	blast	-0.65	-1/-0.8

3.6   S2D: preliminary simulations

3.6.1 C_d coefficient

In this section the C_d coefficient is analysed (see Sec. 1.6.1 for the definition). C_d depends on the obstacle shape (see Sec. 3.5.5) as well as on the avalanche characteristics. In particular an analysis of the dependence of the obstacle dimension on the C_d is carried, using a circular shape. It is clear, from Fig. 3.26, that C_d decreases with a power-law (in this case having exponent -0.6). This tendency was experimentally seen by [195, 200] and numerically by [48]. In fact they supposed:

$$C_d \propto c_1 + \frac{c_2}{Re} \propto c_1 + \frac{c_3}{B} \tag{3.7}$$

since in our case $Re = BU\rho/\nu$ changes due to different sizes B.
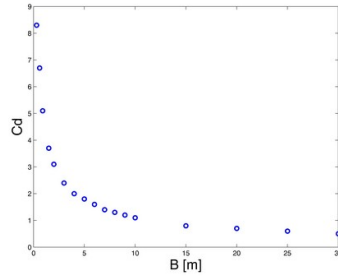
Figure 3.26: Dependence of C_d on the obstacle size B.

These results do not depend on the domain size: for instance for a circular obstacle having diameter of 1.5 m (it is tested for a diameter of 30 m too) the total load simulated with a domain of 60 m x 120 m, or of 600 m x 1200 m is almost the same ($2.24 \cdot 10^5$ Pa·m and $2.23 \cdot 10^5$Pa·m, respectively). The mesh dimension does not influence these results too [46].

Chapter 4

Experimental measure of avalanche mechanics: the Italian test site

4.1 The experimental site

The test site, called Seehore [138], is located at Gressoney-La-Trinité in the Aosta Valley (NW of Italy) and it belongs to the authority Regione Autonoma Valle d'Aosta. Built during the Operational programme Italy - France (Alps - ALCOTRA), Project "DynAval - Dynamique des avalanches: départ et interactions ecoulement/obstacles", it is operative since winter 2009/2010, and it is equipped by an instrumented obstacle from November 2010. Since it is included in the Monterosa Ski resort (Fig. 4.1), the avalanche of Seehore has to be artificially released, after critical new snow amount has been reached and/or snow drift occurred, in order to guarantee the safety of the ski-runs. Its accessibility is easily allowed by the proximity to the Staffal-Gabiet cableway station, giving a location for the control room of the measuring system too.

The slope, with an elevation difference of about 300 m (from 2300 to 2570 m asl), has a mean slope angle of about 28°and a NNW aspect. The release, track and deposition zone have a mean slope angle of about 39°, 35° and 17°, respectively.

The avalanche width varies from about 80 m at the top near the ridge to 40 m in the middle of the avalanche track, to more than 100 m in the deposition zone. The ground roughness is very high (see Sec. 4.2.3), as the path is covered by debris of different size, with single rocks up to 4 m of diameter.

In local ground measurements targets were measured from both a total station and a GPS-RTK approach. A global survey of the whole area was performed by heli-

Figure 4.1: View of the Seehore test site: 27th of March 2010 event. The ski run at the bottom is well visible. Photo E. Bovet.

copter borne laser scanner carried out by Helica Company in order to get the highest resolution from the digital terrain model (survey resolution of 20 points/m^2, vertical accuracy of 10 cm and horizontal accuracy of 18 cm) and ortho-image (resolution of 10 cm) [138].

In this test site researchers of the Department of Structural, Geotechnical and Building Engineering of the Politecnico di Torino (M. Barbero, M. Borri Brunetto, F. Barpi, E. Bovet, B. Chiaia, V. De Biagi, B. Frigo, O. Pallara), researchers of the Department of Agricultural, Forest and Food Science and NatRisk-LNSA, University of Turin (E. Ceaglio, M. Freppaz, M. Maggioni, D. Godone, D. Viglietti, E. Zanini) as well as technicians of the Regione Autonoma Valle d'Aosta (L. Pitet, V. Segor), Fondazione Montagna Sicura (N. Durand), AdHoc society (L. Bornaz) and Monterosa Ski resort (A. Welf) collaborate in the research [138].

4.1.1   Snow and climate conditions

According to a regional spatial division based on similar snow and climatic conditions [24] the test site is located in the south-eastern sector of the Aosta Valley, where the most abundant snowfalls in the region are recorded. The meteorological conditions most favorable for a successful avalanche experiment are a NNW precipitation and a wind from SSE, that tends to overload the slope with snowdrift accumulation. At less than 1 km from the test site a manual weather station (Lago Gabiet, 2340 m asl) is located. There air temperature, snow height, new snow depth are recorded every

morning since 1919. The average annual cumulated snowfall is 631 cm (period 1928-2001). In the area also an automatic weather station (Gabiet, 2379 m asl) recorded snow depth, air temperature, wind intensity and direction (every 30 minutes) since 2002 [138].

The snow depth during winter 2008-2009 was always above the mean value (maximum snow depth of 337 cm). Winter 2009-2010 was characterized by a lower snow depth (maximum snow depth of 157 cm) than in the previous winter but with more frequent snowfalls of low intensity. Winter 2010-2011 started with values above the mean, but then January and February were dry, and the snow cover completely melted one month before the mean (maximum snow depth of 160 cm) [21, 138].

4.1.2   Avalanche general data

Since the threshold to operate an artificial release is around 30 cm of new snow, the release volume is typically between 200 and 400 m^3, even if it can reach 800 m^3 if a thick slab is released.

Avalanches usually stop within the slope at deposition angles still high (see Sec. 5.1), but seldom reach the ski-run. Dense-flow slab avalanches are the most common, even if also powder clouds may occasionally form, especially in high winter conditions with dry and cold snow. During spring spontaneous wet, loose snow avalanches can be formed too.

Since at different snow avalanche conditions correspond a peculiar approach for the study of the impact force (see Sec. 1.4), this test site is suitable to analyse the interaction between avalanches and structures. Hence the site is instrumented with a steel obstacle (see Sec. 4.2), which measures the effects of avalanches impacting on it.

4.2   The obstacle device

4.2.1   Architectural design

The obstacle device, located at 2420 m asl (x=410186 y=5078430 in UTM-ED50 coordinates), is composed by (see Fig. 4.2.a) [21]:

- a concrete foundation: 3 m long by 3 m wide and 0.6 m thick. The relatively small size of the foundation is conceived in order to limit the excavation works on the steep slope, and to exclude, for instance, micro-piles or anchors economically more expensive;

- a vertical obstacle made of galvanized steel profiles (4.0 m high, protruding 2.8 m from the natural slope profile), consisting of:

    - a lower section bolted to the concrete foundation, serving as a support;

- a upper structure which carries the sensors, directly exposed to the avalanche impact. This part can be easily changed to allow the installation of obstacles with different shapes. The impact surface (total area of 1 m^2) is made of an array of 5 aluminium grooved plates placed at different heights. The position can be changed since each plates are supported by two load transducers, mounted on slides that can be easily moved along vertical guides. The surface is arranged in a vertical plane (see Sec. 5.3.1) and not perpendicular to the main flow direction, in order to better simulate the interaction between avalanche and buildings;

- a connection between the two parts conceived as a weak point (Fig. 4.2.b): when the impact force reaches a defined limit value, the upper part, conceived as sacrificeable, is detached in order to prevent any damage to the platform in extreme events. For instance, the avalanche of 19th of March 2011 (Fig. 4.2.c) dragged the upper part about 20 m downslope and ripped all the electrical wires. However the lower part and the platform underneath was preserved from damage. After this event the wiring of the sensors system has been modified to allow a fail-safe sectioning in extreme events;

- a sealed electric cabinet (Fig. 4.2.d) that hosts the acquisition and control systems, the terminal of the power supply line and the optical fiber of the data transmission line, connected to the upper station of the Staffal-Gabiet cableway;

- a galvanized steel shed that protects the cabinet from the direct impact of the avalanches and provides also a walking surface to reach the upper part of the obstacle for inspection and maintenance works.

4.2.2   Acting loads

Lacking specific information on the values of the expected forces, since principal object of the research of the site, a design pressure of 50 kPa was assumed, based on simulation done with the AVAL-1D [63] and on the comparison with the pressure of Col du Lautaret (35 kN [200]). Other loading conditions, as gliding action and wind pressure, had been taken into account in the design [21]. In addition geological and geophysical surveys (see Sec. 4.2.3) as well as structural tests, were carried out. In particular a number of tests (see Sec. 4.2.4 and Sec. 4.2.5) were performed at the laboratory of structural mechanics of the Department of Structural, Geotechnical and Building Engineering of the Politecnico di Torino at the beginning of September 2010.

4.2.3   Geological and geophysical surveys

Geological and geophysical surveys were carried out and slope stability was analysed into details [21]. In the obstacle area gravitational deposits of a scree and an alluvial
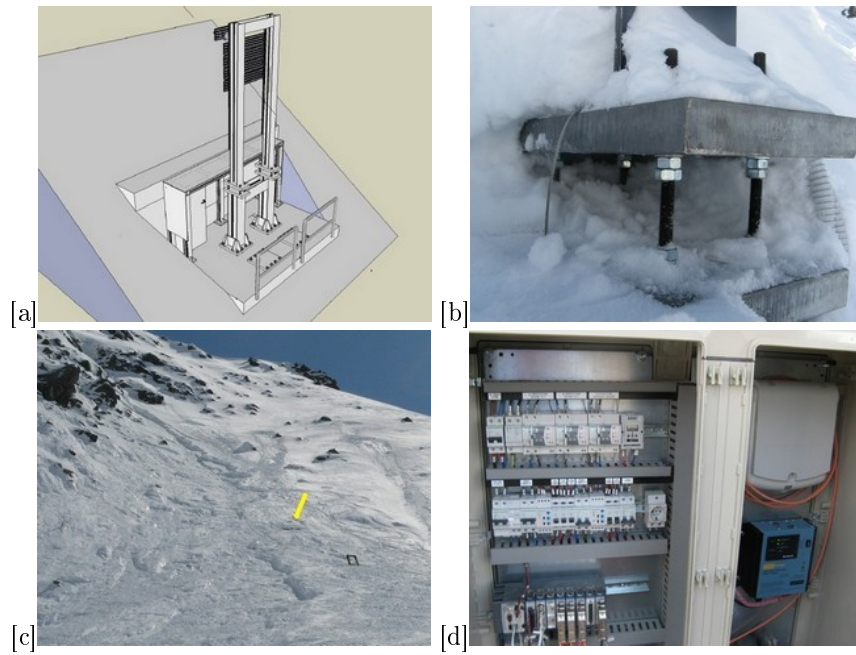
Figure 4.2: [a] Sketch of the platform with the obstacle and the shed behind, from [21]. [b] Detail of the load limiter device linking the two parts of the obstacle after an event. [c] The 19th of March event. The yellow arrow indicates the previous position of the obstacle. The release zone, lower in altitude than the previous events, as well the huge erosion are well visible. [d] Particular of the electric cabinet. Photos E. Bovet.

fan as well as an accumulation of rockfall blocks are observed. The measurements, interpreted with tomographic technique, detected the presence of bedrock, highly fractured and not saturated, only at the sides of the couloir and nowhere else. In fact the stratigraphy of the rock mass is constituted by a layer of detritus deposit, without clay fraction, having a thickness of about 10 m, lying upon a highly fractured and weathered bedrock with poor quality. Besides, although the slope near the obstacle is naturally stable, the debris layer could release shallow landslides when avalanche impact forces act on the ground through the obstacle foundation. The four families of discontinuities identified are very critical for the stability [21].

4.2.4   Dynamical tests

The complete structure was assembled within a specially built testing frame (Fig. 4.3.a, b) in order to place the obstacle in a horizontal position [21].

In particular, experimental modal analysis was performed to assess the dynamic properties of the obstacle. During the campaign 8 acquisitions setup were considered (Fig. 4.3.c), for instance with accelerometers only on a vertical beam (setup "local") or on the plates (setup "plates" Fig. 4.3.b), following the procedures indicated in [14]. In this document the position of the accelerometers (Fig. 4.3.d), the points to be hit by an instrumented hammer (Fig. 4.3.e) and the acquisition procedures (Fig. 4.3.f) are indicated.

The dynamic identification of the structure, in terms of frequencies, shapes and softening modes was done in the time domain. Data were acquired in terms of nodal accelerations on some freedom degrees of the structure, opportunely instrumented.

By the analysis in the frequency domain (Fig. 4.4) two peaks are visible at about 7 and 12 Hz, to which values the lower modes of vibrations of the structure corresponded. Twenty modes of vibrations (the first ones are shown in Fig. 4.5) were identified by [13].

The modes of vibrations found validated the results obtained by Borri-Brunetto and Barpi [21] from numerical analyses, performed with the finite element code AD-INA [2]. However, the identified frequencies found by [13] are lower than those simulated in ADINA, probably due to the impossibility to create an infinitely rigid constraint in laboratory. In fact, the structure was in-built to a deformable support [13].

4.2.5   Static tests

Static tests (Fig.4.7.a) leading to failure of the load limiter device were conducted, simulating different real loading conditions. During the load phase of the structure, occurred thanks to a oleodynamic actuator (Fig.4.7.b), the load was controlled (Fig.4.7.c) and the displacement measured through displacement transducers (Figg.4.7. d,e). Such tests were carried out for different distances of the load limiter plates, i.e.,

Figure 4.3: [a] The obstacle at the testing time in the "global" setup. [b] The supporting structure conceived as a joint. [c] Configuration example for the acquisition: the "plates" setup. [d] Accelerometer. [e] Instrumented hammer. [f] Screen shot taken during the acquisition time. Photos E. Bovet.
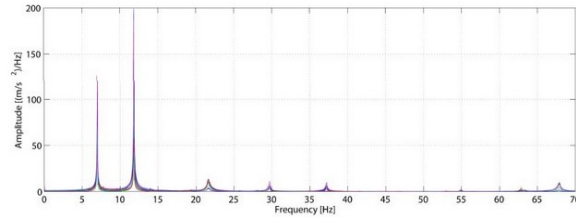
Figure 4.4: FFT of the signal, from [13].

[a]   [b]   [c]
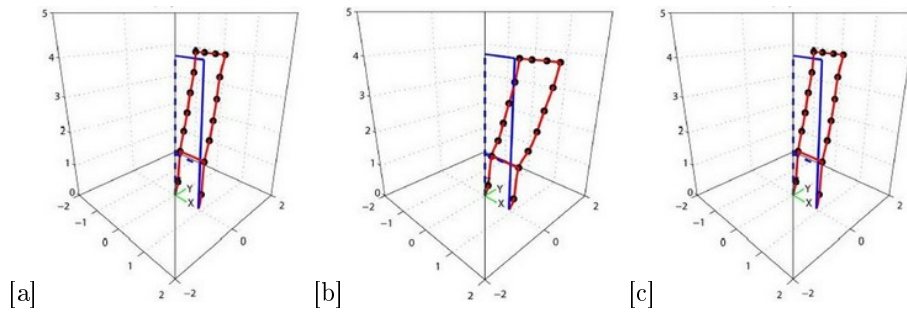
Figure 4.5: [a] Mode 1: bending mode with frequency of 6,9775 Hz. [b] Mode 2: transversal mode with frequency of 7,7201 Hz. [c] Mode 3: torsional mode with frequency of 11,8075 Hz, from [13].

Figure 4.6: First three modes of vibrations, corresponding to the lowest frequencies, obtained through a numerical simulation in ADINA, from [21].

for different length of the steel bars linking the lower and the upper part of the obstacle. The final deformation of the steel bars (Fig.4.7.f), translated in a displacement of the upper part of the obstacle (Fig.4.7.g) was well visible.

Some results are presented in Fig.4.8, where the total load applied by the testing machine on the obstacle is plotted against the relative displacement of the load limiter plates [21].

4.2.6 Instrumentation

The obstacle is equipped with several sensors that measure different parameters [21]:

the impact force: 10 transducers U10M (Fig. 4.9.a) with nominal load of 5, 12.5 and 25 kN and accuracy of 0.2 %, are placed at different heights. After some failures due to overloading occurred during the first operating season, in fact, the nominal range of the transducers in the lower position was increased. To avoid bending moments, the load transducers are connected to the plates with an hinged joint together with a sliding connection. The impact forces are hence directly measured without a processing of cumbersome deformation analysis, as in other test sites [38];

the acceleration caused to the structure itself by the impact: 4 accelerometers were fixed to the upper part of the obstacle, in different positions and orientations (Fig. 4.9.b);

the air temperature: 4 temperature transducers are located on the upper part of the obstacle, at elevations of 0.1, 1.0, 1.9, and 2.8 m above the intermediate flanges;

the atmospheric pressure: 1 pressure transducer is fixed to the upper part of the structure, near its maximum elevation to not be directly hit by the dense core of the avalanche;

the velocity: velocity sensors will be mounted in the next future.

The measured data are temporarily stored in the data logger located on the platform, below the obstacle. Files contain each one 1 s of recording, with sampling frequency of 2 kHz, with the exception of the temperature measurements. They are transmitted thanks to an optical fiber to the PC located in the control room at the Staffal-Gabiet station. After a period of a manual recording procedure activated by an on-site operator or by a remote operator (via Internet), the system is now ameliorated to record automatically data, by a self-activation when a given threshold is attained by one of the signals [21].

Figure 4.7: [a] The static test set-up. [b] Oleodynamic actuator. [c] Screen shot taken during the acquisition time. [d] Displacement transducers. [e] Particular of a displacement transducer. [f] Example of the deformed steel bars. [g] Final displacement of the obstacle tip. Photos E. Bovet.
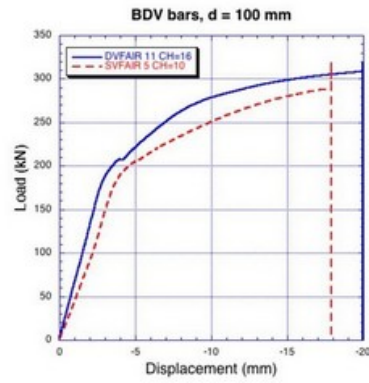
Figure 4.8: Total load vs. relative displacement for left (dashed) and right (solid) load limiter device (distance of load limiter plates equal to 100 mm), from [21].
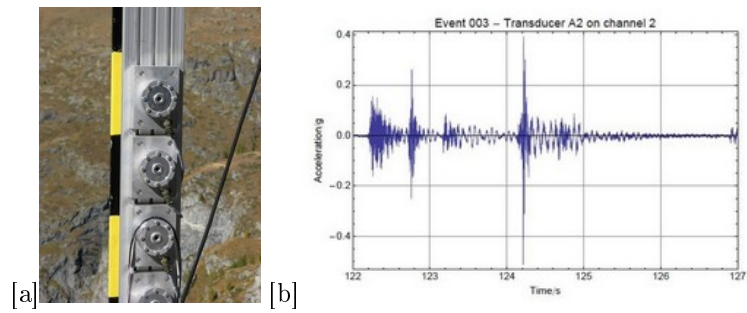

Figure 4.9: [a] Transducers during the installation time. Photo E. Bovet. [b] Example of measurements of acceleration plotted vs. elapsed time, from [21].

Table 4.1: Releases during winters 2009-2010 and 2010-2011.

Date	Triggering method	n° shots
04/12/2009	Vassale	1✓
26/12/2009	spontaneous	
06/02/2009	®Daisy Bell	1 X
20/02/2010	Vassale	2✓
27/03/2010	®Daisy Bell	3✓
31/03/2010	Vassale	2✓
04/04/2010	spontaneous	
05/04/2010	Vassale	2 X
28/05/2010	spontaneous	
1-4/11/2010	spontaneous	
24/11/2010	®Daisy Bell	2 X, 1✓
07/12/2010	®Daisy Bell	1✓
27/12/2010	Vassale	1✓
16/02/2011	spontaneous	
17/02/2011	Vassale	1✓
01/03/2011	®Daisy Bell	2✓
05/03/2011	®Daisy Bell	1X, 2✓
18/03/2011	Vassale	2 X, 1✓
19/03/2011	®Daisy Bell	1✓
20/03/2011	Vassale	5 X, 3✓

4.3 First experiments

During the winter seasons 2009–2010 and 2010–2011, several avalanches (spontaneous and artificial ones) were released at the site, for a total of 14 experiments (Tab. 4.1). The triggering usually performed at around 8:30 am by helicopter using the ®Daisy Bell or the Carica Vassale (Fig. 4.10).

Before and after the avalanche triggering, a laser scanner survey can carried out (see Sec. 5.1.1). A new simple method to evaluate the erosion along the track (straw test) has been developed (see Sec. 5.1.2). During the avalanche motion, videogrammetry (see Sec. 5.1.1) is performed in order to determine, by geo-referencing the scans, the front velocity along the whole track. After the event, a GPS survey of the avalanche outline is made, together with measurements of the snow depth in some points around and within the avalanche deposit and track. Granulometric measurements of the avalanche deposit are also taken [72]. Snow stakes placed in the release zones allow remote snow depth estimation [138].
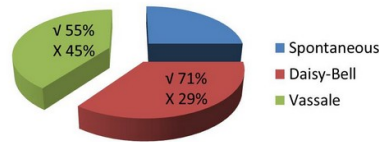
Figure 4.10: Avalanches can be spontaneous or artificially triggered using the ®Daisy Bell or the Carica Vassale. The success percentages are reported.

A detailed survey (density, deposit shape, temperature, analysis of the streamlines and dead zone) in the obstacle area is made. The obstacle placed along the track measures the impact forces of the avalanche flow (see Sec. 4.2).

In the release zone, along or near the fracture line, snowpack properties (density, hardness, humidity, crystal shape and dimension) are measured by digging a snow pit. The slabs were mostly made of partly decomposed precipitation particles (DFdc) with a mean density of 174 ± 100 kg/m^3 and a low hardness (hand hardness index equal to 1). Most of the time, the slabs slid over a thin layer of graupel or over a melt-freeze crust. The stability tests (Extended Column Test) performed show, in almost all the experiments, that the snow cover is classified as moderately unstable. The fracture depth (mean value 34 ± 21 cm) is measured or estimated from below depending on the safety conditions. The mean snow depth is 128 ± 37 cm. The time the avalanche needs to stop in the deposition zone is about 37 ± 14 s [138].

The site is equipped with snow drift sensors in the release area, since winter 2012-2013. In future velocity sensors will be installed too.

For a complete exposition, let note that close to the Seehore test site, near the Gabiet lake, an experimental snowfield was realised on 31th of March 2010 with the aim of analyse the response of snowpack to explosives [98]. 24 charges were separately detonated (Fig. 4.11.a) changing the explosive type (dynamite and emulsion), elevation from the snowpack (on the snow surface, at 0.5 m, 1 m, and 0.5 m below the surface) and quantity of explosive (1, 2 and 3 kg). Passive seismic sensors and sound devices measured energy propagation from blasts on the snowpack and on air, respectively. The geophysical investigation estimated the mechanical properties of the snowpack and detected changes in the snowpack properties (as snow depth and density) before and after the explosion. Finally a survey of the craters (Fig. 4.11.b) was conducted.

In the following the events analysed in Ch. 5 are described.
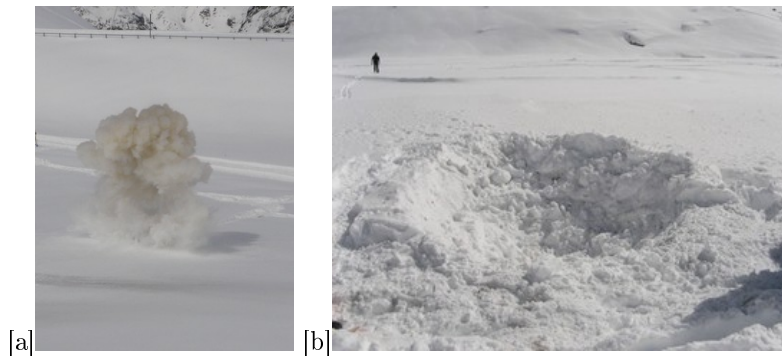
Figure 4.11: Example of [a] a shot and [b] a crater during the 31th of March 2011 experiments near the Gabiet lake. Photos E. Bovet.

4.3.1   Avalanche 27th of March 2010

On 27th of March 2010, three avalanches were artificially released from the helicopter, using the ®Daisy Bell system. The first shot generated a small slab avalanche that flew well confined in the little couloir on the right side of the avalanche path, the second one detached a slab avalanche with a release width of about 40 m, while the third shot released a small portion of the slope above the second release area. They were all dense avalanches. The fracture depth was about 25 cm, slightly irregular along the fracture line, probably due to the wind blowing of the previous days. Field works allowed to record the snowpack structure, showing 25 cm of new snow with a density of 180 kg/m^3 at the surface. The avalanche deposit presented a dual-lobe shape with a maximum deposition height of about 1 m on the left lobe, at an elevation close to 2380 m asl (Fig. 4.1). For a detailed analysis of the erosion and deposition processes see Sec. 5.1.

4.3.2   Avalanche 5th of March 2011

On 5th of March 2011, the helicopter equipped with the ®Daisy Bell system firstly (1) released a small sluff on the right side of the slope and then (2) a small slab avalanche from the top, at 2570 m asl. This slab avalanche showed mostly a dense behavior but also a powder component was well visible. The release zone was about 40 m wide and the crown face depth around 30 cm. The snow height was 107 cm. A small secondary release was triggered by the main avalanche flow at around 2460 m asl on the left side of the main path. The snow density of the surface layer (30 cm thick) was 180 kg/m^3. The avalanche deposit presented a slight tri-lobe shape with a maximum deposition of about 1.4 m on the left lobe, at an elevation of 2380 m asl
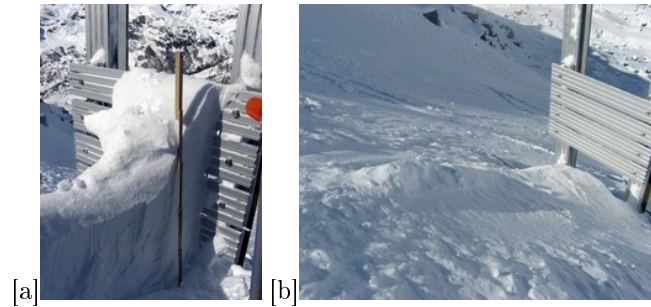
Figure 4.12: [a] A section of the deposit after the 5th of March 2011 event. [b] The deposit after the 1st of March 2011 event. Photos E. Bovet.

(Fig. 4.13).

The particular shape of the snow found upward the obstacle during the event of 5th of March was object of a detailed survey (Fig. 4.12.a), since never before seen. Probably it was influenced by previous deposit, in particular that of the 1st of March 2011 event, that partially fill the space under the bars (Fig. 4.12.b).

In the next the data available concerning the 5th of March 2011 event are shown.

Velocity front

The velocity front is calculated using the images taken with the camera every second, opportunely georeferenced in the software AdHoc [1]. By a localization of the fronts some profiles are calculated (Fig. 4.13). It is important to note that the velocity is calculated in the local reference system, and not in the regional used UTM-ED50, that is a projection. Let note that in the regional system the velocity could is slightly different.

An example of the front velocity is shown in Fig. 4.14. The velocity at the obstacle is evaluated to be between 18-19 m/s (Fig. 4.14). A velocity of 18 m/s will be chosen in the following. Further profiles are reported in Sec. 5.1.1. It is important to underline that these values are representative only of the avalanche front since, generally, velocity decreases in the tail.

A comparison between the values found in the central part of the avalanche with the values found laterally is shown in Fig. 4.15. This shows, as expected, that the velocity decreases with the distance from the central part of the avalanche.
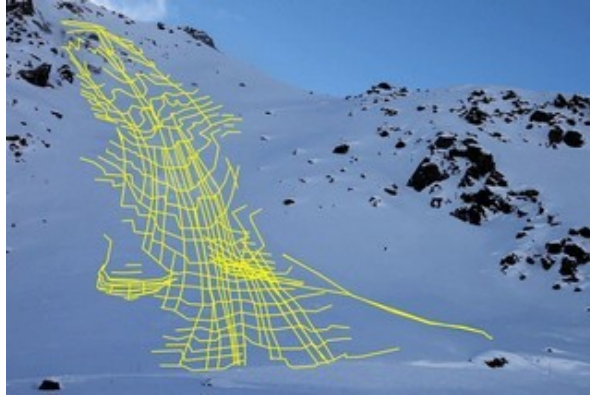
Figure 4.13: Avalanche fronts and profiles calculated of the 5th of March event.
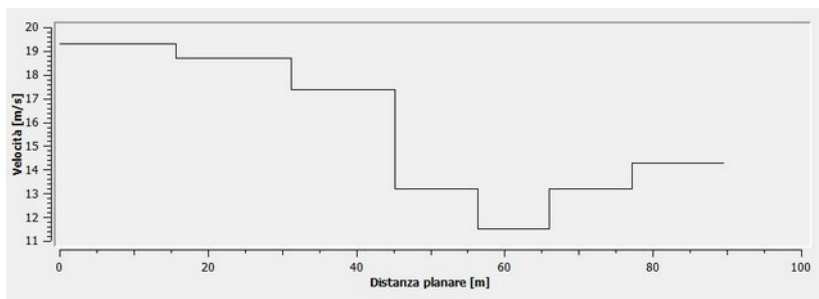

Figure 4.14: Example of the front velocity along a profile involving the obstacle. In particular the impact happens during the second horizontal step.

[a] [b]
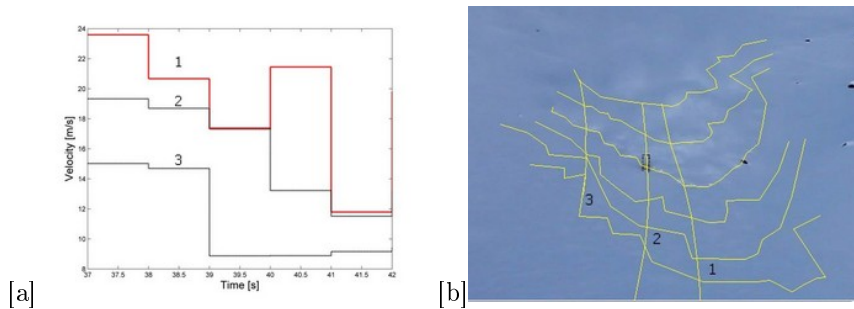
Figure 4.15: [a] The velocities recorded at the same time in the central part (red line) and laterally. [b] The lines along which the front velocities are calculated and the fronts at 37-42 s are shown. The picture is relative to the 39^{th}s.

Pressure

As seen in Sec. 4.2.6 on the obstacle, the forces are measured by load cells. The total impact force is converted in pressure (in particular I acknowledge Ing. M. Borri Brunetto), taking into account that only 6 loads cells worked correctly. The maximum of the pressure, taken with a frequency of 1/2000 Hz, corresponds to 30.7 kPa (Fig. 4.16.a). However, doing an average in time each 0.05 s, 0.1 s or 1 s, this value decreases to 28.7 kPa, 25.4 kPa and to 16.5 kPa respectively. The presence of oscillating peaks probability means that the flow impacting the obstacle has not only the dense component, but the saltation or the suspension layer too.

Since the mean is such variable, we decide to use the characteristic time, i.e. calculated as the ratio between the velocity and the distance of reference. The values of 18 m/s (front velocity at the obstacle impact) and of 1 m (obstacle width) are chosen, giving a time of reference of 0.056 s. Therefore, averaging the pressure each 0.056 s the maximum of pressure is 28.6 kPa.

Density

From a snow pit survey the upper layer in the release area has a density of about 270 kg/m^3 [11]. However, we suppose that the density of the release zone is about 180 kg/m^3, corresponding to the underlaying layer.

No measurements concerning the density of the avalanche flow at the obstacle are available. The oscillation in pressure (due probably to different clusters of snow impact) as well the video, shows that not only the dense core, but a saltation and a powder part impact the obstacle too. These considerations should be taken into account in the density estimation.

[a]   [b]
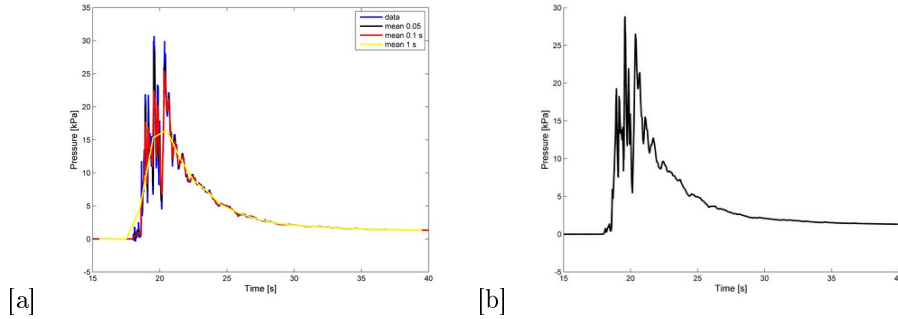
Figure 4.16: [a] Pressure: data, mean each 0.05 s, 0.1 s and 1 s. [b] Pressure estimated with the mean done using the characteristic time of 0.056 s.

Table 4.2: Density values expressed in [kg/m^3] measured upwards the obstacle (in Fig. 4.12.a). H is the height of the snow and D the distance along the slope from the obstacle (see Fig. 4.18).

H **[cm]**	D**=0 cm**	D**=15 cm**	D**=30 cm**	D**=45 cm**
150-140	340	340		
140-130	360	340	340	
130-120	350		350	320
100-90	330		350	
90-80	340	340		

Around the obstacle the density of the deposit is about 320-360 kg/m^3 (Fig. 4.17). Downwards the obstacle, the density was equal to 360 kg/m^3 in the central zone, 250 kg/m^3 behind the supporting structure of the obstacle and 270 kg/m^3 at a distance of about 1.5 m downwind.

From data in Tab. 4.2 the density results almost constant in the obstacle proximity. No trend of augmentation or diminution of the density value with the height or with the proximity to the obstacle is seen. The density decreases only for higher distances D from the structure (Fig. 4.17).

Fig. 4.17 shows even a tongue of about 0.30 m of not eroded snow found until to 1 m upward the obstacle. At a minor distance it opens as a fan. At about 0.55 m upwind the structure the deposit begins to rise along the horizontal bars. In this zone the snow is more compacted, as the density measurements and the hand test confirm.
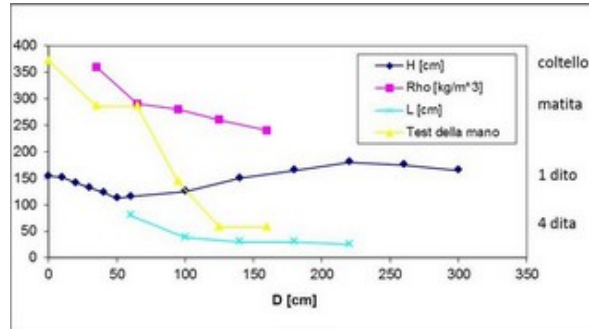
Figure 4.17: Height H of the snowcover, density ρ, hand test (*Test della mano*) and width L of the shape left upwards the obstacle. D is the distance along the slope from the obstacle (see Fig. 4.18).

Figure 4.18: Height H of the snowcover, width L of the shape left upwards the obstacle and distance D along the slope from the obstacle.

Erosion/deposition

For a detailed analysis of those data see Sec. 5.1.

Flow height at the obstacle

As concerns the flow height, from the video images it is possible to conclude that the avalanche is taller than 3 m, since the powder part overlaps the obstacle.

Chapter 5

Analysis of experimental data

5.1 Erosion: different surveys techniques

In this section some of the existing survey techniques, as laser scan, and analytical and numerical models, used to assess and to analyze the snow erosion and deposition processes are used in combination. Moreover, we present a new simple test to assess the net eroded and deposited snow along the avalanche path. We refer in particular to the activities made at the Seehore test site in Aosta Valley, NW-Italy (see Ch.4). This site gives us the possibility of studying small avalanches. We consider more in detail the influence of the site morphology on erosion and deposition processes, as for example the presence of rocks, as well as to explain some results related to the proposed analytical models. We refer in particular to the events triggered on 27th of March 2010 and 5th of March 2011, when laser scan measurements were performed. They were small slab avalanches with release volumes around 300 m^3. See Sec. 4.3 for details on these experiments.

Snow erosion and deposition processes within a snow avalanche flow have been studied in Russia, Norway, Italy, France and Switzerland, with the aid of both laboratory [22] and full-scale test sites, as well as of analytical and numerical models [193]. In the full-scale approach, different techniques are used to evaluate the mass balance of an avalanches. In the beginning, only field measurements concepts were developed. Later, more sophisticated techniques have been used: photogrammetry [191, 207], terrestrial [171] or aerial laser scanning and FMCW radars [107].

5.1.1   Laser scan technique and photogrammetry

Method

In some experiments, before and after the avalanche triggering, terrestrial laser scanner surveys are carried out with a Riegl LMS-Z420 and a Riegl VZ400, in order to get information about the snow erosion and deposition along the track [11, 138]. These estimates are obtained by comparing the digital surface models (DSM) generated from laser scan data of the slope scanned before and after the avalanche release [171].

Moreover, during the avalanche motion, photogrammetry is performed with two Canon 5D cameras, with calibrated lens and fix focal length (24 and 50 mm), in order to determine, by geo-referencing the scans, the front velocity all along the track. Besides the winter surveys, in summer 2009 an aerial laser scanning was made by helicopter, in order to get a summer DEM with a resolution of 50 cm on the z and an ortophoto with a resolution of 10 cm.

In this work, we analyzed the laser scan data of the events triggered on 27th of March 2010 and 5th of March 2011. In particular, we used the data from laser scan to determine the variation of the snow height ($h_\delta = h_2 - h_1$) before (h_1) and after (h_2) the avalanche events. The difference between the snow height after the event and the summer DEM gave information about the spatial distribution of the avalanche deposit. Laser scan detected points each 20 cm with a precision of 5 cm.

Only for the event triggered on 5th of March 2011 also photogrammetry was performed [11]. These data allowed us to obtain additional information concerning the avalanche dynamic, such as for example the avalanche type (dense or powder) and the front velocity. Coupling these information with the laser scan data, some qualitative results on erosion and deposition could be found.

Results and discussion

The difference between the snow height after and before the avalanche triggering are shown in Fig. 5.1.a and Fig. 5.1.b.

Thanks to the laser scan technique an estimation of the deposition volume could be done, being aware of the uncertainty related to the fact that laser scan is able to detect only the net difference between erosion and deposition.

For the avalanche of the 27th of March 2010, for which a volume of about 260 m^3 was triggered, a deposition of 600 m^3 was found: 400 m^3 deposited on the left lobe, 165 m^3 on the right one and 35 m^3 in the zone at an elevation comprised between 2400 and 2420 m asl, where both erosion and deposition processes occurred (Fig. 5.1.a). As in the upper part of the path there were missing data from the laser scan (see Fig. 5.1.a), we supposed that, on those areas, the erosion was equal to 25 cm, that was the amount of new snow measured in the field (see Sec. 4.3.1). The total erosion (including the release volume) was estimated, even if with the approximation explained before, equal
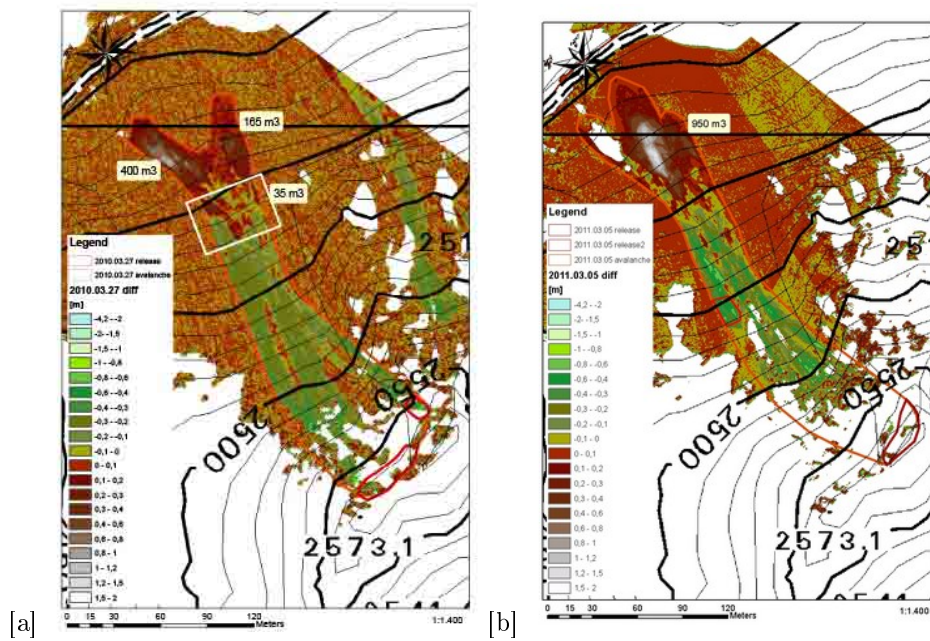
Figure 5.1: Snow height variation h_δ resulting from the difference between the DSMs obtained by the laser scan measurements performed after and before the event triggered on [a] 27th of March 2010 and [b] 5th of March 2011. The areas where data are missing are well visible. See the text for the explanation of the number in the three boxes.

to about 1500 m^3. Hence, the avalanche eroded and respectively deposited a volume of snow 6 and 3 times its release volume. It implies that the final density was 2.5 times the initial one. Unfortunately, we took no density measurements in the runout zone, therefore the previous hypothesis could not be confirmed by field data.

For the 5th of March 2011 a release volume of 200 m^3, plus a secondary release volume of about 115 m^3 corresponded to a deposit of about 950 m^3 in the right lobe (Fig. 5.1.b). Unfortunately, the laser scanning of the area did not include (Fig. 5.1.b) an area of about 400 m^2 in the deposition zone, because the relative inclination to the instrument was not suitable for such measurements [171]. The total erosion (including the release volumes) was estimated equal to about 2200 m^3. As in the case of 27th of March 2010, we included a volume of eroded snow, supposing that the erosion in the area not measured by the laser scanning was equal to 30 cm, that corresponds to the new snow (see Sec. 4.3.2). Hence, the avalanche eroded a volume of snow equal to about 6 times the volume in the release area.

An analysis of the influence of the slope morphology on the deposit was performed too, focusing the attention on the 5th of March 2011 event. In particular, it is clear how the presence of large rocks influenced the avalanche flow creating some deposit upwards them, up to about 80 cm depending on the rocks height. Fig. 5.2 shows the influence of some large rocks on the avalanche flow. From laser scan data we detected the following pattern: 1) some deposition is well visible upwards and above the rock, 2) an area of null erosion/deposition is present immediately downwards the rock, 3) further downslope some erosion is again visible. Rocks on the avalanche path influenced the avalanche dynamics too. The avalanche front position was determined from the georeferenced images taken with photogrammetry. When the flow impacted on a rock, a velocity decrease (Fig. 5.3), a flowheight increase and the creation of a powder component were observed. Instead, the lack of manual surveys did not allow us to state that the areas downwards the rocks, where the net erosion/deposition was zero from laser scan measurements, are related to the presence of the jet formation [108]. Similar to the rocks, the obstacle acted on the avalanche flow, creating a dihedral deposit upwind it [42]. In order to correctly interpret the laser scan data in the next winter manual surveys will be done around the rocks, for instance using the straw test technique (see Sec. 5.1.2).

We also observed how the presence of a former deposit influenced the avalanche dynamics. In particular, for the event of 5th of March, we analyzed the avalanche flow in the area shown in Fig. 5.4.a. In this area, two following waves traveled along the profile f11 shown in Fig. 5.4.a. The first wave went straight and deposited most of the mass at around 2370-2380 m asl; the second wave impacted against the previous deposit and sharply decelerated. Some of the mass deposited along the profile f11 before the previous deposit (in the circle in Fig. 5.5), while most of the mass turned left, eroded some more snow and moved for a longer distance along the profile f10.

By a comparison of the images taken with the camera every second and the laser
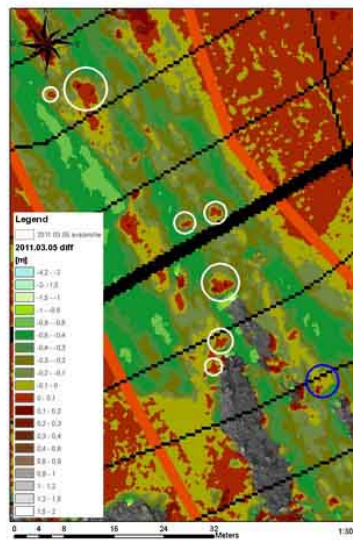
Figure 5.2: 5th of March 2011: height variation h_δ around some large rocks at an elevation around 2450 m slm: upwards the rocks the snow is deposited, immediately downwards the difference is zero and further downslope the snow is again eroded. The blue circle indicates the rocks analyzed more in details (see the text and Fig. 5.3).
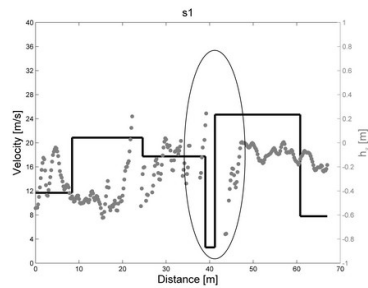

Figure 5.3: Front velocity and h_δ along a profile including the large rock at an elevation of 2470 m asl highlighted in the ellipse (see Fig. 5.2 for its exact location).
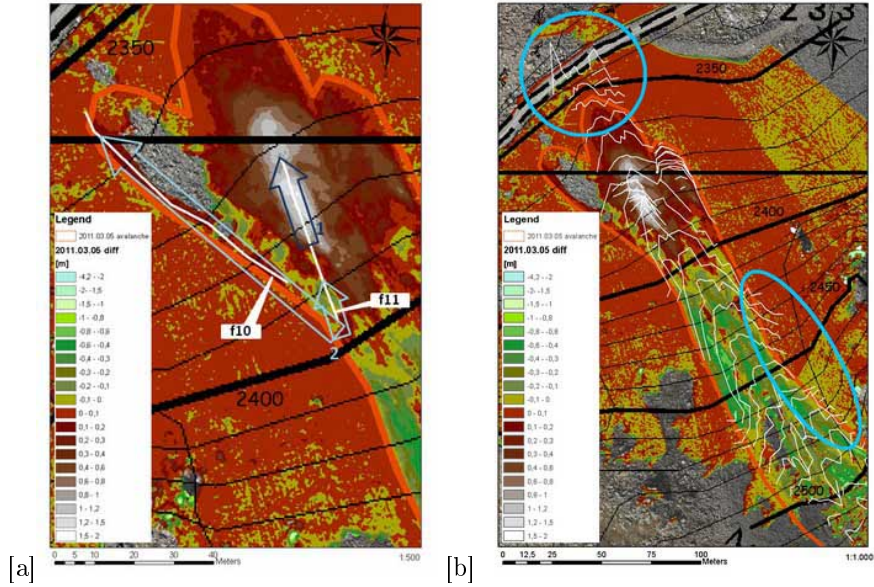
Figure 5.4: 5th of March: [a] deposition zone. The arrows shown the two different waves that flew along the profiles shown in white. [b] Position of the avalanche fronts in different time step. In both figures, the missing data leave see the bottom orthophoto layer. The light blue circles show the area of influence of only the powder part of the avalanche.
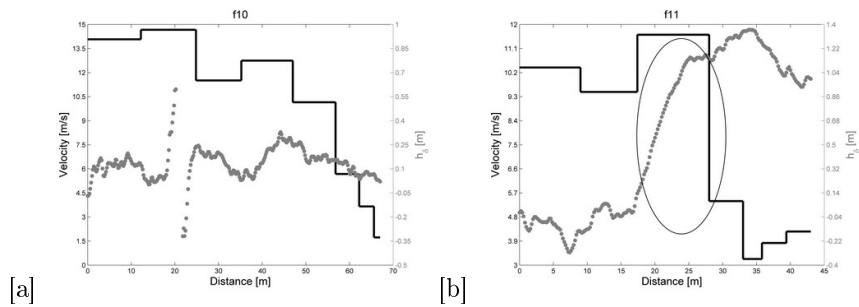
Figure 5.5: h_δ and front velocity of the second wave traveling along the profile [a] $f10$ and [b] $f11$.

[a] [b] [c]

[d] [e] [f]

[g] [h] [i]
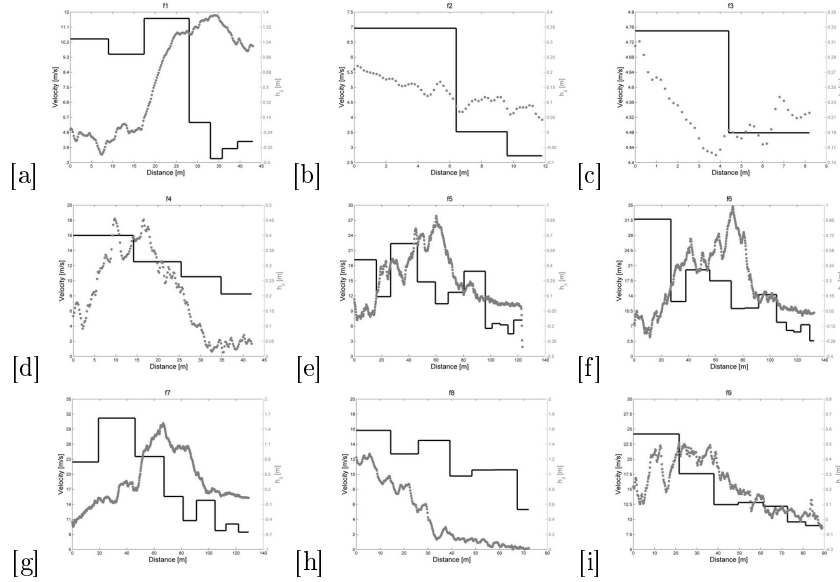
Figure 5.6: Front velocity and h_δ along the three profiles $f1$ to $f9$ shown in Fig. 5.7.

scan measurements, the following remarks were done. Firstly, it is possible to tell that, for instance at an altitude between 2420 and 2480 m asl, as well as in the final part after the dense part stopped, the powder avalanche flews with a width of 5-10 m larger than what it was detected by the laser scan (Fig. 5.4.b). In fact, there were no traces of passage there, both from image analysis and field work. A possible explanation could be that the avalanche was composed by a confined dense core with a wider powder component; this latter neither eroded nor deposited in that area. This behaviour is typical for all mixed avalanches.

Hence, from these results, it seems that erosion and deposition are not only a function of the velocity of the avalanche as in some models is supposed, but depend also on the avalanche type. In addition the variation of the velocity is probably related to the variation of the slope angle: steeper slopes allow quicker flows. Fig. 5.6 show the deposition heights (h_δ) from laser scan and the front velocities from photogrammetry along different profiles in the run-out area of the avalanche, shown in Fig. 5.7. On the right lobe (Figg. 5.6.a,b,c) the velocities are lower (5-7 m/s) than the other avalanche sectors and consequently the avalanche stopped. On the central part of the avalanche path (Figg. 5.6. d-i), the dense core of the avalanche stopped, while the powder part flew longer, leaving a negligible deposit.

From Fig. 5.6 it seems that at a first sharp decrease of the front velocity corre-
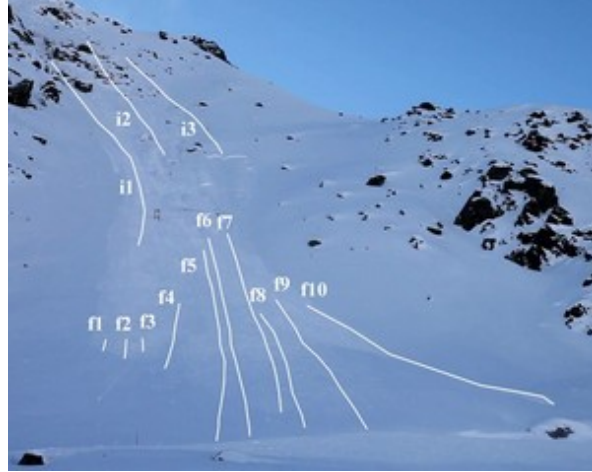
Figure 5.7: Different profiles along which the front velocity was calculated.

sponded to an increase of the value of h_δ, while later on, when the front velocity further decreased, also the value of h_δ decreased. This could be explained with the fact that when the front velocity suddenly decreased, the following flowing mass was slowered down and deposited most of the mass. After this largest deposit only little mass remained available for deposition, consequently h_δ, that in the very last part of the deposition zone can be taken as equal to h_d, naturally decreased. Along the profiles considered on the left lobe, the front velocities were too high to explain the deposit, which therefore occurred in the avalanche tail. Except for the largest deposit that is related to the first sharp front velocity decrease, the deposition, cannot be related to the avalanche front velocity, but must obviously be related to the physical processes that occur in the avalanche tail.

Concerning the snow erosion, we analyzed three different profiles in the first part of the track. We assumed that $h_\delta = h_e$, i.e. only erosion occurred, where h_e is the eroded height. We did not find a dependence of the erosion processes on the front velocity (Fig. 5.8). Let underline that we do dot measure the internal velocity of the avalanche and hence we cannot extend our obtained results for the front velocity to the velocity in general.
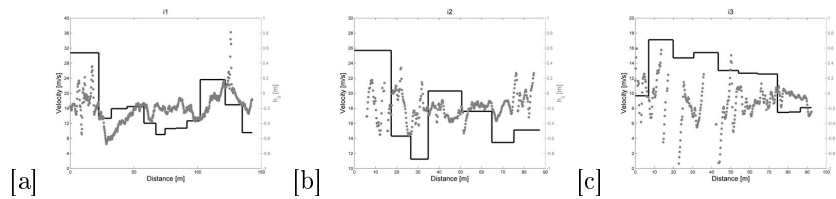
Figure 5.8: Front velocity and h_δ along the three profiles $i1$, $i2$ and 13 shown in Fig. 5.7.

5.1.2 Straw test

Method

The straw test was ideated by E. Bovet and L. Pitet, consultant of the Regione Autonoma Valle d'Aosta, during winter 2010-11, in order to have a simple and cheap method to distinguish, after an event, the avalanche deposit from the undisturbed snow cover and also the eroded and deposited snow along the avalanche path. It is based on the analysis of the numbers and position of plastic straws opportunely placed within the snow cover. Only very cheap materials are necessary: plastic straws of fixed length, a metallic pole with a diameter inferior to that of the straws (for example a wire straightened up) and a resistant thread. The following steps have to be followed (Fig. 5.9):

- join the metallic pole with the thread thanks to an adhesive tape at the point A;

- enumerate the straws by an alphanumeric code XY, with X a letter indicating the position of the test, and Y a progressive number indicating each inserted straw in an ascending order from B to A;

- insert the straws from A to B;

- join the extremities C and A;

- insert vertically the whole system in the snow cover (A at the top and B at the bottom) leaving some straws to come out of the snow cover, which later must be fixed with some snow;

- pull out the metallic pole and the thread, holding the upper straw in one hand;

- repeat the above procedure for more locations along the avalanche path.
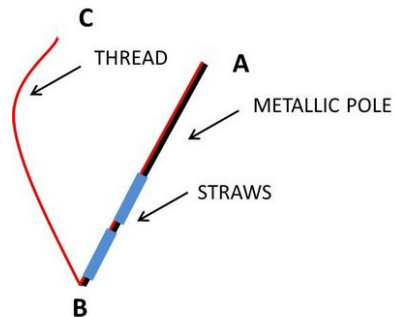
Figure 5.9: The material used for the straw test.

Different variables (Tab. 5.1) must be scheduled at the set-up time, before and after the avalanche, and then analyzed to obtain information about the net eroded and deposited snow along the path. The analysis of the test is based on the amount of new snow (HN) and on the code number of the first straw found near the surface after the avalanche event. After the registration of all the variables (see Tab. 5.1), it is necessary to compare the results with the potential outcomes (see Fig. 5.10) and therefore evaluate the snow erosion and deposition height.

For example, case 2 of Fig. 5.10 means that before the avalanche the amount of new snow do not bury the straws. Since the straw found at the top after the avalanche has a code number j lower than i, it is possible to conclude that: 1) first the avalanche eroded the snow cover until the straw X_j for the height indicated by the red arrow; 2) then it deposited a snow height represented by the green arrow.

Results and discussion

In winter 2010-2011 four monitoring points were used in the proximity of the obstacle (Fig. 5.11.a). We focus the attention on the position A after the 5th of March 2011 event.

After the avalanche released on 5th of March 2011, we found, at the position A (Fig. 5.11.b), the situation n. 7 as reported in Fig. 5.10. At the set-up time two straws of 13.5 cm each, for a total height of 27 cm, were left out of the snow cover. The code number of the top straw was $A12$. The day before the triggering, 30 cm of new snow felt on the previous snow cover (data from the near weather station of the Gabiet lake confirmed in the field). Since the set-up occurred only few days before (the 2nd of March 2011) we can suppose that HN was 30 cm. The wind transport is not considered here. After the avalanche, we found the straw $A11$ on the surface of
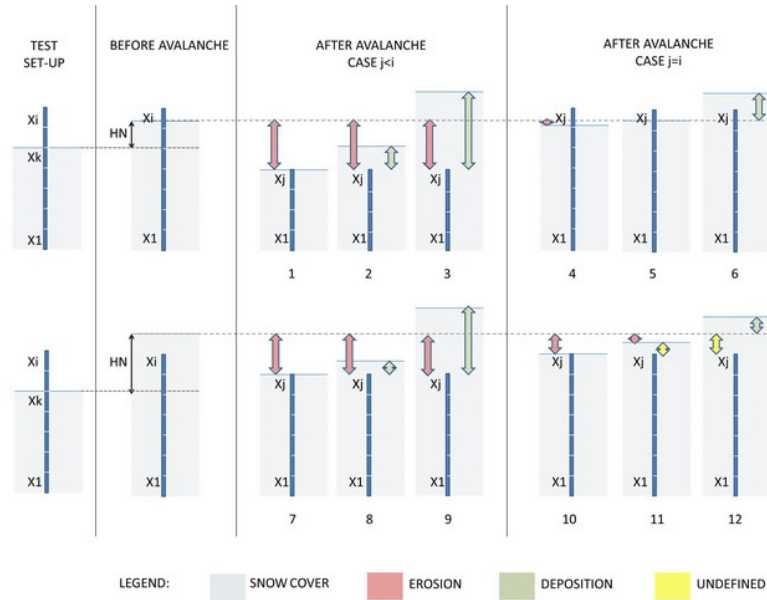
Figure 5.10: Analysis of the straw test in some situations potentially found after an avalanche. See Tab. 5.1 for the description of the variables.
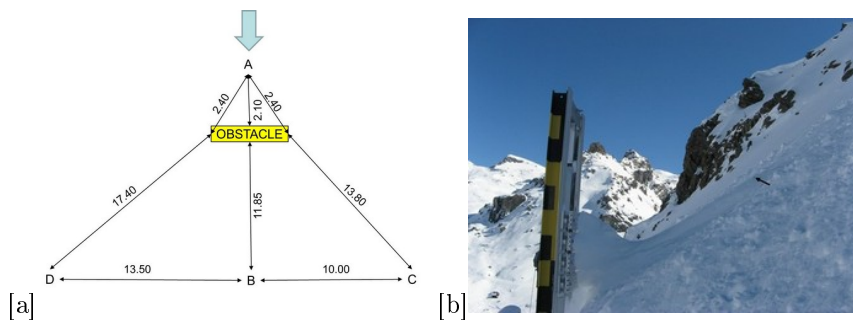
Figure 5.11: [a] Distances of the 4 straw tests from the obstacle (in meters) during winter 2010-2011. The picture is not on scale. [b] Shape of the snow upwards the obstacle after the avalanche of 5th of March 2011. The arrow indicates the location of the straw test A.

Table 5.1: Fundamental variables of the straw test at the three different phases. HN is measured during the snow pit dug after the avalanche event in an undisturbed area close to the avalanche release zone. H_{up} is positive if above the straw, negative if below the straw.

CODE [units]	VARIABLE DESCRIPTION
TEST SET-UP	
X_k [-]	code of the straw at the snow surface
H_k [cm]	snow height from the terrain to the snow surface
X_i [-]	code of the straw at the top
BEFORE the AVALANCHE	
HN [cm]	new snow height
AFTER the AVALANCHE	
X_j [-]	code of the straw at the top
H_j [cm]	snow height from the terrain to the straw at the top
H_r [cm]	snow height from the terrain to the snow surface
H_{up} [cm]$=H_r - H_j$	snow height at the straw at the top

the snow avalanche deposit. This finding means that at point A, about 17 cm of snow were eroded and no deposition processes occurred. Therefore, at least at a distance equal to 2.10 m upwards the obstacle, the shape of the accumulated snow (Figg. 5.11.b and 5.36) was due to the erosion and not to the deposition process. Besides, laterally to the straw A, the snow cover was more eroded, as shown in Fig. 5.36.

We suppose that the particular shape of the snow found until 2.5 m upwards the obstacle was generated by the particular shape of the streamlines of the flow, which were influenced by the presence of the obstacle. In fact, we explain the situation as follow: 1) initially, the avalanche eroded 17 cm of new snow; 2) then, when it felt the presence of the obstacle, the avalanche began to flow following the streamlines as in reported in [42] (see Fig. 5.32 in Sec. 5.3.2), and 3) finally, it continued to erode only laterally in the central dihedral deposit, for a total estimated of 40 cm. This hypothesis is confirmed by the snow crystal analysis and the density measurements [11]. In fact, we recognized partly decomposed precipitation particles (Dfdc) of 1 mm (recorded also at the top of the snow cover in the snow pit dug closed to the release area) at distances upwards the obstacle equal to 160 to 125 cm, and graupel (PPgp) (recorded at 20 cm depth in the snow pit) at distances lower than 95 cm. These data confirm that the snow was eroded at higher distances upwards the obstacle, while the avalanche began to deposit only in the proximity of the obstacle, where a layer of about 20 cm of small rounded particles (RGsr) were found over the graupel. Downwards the obstacle, the density was equal to 360 kg/m^3 in the central zone, 250

kg/m^3 behind the supporting structure of the obstacle and 270 kg/m^3 at a distance of about 1.5 m. Looking both at the shape of the snow left by the avalanche in the area around the obstacle (Fig. 5.36) and at the density values, we concluded that probably the avalanche flew under the bars horizontally placed on the obstacle at the first instants of the impact, compacting the snow just behind the obstacle, and later started to deposit upwards the obstacle. The lateral vertical poles played a role of protection, creating a dead zone of less than 1.5 m immediately downwards, where the snow was less dense.

5.1.3 Analytical models

Method

In this section the data from laser scan concerning the difference h_δ between the snow height after and before the avalanche events of 27th of March 2010 and 5th of March 2011 are used, with the specific aim of evaluating the influence of the slope angle on the deposition height h_d. Since h_δ is the result of both erosion and deposition, the first step consisted on depurating h_δ from the contribution of the erosion h_e, in order to obtain the deposition height given by:

$$h_d = h_\delta + h_e \tag{5.1}$$

To explain the relationship between the deposition depth $d_d = h_d \cos\theta$ and the slope angle θ, we applied two analytical models (the cohesive-frictional and Pouliquen ones), following the approach presented in [194].

The cohesive-frictional model considered the snow cohesion within an avalanche flow when the avalanche moves as a plug, as in the deposition zone or in the wet flows, from head to tail. Cohesion is determined by the continuous contacts between snow particles, which, in the deposition zone, are more frequent due to the plug structure of the flow. Assuming that the gravity force is balanced by a drag force, described with a simple Mohr-Coulomb frictional model with cohesion [168], a characteristic snow height h_d for which the snow stops, can be found:

$$h_d = c/[\rho g(\sin\theta - \mu_c \cos\theta)] \tag{5.2}$$

where c is the cohesion, ρ the density, g the gravity acceleration and μ_c the tangent of the internal friction angle.

The Pouliquen model [169] is based on experimental results which showed how the granular flow stopped with a snow thickness (h_{stop}) corresponding to the clusters size and depending on the slope angle:

$$h_{stop} = L\log[(\tan\theta_2 - \tan\theta_1)/(\tan\theta - \tan\theta_1)] \tag{5.3}$$

[a]   [b]
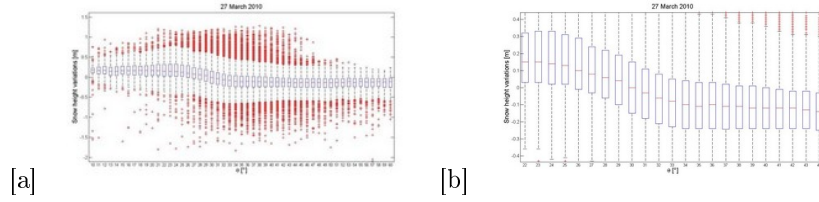
Figure 5.12: Snow height variation found for the 27th of March 2010 avalanche event. The zoom is on the range used for the fit (see text for explanation).


[a]   [b]
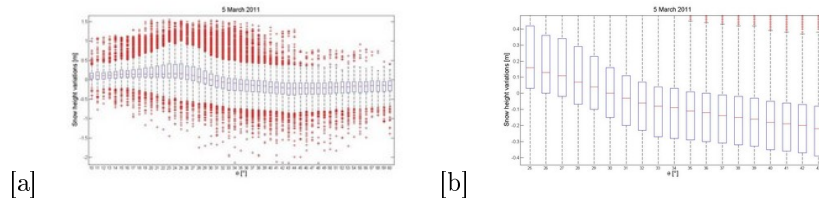
Figure 5.13: Snow height variation found for the 5th of March 2011 avalanche. The zoom is on the range used for the fit.

where θ_1 and θ_2 are slope angles. For $\theta < \theta_1$ no steady flow is possible and deposits of any depth can occur. For $\theta > \theta_2$ the flow cannot rest. $L(= \alpha_p d)$ is a length scale, where α_p is a coefficient, generally comprised between 2 and 8, and d is the particle diameter. The original theory is applied on the flowing zones (and hence in the steep slopes), where the deposit is not contaminated by multiple surges. In this thesis the Pouliquen theory is extended to the deposition too.

Results and discussion

The first step of this analysis was to depurate the laser scan data h_δ from the erosion height h_e. The erosion height h_e was estimated supposing that all the new snow available was entrained. Imaging that on steep slope angles only erosion occurs (Figg. 5.12 and 5.13): h_e was equal to 17 and 26 cm for the avalanche of 27th of March 2010 and 5th of March 2011, respectively (Tab. 5.2). These values were comparable to the values of the new snow measured in the snow pit, equal to 25 and 30 cm, respectively.

The values of h_e were taken constant for the whole avalanche area, which has an altitude difference of only 300 m. The deposition height was then evaluated through Eq. 5.1.

By considering the slope angle at which the majority of the mass is deposited,

Table 5.2: Least square fit of the cohesive-frictional model to the d_d data and of the Pouliquen model to the h_d.

	27.03.10	05.03.11	[194]
Fit range [°]	22-44	25-43	21-33
h_e [m]	0.14	0.22	0.95
c [Pa]	75	88.9	126,143
μ_c [-]	0.33	0.39	0.35,0.36
R^2	0.79	0.88	-
ρ [kg/m3]	300	300	300
L [m]	0.16	0.18	0.31, 0.19
θ_1 [°]	17.6	21.4	21.4, 22.5
θ_2 [°]	41.1	42.6	34.7, 34.4
R_2	0.94	0.99	-
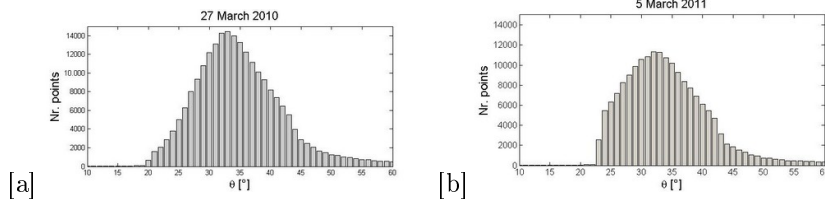
Figure 5.14: Distribution of the number of points in the dataset of h_δ concering the [a] 27th of March 2010 and [b] 5th of March 2011 events.

checked that on those angles the data are enough for significant statistics (Fig. 5.14), we limited the analysis to a specific range of slope angles (Tab. 5.2). Fig. 5.15 shows the slope angle.

Tab. 5.2 also summarizes the results of the least square fit (shown in Fig. 5.16.a), done on the median of the data, of the cohesive-frictional and the Pouliquen models, as well as the values reported by [194] for an easier comparison.

Concerning the cohesive-frictional model, our fit is in agreement with the experimental data, even if for high slope angles the fit accuracy decreases, as reported by [194]. Nevertheless, we expected this behavior because a characteristic of the cohesive-frictional model is that cohesion is supposed to be never null even for large values of the slope angle. The value obtained for c is lower than the data reported in literature. We think that this determination is affected by large uncertainties in the snow density estimation (see Eq. 5.2), which we could not measure. Therefore,
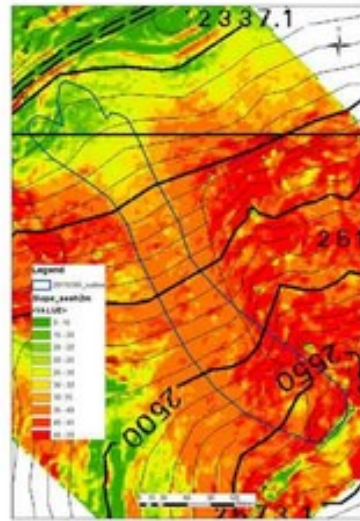
Figure 5.15: Slope angle. The blue line indicates the outline of the 5th of March 2011 event.
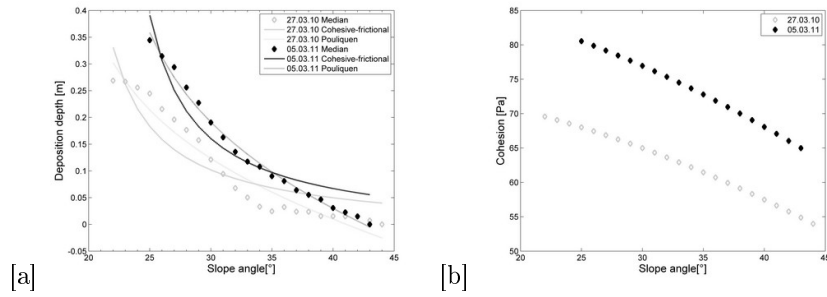
Figure 5.16: [a] Fit of the data to the cohesive-frictional and the Pouliquen models. [b] Variable cohesion at different slope angles.

we analyzed more in details the cohesion. In Fig. 5.16.2 we plotted the values of c, calculated with constant μ_c and ρ (for values see Tab. 5.2), versus the slope angle. Cohesion decreased almost linearly from gentle to steep slope angles. As in [194], we explain this with the fact that cohesive forces have significant effects only when the avalanches move slowly, while on steeper slopes they become insignificant.

In addition, note that if the avalanche density was let variable along the path, increasing from the release to the deposition zone, the cohesion would decrease more rapidly from gentle to steep slope angles. [168] found that cohesion should depend on the snow properties: wet snow results in higher cohesion. However, this statement was not verified in [194] since the snow properties of the two considered avalanches was the same (even if the sliding surface was different), as they were triggered at the same morning, while the cohesion was slightly different (126 Pa and 143 Pa). We think that the different cohesion found at Vallée de La Sionne by [194] is due to the fact that the amount of snow mass involved were different and it should also play a role in the determination of the cohesion. This idea can explain also the fact that for the event of 5th of March 2011, with a release volume of about 310 m^3, we found a higher cohesion than for the event of 27th of March 2011, with a smaller release volume equal to 260 m^3. This theory is however in contrast with [168] that found different values of cohesion for avalanches with similar release volume. A further possible explanation of the low cohesion found, for the two avalanches triggered at the Seehore test site compared to those triggered at the Vallée de la Sionne test site, is that cohesion is related to the size of the avalanche site. Higher cohesion for bigger avalanches might be physically explained by the fact that an avalanche compacts itself while sliding down a slope; hence, more time it runs more cohesive it becomes. However, this is contrast with the experiments by [168], for which a very little cohesion should be recorded in coherence with this theory, while they found a spread interval of higher values. Hence, we conclude that cohesion depends both on the avalanche volume, the test site size and snow properties. Let underlines, however, that our data are not directly comparable with those of the Vallée de la Sionne, since [194] excluded the area where the deposit was presumably built up by overrun of successive waves.

Concerning the Pouliquen model, we found a good fit, shown in Fig. 5.16.a. If we consider $d = 10$ cm as estimated by [72], the value of α_p is in the correct range. We found higher values of θ_2 than those reported by [194]. It might be related to the size of the avalanches. In fact, a small avalanche, as in our case, can generally show a steady flow conditions on slope steeper than those where a larger avalanche flows.

Fig. 5.17 show a particular result that we found for the avalanches analysed: a relationship between the deposition height and the variation of the curvature. It seems that a maximum in the deposition height occurred where there is a variation of the slope of the line fitting the slope angles, that physically corresponds to the curvature. Moreover, the ratio between the variation in slope $\Delta\Psi(z_i)$ of the linear fit at the altitude z_i where the maximum deposition $H_{snmax}(z_i)$ occurred, and $H_{snmax}(z_i)$ is
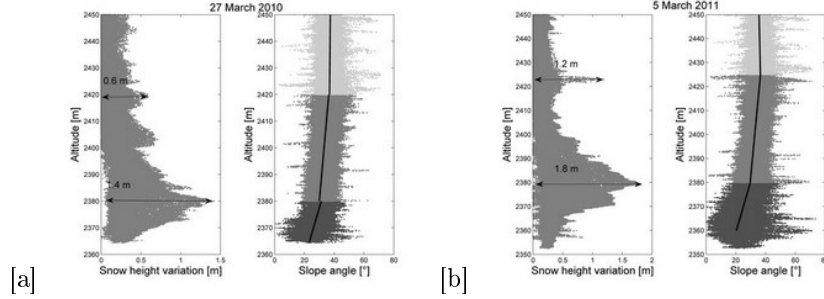
Figure 5.17: [a] 27th of March 2010 and [b] 5th of March 2011: relationship between the maximum of snow deposition height ($h_d = h_\delta + h_e$) and the curvature.

Table 5.3: Ratio $\Delta\Psi(z_i)/H_{snmax}(z_i)$ [°/m].

Event	z_i	$\Delta\Psi(z_i)[°]$	$H_snmax(z_i)$**[m]**	$\Delta\Psi(z_i)/H_{snmax}(z_i)$ **[°/m]**
27.03.10	2380	18.5	1.4	13.0
27.03.10	2420	8.0	0.6	13.6
05.03.11	2380	16.3	1.8	9.2
05.03.11	2425	10.8	1.2	9.1

almost constant (see Tab. 5.3).

5.1.4   Avalanche dynamics simulations

Method

We used the module avalanche of the program RAMMS developed by the WSL-SLF of Davos (CH) to simulate the two considered events. See Sec. 1.2.3 for the model details.

Results and discussion

The simulated avalanches of both the triggered events of 27th of March 2010 and 5th of March 2011 matched well with real data. The input data are reported in Tab. 5.4.

Parameters as fracture depth, height and density of erodible snow were chosen according to field measurements and observations. The values related to the random kinetic energy (generate, decay and R_0) were chosen according to the available literature [65], taking into account the snow temperature recorded in the snow pits. In this

Table 5.4: Input parameters for the two considered avalanches.

	27.03.2010	05.03.2011
fracture depth [m]	0.25	0.3
release volume [m^3]	233	204
density [kg/m^3]	400	400
μ_0 [-]	0.6	0.7
ξ_0 [m/s^2]	2000	2000
e_f [-]	0.6	0.75
H_e [m]	0.25	0.6
ρ_e (kg/m^3]	180	180
generate	8	8
decay	1	1
R_0 (kJ/m2)	1.5	1.5
DEM res (m)	2	2
grid res (m)	2	2

section, we compared the output of RAMMS with the estimation of the eroded and deposited volumes resulting from the analysis of the laser scan data. We also made some spatial comparison between the output of RAMMS and the laser scan data h_δ . In the analysis of the laser scan data, we kept in mind that the laser scan technique gives information only on the net difference between erosion and deposition, but it is not able to determine the real erosion and deposition heights. This means that it is not able to describe exactly the areas where both erosion and deposition occur. Then, we first subtracted the eroded snow from the deposit as calculated by RAMMS and simply visually compared these values (called $h_{\delta RAMMS}$) to h_δ from the laser scan measurements. As the outputs of RAMMS are along the perpendicular direction to the slope, we divided them by cosθ where θ is the slope angle. Considering the 27th of March 2010 avalanche, $h_{\delta RAMMS}$ presents the area with the maximum negative values between 2450 and 2370 m asl with most of the values between -20 and -30 cm. From laser scan, h_δ presents the area with the maximum negative values above 2410 m asl with values between -20 and -30 cm. Concerning the 5th of March 2011 avalanche, $h_{\delta RAMMS}$ presents the area with the maximum negative values between 2460 and 2370 m asl with most of the values between -20 and -40 cm. From laser scan, h_δ presents the area with the maximum negative values between 2460 and 2410 m asl with values between -20 and -40 cm. Also the maximum values, though not so significant as localized on very small portions, were consistent: -60 cm for RAMMS and -65 cm for the laser scan.

As concern the erosion law, from the laser scan and photogrammetry, we did not
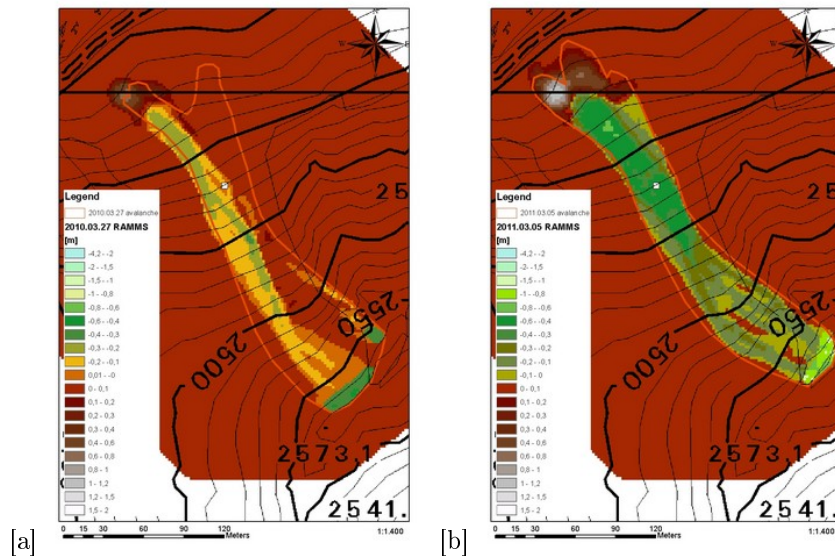
Figure 5.18: [a] 27th of March 2010 and [b] 5th of March 2011: net difference between erosion and deposition as determined by RAMMS. The orange line indicates the real avalanche contour as detected by laser scan.

find a dependence of the erosion with the front velocity. However, this is not in contrast with the RAMMS modeling of the erosion, since there the erosion rate and the velocity of the flow are considered and not erosion height and the front velocity. In addition to be able to reproduce the two events, we must use values for e_f lower than 1, since the erosion is supposed not only frontal but basal too. Hence the velocity of the avalanche body plays an important role and not only the frontal one. For both events, the shape of the eroded areas were quite similar, while the shape of the deposits were slightly different. In particular, RAMMS was able to reproduce the tri-lobe shape of the event of 5th of March 2011, but not the dual-lobe shape of the event of 27th of March 2010. As concern the deposition height, in the deposition zone we compared the laser scan data h_δ (Fig. 5.1) to the net erosion/deposition as determined by RAMMS ($h_{\delta RAMMS}$) (Fig. 5.18).

The erosion at the obstacle measured by RAMMS is 42 cm as Fig. 5.19.a shows. Let note that by the analysis of the entrainment rate (Fig. 5.19.b) the avalanche erodes more in its head than in its tail.

We also plotted the snow depth as simulated by RAMMS versus the slope angle (Fig. 5.20), checked that on those angles the data are enough for significant statistics,

[a]   [b]
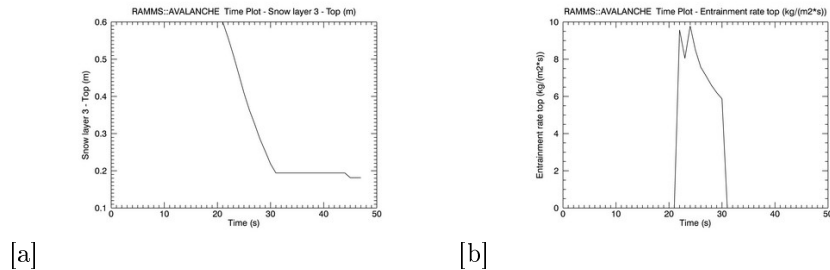
Figure 5.19: [a] Snow layer top and [b] entrainment rate at the obstacle.

[a]   [b]
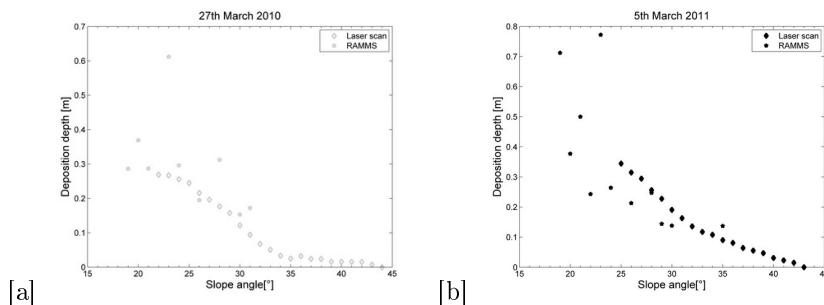
Figure 5.20: [a] 27th of March 2010 and [b] 5th of March 2011: deposition depth determined by laser scan and RAMMS.

similar to what we did for the laser scan data in Fig. 5.16. The higher values found in RAMMS at lower slopes are in the range of the experimental data found (Figg. 5.12 and 5.13).

For the 27th of March 2010 $h_{\delta RAMMS}$ presents the maximum deposit of 65 cm at an elevation of 2360 m asl, while h_δ has a maximum of 1 m at 2380 m asl. For the 5th of March 2011 $h_{\delta RAMMS}$ presents the maximum value of 1,1 m at an elevation of 2360 m asl, while h_δ has a maximum of 1,4 m at 2380 m asl. For both events, the areas where h_δ and $h_{\delta RAMMS}$ are larger differs in altitude, being the former at a slightly higher elevation than the latter. We explain this fact with the presence of previous deposits, that influenced the terrain inclination, making it flatter, and retarded the avalanche flow, that therefore deposited (Fig. 5.21). These previous deposits could not be included in the simulations, thought RAMMS has this possibility, as we did not have information of their volumes. These previous deposit influenced also the
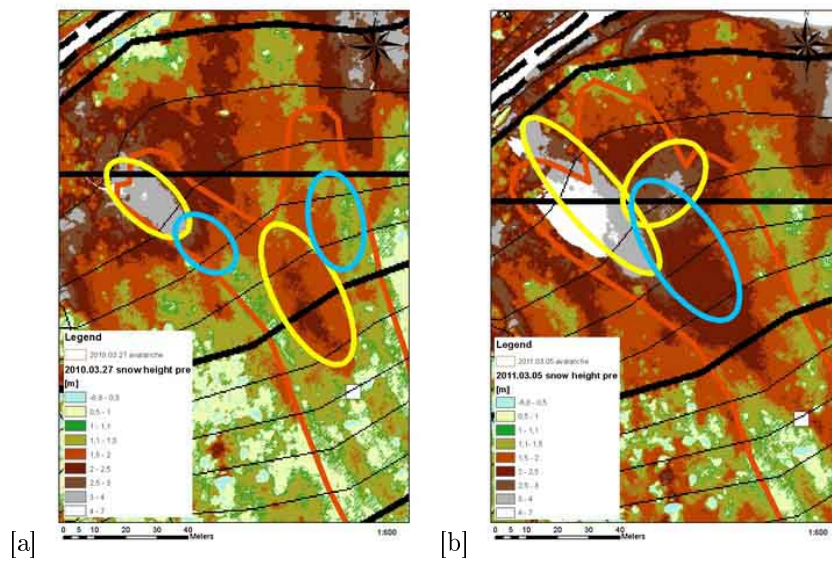
Figure 5.21: Snow height at ground before the triggering of the avalanches on [a] 27th of March 2010 and on [b] 5th of March 2011. Some older deposits are well visible (yellow ellipses). The blue ellipses indicates the location of the maximum deposits as measured by laser scan.

direction of the avalanche flows. In fact, due to a previous deposit, the real avalanche triggered on 27th of March 2010 split in two arms, while the simulated avalanche, running on the summer DEM, went straight (see Fig. 5.18.a). The real avalanche triggered on 5th of March 2011 did not follow the natural shape of the terrain that turns a bit on the left, but went straight, while the simulated avalanches, running on the summer DEM, turned left (see Fig. 5.18.b). However, as concern the deposit volumes, RAMMS matched well the data: 650 m^3 for the 27th of March 2010 and 900 for the 5th of March 2011, compared to the 600 m^3 and 950 m^3 of the two events measured by laser scan.

5.1.5 Comparisons

In the previous sections we showed and discuss the results obtained by each single method, while the aim of this section is to compare them. Firstly, in Fig. 5.22 we report the positive and negative findings of each method, together with the encountered problems and possible solutions. The last column of Fig. 5.22 indicates to which other methods the examined technique can be compared, as not all of them can be cross-compared.

For example, a comparison between the straw test and the results of the analytical models makes no sense. In fact, the former gives punctual information, that are for sure affected by the local morphology or, as in our case, by the presence of the obstacle, while the latter give results in term of the median values. The straw test could be compared with the results of the simulations, only in the case where it is representative of a large area. In our specific case, the straw test felt the effects of the obstacle, not represented in the simulations, and thus a comparison has no sense for that avalanche. Actually, in its first use, the straw test had the specific aim exactly of analyzing the avalanche interaction with the obstacle, therefore on 5th of March the straw tests were placed only around the obstacle. If more tests were placed along the avalanche path we could be able to spatialize the information about the net eroded and deposited snow and compare it with the simulations outputs. From a theoretical point of view, the straw test could be compared with the laser scan, but it is difficult to determine with precision the location of the straw test on the surface scanned by laser scan. Concerning the comparison between the laser scan and the straw test, we want to underline the fact that only the straw test, even if punctually, is able to give information about the net eroded and deposited snow. As an example, in the situations 2,8 (and 3,9) of Fig. 5.10 for the laser scan only erosion (deposition respectively) occurred, while the straw test is able to give information of both h_e and h_d.

The only possible comparison at the same scale is between the laser scan measurements and the simulations, which give results spatially distributed. Here we report the general conclusions of the comparisons already described in details in pre-

Technique	Advantage	Disadvantage	Problems	Possible solutions	Comparable to
Laser scan and photogrammetry	Measure of the whole avalanche area	Expensive No information on the net eroded and deposited snow	No measurement of the release zone, no data in a zone within the deposition area and behind rocks	Use a powerful instrument from the opposite slope or use it in combination with aerial photogrammetry on the release zone and on the hidden zones	Simulations
Straw test	Cheap Direct measure of the net eroded and deposited snow	Punctual measures and limited number of measures	Each location requires time for the set up and for the retrieval	Increase the number of the locations Preparation of the straws at home and use of a compass or Recco devise to speed up the retrieval	
Analytical models	No costs	No representation of the variability of the snow deposit	Solutions depend on the initial condition	Use of more refined statistical methods	Simulations
Avalanche dynamics simulations	Quick Flexibility in the time of the analysis (not real time analysis) Good results for deposition volume	No good representation of the erosion in the release zone and in the first part of the track	Difficulties to find correct parameters to match both the snow deposit and the avalanche velocity		Laser scan, Analytical models

Figure 5.22: Comparison among the different methods to assess erosion and deposition for the avalanches triggered at the Seehore test site.

cious sections. In general, the net difference between erosion and deposition could be compared, as well as the localization of the areas where the maximum erosion or deposition occurred. We could explain how previous deposits detected by the laser scan measurements influenced the real avalanche flow, which took different direction than the simulated one, running on the summer DEM.

In order to confirm the goodness of the laser scan measurements, the measures of the snow height taken manually with a snow probe after the events were compared with the snow height obtained by the difference of the DSM of the post event minus the summer DEM. We found good agreement between those data; the error, estimated of about 20%, is probably related to the error on the localization of the points with the GPS. In fact the GPS error was of about 10 m for the event of 27th of March 2010 and of 8 m for the event of 5th of March 2011. Another comparison we did is between the analytical models and RAMMS. The cohesion-frictional and the Pouliquen analytical models, as well as RAMMS, describe (Figg. 5.16.a and 5.20) the deposition height as inversely related to the slope angle. This fact means that an avalanche travels for longer distances when the flow height is large, reaching area characterized by lower slope angles. This is due to the fact that the Coulomb friction changes within the avalanche flow. The Coulomb friction is defined as the ratio between the shear stress S and the normal stress N [168]. In fact it is well-known as the runout distance depends essentially on the Coulomb friction μ: the higher is μ the shorter the avalanche run out distance is. The observations showed a distribution of the deposit along the slope, which can be explained only with a variable μ, higher at the tail than at the front. The cohesion-frictional, Pouliquen and RAMMS models consider all this fact. For the cohesive-frictional model the Coulomb friction $\mu = (\mu_c + cN)/N$. Note, in fact, that $c = dS/dN$ and not directly S/N as in the Pouliquen model. From experimental measures [168] μ is inversely related to N, i.e. it is inversely related also to the flow height. Therefore, the deposits are higher at lower slope angles and smaller for steeper slope angles. In the Pouliquen model [169], μ is a function of the flow height h and the velocity u. In particular $\mu \to \tan\theta_1$ for high values of h (when $h \to \infty$), while $\mu \to \tan\theta_2$ when $h \to 0$. The relationship $\tan\theta_1 < \tan\theta_2$ implies that the maximum deposit presents a lower Coulomb friction and it is found at lower slope angles. Smaller deposits are related, conversely, to a higher Coulomb friction and thus the mass can stop at higher slope angles. Finally, in the RKE model in RAMMS, the Coulomb friction μ depends exponentially on the Random Kinetic Energy R and varies within the avalanche flow [30]. At the avalanche front R is higher than on the tail therefore the Coulomb friction is lower than on the tail. R is a direct function of the flow height h. Therefore, as thicker flow heights are typical of the avalanche front that travels longer due to a lower friction, the thicker depositions are found at lower slope angles.

Further improvements and conclusions

The first analysis of the data we obtained at the Seehore test site in its first operational seasons highlighted some deficiencies and suggested possible improvements we need to made both on data collection and analysis. Concerning the straw test, in order to speed up the retrieval of the straws, a compass will be coupled to the meter, a distance measuring laser devise or a RECCO system will be used. Moreover, the number of monitoring points will be increased in order to better describe the zones where both erosion and deposition occurs and where the deposition is prevalent. This will help in evaluating if the assumption, used in the analytical models, of an uniform erosion everywhere is correct. Finally, from the analysis of the data recorded in the first years of experiment, in order to avoid this problem of i=j when some information are lost (Fig. 5.10), results that it is not enough to add at the set up time an adequate number of straws, because the wind action smoothes the surface and covers the straws. In the next winter a more rigid structure will be used at the place of the straws in order to not build a pile of snow to sustain the straws. The idea is to use materials having an higher diameter (i.e. the electrical pipes) superposing different colors. In this way, using a binocular it would be possible to check the true quantity of snow HN and how many straws are out of the snowcover before an event. Hence, the uncertainly due to the variability of the snow depth distribution in this slope will be overcome. Furthermore, the straw test will be used around the rocks, in order to estimate the dead zone created upwards and downwards them. These data could be used to evaluate if the theory proposed by [92], concerning the effect of dams on avalanche flows, applies also to rocks, and if the shape of the deposit upwards the rocks corresponds to a dihedral deposit [26].

Future work will focus the attention on the new interesting findings concerning the possible dependency between deposition height and slope curvature. Moreover, we would like to check if a similar pattern is visible in other test sites with different morphology and size, in order to tell if this fact is related to the characteristics of our test site or if we might find a general parametric law.

In addition, an experimental investigation of the relationship between cohesion and slope angle will be done during winter 2012-2013 using a shear box [20]. This instrumentation, in fact, is conceived for the study of the normal and tangential stress of the snow at rest. From these measurements the cohesion can be calculated by using the well-known formula knowing the shear stress and the normal stress [168]. Since we concluded that cohesion might depend on both avalanche volume, test site and snow properties, we think that a non-dimensional approach to the problem, for example by dividing the results by a factor dependent on volume, size and density, would probably find a general low for the cohesion.

Concerning the simulations, as in the next seasons we will be able to scan the slope entirely, including the release area, we will use the DSM generated from the laser scan before the event as input to RAMMS. This will allow us to consider the

influence of eventual previous deposits on the avalanche dynamics.

To conclude we presented different methods to approach the topic of snow erosion and deposition processes. In particular, we showed the potentiality of the new straw test to measure the real eroded snow in small avalanches. The combination of the straw test and the laser scan technique could probably help extending the punctual information of the straw test to a larger area. Thanks to the laser scan data, we showed that the dependency between the deposition depth and the slope angle can be explained by both a cohesive-frictional model and the Pouliquen model. We also showed how the RKE model in RAMMS is able to simulate erosion and deposition for avalanches of only about 200-300 m^3 including a variable friction along the avalanche. In general, we highlight the importance of combining different methods to study snow erosion and deposition processes in small avalanches.

5.2 Study of the avalanche dynamic: RAMMS application

In this section the results of the simulations are compared with the measurement in the field (see Sec. 4.3.2), not only concerning the erosion/deposition processes as in the previous Sec. 5.1.4, but also analysing the dynamical quantities (i.e. velocity, pressure...).

Runout distance

The runout distance calculated in RAMMS describes correctly the real event. In particular it is able to reproduce the three lobes of the deposit, as Fig. 5.18.b shows.

True Flow height at the obstacle

The maximum value of the dense part (true flow height) is 1.1 m (Fig. 5.23.a), while the maximum of the height of the powder part is 5.7 m (Fig. 5.23.b). Using formulae in Sec. 1.7.2, at a height of the dense part of 1.1 m corresponds a saltation layer of 1.8-5.4 m thick and a powder layer of h_p=0.75 m, since $l_{track} = 230$ m. Therefore the data obtained in RAMMS are compatible with the real observations and with the European recommendations [117].

Velocity

Velocity at the obstacle. The maximum of the velocity measured at the obstacle is 13.1 m/s, underestimating the real measurement. RAMMS allows to calculate,

[a]   [b]
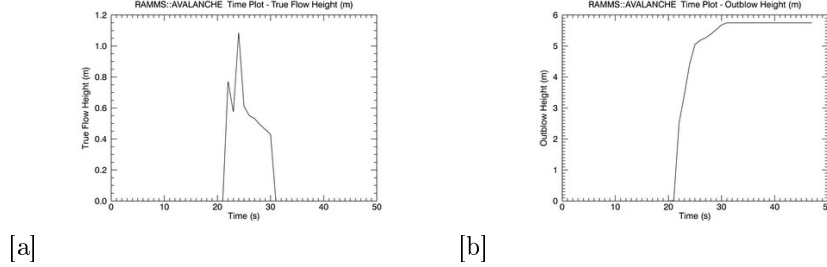
Figure 5.23: [a] Variation of the height of dense flow [b] and of powder part at the obstacle.
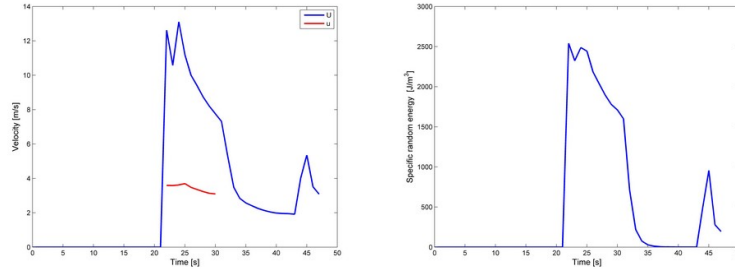
Figure 5.24: [a] Resultant velocity U and fluctuation velocity u obtained by dividing by $\cos(37)$ and [b] random kinetic energy at the obstacle.

through the Random Specific Energy $\hat{R}_\rho$ (having a maximum of 2541 J/m^3), the velocity fluctuations $u = \sqrt{\frac{2\hat{R}}{3\rho}} = 5.8$ m/s (with a mean value of 5.4 m/s). Therefore the velocity can vary in the range of 13.1 ± 5.4 m/s, that is between 7.7 m/s and 18.5 m/s, in agreement with the field measurements.

Front velocity. Fig. 5.25 shows an example of the RAMMS velocity along a profile. In particular the maximum velocity estimated by RAMMS is compared to the front velocity measured by photogrammetry. The velocity of the final part of the selected profile is associated to the powder part. Hence, the experimental data show a higher value (corresponding to the saltation and suspension part), while RAMMS well represents the dense part that has a velocity decay since it is depositing.
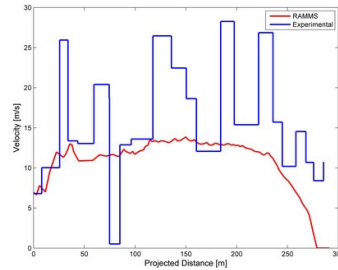
Figure 5.25: Front velocity in experimental data and maximum velocity in RAMMS along a track.


[a] [b]
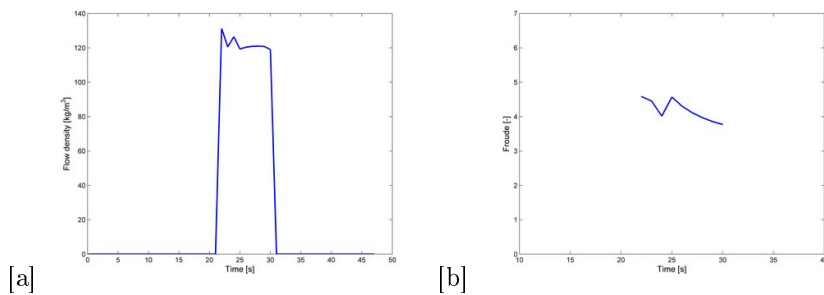
Figure 5.26: [a] Density and [b] Froude number at the obstacle.

Density

The maximum density value at the obstacle is 131 kg/m^3 and its mean value is 122 kg/m^3 (Fig. 5.26.a). Those values are compatible with the considerations experimentally made, considering not only the dense component but the saltation and suspension parts too.

Pressure at the obstacle

The classical relationship Eq. 1.41 is used to relate the pressure with the variation in time of the density (Fig. 5.26.a) and of the mean velocity U (Fig. 5.24.a). The obtained pressure is shown in Fig. 5.27 with a maximum of about 3.4 kPa (the continuous blue line). The pressure is calculated considering the contribution of the velocity fluctuations too (the dotted blue lines).
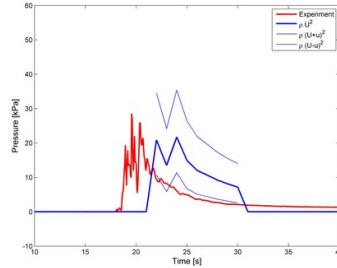
Figure 5.27: Pressure calculated in RAMMS with the mean velocity (continuous blue line) and with the fluctuations (dotted blue line) compared to the experimental pressure (red).

The duration of the impact is 9 s, that is comparable to the recorded values. Let note that since $Fr \geq 1$ (in particular it is $4.7 \leq Fr \leq 5.7$) (Fig. 5.26.b) the hypothesis of using the classical formula without the contribution of the hydrostatic pressure is correct. Since the avalanche in RAMMS does not take into account the obstacle, there is not deposition upwind the obstacle. Hence RAMMS is not able to describe the residual pressure experimentally recorded, probably due to the dihedral shape formed upward the structure. A model to consider this aspect is described in Sec. 5.4.2.

Erosion/deposition process

For a detailed analysis of those data see Sec. 5.1.4.

5.3   Interaction avalanche-obstacle : COMSOL application

In this section we want to compare the simulation results with the data collected at the P.ta Seehore test site, and in particular with the experiment surveys done on the 5th of March 2011 event. The model is in its two-dimensional version in the slope plane (see Sec. 3.1.2). For this reason the obstacle can be reduced to a rectangle. As input of the programme some information are needed: the density, the viscosity and the velocity impacting the obstacle.

As the density concerns, firstly a value equal to 270 kg/m^3 was considered, equal to the density measured in the upper layer in the release area [11]. However, examining the video recorded, at the obstacle the avalanche has a suspension/saltation layer too

(see Sec. 4.3). Consequently, this value has to be diminished, as explained in the detail later.

Another important input for the model is the velocity of the incoming avalanche. To obtain velocity data the photogrammetry method is used (see Sec. 4.3.2 and Sec. 5.1.1). In particular, the flow impacts against the obstacle with a velocity of about 18 m/s. Consequently, on the right edge of the calculus domain, the velocity of 18 m/s is imposed for the entering flow. An open slope condition is imposed on the other domain boundaries, allowing the avalanche to expand outside the domain. Finally a slip condition is imposed on the obstacle.

The last input of the programme is the dynamic viscosity of the avalanche. This value cannot be measured directly in the field. In the literature its value can vary depending on the rheological law used, as summarized in [49], and which part of the flow is considered (shear layer at the base or plug flow above). In [46], for instance, it was estimated by a back analysis of the pressure derived by the damages analysis. In the present section a kinematic viscosity of 2.1 m^2s^{-1}, as in the plug part of the Cross model [123], has been used. In fact the majority of the flow impacted against the obstacle belongs to the upper part of the flow, where a plug flow is present. Therefore a dynamic viscosity μ of 2.1·ρ [kg/ms] is used.

Before to continue with our analysis a digression is necessary. A study concerning the variation of the pressure on the obstacle depending on the values of ρ and μ is pursued. Fig. 5.28.a shows the variation of the pressure along the obstacle length with a density increasing from 50 kg/m^3 to 150 kg/m^3 and a viscosity $\mu = 2.1 \cdot \rho$. Fig. 5.28.b shows the values of the integral done along the whole bar. Let is note that, in this way, doubling the ρ value, and consequently the viscosity too, the pressure is doubled.


[a]   [b]
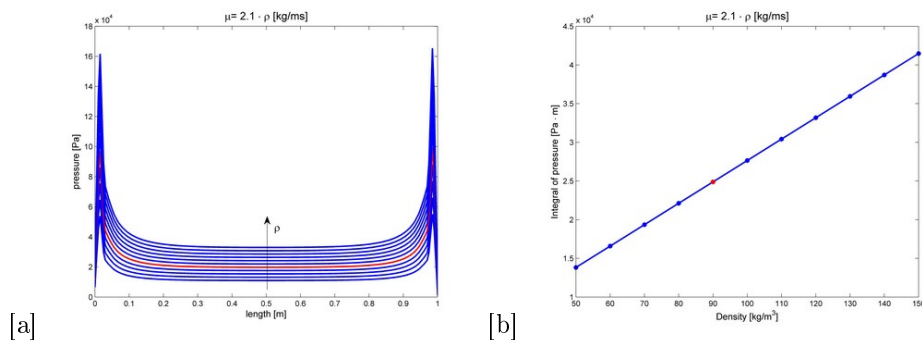
Figure 5.28: [a] Pressure and [b] integral of the pressure depending on a density varying from 50 kg/m^3 to 150 kg/m^3 and a viscosity $\mu = 2.1 \cdot \rho$. In red the value corresponding to ρ=90 kg/m^3.

Instead, if the density remains constant ($\rho = 90$ kg/m^3) but the viscosity changes, the pressure changes too (Fig. 5.29.a). However, since for the avalanches the relation of a pressure proportional to the density is experimentally seen in many situations leading to Eq. 1.41, we exclude the possibility of changing the viscosity value. In addition if the viscosity remains constant ($\mu = 2.1 \cdot 90$ kg/ms) the pressure, for instance, does not double if the density doubles (Fig. 5.29.b).
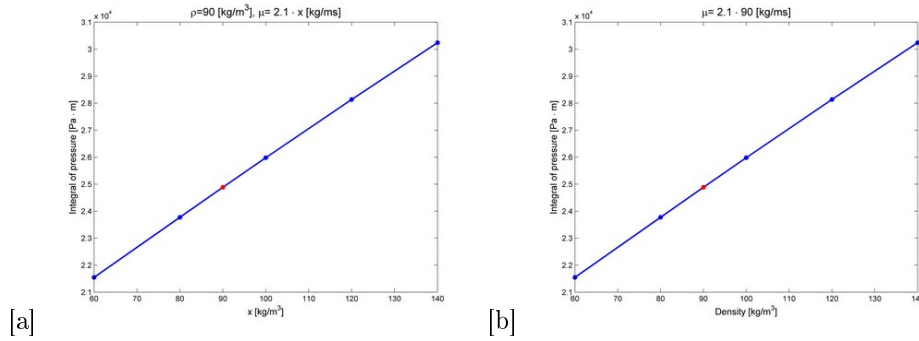

Figure 5.29: Integral of the pressure along the bar [a] taking the density ρ=90 kg/m^3 and the viscosity changing as $\mu = 2.1 \cdot x$ [kg/ms] and [b] taking the viscosity equal to $\mu = 2.1 \cdot 90$ [kg/ms] and the density variable. In red the simulation with ρ=90 kg/m^3 and $\mu = 2.1 \cdot 90$ kg/ms.

The results of simulations are compared with the pressure measured and with the structure of the snow around the obstacle. As seen in Sec. 4.3 the maximum of the pressure corresponds to 30.7 kPa (Fig. 4.16).

The simulations done by the software with a density of ρ=270 kg/m^3, that corresponds to the density of the first part of the untouched snowcover, and with the dynamic viscosity of $\mu = 2.1 \cdot 270$ kg/ms or $\mu = 2.1 \cdot 400$ kg/ms (as in the Cross model [124]) overestimates the pressure: the integrated pressure is of 74.7 kPa·m and 88.6 kPa·m respectively.

In order to evaluate the correct density value, a back-analysis can be done concerning the pressure. The well known formula Eq. 1.41 is applied with C_d=2 as in [183]. Substituting the maximum recorded pressure (30.7kPa), the value for the density ρ=95 kg/m^3 is calculated. The integral of the pressure is 26.3 kPa·m, that is lower than the maximum of data recorded but bigger than the pressure averaged each 0.1 s or each 0.056 s (the characteristic time). At this point we can follow three ways: (i) to increase the density value to about 110 kg/m^3 (Fig. 5.28.b) to reach the maximum of the data pressure (ii) to take the density equal to 95 kg/m^3 and vary the kinematic viscosity 2.1 m^{2}s^{-1} to reach the maximum of the data pressure (iii) to

decrease the density to 90 kg/m^3 that is more in agreement with the mean done each 0.1 s. We chose the third way, for not change the value of the kinematic viscosity presented in [124]. In addition we suppose that a meaning data of the pressure is more representative of the impact. Finally let is note that the variability between 90-110 kg/m^3 is not so elevate and we have an incertitude on the velocity too.

5.3.1 Influence of the verticality of the obstacle on the pressure

A further consideration is now done considering the fact that the avalanche does not impact perpendicularly the obstacle. In fact the obstacle was conceived to be vertical as well as the majority of structures of interest, such buildings (see Sec. 4.2). Hence, since the problem is not symmetric, it is not possible, as done for the deflection angle in the horizontal plane, to find pressure simply by multiplying the velocity value for the $\cos\theta$, where θ is the slope angle.

Therefore, to take into account this problem, a numerical investigation is carried. Several simulations are done varying the inclination of the obstacle considering, for simplicity a two dimensional problem (Fig. 5.30) in the stationary case. The density is $\rho = 90$ kg/m^3 and the viscosity is $\mu = 2.1 \cdot \rho$ kg/ms. A slip condition is given on the obstacle and along the slope. An inflow velocity equal to u=18 m/s is imposed. The gravity and the friction forces are omitted here since the flow is considered in its stationary situation, with the consequence that the resultant of all the forces (driving ones and frictional ones) acting on the fluid is null.

The pressure, found for different slopes, is integrated along the edge upwind and normalised with the value of the pressure $p_\perp$ of the obstacle considered perpendicular to the terrain (that is for $\alpha = 0$), as Fig. 5.31 shows. It is supposed that the pressure acting on an inclined obstacle is proportional to the pressure impressing an obstacle perpendicular to the slope through a factor C_α that is a function of the slope:

$$p_\alpha = C_\alpha \cdot p_\perp \tag{5.4}$$

Let be $\beta = 90 + \alpha$ the anti-clock angle between structure and slope. In particular Fig. 5.31 shows as for values of $\alpha \geq -40°$ $C_\alpha = 1 - \sin\alpha = 1 + \cos\beta$: higher β is lower the pressure is. The formula means that the pressure is equal to the pressure of a perpendicular obstacle plus its component parallel to the inclined obstacle. For values $\alpha < -40°$, instead, the pressure decreases probably due to a formation of a stagnation zone.

To apply this concept to our problem we consider $\alpha = -37°$. Hence C_α= 1.6 and thus, the pressure should be not 30.7 Pa but 19.2 kPa. Thus, the result of our simulation in the two-dimensional along the slope should be compared with this value. Let in addition note that for a more precise result a three-dimensional analysis
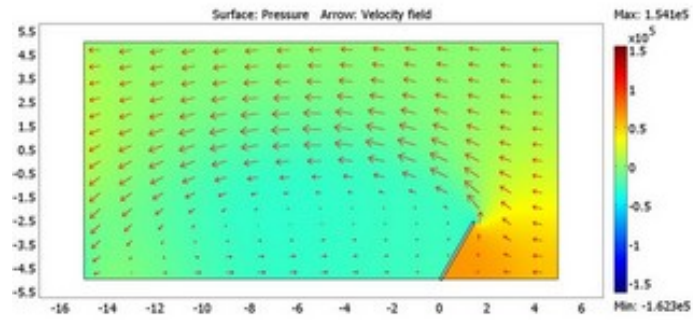
Figure 5.30: Simulations in COMSOL. The flow arrives from the right side, as the arrows, indicating the velocities, show. The pressure, indicated by the color surface, is positive (red) upward the obstacle and negative (blue) downward.
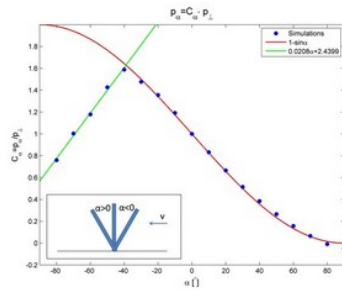

Figure 5.31: Variation of the C_α coefficient with the angle.

Table 5.5: Values of pressure found for different densities. The case of ρ=130 kg/m^3 corresponds to the RAMMS output (see Sec. 5.2). The value chosen for the next simulations is ρ=100 kg/m^3.

Density	Pressure in the central point	Integral of pressure along the obstacle
120 kg/m^3	26.4 kPa	33.2 kPa·m
100 kg/m^3	22.0 kPa	27.6 kPa·m
110 kg/m^3	24.2 kPa	30.4 kPa·m
130 kg/m^3	28.6 kPa	35.9 kPa·m

should be done. In fact, as in [46], the values of the coefficients diminish if a three-dimensional model is used instead a two-dimensional one. However, since in literature no information are given to take into account C_α, waiting for a deeper investigation, we decide to not use this concept. Only [16] deals with the problem of the orientation in respect of the verticality that can modify the results. An inclination <90° produces a major force than in the case of inclination >90°. However a deeper analysis is not reported there.

5.3.2 Deposit shape upward the obstacle

The following results are related to both simulations presented in [42] with ρ=28 kg/m^3 and u=18 m/s (based on previous wrong pressure data, calculated with a uncorrect factor of conversion) and to simulations carried with ρ=100 kg/m^3 and u=18 m/s, based on the corrected pressure data. In particular the density of ρ=100 kg/m^3 is chosen on the basis of the pressure found (see Tab. 5.5), compared to the 28.6 kPa experimentally measured (see Sec. 4.3.2).

Figg. 5.32.a,c show the simulation results, and in particular the velocity field. It is clear that the flow reduces its velocity close to the obstacle. Figg. 5.32.b,d show the velocity decrease in the last 3 m and 4.5, respectively, upwind the central point of the obstacle. We decided to consider the flow as stopped under a threshold value, in coherence with the fact that the snow is not an elastic material and therefore it looses energy and velocity when an impact occurs.

This supposition can be validated coupling two experimental results. The first one concerns the fact that the flow stops if its depth h is lower than a threshold value h_{stop}, depending on the slope angle (Eq. 5.3 of Sec. 5.1.3, [169]). The second one relates the velocity to the flow depth:

$$u = \beta g^{1/2} h^{3/2} / h_{stop}(\theta) \tag{5.5}$$

In [194] it was shown that, in the Vallée de la Sionne (CH) test site, the flow stops with a depth of $h(\theta_2) \sim 0.1$ m for steepest slope θ_2, corresponding to the
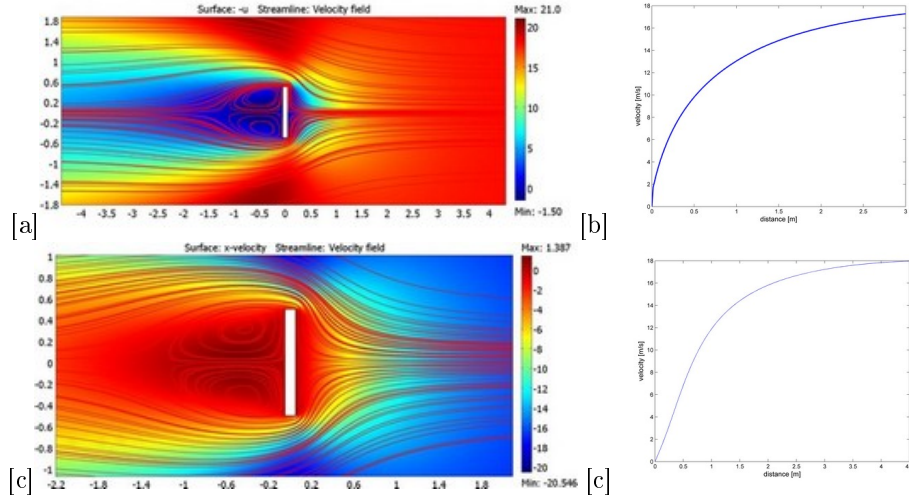
Figure 5.32: [a] Velocity around the obstacle and [b] in the 3 m upwind in the ρ=28 kg/m^3 case. [c] Velocity around the obstacle and [d] in the 4.5 m upwind in the ρ=100 kg/m^3 case. In [a] and [b] the avalanche flow comes from the right side.

inclination below which steady flow is possible and of $h(\theta_1)) \sim 1$ m for less steep one, corresponding to the inclination θ_1 below which no flow is possible. Based on these parameters, the beta value can be estimated. We suppose that in the obstacle area we are, at the large scale, in the zone of θ_2. There the velocity is 18 m/s and the flow depth is 2.5 m. Hence, we obtain $\beta = 0.1454$, very close to the value ($\beta = 0.136$) estimated by [169]. At a more refined scale, upwind the obstacle there is a little zone in which the slope decreases, due to installation works. For simplicity, we suppose that there $\theta = \theta_{min}$. Hence the velocity, from Eq. 5.5, becomes equal to $u_{lim} = \beta (gh(\theta_{max}))^{1/2} \sim 0.5$ m/s. Consequently, for this study we consider as a threshold the value u_{lim}=0.5 m/s. In addition a more detailed study is done using the data collected by the laser scan measurements done the 5th of March 2011 (see Sec. 5.1). In particular, using Eq. 5.3 whit the values found there ($\theta_1 = 21.4°$, $\theta_2 = 42.6°$, $L = 0.18$ m), at the slope angle of the obstacle $h_{stop}(37)$=0.068 m. Hence $\beta = 0.34$ and consequently u_{lim}=0.28 m/s, very close to the 0.5 m/s used in the first simulation. The concept of a threshold for the deposition is used by [155] too. Fig. 5.33 and Fig. 5.34 show the different steps to obtain the final deposition shape. The dihedral has a height of 0.55 m, corresponding to the measured one.

Under this assumption, the deposition of snow upwind the obstacle is possible. By a first analysis of streamlines analysis (Fig. 5.32.a and c), it is possible to suppose
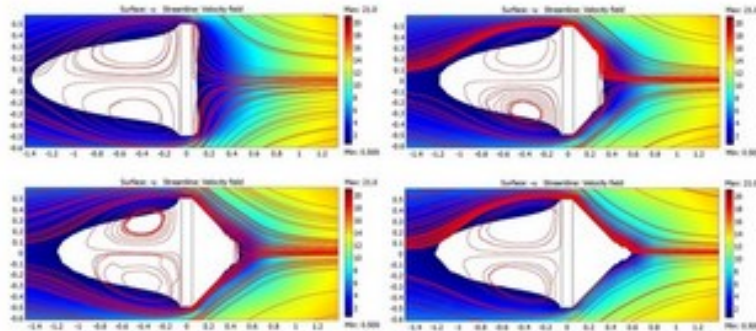
Figure 5.33: Some of the different steps carried to obtain the final shape, in which no area has a velocity lower than 0.5 m/s, in the case of ρ=28 kg/m^3. The avalanche flow arrives from the right side.

that the flow deposits with a dihedral shape. As shown in [200], the streamlines are hyperbolic. From a numerical point of view, to show how the snow deposits upwind the obstacle, the area where the velocity is lower than u_{lim} is considered as constituted of only deposited snow. Hence, further simulations are carried out supposing that the obstacle has an additional wedge shape positioned upwind it (Fig. 5.33 and Fig. 5.34). This procedure is repeated until the flow gets always a velocity larger than u_{lim} (see the last step of Fig. 5.33 and Fig. 5.34) [42].

For simplicity a regular shape is introduced (Fig. 5.35.a), in the case of ρ=28 kg/m^3. It is important to underline that in reality we should decrease at each step the boundary velocity too, since as described before, in the tail the snow velocity decreases in respect to the avalanche front. However, an analysis in which the entering velocity is lower (we used a velocity of 6 m/s in the avalanche tail), shows that the results do not change significantly (Fig. 5.35.b).

The obtained shape is compared with the survey in the field. In particular the snow upwind the obstacle has a width of almost 30 cm until 1 m of distance and then it opens like a fan for closer distances, obtaining the shape seen in Fig. 5.36. At a distance D of about 0.55 m the snow is deposited and begins to grow up (see Sec. 4.3). The dihedral snow deposit has slides slightly concave as in [200]. Our simulations are in agreement with this measurement: a length of 0.55 m is in fact found.

At the distance of 2.1 m the snow cover is eroded, meaning that the avalanche is here flowing, as the measurements obtained by the straw test confirm (see Sec. 5.1.2). From a numerical point of view, this is coherent with the presence of streamlines at this point.
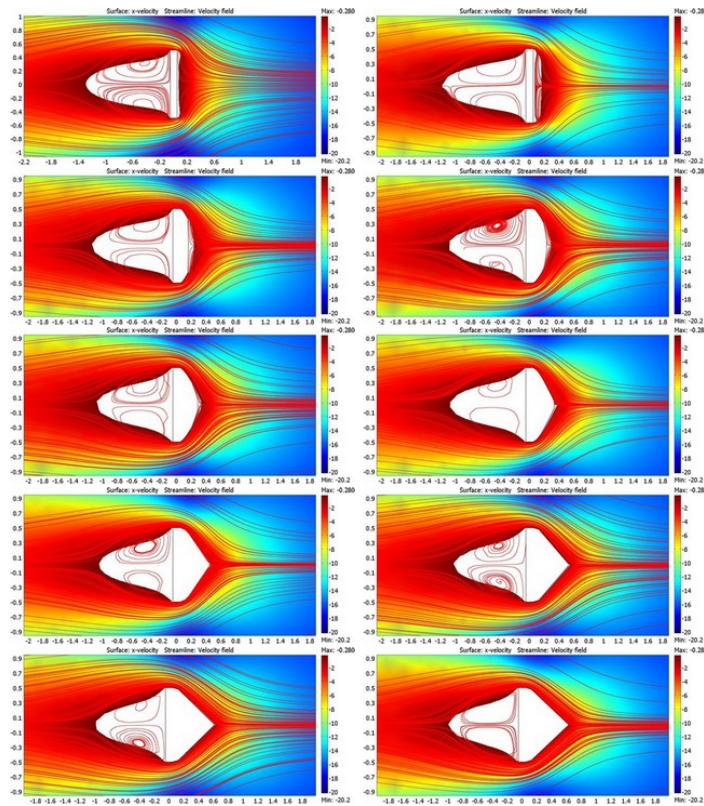
Figure 5.34: Steps n. 0,1,2,3,4,5,10,15,20 and 22 carried to obtain the final shape (step 22), in which no area has a velocity lower than 0.28 m/s, case ρ=100 kg/m^3. The avalanche flow arrives from the right side.
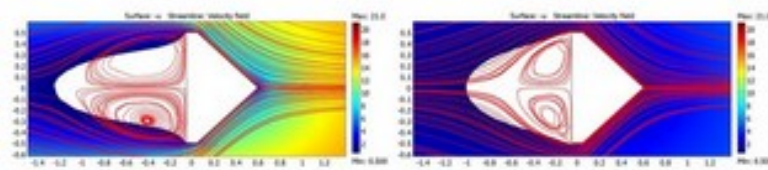

Figure 5.35: The triangular shape with the incoming velocity of 18 m/s (on the left) and of 6 m/s (on the right), in the case of ρ=28 kg/m^3. The avalanche flow arrives from the right side.

Figure 5.36: Shape of the snow upwards the obstacle after the avalanche of 5th of March 2011. The black point is the place of the straw test A (see Sec. 5.1.2).

5.3.3 C_p and C_d coefficient

The pressure on the impacting edges of the triangular shape of Fig. 5.35.a is shown in Fig. 5.37. As well as for Fig. 5.28, as concerns the C_p coefficient, Fig. 5.37 shows that the pressure is not uniformly distributed along its width: in fact there is a clear concentration at its corners.

Finally we focus the attention on the pressure on the obstacle. The integration on the impacting area, that corresponds to the right edge (in the rectangular case) or to the inclined edge (in the triangular case), of the horizontal force per area (Tx) is calculated in the situations of rectangular and traingular cases, for the case of $\rho=$ 28 kg/m^3. Its ratio $r = Tx_{rect}/Tx_{triang}$=8667.90/6331.3 =1.37 shows that, at the beginning, the force exerted on the obstacle is higher than at the end, when the dihedral shape is present. This results corresponds to the ratio between the drag coefficient (see Sec.1.6.1) of the two different shapes: $C_{drect}/C_{dtriang}$=2/1.5=1.33 [42].

Finally the two peaks in pressure on the corners, shown in Fig. 5.37, if translated in a bigger velocity, could be responsible of the fact that snow deposit on the obstacle edge is not present there (Fig. 5.36): a higher velocity sweeps away the snow.
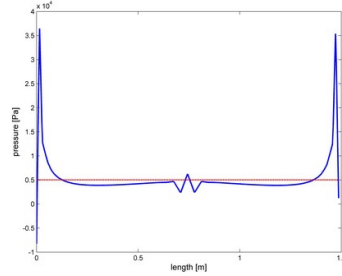
Figure 5.37: The simulated pressure on the impacting edges of the triangular shape. The mean value is $5 \cdot 10^3$ Pa corresponding to ρ=28 kg/m^3 and u=18 m/s.

5.4   Interaction between avalanche and obstacle: analytical approaches

5.4.1   Compressibility and peak of pressure

To take into account the snow compressibily Eq. 1.63, with $p = 28.6$ kPa (and $p = 30.7$ kPa), ρ_F=800 kg/m^3 is applied in two cases:

- Assuming the final density equal to ρ=340 kg/m^3, that can be considered the mean value of the density in the deposit (Fig. 4.17), the initial density becomes ρ_0=292 kg/m^3 (and ρ_0=289 kg/m^3 respectively);

- Assuming the initial density ρ_0=180 kg/m^3, that is the density at the release, the final density becomes ρ=217 kg/m^3 (and ρ=220 kg/m^3 respectively);

without giving satisfied results. For this reason we suppose that the pressure measured by our instrument doesn't record the initial peak of pressure. Thus, from Eq. 1.63 the pressure is found:

$$p = \frac{p_0}{\frac{\rho}{\rho_0} + \frac{\rho}{\rho_F} - 1} \tag{5.6}$$

Considering the deposit density of ρ=340 kg/m^3, and the flow density using ρ_0=180 kg/m^3 (and ρ_0=120 kg/m^3 in the coherence to RAMMS results, see Sec. 5.2) the impact pressure should be 76.1 kPa and 44.3 kPa respectively. This corresponds to a factor of peak of 2.7 and 1.5, similar to the 2-3 indicated in Sec. 1.7.2.

However, as seen in Fig. 4.16, the initial peak is not recorded. In our case it is not imputable to the precision of the instrument of measure of pressure, since data are recorded each 0.0005 s. Probably it is due to the fact that some snow particles arrive before the main part of the flow, impact the obstacle and compact themselves. Hence,

probably, the peaks of pressure act only in the impact area of the single particles without having effects on the mean pressure acting on the total area of the obstacle. A deeper analysis should be done for instance for each horizontal bar. Unfortunately the data are not yet processed and so they can be used.

5.4.2 Mohr-Coulomb criterion and HPEP coefficient

In this section the approach proposed by [26] (see Sec. 1.4.2) is used in order to estimate the pressure acting on the obstacle during the event of 5th of March 2011. We decide to apply this approach to the 5th of March 2011, even if the avalanche was not wet, because of the characteristic shape of the deposit upwind the obstacle that is suitable to this approach. In fact a dead zone of sticking snow remains on the obstacle. Besides, since this yield criterion is relevant under the conditions of slow-flow regime and low shear rates, we suppose that it can be applied to the final part of our avalanche, where the velocity and the Froude number are more similar to those of a slow wet avalanche. In our model, following the approach from [26], we assume that a dead zone forms locally against the obstacle and that its inclination follows the failure surfaces (related to the angle α). In Tab. 5.6 the geometrical and snow parameters used to estimate K'_p are reported. Since we suppose that the dead-zone boundary on the obstacle corresponds to the shear failure surface, α (Tab. 5.6) can be found in field with $2h$=0.66 m and $D = 0.55$ m (Fig. 5.38). h, w and e can be measured by the geometry of the deposit and of the obstacle, taking into account the impacted area. The density ρ is measured at a distance of 0.45 m above the obstacle (see Sec. 4.3.2).


Figure 5.38: The dihedral deposit on the obstacle.

For μ the value obtained in [43] is used (see Sec. 5.1.3), while δ is found by $\mu = \tan \delta$. Hence, by adding the contribution acting on each horizontal bar, the pressure found by means of Eq. 1.33 is p=1.43 kPa. This value is in a good agreement

Table 5.6: Parameters values in input and output of the model used.

Parameter	Value
α	31°
ϕ	28°
μ	0.39
δ	21°
h	0.33 m
w	0.6 m
e	0.1 m
ρ	320 kg/m^3
K_p	1.35
K_p'	3.02

with the final value of the pressure measured by the obstacle, where it is of order 1.4-1.8 kPa (Fig. 4.16).

5.4.3   Application of recommendations for small and large obstacles

In this section the formulae proposed in Sec. 1.7 and Sec. 1.8 for the pressure calculation are applied. The values generally used are: reference pressure 28.6 kPa, density $\rho = 122$ kg/m^3 and velocity $u = 18$ m/s. To deduce some general trend, the quality and the limitations of each model, more cases of study should be applied.

Swiss recommendations

The Swiss recommendations, for large obstacles, consider $C_d = 2$. The pressure found is than 39.5 kPa, slightly overestimating, the reference value.

European recommendations

The European recommendation give p_{peak}=118.6 kPa, overestimating the reference value. For the dense component, with $\rho_1 = 122$ kg/m^3, and $\rho_2 = 340$ kg/m^3, $Fr_1 = 5.7$, $h_1 = 1$ m with $h_2/h_1 = 3$ (and 8, that are the range recommended) it is obtained $f(Fr_1)$=1.14 kPa (and 1.05 kPa respectively), that is close to the 1.2 recommended and p_d=15.2 kPa (and 5.25 kPa respectively), underestimating the reference value.

Non-newtonian viscous model for small obstacles

With this example we want to show as the formula presented in Sec. 1.8.3 is not applicable for the Seehore test site. In fact introducing as parameters: D=1, n=0.8,

$\psi = 37°$, u=18 m/s, ρ=122 kg/m^3, to obtain a pressure of 28.6 kPa, it is necessary to have a flow of about h= 6.8 m, corresponding to a coefficient $C_d(Re, n)$= 1.47 (Fig. 5.39). For h= 1 m the pressure would be 3.9 kPa.
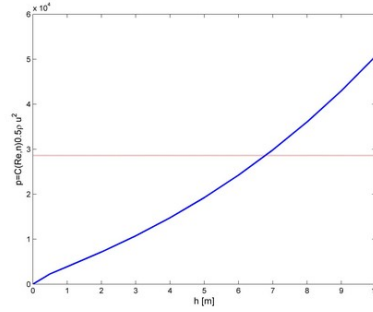

Figure 5.39: Pressure dependence on the flow height h using the model for small obstacle.

Frictional model of large flow at obstacles

Using the model for large obstacles [90] the pressure is been estimated too.

The starting data are the following (see [90] for the notation): θ_{min}= 21.4°, $\theta = 37°$ (data from Sec. 5.1.3), $\theta_{max} = 42.6°$, l= 1 m, l_a= 30 m, β= 1, $H = h$= 1 m, e= 0.1, u= 18 m/s, Fr= 6.4308. In addition it is supposed that $\delta_h = \delta_h^L$ and $\delta_u^L = \delta_u$, and that $V_0 = 0.5 \cdot [L \cos\theta \cdot (h/\cos\alpha + H + h/\cos\alpha)]$ in order to take into account of the verticality of our obstacle, and hence a different volume disturbed upstream the obstacle.

For the three-dimensional version (referring on Eqq. 14 and 15 of [90]) the results are: α =0.8496, α_{zm}=0.6390, α_{sl}=1.0602, γ=0.1387 and thus the contribution due to the dynamic force (Eq. 14 of [90]) is 0.9888 while the contribution of the sum of the incoming pressure force, the weight and the basal friction force (Eq. 15 of [90]) is 0.0247. Hence the inertial contribution is more important.

For the two-dimensional version (referring on Eq. 4 of [90]) the results are: α_{zm}= 0.2723, α_{sl}=0.2748, α=0.2736. Hence the result of the normalised force (Eq. 4 of [90]) is 0.3887.

In this way, having ρ= 122 kg/m^3, the forces found are equal to 7.68·10^{3}N, for the two-dimensional version, and F_u=5.86·10^5 N (Eq. 14) and F_{h+w-f}=1.46·10^4 (Eq. 15).

Chapter 6

Case study: the avalanche of Les Thoules, 2008

6.1 Avalanche impacting Les Thoules village

The purpose of this chapter is to analyse the destructive power of snow avalanche by the comparison of a real case study with simulations. In particular the avalanche occurred on 15th of December 2008 in the village Les Thoules in Valsavarenche (Aosta Valley-NW of Italy) (Fig. 6.1.a) at an altitude of 1600 m asl, is analysed. This avalanche, called *La Frange*, was registered only 3 times (the Regional Avalanche Cadastre of Aosta Valley reports on February 1971, on 14th of February 1974 and in winter 1981-1982) with a marginal interesting of the alluvial fan, never attending the extension of the 2008. In particular it never interfered with the houses or the viability. Furthermore, the area was principally agricultural and shepherd used [175], only in the 1950s for tourism purpose vacation houses and roads were built. In 2009, to mitigate the avalanche risk, 2.6 km of "snow umbrella" (Fig. 6.2) were located above the village in the area *Plan de la Tour* (see Sec. 1.1.2 for the illustration of this test site) [19].

6.1.1 Snow and meteorological conditions

In the Aosta Valley, Valsavarenche included, the period between the 13th to 17th of December 2008 was characterised by a snowfall with 3-15 cm/h. In such days in the whole Region 419 events were recordered: 69 of these overcame the perimeters of the Regional Avalanche Cadastre of Aosta Valley and 68 were classified as "new avalanches". In the alone Valsavarenche 47 avalanches were registered. In the whole winter 2008-2009, 1200 events were recorded by the Avalanche Forecasting Service of

Figure 6.1: [a] Localisation of Valsavarenche - Aosta Valley (IT), from [6]. [b] The path of La Tour avalanche on December 2008: in red the starting zone, in yellow the slope and in green the run-out zone, from [175].
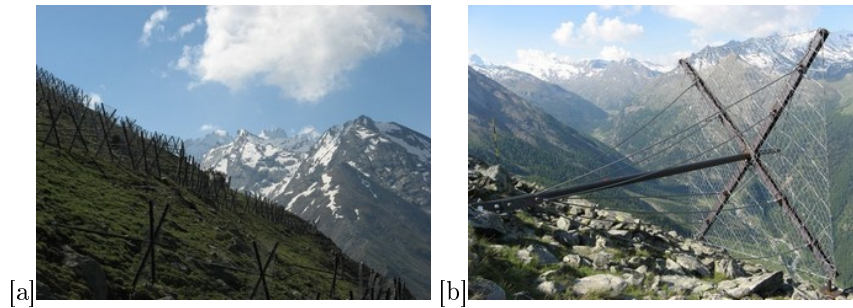

Figure 6.2: [a] Some rows of snow umbrella in the release area named *Plan de la Tour* and [b] a particular one. Photos E. Bovet.

Aosta Valley and 300 of those events had never occurred previously.

On 15th of December, the nivo-meteorological station closer to Les Thoules village (Dégioz at 1500 m asl) and the one at 2000 m asl (Orvielle) reported 110 cm and more than 150 cm of new snow, respectively. The snowfall increased the snow depth to 150 cm and to 300 cm at 1500 m and 2000 m asl, respectively. After the heavy snowfall, the meteorological conditions were characterized by a rise in temperature and by a moderate (sometimes strong) wind activity. For those reasons the Avalanche Bulletin reported a degree 5 of the avalanche danger scale on Monday 15th of December 2008.

6.1.2 The event of 15th of December 2008

Fig. 6.1.b shows the avalanche path released on 15th of December 2008 at about 1:00 p.m. from the slope named *Plan de La Tour* [175]. The release zone is located at an altitude of about 2430-2320 m asl (south-west exposition) with 45°-55° of slope inclination and it is covered by grass and rocks of small size. A thick and soft snow slab of about 50000 m^3 (maximum width of 350 m and thickness up to 1.5 m) released. The flow stops, after a difference in height of about 880 m in Les Thoules village.

The released thick and soft slab induced 3 avalanches: n.039 *La Frange* which impacted Les Thoules village; n.082 *Pro-Lombard nord* which arrested before the alluvial fan; n.083 *Pro-Lombard sud* which crossed the valley and interrupted the regional road arresting in the Savara river [175]. Because of the topography (in the next we will speak of a natural dam) in the run-out zone, the avalanche n. 039 split into two branches just before the regional road. The branch on the left side of the basin destroyed 4 houses [46] whereas the branch on the right side impacted two chalets and one house [41]. Other 5 houses were partially damaged (Fig. 6.3, 6.4.a-e). In addition a telephone and power poles was crushed and a high voltage pylon is damaged (Fig. 6.4.f). The regional and the municipal roads were interrupted (Fig. 6.4.g). Trees was uprooted (Fig. 6.4.h), and about 10 animals was killed. Luckily, nobody was in the houses, and consequently no casualties occurred [175].

6.2 Analysis of damages

6.2.1 Structural characterisation

To study the avalanche impact on the buildings, a back analysis of the structural damage was performed for all the houses involved by the event of 15th of December 2008 [41, 73, 101].

In particular the attention is focused on the houses n.1, n.2, n.3, n.5 and n.6 (Fig. 6.3).

Chalet n.1 and 2 were traditional wooden houses, called *chalet*, resting on a concrete foundation with a large terrace. The whole building was composed by three

Figure 6.3: Observed area of influence, from [175]. In red the houses destroyed, in yellow those only damaged.

levels: the lowest one was made of the concrete basement, while the second and the third were made of timber. The chalet structure was in softwood beams blocked each other by carved hinges (*blockbau* technique), while the internal partitions were composed of wooden panels. The wooden roof was covered by traditional plate stones (*lauze*). Ground elevation around the houses is different: east side apparently has only two levels. The roof of chalet n.2 is supported by an internal concrete pillar. Solid softwood columns, supporting the external structural planking (thickness equal to 7 cm), were placed at the corners and near the main openings [41].

The building n.5 was a small vacation house composed by n.3 floors with a rectangular plan (8 m x 5 m) with the maximum total height of about 760 cm and east-west orientation. The construction presented a reinforced concrete basement and an upper 30 cm thick structural masonry structure. Its roof was made of wood. It was destroyed by the avalanche which arrived against the east side: only a little part of the basement survived thanks to the topography of the slope (Fig. 6.7).

The building n.6 was a larger house composed by n.3 floors with a rectangular plan (12 m x 9 m) with the maximum total height of about 760 cm and east-west orientation. The construction presented a reinforced concrete basement and an upper 50 cm thick structural masonry structure. Its timber roof was covered by *lauzes*. The house was completely destroyed by the avalanche which hit the east side (Fig. 6.8). Only few parts of the retaining wall were found intact. Hollow bricks, unsuitable for structural walls, showed the poor quality of the construction [73].

Close to the house, a small building used as a garage was composed by n.2 floors with a rectangular plan (7 m x 5 m) with maximum total height of about 400 cm and east-west orientation. The construction presented a reinforced concrete basement and an upper 30 cm thick structural masonry structure. Its roof was a traditional alpine roof made of wood. Thanks to the topography of the slope, the basement of garage survived.

Figure 6.4: [a] House n. 3 destroyed. [b]-[e] Houses damaged. [f] High voltage pylon damaged. [g] Deposit on the road. [h] Trees crushed. Photos RAVDA.
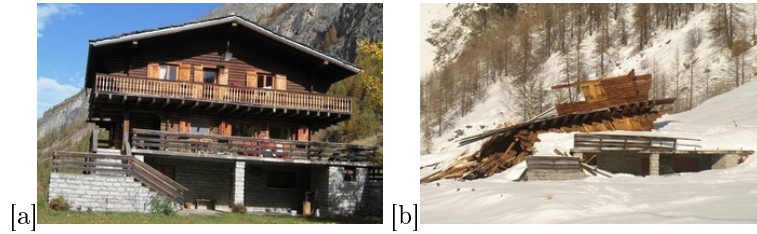
Figure 6.5: Chalet n.1 [a] before (Photo Chiaraviglio) and [b] after the avalanche (Photo RAVDA, from [175]). Note the concrete basement over which the entire upper timber structure moved.

Figure 6.6: Chalet n.2, partially damaged after the event. In [a] the roof of chalet n.1 is also visible. Photos RAVDA. In [c] and [d] particular of damages. Photos E. Bovet.

Figure 6.7: Building n.5: [a] before (Photo Rosai) and [b] after (Photo Fusinaz) the avalanche event of 15th of December 2008.
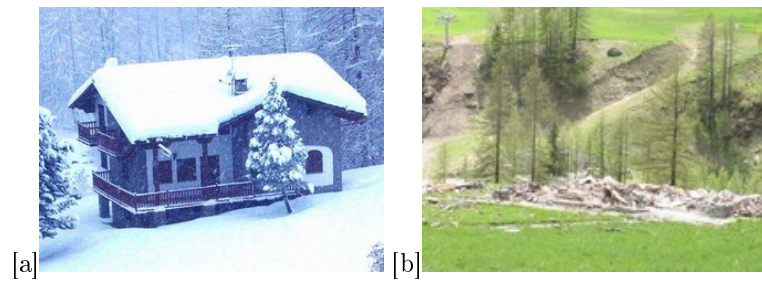

Figure 6.8: Building n.6: [a] before (Photo Cella) and [b] after (Photo Fusinaz) the avalanche event of 15th of December 2008.

6.2.2   Structural back-analysis

The event of 15th of December caused the total collapse of the timber structure of chalet n.1. As it is shown by post-event pictures, i.e. Figg. 6.5.b and 6.9, avalanche flow impacted the north-east corner of the building and caused a combined rotation and translation of the upper part. By a rigid body model, using equilibrium equations [41] and the fact that initially the body was at rest, the minimum force able to displace the upper timber part is about 900 kN [41]. The above model supposes rigid body
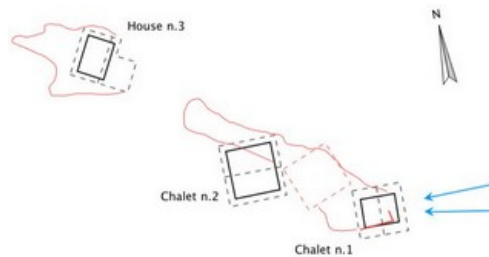

Figure 6.9: Blue arrows represent the most likely impact angle, red lines represent the perimeter of debris, red-dot line is the roof of chalet n.1 in the final displaced position, from [41].

rotation, therefore it overestimates the impact force. Considering the impact area, the average pressure is then equal to 54.5 kPa [41].

During the impact of 15th of December event, avalanche flow stroke the north-east corner of the building causing partial collapse of the structure of chalet n.2. The rupture of the bearing planking, structurally weakened by window openings, increased the lack of vertical restraint for the roof, which started to rotate. A back-analysis of the event is carried out in order to calculate an indicative value of flow velocity and impact pressure. Modeling roof dynamics as a plastic hinge on top of a timber beam, which supported half of the roof, the dynamical equilibrium equation is written [41, 73]. Found the time necessary to rotate, considered the volume of mass entered and accumulated into the building, and the impact area the estimated average velocity was 13.2 m/s [41]. Besides, the impact pressure can be calculated with reference to the collapse mechanism. Considering a timber cantilever of length $l = 2.50$ m subjected to an uniform distributed pressure, the collapse occurs at 18.8 kPa which represents a lower bound estimation if σ_{rupt}=12 MPa [41].

To estimate the impact pressure induced by the avalanche on the houses n.5, n.6 and on the garage n.6g, the analysis of damage, the mechanism of collapse and the direction of the dense flow are taken into account.

Regarding house n.5, we considered that the avalanche impacted the house against

the east side with a perpendicular direction, removing part of the building emerging from the slope (the first and the second floors). The collapse mechanism of the building is considered activated by the minimum impact force of the avalanche able to displace the destroyed part of the building. The weight of the structure, taking into account all parts of the building made in different materials, and the impact surface [101] were evaluated. The impact pressure is than estimated as about 45 kPa. In addition different modes of rupture are supposed. Firstly, a translational collapse mode considers the longitudinal walls acting as shear resisting elements. Secondly, a rotational collapse mode in which the internal partition walls stiffened the whole upper part, that behaved like a rigid body on the concrete basement. 25kPa were considered a lower estimation of the impact pressure [73].

Regarding the building n.6, the pressure estimated [101] is about 40 kPa, obtained by observations concerning (i) the mechanism (application of the arch-resisting pressure theory) [4] and the order (the east wall was the first to be damaged) of the collapse, (ii) the presence of windows, (iii) the fact that the building was completely destroyed, (iv) the presence of debris, (v) the location furthered downhill with respect to building n.5. Instead supposing that avalanche caused a local damage, which evolved into a global collapse, a lower value of 12 kPa is estimated [73].

6.3 Numerical methods to estimate impact pressure

The determination of the pressure acting upon the different houses was carried out by means of a numerical approach. In particular to reproduce the interaction between the avalanche and the different structures located along its path three different procedures are used, based on a stationary approach and on a transient one (Ch. 3). In all the cases the avalanche is considered as an incompressible fluid having density $\rho_{av} = 130$ kg/m^3 and viscosity $\eta_{av} = 10 \cdot \rho_{av}$ kg/ms, as in [41, 46]. The Navier-Stokes equations can be used Eq. 3.1. It is supposed that the avalanche was in its stationary phase, hence it did not accelerate or decelerate: consequently $F = 0$, that is, the gravitational force is balanced by the friction.

6.3.1 Two and three dimensional stationary approaches

In the first approach presented the whole final area (see Fig.6.3) is occupied by the snow in movement. The velocity at the end of the channel (boundary number a) is set equal to $|\mathbf{u}_0|$, as well as the initial condition. The value of $|\mathbf{u}_0| = 25$ m/s is been estimated by [101] using the Voellmy-Salm model. In the final part of the channel (boundaries b-h) the slip condition ($\mathbf{v} \cdot n = 0$) and $\mathbf{t} \cdot [p\mathbf{I} + Z(\nabla\mathbf{u} + (\nabla\mathbf{u})')] \cdot \mathbf{n} = \mathbf{0}$ are imposed, to indicate that the avalanche is channeled. Afterwards the open slope allows the avalanche expands itself outside the domain. For this reason, as boundary conditions $[Z(\nabla\mathbf{u} + (\nabla\mathbf{u})')] \cdot \mathbf{n} = \mathbf{0}$ and $p = 0$ are imposed. The Navier-Stokes

equations are consequently solved with Comsol Multiphysic [3]. The fluid used is newtonian: in fact we consider a model in the dimension of the slope, consequently variations along the avalanche depth, taken into account for instance by the non-newtonian flow, can not be described.

The same laws are solved even in their three-dimensional version always with the Comsol Multiphysics software.

6.3.2   Two dimensional transient approach

In the transient case, in the only avalanche area the velocity is imposed equal to $|\mathbf{u}_0|$. The boundary conditions are the same of the previous analysis, less the boundary a. The Navier-Stokes equations and the advection one are thereby solved in the transient analysis with the Comsol Multiphysic software.

The avalanche arrived in the building area with an initial velocity of $|\mathbf{u}_0| = 25$ m/s, as Fusinaz [101] estimated using Voellmy-Salm model. The other domain boundaries are considered as an open slope, allowing the avalanche to expand outside the domain.

In order to evaluate the impact pressure on the buildings, the stationary Navier-Stokes equations were solved in Comsol Multiphysics too.

6.4   Simulations results

6.4.1   Streamlines analysis and flow direction

The firsts simulations in the stationary situation are done using the viscosity of 10ρ kg/ms, considered suitable for the dry snow saltation layer. The choice is based, in fact, on the analysis of the streamlines around the obstacles in the deposit area (Fig. 6.10). For a major value of the viscosity, in fact, the flow wraps the obstacles and assumes the configuration as in Fig. 6.10.b [46].
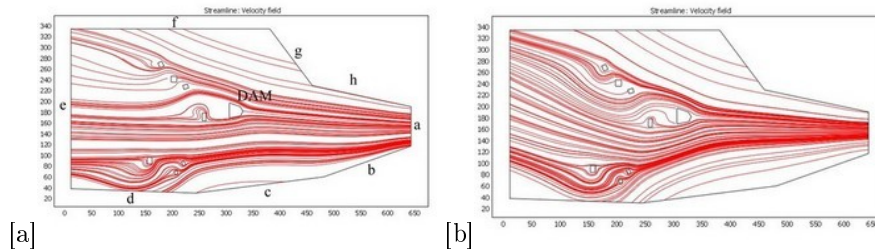

Figure 6.10: Streamlines in the final avalanche domain with [a] $\eta = 10 \cdot \rho$ kg/ms and [b] $\eta = 50 \cdot \rho$ kg/ms. Avalanche enters from the right side a.

The streamlines show as the flow is divided by the dam created by the morphology. The flow directions (Fig. 6.10.a) agree with these observed on the site (Fig. 6.3). In our simulation, contrarily to the real case, the flow after the dam can rejoin itself, since it cannot consider the differences in aspect. In addition the house n.4, really damaged, results not protected by the dam, as the streamlines confirm. On the contrary, the yellow structures near it (Fig. 6.3) have a reduced pressure since in the previous impact with the house n.4 the avalanche looses energy [46].

6.4.2   Left branch: houses n.5 and n.6

As concerns the left branch, a simulation is carried. Initially the velocity direction is proposed only horizontally. In this way, for the house n.5 and the garage n.6g the pressure values (of order of 40 kPa) obtained agree with those found in Sec. 6.2.2 by a back analysis of the damages occurred. On the contrary the house n.6 has an underestimated pressure (Fig. 6.11.a) [46].
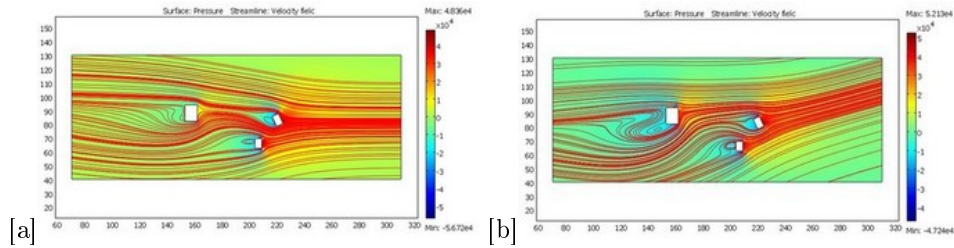

Figure 6.11: [a] The values of pressure agree with the real ones for the structures n.5 and n.6g [b] The simulated pressure is correct if the flow direction is oriented as in Fig.6.10.

Changing the position of the structure n.5 the pressure upwind the building n.6 is always too low (14 kPa), in fact it results protected by the previous house. On the contrary, modifying the impact angle φ of the flow (that corresponds to give as initial condition $u_0 = |\mathbf{u}_0| \cdot \sin\varphi$ and $v_0 = |\mathbf{u}_0| \cdot \cos\varphi$), in coherence with the streamlines indicating in Fig. 6.10, the pressure of about 40 kPa is registered on all the obstacles (Fig.6.11.b and Tab. 6.1) as in Sec. 6.2.2 [46].

Hence, the flow direction, and in particular the angle of incidence, plays a fundamental role in the magnitude pressure values. As in the Swiss procedure [80, 183], (see Sec. 1.7.1), the impact pressure is related to the incidence angle through the following relation:

$$p = p_{ref} \sin^2 \varphi \tag{6.1}$$

Table 6.1: Impact pressures simulated and calculated with a back-analysis.

House	Structural back-analysis	Simulations
Chalet n. 1	54.5 kPa	57.7 kPa
Chalet n. 2	18.8 kPa	10.7-35.5 kPa
House n. 5	45 kPa	~ 40 kPa
House n. 6	40 kPa	~ 40 kPa

Table 6.2: Simulated and calculated pressure by Eq. 6.1.

Degree	Simulated pressure	Calculated pressure (Eq. 6.1)
45°	$2.57 \cdot 10^4$ Pa	$2.60 \cdot 10^4$ Pa
60°	$3.93 \cdot 10^4$ Pa	$3.91 \cdot 10^4$ Pa
75°	$4.86 \cdot 10^4$ Pa	$4.86 \cdot 10^4$ Pa
90°	$p_{ref} = 5.21 \cdot 10^4$ Pa	$p_{ref} = 5.21 \cdot 10^4$ Pa

This law is verified for a rectangular shape having dimension 5 m x 5 m. As p_{ref} the upwind pressure calculated for a structure with $\varphi = 90^o$ is considered (Tab. 6.2).

6.4.3   Chalets n.1, n.2 and n.3

The aim of these simulations is to understand with which angle the avalanche impacted the buildings. From the damage analysis, in fact, chalet n.1, totally destroyed, protected the south angle of chalet n.2. On the contrary, house n.3 was not protected (Fig. 6.12) [41].

For this reason, different angles between 0°-15° range were investigated. Consequently, the streamlines were analysed (see Fig. 6.13), as well as the pressure values on the different impacted walls [41].

Notice that the model considers a constant slope angle: consequently the detailed morphology of the site was not taken into account in the analysis.

Fig. 6.14 shows the pressure acting on chalet n.1, for different impact angle.

With the second simulations, the pressure values measured on chalet n.2 were evaluated focusing the attention on the protection role played by chalet n.1. Consequently, the impact pressure and the velocity field generated with and without the presence of chalet n.1 are compared in Figg. 6.15, 6.16 and 6.17. In particular, for an increasing value of the impact angle, the south angle of chalet n.2 is more protected. For $\alpha = 90° - \varphi = 15°$ the whole east edge is protected. On the contrary, as Figg. 6.15 and 6.17 show, house n.3 results in any case not protected by chalet n.1.

Figure 6.12: Chalets n.1, n.2 and n.3. The house on the left was not damaged. Photo E. Bovet.
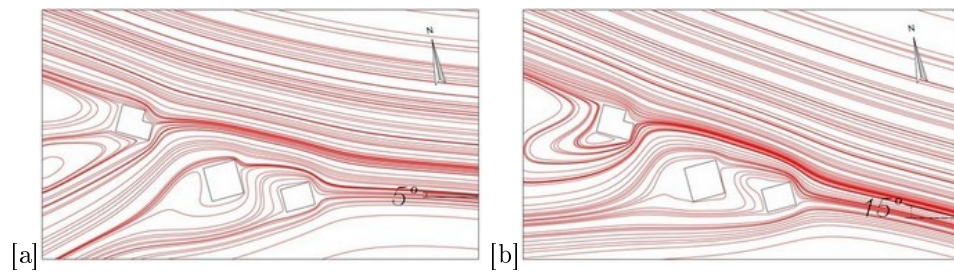
Figure 6.13: Streamlines for different impact angles: [a]$\alpha = 90° - \varphi = 5°$ and [b] 15°.
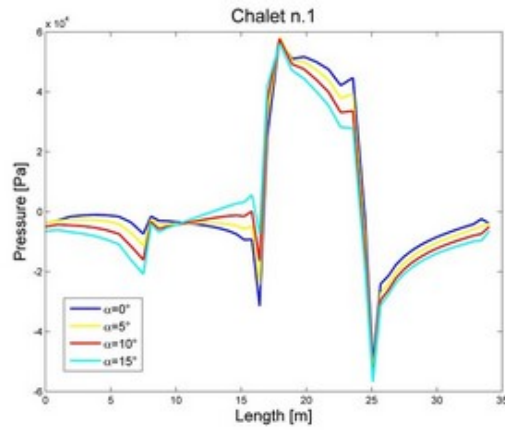
Figure 6.14: Pressures against chalet n.2 for different impact angles ($\alpha = 90° - \varphi = 0°, 5°, 10°$ and $15°$).
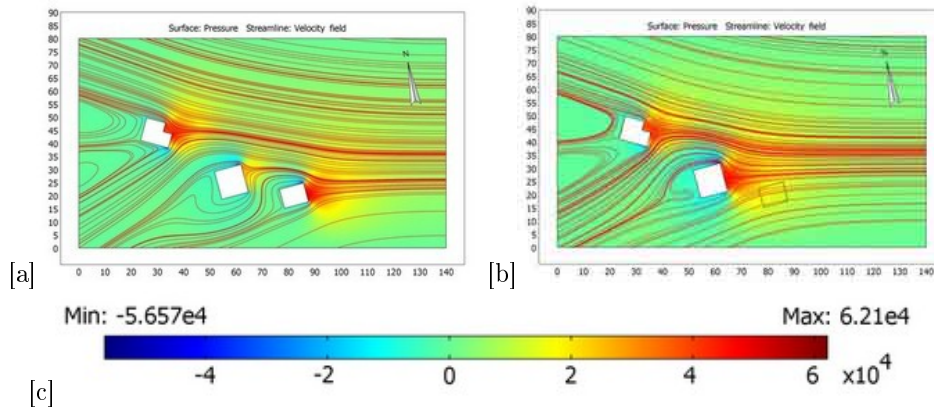

Figure 6.15: Chalet n.1 protects chalet n.2 from the avalanche stream: [a] with the chalet n.1 the pressure on chalet n.2 is lower than in the case of [b] without chalet n.1. [c] The range of pressure.
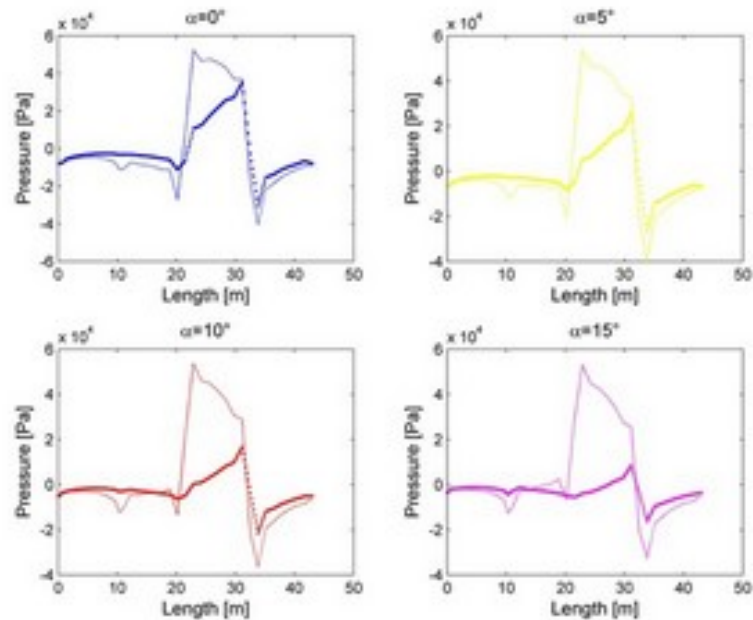
Figure 6.16: Pressures against chalet n.2 for different impact angles ($\alpha = 90° - \varphi = 0°, 5°, 10°$ and $15°$), corresponding respectively to the presence (dotted-line) or the absence (continuous-line) of chalet n.1.

The pressure distribution on chalet n.2 walls explains why the north side of the roof collapsed, whereas the south and west balcony were not damaged directly [41].

Both structural and numerical *a posteriori* analyses were performed to assess avalanche dynamics. From the previous results, the following aspects can be pointed out.

Referring to chalet n.1, the maximum pressure obtained from numerical analysis reaches the value of 57.7 kPa, while the minimum value obtained from the structural back-analysis is 54.5 kPa (Tab. 6.1). Thus, both previous results show that impact pressure might be about60 kPa. Due to confinement of the flow, the impact area in the real case was limited to the north-east corner. On the contrary, in the numerical model, the whole volume was considered in the avalanche flow, therefore pressure was distributed upon the entire east wall, with a maximum on the south-east corner because of flow direction. Referring to chalet n.2, impact pressure from numerical analysis varies from 10.7 kPa to 35.3 kPa, thus the lower estimation obtained from
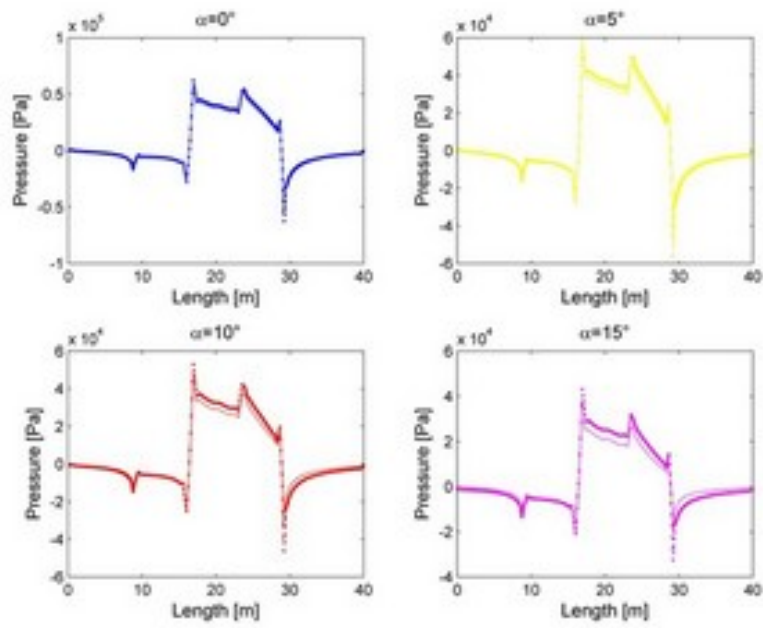
Figure 6.17: Pressures against chalet n.3 for different impact angles ($\alpha = 90° - \varphi = 0°, 5°, 10°$ and $15°$), corresponding respectively to the presence (dotted-line) or the absence (continuous-line) of chalet n.1.

the structural back-analysis, 18.8 kPa (Tab. 6.1), is considered as correct [41].

In the numerical model, the boundary flow velocity is $|\mathbf{u}_0|$=25 m/s [101], and no friction was imposed. The flow decelerates both close to the edges of the houses, since no-slip boundary conditions were applied, and in the down-wind death zone. Therefore, the numerical velocity field near the edge, equal to zero, cannot be compared with the results of the structural back-analysis. Hence, the Bernoulli's equation (Eq. 1.41, i.e. $p = \frac{1}{2}C_d\rho|\mathbf{u}_0|^2$), taking into account the drag coefficient C_d=2.00 for a square shape and flow density ρ=130 kg/m^3, was used. The maximum impact pressure on chalet n.2, obtained from the numerical analysis, is about 35.3 kPa, thus the velocity is 16.5 m/s. The corresponding value calculated from the back-analysis is 13.3 m/s [41].

From the previous considerations, we can conclude that chalet n.1 deviated the flow in such a way that the south-east corner of chalet n.2 was protected. As can be seen in Fig. 6.16, the removal of the upstream structure would cause higher pressures on the east face of chalet n.2 [41].

Comparing Fig. 6.9 with Fig. 6.15 similarities in debris directions appear. Therefore, the supposed impact angle might be correct. This hypothesis is also confirmed by the morphology of the site, if the gradient of the topographical surface is taken into account [41].

Fig. 6.18 shows the pressure acting on chalets n.1 and n.2 with the three dimensional simulations too.
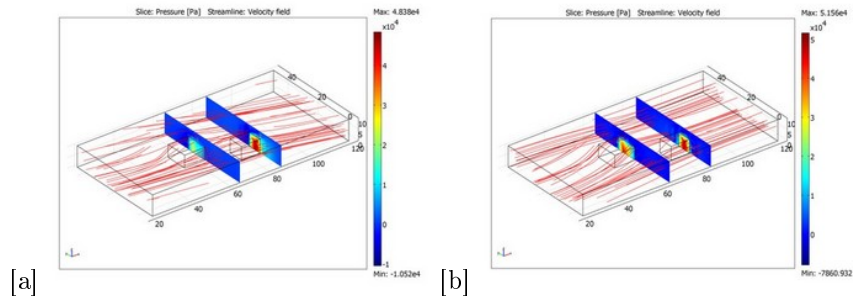

Figure 6.18: The impact pressure on chalets n.1 and n.2 with the three dimensional model for different impact angles ([a] $\alpha = 90° - \varphi = 0°$ and [b] 15°).

6.4.4   House n.3

Analysis of the C_d coefficient

For instance, for the house n.3 having dimension of 8 m x 10 m x 8 m the C_d obtained using the total force simulated is 1.9 in the case of a two-dimensional stationary simulation, agreeing with the values in literature, and it is 1.59 in the three-dimensional stationary one. Usually, in fact, the C_d obtained in a three-dimensional analysis is lower than in a two-dimensional one [46].

Analysis of the C_p coefficient

The pressure assumes different values, along the edges of the structures, depending on the C_p coefficient. This analysis seeks the evaluation of the parts that should have been more resistant. In particular, upwind C_p is positive, while laterally and downwind it is negative, indicating a depression. This is in coherence with the wind effects (see Sec. 1.7.4). Fig. 6.19 shows, in the stationary two-dimensional simulation, the ratio between the pressure and the maximum positive pressure for the house n.3, supposing a perpendicular impact.
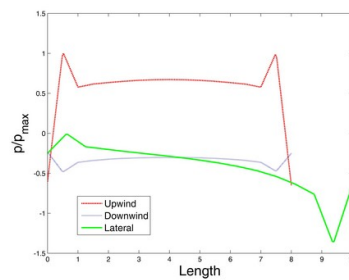
Figure 6.19: The pressure values along the different edges of the house having dimension 8 m x 10 m scaled with the maximum positive pressure.

In the three dimensional approach too, it is possible to visualize the different values of the pressure, as in Fig. 6.20. For instance the upwind pressure is close to 40 kPa. In particular the values characterizing the roof can be evaluated too. Let us note that in this case the flow depth is introduced [46].

Time evolution

In addition, thanks to a transient analysis, it is possible to evaluate the time history of the characteristics of the avalanche. For instance, in Fig. 6.21 the pressure in the
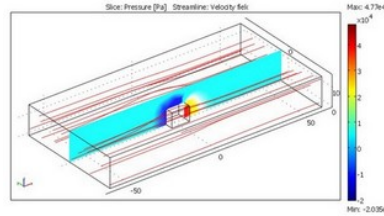
Figure 6.20: The impact pressure on the house n.3 with the three dimensional model.

central point upwind the house n.3 is shown. Three phases can be distinguished. In the first one, an initial peak probably means that the impacting snow compresses itself (see Sec. 1.7.2). In the second one, a stationary situation gives a pressure similar to the simpler two-dimensional stationary analysis. The third phase shows how in the avalanche tail the pressure decreases to zero [46]. Let is note that the peak value is about 3.7 times the stationary value, higher than the value of 3 recommended in [117] (see Sec. 1.7.2).
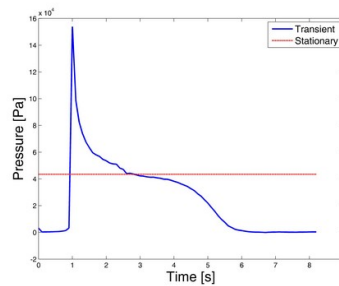
Figure 6.21: The evolution in time of the pressure in the central upwind point of the house n.3.

6.4.5 Small obstacles: the case of a tree

The situation of a 30 cm tree is analysed in Fig. 6.22 too, plotting directly on the boundaries the values of the pressure, scaled with the maximum positive pressure [46].

Finally, Fig. 6.22.b shows as the obstacles of negligible dimension, like trees of 30 cm of diameter, do not deviate the flow [46].
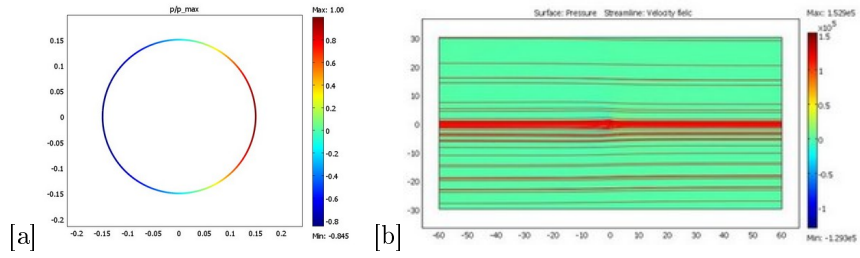
Figure 6.22: A tree of diameter of 30 cm: [a] its pressure values, along its circumference, scaled with the maximum positive pressure value. [b] A tree does not change the flow direction.

Conclusions and outlook

To conclude the main results of the thesis, the future outlooks and the weak points to be ameliorated are analysed. It is important to underline as many future implementation and research topics are born.

In this PhD thesis the complexity of the problem of the interaction between avalanche and structure is analysed, showing the importance to couple different study approaches. In fact each method has its points of force but its limits too. In the back-analysis of the damages the effects of the impact are clear but information on the dynamics and initial conditions are often missing. The full-scale experiments have the advantage of describing the real physics and processes but are limited by the elevate costs, the dependence on meteorological conditions in term of numbers and characteristics of the events, such as release height and area. The laboratory tests allow to know and to change the initial conditions and to repeat the experiments, investigating the physics of the problem, but they have problems in respect of the similitude criterion. The analytical and numerical approaches permit to keep the real scale and to decide the input of the problem but they are, for definition, "models" and hence they simplify the reality and suppose laws for the physical processes. Therefore, coupling all the methods a more real and complete analysis of the avalanche impact against structures process can be pursued.

The new dynamics model proposed has the advantage to define in all points the values of pressure and velocity without a depth averaged process, that considers only the mean values. In addition the pressure is not defined by the user by imposing a relationship with the velocity. Nevertheless in the model on the slope plane the flow depth cannot be calculated. Besides it is not suitable to be used to describe the avalanche motion from the release to the deposit because of its too long computational time. For the same problem the two-dimensional transient analysis is not extensible to a more complete three-dimensional one. However, the model is suitable to study the interaction with the structures, since in this way the calculus domain is reduced. To have the initial condition, as the velocity of the incoming flow, it is sufficient to couple it with a quicker depth averaged model. The new model for the erosion has the strong point that takes into account the influence of snow and avalanche properties,

the avalanche depth, the slope angle, and the position in the avalanche (front or tail). However it requires the knowledge of the parameters characteristics of the snow rheology. In future we would like to adapt it to insert into the commercial dynamics model RAMMS.

Going into the avalanche-structure interaction a first validation of the model, based on the state of the art notions and on real cases values (test site measurements and back-analysis of damages), is proposed. It is interesting as different features can be analysed, starting from the creation of a dead zone upstream an obstacle and arriving to the pressure distribution on the different parts of a structure. From a practical point of view, our simulations show the importance in the design of the structure shape and dimension as well as in the areal contest (if the obstacle is in a channel or in a open slope). In addition our analysis reveal the importance of considering the peak of pressure in the first instant of the impact, as well as the concentration of higher pressure values on the building corners, translated in the fact that these zones have to be more resistant, features that usually are not taken into account. The protection role of a structure on buildings farther down the slope, and the creation of dead zones downwind, should be considered too. The role played by the verticality of the buildings, i.e. having walls not perpendicular to the avalanche flow, is worth deepening. In fact probably since now the impact pressure estimated is lower than the real one, because the impact forces are evaluated basing on laws born for obstacles perpendicular to the slope. The dependence of the dead zone geometry on the obstacle characteristics, such as dimension and shape, and on the avalanche features, such as density and velocity, will be analysed too.

Future research topics are the study of the influence of the Froude number Fr on the impact pressure, in particular for values of $Fr < 1$. A turbulence model should be added to more correctly investigate the airborne avalanche and the avalanche-structure interaction. In addition the compressibility of the snow and the role played by the temperature should be taken into account, for instance using the more general Navier-Stokes equation for compressible fluids with the energy equation conservation too. Finally, for the transient model in the slope plane the change in the flow depth should be introduced.

As concern the experimental data, a detailed investigation will be made on the pressure and on the velocity profiles, when they will be available. The aim is to characterise the snow rheology, the boundary conditions (slip velocity values) and the dependence or not of the pressure on the velocity and on the flow regime. The analysis of the accelerometers measurements on the obstacle will allow an investigation of the dynamical effects of the impact on a structure too.

With regard to the erosion process, the potentiality of the new straw test to measure the real eroded snow in small avalanches is shown in the thesis. Moreover, the number of monitoring points will be increased along the whole path in order to better describe the zones where both erosion and deposition occur and where the

deposition is prevalent. The interesting relationship between the curvature and the deposition height will be validated using future experimental results. In addition the existence of a threshold velocity under which the avalanche stops will be analysed, maybe using the peculiarities of the non-Newtonian fluids.

Finally, for the slow movements the relationship among creep, glide and pressure on defence structures will be investigated.

Bibliography

[1] AdHoc software, url = http://www.adhoc3d.com/.

[2] ADINA, url = http://www.adina.com/.

[3] COMSOL Multiphysics, url = http://www.comsol.com/.

[4] *EN 1996 Eurocode 6 - Masonry - Part 1-1: General rules for buildings - Rules for reinforced and unreinforced masonry.*

[5] *Istruzioni per la valutazione delle azioni e degli effetti del vento sulle costruzioni, CNR-DT 207/2008.* ROMA – CNR 19 febbraio 2009.

[6] RAVDA, url = http://www.regione.vda.it/.

[7] *ENV 1991-2-4:1995. Eurocode 1. Basis of design and actions on structures. Part 2-4: Actions on structures - Wind actions.* 1995.

[8] *Norme Suisse: Actions sur les structures porteuses SIA 261:2003 Bâtiment, génie civil.* 2003.

[9] Action d'avalanche sur les galeries de protection. *Astra 12 007*, 2007.

[10] *Norme tecniche per le Costruzioni, DM 14 gennaio 2008.* 2008.

[11] AA. VV. Speciale progetto DYNAVAL. *Neve e Valanghe*, (73), 2011.

[12] AA. VV. *Manuale per lo studio dell'interazione del flusso valanghivo con un ostacolo.* Regione Autonoma Valle d'Aosta, 2012.

[13] G. Abbiati and R. Ceravolo. Identificazione dinamica di sistema "paravalanghe", 2010.

[14] G. Abbiati and R. Ceravolo. Progetto prove dinamiche su struttura paraneve, 2010.

[15] C. Ancey. Snow avalanches, 2004.

[16] C. Ancey. *Dynamique des avalanches.* École Polytechnique Fédérale de Lausanne, Lausanne, 2006.

[17] T. Aste, T. D. Matteo, and A. Tordesillas. *Granular and complex materials.* 2007.

[18] S. Bakkehoi, U. Domaas, and K. Lied. Calculation of snow-avalanche runout distance. *Annals of Glaciology*, 4:24–29, 1983.

[19] M. Barbero, F. Barpi, M. Borri-Brunetto, E. Bovet, E. Bruno, E. Ceaglio, B. Chiaia, V. De Biagi, M. Freppaz, B. Frigo, M. Maggioni, O. Pallara, L. Pitet, V. Segor, C. Vicari, and E. Zanini. A new test site in Aosta Valley (northwestern Italian Alps) for measuring the effects of snow-gliding on avalanche defence structures. *Geophysical Research Abstracts, 2011 EGU General Assembly 2011 and Vienna*, 13:EGU2011–10840, 2011.

[20] M. Barbero, F. Barpi, M. Borri-Brunetto, and O. Pallara. An apparatus for in-situ direct shear tests on snow experimental techniques. Submitted.

[21] M. Barbero, F. Barpi, M. B. Brunetto, E. Bovet, B. Chiaia, V. De Biagi, B. Frigo, O. Pallara, M. Maggioni, M. Freppaz, E. Ceaglio, D. Godone, D. Viglietti, and E. Zanini. A new experimental snow avalanche test site at Seehore peak in Aosta Valley (NW Italian Alps) – Part II: engineering aspects. *Cold Regions Science and Technology*, submitted.

[22] M. Barbolini, A. Biancardi, F. Cappabianca, L. Natale, and M. Pagliardi. Laboratory study of erosion processes in snow avalanche. *Cold Regions Science and Technology*, (43):1–9, 2005.

[23] M. Barbolini, F. Cappabianca, D. Issler, P. Gauer, and M. Eglit. Wp5: Model development and validation. Erosion and deposition processes in snow avalanche dynamics: report on the state of the art. Technical report, SATSIE PROJECT, 2003.

[24] M. Barbolini and F. Ferro. Definizione dei valori di progetto di parametri nivometrici standard per la prevenzione del rischio valanghivo sul territorio valdostano, 2005.

[25] M. Barbolini, L. Natale, G. Ticilla, and M. Cordola. *Linee guida metodologiche per la perimetrazione delle aree esposte al pericolo di valanghe.* AINEVA.

[26] D. Baroudi, B. Sovilla, and E. Thibert. Effects of flow regime and sensor geometry on snow avalanche impact-pressure measurements. *Journal of Glaciology*, 57(202):277–288, 2011.

[27] F. Barpi. Fuzzy modelling of powder snow avalanches. *Cold Regions Science and Technology*, (40):213–227, 2004.

[28] F. Barpi, M. Borri-Brunetto, and L. D. Veneri. Cellular-automata model for dense-snow avalanches. *Journal of Cold Regions Engineering*, 21 (4):121–140, 2007.

[29] M. Barsanti. Calcolo della distanza di arresto delle valanghe sulla base di parametri topografici del pendio. *Neve e Valanghe*, 9:86–97, marzo 1990.

[30] P. Bartelt, Y. Buehler, O. Buser, M. Christen, and L. Meier. Modeling mass-dependent flow regime transitions to predict the stopping and depositional behavior of snow avalanches. *Journal of Geophysical Research*, (117):F01015, 28 pp., 2012.

[31] P. Bartelt and O. Buser. Frictional relaxation in avalanches. *Annals of Glaciology*, (54):98–104, 2009.

[32] P. Bartelt and O. Buser. Production and decay of random kinetic energy in granular snow avalanches. *Journal of Glaciology*, 55(189):3–12, 2009.

[33] P. Bartelt, O. Buser, and K. Platzer. Starving avalanches: Frictional mechanisms at the tails of finite-sized mass movements. *Geophysical research letters*, (34):L20407, 1–6, 2007.

[34] P. Bartelt, B. Salm, and U. Gruber. Calculating dense-snow avalanche runout using a Voellmy-fluid model with active/passive longitudinal straining. *Journal of Glaciology*, 45(150):242–254, 1999.

[35] G. Beavers and D. Joseph. Boundary conditions at a naturally permeable wall. *Journal Fluid Mechanics*, 30:197–207, 1967.

[36] P. Beghin and X. Olagne. Experimental and theoretical study of the dynamics of powder snow avalanches. *Cold Regions Science and Technology*, (19):317–326, 1991.

[37] P. Berthet-Rambaud, A.Limam, P. Roenelle, F.Rapin, J.-M.Tacnet, and J.Mazars. Avalanche action on rigid structures: back-analysis of Taconnaz deflective walls' collapse in February 1999. *Cold Regions Science and Technology*, (47):16–31, 2007.

[38] P. Berthet-Rambaud, A. Limam, D. Baroudi, E. Thibert, and J. M. Taillandier. Characterization of avalanche loading on impacted structures: a new approach based on inverse analysis. *Journal of Glaciology*, 54(185):324–332, 2008.

[39] D. Bertrand, M. Naaim, and M. Brun. Physical vulnerability of reinforced concrete buildings impacted by snow avalanches. *Natural Hazards and Earth Systems Sciences*, 10(7):1531–1545, 2010.

[40] E. Bovet. *Dinamica delle valanghe: modelli matematici e legami costitutivi.* Tesi. Politecnico di Torino, 2005.

[41] E. Bovet, B. Chiaia, V. De Biagi, and B. Frigo. Pressure of snow avalanches against buildings. *Applied Mechanics and Materials*, 82:392–397, 2011.

[42] E. Bovet, B. Chiaia, and B. Frigo. Modelling and testing of avalanche impact on structures. *Proceedings XX Congresso AIMETA*, 2011.

[43] E. Bovet, B. Chiaia, M. Maggioni, D. Godone, and M. Freppaz. Snow erosion for small avalanches artificially triggered at the Seehore test site (NW italian alps).

[44] E. Bovet, B. Chiaia, M. Maggioni, D. Godone, and M. Freppaz. Different surveys techniques to assess the snow erosion and deposition at the Punta Seehore avalanche test site. *2012 International Snow Science Workshop, September 16-21, Anchorage (Alaska)*, 2012.

[45] E. Bovet, B. Chiaia, and L. Preziosi. Numerical analysis of snow avalanche mechanics and of its interaction with structures. *Proceedings XIX Congresso AIMETA, Ancona*, 14 - 17 September 2009.

[46] E. Bovet, B. Chiaia, and L. Preziosi. Interaction avalanche-obstacle: a first attempt of comparison between a real case study and numerical simulations. *2010 International Snow Science Workshop, October 16-22, Lake Tahoe (CA)*, pages 724–729, 2010.

[47] E. Bovet, B. Chiaia, and L. Preziosi. A new model for snow avalanche dynamics based on Bingham fluids. *Meccanica*, (45, issue 6):753–765, 2010.

[48] E. Bovet, B. Chiaia, and L. Preziosi. Two dimensional numerical analysis of snow avalanche interaction with structures. *Geophysical Research Abstracts*, 12:EGU2010–1857–1, 2010.

[49] E. Bovet, L. Preziosi, and B. Chiaia. Rheological models and slip velocity for avalanche dynamics with snow entrainment. *Journal of Glaciology*, submitted.

[50] E. Bovet, L. Preziosi, B. Chiaia, and F. Barpi. The level set method applied to avalanches. *Proceedings of the European COMSOL Conference 2007 in Grenoble, France*, 1:321–325, 2007.

[51] A. Briukhanov, S. Grigorian, S. Miagkov, M. P. I. Shurova, M. Eglit, and Y. Yakimov. On some new approaches to the dynamics of snow avalanches. *Physics of Snow and Ice: proceedings*, 1(2):1223–1241, 1967.

[52] G. Brugnot and R. Pochat. Numerical simulation study of avalanches. *Journal of Glaciology*, 27(95):77–88, 1981.

[53] O. Buser and P. Bartelt. Production and decay of random kinetic energy in granular snow avalanches. *Journal of Glaciology*, 55(189):3–12, 2009.

[54] O. Buser and H. Frutiger. Observed maximum run-out distance of snow avalanches and the determination of the friction coefficients μ and ξ. *Journal of Glaciology*, 26(94):121–130, 1980.

[55] G. Casassa, H. Narita, and N. Maeno. Measurements of friction coefficients of snow blocks. *Annals of Glaciology*, (13):40–44, 1989.

[56] R. Castaldini. Sul calcolo della distanza d'arresto delle valanghe. *Neve e Valanghe*, 21:50–61, marzo 1994.

[57] A. Casteller, M. Christen, R. Villalba, H. Martinez, V. Stoeckli, J. Leiva, and P. Bartelt. Validating numerical simulations of snow avalanches using dendrochronology: the Cerro Ventana event in Northern Patagonia, Argentina. *Nat. Hazards Earth Syst. Sci.*, (8):433–443, 2008.

[58] B. Chanut, T. Faug, and M. Naaim. Time-varying force from dense granular avalanches on a wall. *Physical Review E*, 82(4):041302, 2010.

[59] B. Chiaia, P. Cornetti, and B. Frigo. A shear lag model for the onset of dry slab avalanches. In *6th European Solid Mechanics Conference ESMC 2006 28 August – 1 September, 2006 Budapest, Hungary*, 2006.

[60] B. M. Chiaia, P. Cornetti, and B. Frigo. Triggering of dry snow slab avalanches: stress versus fracture mechanical approach. *Cold Regions Science and Technology*, (53):170–178, 2008.

[61] B. M. Chiaia, P. Cornetti, B. Frigo, and A. Luisi. Triggering of dry snow slab avalanches and a new concept of active protection. 2005.

[62] M. Chiou, Y. Wang, and K. Hutter. Influence of obstacles on rapid granular flows. *Acta Mechanica*, (175):105–122, 2005.

[63] M. Christen, P. Bartelt, and U. Gruber. AVAL-1D: an avalanche dynamics program for the practice. In *International Congress INTERPRAEVENT 2002 in the Pacific Rim – MATSUMOTO / JAPAN Congress publication, vol. 2*, pages 715–725, 2002.

[64] M. Christen, P. Bartelt, and J. Kowalski. Back calculation of the In den Arelen avalanche with RAMMS: interpretation of model results. *Annals of Glaciology*, 54(51):161–168, 2010.

[65] M. Christen, P. Bartelt, J. Kowalski, and L. Stoffel. Calculation of dense snow avalanches in three-dimensional terrain with the numerical simulation program RAMMS. *2008 Proceedings of the International Snow Science Workshop, September 21-27, Whistler (BC)*, 2008.

[66] M. Christen, J. Kowalski, and P. Bartelt. RAMMS: Numerical simulation of dense snow avalanches in three-dimensional terrain. *Cold Regions Science and Technology*, 63:1–14, 2010.

[67] Comsol. Comsol Multiphysics: rising bubble modeled with the Level Set Method, 2005.

[68] P. Coussot and C. Ancey. *Rhéophisique des pates et des suspensions*. EDP Sciences, 1999.

[69] P. Coussot, S. Proust, and C. Ancey. Rheological interpretation of deposits of yield stress fluids. *Journal of Non-Newtonian Fluid Mechanics*, 66(1):55 − 70, 1996.

[70] W. O. Criminale, J. L. Ericksen, and G. L. Filbey. Steady shear flow of non–newtonian fluids. *Archive for Rational Mechanics and Analysis*, (1):410–417, 1958.

[71] D. Daudon, J. Baroth, P. Szczurowska, M. Ying, and P. Perrotin. Finite element models and sensitivity analysis of the vulnerability of an avalanche protection gallery. *International Snow Science Workshop, Davos 2009, Proceedings*, 2009.

[72] V. De Biagi, B. Chiaia, and B. Frigo. Fractal grain distribution in snow avalanche deposits. *Journal of Glaciology*, 58(208):340–346, 2011.

[73] V. De Biagi, B. Chiaia, and B. Frigo. Structural back-analysis of avalanche impact on buildings. *Cold Regions Science and Technology*, submitted.

[74] J. Dent, K. Burrell, D. Schmidt, M. Louge, E. Adams, and T. Jazbutis. Density, velocity, and friction measurements in a dry snow avalanche. *Annals of Glaciology*, (26):247–252, 1998.

[75] J. D. Dent and T. E. Lang. Modeling of snow flow. *Journal of Glaciology*, 26:131–140, 1980.

[76] J. D. Dent and T. E. Lang. A biviscous modified bingham model of snow avalanche motion. *Annals of Glaciology*, 4:42–46, 1983.

[77] F. Domine, M. Albert, T. Huthwelker, H. Jacobi, A. A. Kokhanovsky, M. Lehning, G. Picard, and W. R. Simpson. Snow physics as relevant to snow photochemistry. *Atmos. Chem. Phys.*, 8:171–208, 2008.

[78] EAWS. Glossary snow and avalanches, 2012.

[79] W. Eckart, S. Faria, K. Hutter, N. Kirchner, S. Pudasaini, and Y. Wang. *Continuum description of granular materials*. Politechnical Institute, Turin, 2002.

[80] T. Egli. *Richtlinie Objektschutz gegen Naturgefahren (Translated Protection des objets contre les dangers naturels gravitationnels)*. Gebaudeversicherungsanstalt des Kantons St. Gallen, 1999.

[81] M. Eglit. Mathematical and physical modelling of powder-snow avalanches in Russia. *Annals of Glaciology*, (26):281–284, 1998.

[82] M. Eglit, V. Kulibaba, and M. Naaim. Impact of a snow avalanche against an obstacle. Formation of shock waves. *Cold Regions Science and Technology*, (50):86–96, 2007.

[83] M. E. Eglit and K. S. Demidov. Mathematical modeling of snow entrainment in avalanche motion. *Cold Regions Science and Technology*, (43):10–23, 2005.

[84] A. Farina. Waxy crude oils: some aspects of their dynamics. *Mathematical models and methods in applied sciences*, 7(4):435–455, 1997.

[85] A. Farina and A. Fasano. Flow characteristics of waxy crude oils in laboratory experimental loops. *Mathl. Comput. Modelling*, 25(5):75–86, 1997.

[86] A. Farina and L. Preziosi. Flow of waxy crude oils. *Progress in Industrial Mathematics*, pages 306–313, 1997.

[87] T. Faug. *Simulation sur modele reduit de l'influence d'un obstacle sur un écoulement à surface libre*. PhD thesis, University Joseph Fourier, Grenoble, 2004.

[88] T. Faug, R. Beguin, and B. Chanut. Mean steady granular force on a wall overflowed by free-surface gravity-driven dense flows. *Physical Review E*, 80(2):021305, 2009.

[89] T. Faug, P. Caccamo, and B. Chanut. Equation for the force experienced by a wall overflowed by a granular avalanche: experimental verification. *Physical Review E*, 84:051301, 2011.

[90] T. Faug, B. Chanut, R. Beguin, M. Naaim, M. Thibert, and D. Baroudi. A simple analytical model for pressure on obstacles induced by snow avalanches. *Annals of Glaciology*, 51(54):1–8, 2010.

[91] T. Faug and M. Naaim. Modelling a snow avalanche flowing past a protection dam: experimental investigations. In *Proceedings of the International Conference Avalanches and Related Subjects. Kirovsk, Russie, 4-8 september 2006*, pages 30–38, 2006.

[92] T. Faug, M. Naaim, and A. Fourrière. Dense snow flowing past a deflecting obstacle: an experimental investigation. *Cold Regions Science and Technology*, (49):64–73, 2007.

[93] T. Faug, M. Naaim, F. Naaim-Bouvet, N. Eckert, E. Thibert, and G. Chambon. Les récents progrès dans l'étude de la dynamique des avalanches de neige, des effets des obstacles et de la pression d'impact. In *Neige, paravalanches et constructions*, pages 69–111. Hermès, Lavoisier. Sous la direction de François Nicot et Ali Limam, 2010.

[94] L. Favier, D. Daudon, F. Donzé, and J. Mazars. Discrete element modelling to compute drag coefficients of obstacles impacted by granular flows. *International Snow Science Workshop, Davos 2009, Proceedings*, 2009.

[95] L. Favier, D. Daudon, F. Donzé, and J. Mazars. Predicting the drag coefficient of a granular flow using the discrete element method. *Journal of Statistical Mechanics: Theory and Experiment*, pages 1–14, 2009.

[96] A. Ferrero. *Simulazioni numeriche di valanghe di neve. Il metodo SPH. Studio di fenomeni valanghivi e simulazione di un evento reale*. Tesi. Politecnico di Torino, 2012.

[97] B. Frigo. *Effetti sulle strutture della componente aerosol delle valanghe: il caso della Valle d'Aosta*. Tesi. Politecnico di Torino, 2003.

[98] B. Frigo, B. Chiaia, M. Cardu, A. Giraudi, A. Godio, and R. Rege. Experimental analysis of snowpack effects induced by blasts. *2010 International Snow Science Workshop, October 16-22, Lake Tahoe (CA)*, pages 66–71, 2010.

[99] R. Fromm and P. Holler. Snow creep: a new and simple observation method and first calculations. *EGU*, pages EGU2010–9767, 2010.

[100] Y. Fukushima and G. Parker. Numerical simulation of powder-snow avalanches. *Journal of Glaciology*, 36(123):229–237, 1990.

[101] A. Fusinaz. *Vulnerabilità delle costruzioni a rischio valanghe: applicazione ad un evento in Valle d'Aosta*. Tesi. Politecnico di Torino, 2010.

[102] P. Gauer and D.Issler. Possible erosion mechanism in snow avalanches. *Annals of Glaciology*, (38):384–392, 2004.

[103] P. Gauer, D. Issler, K. Lied, K. Kristensen, H. Iwe, E. Lied, L. Rammer, and H. Schreiber. On full-scale avalanche measurements at the Ryggfonn test site, Norway. *Cold Regions Science and Technology*, 49:39–53, 2007.

[104] M. Givry and P. Perfettini. Construire en montagne: la prise en compte du risque d'avalanche. Technical report, Ministére de l'écologie et du développement durable. Ministére de l'équipement des transports, du logement, du tourisme et de la mer.

[105] J. M. N. T. Gray, Y. C. Tai, and S. Noelle. Shock waves, dead zones and particle-free regions in rapid granular free-surface flows. *Journal of Fluids Mechanics*, pages 161–181, 2003.

[106] S. S. Grigoryan and A. V. Ostroumov. Mathematical simulation of the process of motion of a snow avalanche. *Journal of Glaciology*, pages 664–665, 1977.

[107] H. Gubler and M. Hiller. The use of microwave FMCW radar in snow and avalanche research. *Cold Regions Science and Technology*, (9):109–119, 1984.

[108] K. M. Hákonardóttir, A. J. Hogg, T. Jóhannesson, M. Kern, and F. Tiefenbacher. Large scale avalanche braking mound and catching dam experiments with snow: a study of the airborne jet. *Surveys in Geophysics*, (24):543–554, 2003.

[109] C. Harbitz. A survey of computational models for snow avalanche motion. Technical report, Oslo, 1998.

[110] S. Hauksson, M. Pagliardi, M.Barbolini, and T. Jóhannesson. Laboratory measurements of impact forces of supercritical granular flow against mast-like obstacles. *Cold Regions Science and Technology*, (49):54–63, 2007.

[111] O. Hungr. A model for the runout analysis of rapid flow slides, debris flows, and avalanches. *Can. Geotech. J.*, (32):610–623, 1995.

[112] H. in der Gang and M. Zupancic. Snow gliding and avalanches. *International Association of Scientific Hydrology Publication 69 (Symposium at Davos 1965– Scientific Aspects of Snow and Ice Avalanches)*, (69):230–242, 1969.

[113] F. Irgens, B. Schieldrop, C. Harbitz, U. Domaas, and R. Opsahl. Simulations of dense-snow avalanches on deflecting dams. *Annals of Glaciology*, (26):265–271, 1998.

[114] D. Issler. Modelling of snow entrainment and deposition in powder-snow avalanches. *Annals of Glaciology*, 26:253–258, 1998.

[115] D. Issler. European avalanches test sites: Overview and analysis in view of coordinated experiments. Technical Report n. 59, Davos, 1999.

[116] C. Jaedicke, M. A. Kern, P. Gauer, M. A. Baillifard, and K. Plat. Chute experiments on slushflow dynamics. *Cold Regions Science and Technology*, (51):156–167, 2008.

[117] T. Jóhannesson, P. Gauer, P. Issler, and K. Lied. The design of avalanche protection dams. Recent practical and theoretical developments. Technical report, European Communities, 2009.

[118] T. Jóhannesson and K. Hákonardóttir. Remarks on the design of avalanche braking mounds based on experiments in 3, 6, 9 and 34 m long chutes, 2003.

[119] T. Jóhannesson, M. Hákonardóttir, K. Lied, D. Issler, P. Gauer, M. Naaim, T. Faug, L. Natale, M. Barbolini, F. Cappabianca, M. Pagliardi, L. Rammer, B. Sovilla, K. Platzer, E. Surinach, and I. Villajosana. Avalanche test sites and research equipment in Europe: an updated overview, in M. Barbolini and D. Issler, eds, 'Deliverable No. 8 of the EU Project SATSIE (Avalanche studies and model validation in Europe), 2006.

[120] K. Johnson. *Contact Mechanics*. Cambridge University Press Cambridge, U.K., 2001.

[121] A. Jones. Review of glide processes and glide avalanche release. *Can. Avalanche Assoc*, (69):53–60, 2004.

[122] K. Kawada, K. Nishimura, and N. Maeno. Experimental studies on a powder-snow avalanche. *Annals of Glaciology*, 1989.

[123] M. Kern and F. Tiefenbacher. Experimental devices to determine snow avalanche basal friction and velocity profiles. *Cold Regions Science and Technology*, (38):17–30, 2004.

[124] M. A. Kern, F. Tiefenbacher, and J. N. McElwaine. The rheology of snow in large chute flows. *Cold Regions Science and Technology*, (39):181–192, 2004.

[125] J. Koegl, A. Graf, L. Rammer, K. Kleemayr, M. Kern, P. Gauer, G. Kapeller, and M. Aufleger. Scaled laboratory experiments on the evolution of fluidised avalanches. *International Snow Science Workshop, Davos 2009, Proceedings*, 2009.

[126] K. Kojima. A field experiment on the rate of densification of natural snow layers under low stresses. *Snow Mechanics Symposium, Grindelwald, Switzerland*, 1974.

[127] K. Korner. The energy line method in the mechanics of avalanches. *Journal of Glaciology*, 26(94):501–505, 1980.

[128] V. M. Kotlyakov, B. N. Rzhevskiy, and V. A. Samoylov. The dynamics of avalanching in the Khibins. *Journal of Glaciology*, 19(81):431–439, 1977.

[129] V. Kulibaba and M. Eglit. Numerical modeling of an avalanche impact against an obstacle with account of snow compressibility. *Annals of Glaciology*, (49):27–32, 2008.

[130] T. Lang and R. Brown. Snow avalanche impact on structures. *Journal of Glaciology*, 25(93):445–455, 1980.

[131] T. Lang and J. Dent. Scale modeling of snow-avalanche impact on structures. *Journal of Glaciology*, 26(94):189–196, 1980.

[132] J. Larsen. Snow-creep forces on masts. *Annals of Glaciology*, (26):19–21, 1998.

[133] J. Larsen, J. Laugesen, and K. K. Kristensen. Snow-creep pressure on masts. *Annals of Glaciology*, (13):154–158, 1989.

[134] C. Leppert and D. Dinkler. A two-phase model for granular flows applied to avalanches. *III European Conference on Computational Mechanics Solids, Structures and Coupled Problems in Engineering*, 2006.

[135] K. Lied and S. Bakkehoi. Empirical calculations of snow-avalanche run-out distance based on topographic parameters. *Journal of Glaciology*, 26(94):165–177, 1980.

[136] Y. Ma, E. Thibert, P. Perrotin, and M. Mommessin. Actions of snow avalanches on a snow shed. *International Snow Science Workshop, Davos 2009, Proceedings*, pages 543–547, 2009.

[137] C. W. Macosko. *Rheology: principles, measurements and applications*. Wiley, 1994.

[138] M. Maggioni, M. Freppaz, E. Ceaglio, D. Godone, D. Viglietti, E. Zanini, M. Barbero, F. Barpi, M. B. Brunetto, E. Bovet, B. Chiaia, V. De Biagi, B. Frigo, and O. Pallara. A new experimental snow avalanche test site at See-hore peak in Aosta Valley (NW Italian Alps) – Part I: Conception and logistics. *Cold Regions Science and Technology*, 2012.

[139] M. Maggioni, M. Freppaz, M. Christen, P. Bartelt, and E. Zanini. Back-calculation of small avalanches with the 2d avalanche dynamics model RAMMS: four events artificially triggered at the Seehore test site in Aosta valley (NW Italy). *2012 International Snow Science Workshop, September 16-21, Anchorage (Alaska)*, 2012.

[140] S. Margreth. Snow pressure on cableway masts: Analysis of damages and design approach. *Cold Regions Science and Technology*, 47(1–2):4 − 15, 2007.

[141] S. Margreth and K. Platzer. New findings on the design of snow sheds. In *Jóhannesson, T., G. Eiríksson, E. Hestnes and J. Gunnarsson, eds., International Symposium on Mitigative Measures against Snow Avalanches Egilsstaðir, Iceland, 11–14 March 2008, Association of Chartered Engineers in Iceland*, pages 32–37, 2008.

[142] D. McClung. Creep and the snow-earth interface condition in the seasonal alpine snow-pack. *IASH Publ.*, (114):236–248, 1975.

[143] D. McClung, J. Larsen, and S. Hansen. Comparison of snow pressure measurements and theoretical predictions. *Canadian Geotechnical Journal*, 21(2):250–258, May 1984.

[144] D. McClung and A. Mears. Dry-flowing avalanche run-up and run-out. *Journal of Glaciology*, 41(138):359–372, 1995.

[145] D. McClung and P. Schaerer. *Manuale delle valanghe (The Avalanche Handbook)*. Zanichelli, 2005.

[146] D. McClung, S. Walker, and W. Golley. Characteristics of snow gliding on rock. *Annals of Glaciology*, (19):97–103, 1994.

[147] D. M. McClung. A model for scaling avalanche speeds. *Journal of Glaciology*, 36(123):188–198, 1990.

[148] D. M. McClung and P. Schaerer. Characteristics of flowing snow and avalanche impact pressure. *Annals of Glaciology*, (6):9–14, 1985.

[149] T. A. McMahon and J. T. Bonner. *Dimensioni e vita*. Zanichelli, 1990.

[150] M. Mellor. A review of basic snow mechanics. *Snow Mechanics Symposium, Grindelwald, Switzerland*, (IAHS-AISH Publication n.114):251–291, 1975.

[151] M. Mellor. Avalanches. *Cold Regions Science and Engineering*, submitted.

[152] M. Naaim and A. Bouchet. Etude expérimentale des écoulements d'avalanches de neige dense. Mesures et interprétations des profils de vitesse en écoulements quasi permanents et pleinement développés. Technical report, UR ETNA - Grenoble, 2003.

[153] M. Naaim, T. Faug, and F. Naaim-Bouvet. Dry granular flow modelling including erosion and deposition. *Surveys in Geophysics*, (24):569–585, 2003.

[154] M. Naaim, T. Faug, E. Thibert, N. Eckert, G. Chambon, and F. Naaim-Bouvet. Snow avalanche pressures on obstacles. *2008 Proceedings of the International Snow Science Workshop, September 21-27, Whistler (BC)*, pages 740–746, 2008.

[155] M. Naaim and I. Gurer. Two-phase numerical model of powder avalanche theory and application. *Natural Hazards*, (117):129–145, 1998.

[156] M. Naaim, F. Naaim-Bouvet, T. Faug, and A. Bouchet. Dense snow avalanche modeling: flow, erosion, deposition and obstacle effects. *Cold Regions Science and Technology*, 39(2-3):193–204, 2004.

[157] M. Naaim, J. M. Taillandier, A. Bouchet, F. Ousset, F. Naaim-Bouvet, and H. Bellot. French avalanche research: experimental test sites. In: M. Naaim and F. Naaim-Bouvet (eds.), Actes de Cemagref Editions, pages 141–169. Colloque "Snow and avalanches test sites", Grenoble (France) November 22–23, 2001. Technical report, 2001.

[158] C. Navier. Sur les lois du mouvement des fluides. *C. R. Acad. Sci.*, (6):389–440, 1827.

[159] K. Nishimura and N. Maeno. Contribution of viscous forces to avalanche dynamics. *Annals of Glaciology*, 13:202–206, 1989.

[160] K. Nishimura, H. Narita, N. Maeno, and K. Kawada. The internal structure of powder-snow avalanches. *Annals of Glaciology*, (13):207–210, 1989.

[161] H. Norem, F. Irgens, and B. Schieldrop. A continuum model for calculating snow avalanche velocities. In *Avalanche Formation, Movement and Effects (Proceedings of the Davos Symposium, September 1986). IAHS Publ., no. 162,1987.*, 1987.

[162] H. Norem, F. Irgens, and B. Schieldrop. Simulation of snow-avalanche flow in run-out zones. *Annals of Glaciology*, 13:218–225, 1989.

[163] H. Norem, T. Kvisterony, and B. D. Evensen. Measurement of avalanche speeds and forces: instrumentation and preliminary results of the Ryggfonn project. *Annals of Glaciology*, (6):19–22, 1985.

[164] S. Osher and J. Sethian. Fronts propagating with curvature dependent speed: algorithms based on Hamilton-Jacobi formulations. *Journal of Computational Physics*, (79):12–49, 1988.

[165] T. Otsuka, Y. Shimizu, I. Kimura, M. Otsuki, and Y. Saito. Fundamental studies on applications of MPS method for computing snow avalanches. *International Snow Science Workshop, Davos 2009, Proceedings*, pages 543–547, 2009.

[166] R. R. Pedersen, J. D. Dent, and T. E. Lang. Forces on structures impacted and enveloped by avalanches. *Journal of Glaciology*, 22(88):529–534, 1979.

[167] R. Perla, T. T. Cheng, and D. McClung. A two-parameter model of snow-avalanche motion. *Journal of Glaciology*, 26(94):197–207, 1980.

[168] K. Platzer, P. Bartelt, and M. Kern. Measurements of dense snow avalanche basal shear to normal stress ratios (S/N). *Geophysical Research Letters*, (34):L07501 1–5, 2007.

[169] O. Pouliquen. Scaling laws in granular flows down rough inclined planes. *Physics of fluids*, 11(3):542–548, 1999.

[170] L. Preziosi and G. Vitale. Multiphase model of tumour and tissue growth including cell adhesion and plastic reorganisation. *Mathematical Models and Methods in Applied Sciences*, 9(21):1901–1932, 2011.

[171] A. Prokop. Assessing the applicability of terrestrial laser scanning for spatial snow depth measurements. *Cold Regions Science and Technology*, 54(3):155 – 163, 2008.

[172] F. Rapin. A new scale for avalanche intensity. *2002 International Snow Science Workshop, September 29 - October 4, Penticton (BC)*, 2002.

[173] F. Rapin and C. Ancey. Occurrence conditions of two catastrophic avalanches at Chamonix, France. *2000 International Snow Science Workshop, October 2-6, Big Sky (MT)*, pages 509–513, 2000.

[174] M. C. Rastello. *Etude de la dynamique des avalanches de neige en aérosol*. PhD thesis, Centre d'Etude du Machinisme Agricole du Génie Rural et Forestier (CEMAGREF), Saint Martin d'Héres (France), 2002.

[175] Regione Autonoma Valle d'Aosta. Direzione Assetto Idrogeologico dei bacini montani. Ufficio Neve e Valanghe. Rendiconto nivometorologico, inverno 2008-2009. Technical report, Regione Autonoma Valle d'Aosta, 2009.

[176] P. Rognon. *Rhéologie des matériaux granulaires cohésifs. Application aux avalanches de neige denses*. PhD thesis, école Nationale des Ponts et Chaussées, 2006.

[177] P. Rognon, F. Chevoir, H. Bellot, F. Ousset, M. Naaim, and P. Coussot. Rheology of dense snow flows: Inferences from steady state chute-flow experiments. *J. Rheol.*, (52(3)):729–748, 2008.

[178] A. Romano, R. Lancellotta, and A. Marasco. *Continuum Mechanics using Mathematica. Fundamentals, Applications, and Scientific Computing.* Birkhauser, 2006.

[179] R. Sailer, L. Rammer, and P. Sampl. Recalculation of an artificially released avalanche with SAMOS and validation with measurements from a pulsed Doppler radar. *Natural Hazards and Earth System Sciences*, (2):211–216, 2002.

[180] B. Salm. Contribution to avalanche dynamics. *International Association of Scientific Hydrology Pubblication 69 (Symposium at Davos 1965 - Scientific Aspects of Snow and Ice Avalanches)*, pages 199–214, 1966.

[181] B. Salm. Snow forces on forest plant. *Proceedings IUFRO Seminar Mountain Forests and Avalanches, Davos*, pages 157–181, 1978.

[182] B. Salm. A short and personal history of snow avalanche dynamics. *Cold Regions Science and Technology*, (39):82–92, 2004.

[183] B. Salm, A. Burkard, and H. U. Gubler. *Berechnung von Fliesslawinen: ein Anleitung für Praktiker mit Beispielen (Calcul des avalanches: une méthode pour le praticien avec des exemples)*. Institut fédéral pour l'étude de la neige et des avalanches, n.47, July, 1990.

[184] S. Savage and K. Hutter. The dynamics of granular materials from initiation to runout: Part I. Analysis. *Acta Mechanica*, (86):201–231, 1991.

[185] P. Schaerer and A. Salway. Seismic and impact-pressure monitoring of flowing avalanches. *Journal of Glaciology*, 26(94):179–187, 1980.

[186] H. Shimizu, T. Huzioka, E. Akitaya, H. Narita, M. Nakagawa, and K. Kawada. A study of high-speed avalanches in the Kurobe canyon, Japan. *Journal of Glaciology*, 26(94):141–151, 1980.

[187] SLF. User manual v1.4 Avalanche.

[188] F. Sommavilla, B. Sovilla, and A. Tomaselli. Il sistema di monitoraggio per l'acquisizione dei parametri dinamici delle valanghe. *Neve e Valanghe*, 31:6–17, 1997.

[189] B. Sovilla. *Field experiments and numerical modelling of mass entrainment and deposition processes in snow avalanches.* PhD thesis, Swiss Federal Institute of Technology, Zurich, 2004.

[190] B. Sovilla and P. Bartelt. Observation and modelling of snow avalanche entrainment. *Natural Hazards and Earth System Sciences*, (2):169–179, 2002.

[191] B. Sovilla, P. Burlando, and P. Bartelt. Field experiments and numerical modeling of mass entrainment in snow avalanches. *Journal of Geophysical Research*, (111):F03007 1–16, 2006.

[192] B. Sovilla, M. Kern, and M. Schaer. Slow drag in wet-snow avalanche flow. *Journal of Glaciology*, 56(198):587–592, 2010.

[193] B. Sovilla, S. Margreth, and P. Bartelt. On snow entraiment in avalanche dynamics calculations. *Cold Regions Science and Technology*, (47):69–79, 2007.

[194] B. Sovilla, J. McElwaine, M. Schaer, and J. Vallet. Variation of deposition depth with slope angle in snow avalanches: measurements from Vallée de la Sionne. *Journal Of Geophysical Research*, (115):F02016 1–13, 2010.

[195] B. Sovilla, M. Schaer, M. Kern, and P. Bartelt. Impact pressures and flow regimes in dense snow avalanches observed at the Vallée de la Sionne test site. *Journal of Geophysical Research*, 113:F01010, 2008.

[196] B. Sovilla, M. Schaer, and L. Rammer. Measurements and analysis of full-scale avalanche impact pressure at the Vallée de la Sionne test site. *Cold Regions Science and Technology*, (51):122–137, 2008.

[197] J.-M. Tacnet, E. Thibert, P. Berthet-Rambaud, A. Limam, M. Naaim, P. Perrotin, and D. Richard. Conception et comportement dynamiques des structures de génie civil : application aux ouvrages paravalanches. *Science, Eaux & Territoires [en ligne], Revue SET*, (2):p. 46–57, 2010.

[198] Y. C. Tai, J. M. N. T. Gray, K. Hutter, and S. Noelle. Flow of dense avalanches past obstructions. *Annals of Glaciology*, 32:281–284, 2001.

[199] H. Teufelsbauer, Y. Wang, S. P. Pudasaini, R. I. Borja, and W. Wu. Dem simulation of impact force exerted by granular flow on rigid structures. *Acta Geothecnica*, 6(3):119–133, 2011.

[200] E. Thibert, D. Baroudi, A. Limam, and P. Berthet-Rambaud. Avalanche impact pressure on an instrumented structure. *Cold Regions Science and Technology*, (54):206–215, 2008.

[201] F. Tiefenbacher and M. Kern. Experimental devices to determine snow avalanche basal friction and velocity profiles. *Cold Regions Science and Technology*, (38):17–30, 2004.

[202] J. Tochon-Danguy and E. J. Hopfinger. Simulation of the dynamics of powder avalanches. In *Mécanique de la neige. Actes du Colloque de Grindelwald*, page 369–380. IAHS Publication No. 114, avril 1974.

[203] B. Turnbull and P. Bartelt. A one-Dimensional mixed flowing/powder snow avalanche model. *WCCM V, Fifth World Congress on Computational Mechanics*, 2002. Vienna.

[204] B. Turnbull and P.Bartelt. Mass balance of a mixed flowing/powder snow avalanche. December 2002. Printed in the Netherlands.

[205] UNESCO. *Atlas des Avalanches*. Paris, 1981.

[206] A. Upadhyay, A. Kumar, and A. Chaudhary. Velocity measurements of wet snow avalanche on the Dhundi snow chute. *Annals of Glaciology*, (A51(54)):139–145, 2010.

[207] J. L. Vallet, U. Gruber, and F. Dufour. Photogrammetric avalanche measurements at Vallée de la Sionne, Switzerland. *Annals of Glaciology*, (32):141–146, 2001.

[208] A. Voellmy. Über die zerstörungskraft von lawinen. *Schweiz. Bauztg*, 73:159–165, 212–217, 246–249, 280–285, 1955.

[209] M. Wieland, J. M. N. T. Gray, and K. Hutter. Channelized free–surface flow of cohesionless granular avalanches in a chute with shallow lateral curvature. *Journal Fluid Mechanics*, (392):73–110, 1999.

[210] H. Zhu, Y. Kim, and D. D. Kee. Non-Newtonian fluids with a yield stress. *J. Non-Newtonian Fluid. Mech.*, (129):177–181, 2005.